Modelling ash deposition during air firing of high percentages of biomass with coal

Peinong Xing

Submitted in accordance with the requirements for the degree of

Doctor of Philosophy

The University of Leeds

School of Chemical and Process Engineering

June 2016

The candidate confirms that the work submitted is his own, except where work which has formed part of jointly-authored publication has been included. The contribution of the candidate and the authors to this work has been explicitly indicated below. The candidate confirms that appropriate credit has been given within the thesis where has been made to the work of others.

The details of Chapters 3, 4, 5, 6 and 7 of the thesis are based on the following published papers respectively:

1. Rizvi, T., Xing, P., Pourkashanian, M., Darvell, L.I., Jones, J.M., Nimmo, W. 2015. Prediction of biomass ash fusion behaviour by the use of detailed characterisation methods coupled with thermodynamic analysis. Fuel. 141(2015), pp.275–284.
2. Xing, P., Darvell, L.I., Jones, J.M., Ma, L., Pourkashanian, M., Williams, A. 2016. Experimental and theoretical methods for evaluating ash properties of pine and El Cerrejon coal used in co-firing. Fuel. 183(2016), pp.39-54.
3. Xing, P., Mason, P., Chilton, S., Lloyd, S., Jones, J.M., William, A., Nimmo, W. 2016. A comparative assessment of X-ray fluorescence and wet chemical analysis methods for ash composition analysis of solid biomass fuels. Fuel. 182(2016), pp.161-165.

Details of the contributions from the candidate and co-authors are as follow:

1. The candidate performed some of the experimental work and analysis.
2. The candidate performed all the experiments, analysis and write up. Mr. Lloyd and Dr Darvell supported the experimental and analytical techniques. Dr Fowell supported in the proof reading. Professor Williams and Professor Jones contributed with the comments, guidance and proof reading.
3. The candidate performed all the experiments, analysis and write up. Mr Lloyd and Mr Mason supported in the experimental and analytical techniques. Professor Williams and Professor Jones contributed with the comments, guidance and proof reading.

Acknowledgements

I would like to thank my project supervisors, Professor Jenny Jones, Professor Mohamed Pourkashanian, Professor Alan Williams, Professor Lin Ma, Dr Amanda Lea-Langton and Mr Simon Lloyd, for their help, guidance and supervision in the review of the literature, the guidance on how to study the ash deposition during air firing of high percentages of biomass and also for believing in me. I am very lucky to have someone as good as them to learn from. I am also deeply grateful to the University of Leeds for the support and the opportunities provided to me.

Abstract

This project is aimed towards an understanding of ash deposition during air firing of high percentages of biomass with coal. Biomass resources are widely used as sustainable, renewable and environmentally friendly materials. There has been an increase in the use of biomass for power generation by means of co-firing with coal as well as by the combustion of 100% biomass. Despite the advantages of biomass in reducing carbon emissions from the electricity sector, the co-firing of high percentages of biomass can potentially aggravate ash related problems in the boiler. In order to develop mitigation strategies for the formation of deposits, an understanding of the ash behaviour during the combustion of high percentages of biomass is required. To understand ash deposition, the influence of the inorganics, crystal types, and complex compound formation should not be neglected. In this work, ash samples from El Cerrejon coal and pine, wheat straw, white wood pellet biomass were characterised for their inorganic composition by X-ray fluorescence (XRF) and wet chemical methods. Relationships between these two methods were found and a modification to the standard test method has been recommended to improve the accuracy of the XRF method. Furthermore, the melting behaviour of ashes from pure El Cerrejon coal, biomasses, and their blends were studied through ash fusion tests and via a method using a simultaneous thermal analyser coupled to mass spectrometer (STA-MS) for the evolved gas analysis. The inorganic composition were used to calculate indices to determine the slagging and fouling potential of pure fuel ash, ash blends and ash produced by ashing blended fuels (fuel blends ash). Base-to-acid ratio ($R_{b/a}$) results indicate that pine ash has a higher slagging potential than coal ash, which is not consistent with the experimental ash fusion measurements. Viscosity models appear to perform better for high-coal content blends than high-biomass content fuel,

and further refinement is required for modelling the viscosity of pure biomass ash as well as high co-firing percentages. Thermodynamic modelling of slag formation was undertaken using the FactSage model and verified by XRD analysis for the solid phase. XRD showed complex interactions between inorganics which changed with biomass type, blend ratio and temperature. The FactSage model was successful in predicting the changes of gas, solid and liquid phases during pure biomass, coal and co-combustion, and for most of the blends studied the prediction of slag formation was within 100°C of the measured experimental ash melting window.

Table of Contents

Acknowledgements.....III

Abstract..... IV

Table of Contents VI

List of Tables IX

List of Figures..... XI

Chapter 1 Introduction.....1

1.1 Background 1

1.2 Current biomass energy policy in UK.....4

1.3 Current biomass energy application.....6

1.4 Ash deposits problems of high percent biomass combustion 8

1.5 Thesis Aim 12

Chapter 2 Literature Review.....13

2.1 Coal combustion technologies 13

2.1.1 Pre-treatment of coal.....14

2.1.2 Coal combustion process 17

2.1.3 Coal combustion systems.....23

2.1.4 CO_2 capture and coal oxy-combustion.....27

2.1.5 Coal combustion issues.....29

2.2 Biomass combustion technologies 31

2.2.1 Pre-treatment of biomass: 31

2.2.2 Biomass combustion process 35

2.2.3 Biomass combustion system.....38

2.2.4 Biomass co-combustion and Oxy-combustion 41

2.2.5 Biomass combustion issues.....43

2.3 Ash composition in combustion.....45

2.3.1 Inorganic compounds in biomass ash 45

2.3.2 Inorganic in El Cerrejon coal ash.....51

2.3.3 Forming mechanism of ash deposition 53

2.3.4 Composition and crystal structures in ash deposition.....61

2.3.5 The prediction of biomass ash behaviours.....63

2.4 The limitations of previous studies 66

Chapter 3 Fuel Analysis and Ash Sample Preparations 68

3.1 Pretreatment of fuel.....68

3.2 Ultimate and proximate tests.....69

3.3 Ash samples preparation 73

3.4 Ash samples from pilot scale test.....77

Chapter 4 Ash Composition Analysis 81

4.1 Methodologies of ash composition analysis 81

4.1.1 X-Ray Analysis.....82

4.1.2 Wet Chemical Analysis.....82

4.2 A comparative assessment of ash composition analysis 86

4.2.1 The accuracy of XRF test.....87

4.2.2 A comparison results of ash composition by different testing methods ...91

4.3 Ash composition of biomass ash, coal ash and co-firing ash.....101

4.4 Crystal analysis of ash composition by XRD 107

4.4.1 El Cerrejon coal ash 107

4.4.2 Pine, wheat straw and white wood pellet ash....111
4.4.3 Ash blends....116
4.4.4 Pilot scale test ash samples....122
4.5 Summaries....126
Chapter 5 Ash Thermal Properties and Fusion Performance....128
5.1 Ash fusion properties....128
5.1.1 The ash fusion characteristic temperatures....129
5.1.2 The change in height of AFT samples....132
5.2 Melting behaviour by simultaneous thermal analysis....138
5.3 Summaries....151
Chapter 6 The Prediction of Ash Fouling and Slagging Potential....153
6.1 Numerical indices of slagging and fouling....154
6.2 Different viscosity models....162
6.3 Equilibrium modelling by FactSage....174
6.3.1 The El Cerrejon coal 1 and pine co-firing model....174
6.3.2 The El Cerrejon coal 2 and wheat straw co-firing model....181
6.3.3 The white wood pellet pure combustion model....189
6.3.4 The PACT ash thermodynamic equilibrium model....191
6.4 Summaries....196
Chapter 7 General Discussion....197
Chapter 8 Conclusions....214
Future Works....217
References....218

List of Tables

Table 2.1 Different types of moisture in coal and methods for removal.....17
Table 2.2 Basic reactions during coal combustion 19
Table 2.3 Analysis of biomass ashes in main oxides. 48
Table 2.4 The formation mechanism of biomass ash. 50
Table 2.5 Summary of El Cerrejon coal. 51
Table 3.1 Pure fuel property results from proximate and ultimate tests. 71
Table 3.2 Fuel blends properties by calculation. 72
Table 3.3 Pure fuel ash sample designations and preparation conditions. 74
Table 3.4 Blending fuel ash and ash blends sample designations and preparation conditions. 75
Table 3.5 Pilot scale test ash samples. 76
Table 3.6 Re-burned ash of collected pilot scale test ash samples. 76
Table 3.7 Experimental parameters for the non-preheated air-firing cases.....77
Table 3.8 Flue gas emissions for the non-preheated and preheated cases.....78
Table 3.9 Ashing process controlling parameters 78
Table 3.10 Ultimate and Proximate analysis and calorific value data of El Cerrejon coal 2 80
Table 4.1 Reference names used for the biomass ash prepared at temperatures of 550/850 ℃. 91
Table 4.2 Wet chemical analytical methods for the major elements in the ash analysis. 92
Table 4.3 Tested inoganic oxides of different biomass ashes composition (%). Case 1: Ash samples prepared in two stages at 550 ℃ then 850 ℃; Samples fused into glass disc at 1200 ℃. 93
Table 4.4 Tested inorganic oxides of ash composition results for biomass ash and standard coal ash at 815 ℃. Case 2: Ash samples prepared in two stages at 550 ℃ then 815 ℃; Samples fused into glass disc at 1100 ℃. 99
Table 4.5 Inorganic oxides components of El Cerrejon coal 1 and 2 ash, pine ash, wheat straw ash and white wood pellet ash blend.....103
Table 4.6 Inorganic oxides components of blending fuel ash and ash blends. 104
Table 4.7 Metal oxidant components of Cerrejon coal ash from PACT. 105
Table 4.8 List of El Cerrejon coal 1 and 2 ash mineral compositions.....110

Table 4.9 List of different biomass ash mineral compositions.....115
Table 4.10 List of El Cerrejon coal 1 and Pine co-firing ash mineral compositions.118
Table 4.11 List of El Cerrejon coal 2 and Wheat straw co-firing ash mineral compositions. 121
Table 4.12 List of El Cerrejon coal 2 combustion ash mineral compositions by PACT. 125
Table 5.1 The summary of ash fusion temperatures.....130
Table 6.1 The calculation of slagging and fouling index 157
Table 7.1 Comparison between relevant temperature of particular viscosity and ash fusion temperatures. 202
Table 7.2 The comparison of mineral phase of El Cerrejon coal 1 and 2 by FactSage prediction and X-ray diffraction.....206
Table 7.3 The comparison of mineral phase of biomass by FactSage prediction and X-ray diffraction.....208
Table 7.4 The comparison of mineral phase of El Cerrejon coal 1 and pine co-firing by FactSage prediction and X-ray diffraction. 210
Table 7.5 The comparison of mineral phase of El Cerrejon coal 2 and wheat straw co-firing by FactSage prediction and X-ray diffraction. 212
Table 7.6 The comparison of mineral phase of original PACT ash and re-burned ash by FactSage prediction and X-ray diffraction. 213

List of Figures

Figure 1.1 Global Greenhouse Gas Emissions: (a). by different sources and (b). in different countries**.** 1

Figure 1.2 The UK versus EU GHG emission targets for different sources of GHG. The UK current policy outcome is shown.....2

Figure 1.3 Schematic of the classification of the conversion of biomass application technologies.....7

Figure 1.4 Examples of ash deposits in different boiler regions, A: superheater; B: burner region and boiler walls; C: boiler walls; D: burner quartz; E,F: superheater tubes in the waste incinerator. 11

Figure 2.1 Coal sizing and cleaning processes 16

Figure 2.2 General coal combustion processes. 21

Figure 2.3 Changing of mineral phase during coal combustion.. 23

Figure 2.4 The structure of fluidized bed coal combustion boiler. 26

Figure 2.5 The structure and combustion process of CFB system. 27

Figure 2.6 Relationship between biomass consumption speeds by combustion associated with the temperature change from thermo-gravimetrical analysis (TGA). 36

Figure 2.7 General Combustion process with air. 37

Figure 2.8 Combination of under stoker furnace with entrained flow reactor for air and fuel staging. The operation process is arranged of (1) Feeding of primary fuel and primary air;(2) Reduction zone;(3) Injection of secondary fuel and consecutively tertiary air;(4) End of post combustion chamber, flue gas exit to convection part and cyclone. 39

Figure 2.9 CFB plant with steam boiler for co-combustion.....39

Figure 2.10 Typical boilers for biomass combustion.....40

Figure 2.11 Forming mechanism of biomass ash deposition.....44

Figure 2.12 Regions of ash related problems in boilers: left — conventional pulverized fuel fired boiler configuration; right — tower boiler configuration.....55

Figure 2.13 Schematic diagram of processes governing the transformation of mineral matter during coal combustion. 56

Figure 2.14 Alkali-induced slagging formation and growth mechanisms during biomass combustion.. 59

Figure 2.15 Phase distribution of metal species with temperature for Wujek coal.....64

Figure 3.1 Location of the combustion observation locations within the test facility (dimensions in mm). 79
Figure 3.2 Ash collection locations in the pilot scale test. 80
Figure 4.1 The connection between XRF results and wet chemical analysis results: (a)-Al_2O_3; (b)-Fe_2O_3; (c)-CaO; (d)-K_2O; (e)-MgO; (f)-MnO_2; (g)-P_2O_5; (h)-SiO_2. ◆: Calibration data set; ∗:PPA1 and PPA2 data. 90
Figure 4.2 The calibration of XRF results by wet chemical analysis results—Case 1. 95
Figure 4.3 (a)-(e) Properties of five different biomass ash fusion properties by STA-MS: (a) White wood pellet (WWP); (b) Olive residue (OR); (c) SRC Willow (SRCW); (d) Miscanthus B (MB) and (e) Wheat straw (WS). 98
Figure 4.4 The calibration of XRF results by wet chemical analysis results-Case 2 100
Figure 4.5 (a)~(c) Analysis of El Cerrejon coal 1 and 2 ash mineral compositions: (a) PCC1 (550 ℃); (b) PCC2 (800 ℃); (c) PCC3 (800 ℃). 109
Figure 4.6 (a)~(f) Analysis of different biomass ash mineral compositions: (a) PPA1(550 ℃); (b) PPA2 (800 ℃); (c) WS1 (550 ℃); (d) WS2 (800 ℃); (e) WWP1 (550 ℃); (d) WWP2 (800 ℃). 113
Figure 4.7 (a)~(c) Analysis of El Cerrejon coal 1 and Pine co-firing ash mineral compositions (Ash produced at 550 ℃ from blended fuel). 117
Figure 4.8 (a)~(c) Analysis of El Cerrejon coal 2 and Wheat straw co-firing ash mineral compositions. 120
Figure 4.9 (a)~(f) Analysed mineral compositions of El Cerrejon coal 2 ashes from pilot scale combustion and re-burned under 800 ℃. 124
Figure 5.1 Phases in the ash melting process. 129
Figure 5.2 Relative deformation of test pieces for different ash during the ash fusion test: (a)-PPA1; (b)-PPA2; (c)-WS1; (d)-WWP1; (e)-PCC1; (f)-PCC2; (g)-PCC3; (h)-CA82; (i)-CA55; (j)-CA28; (k)-BFPC82; (l)-BFPC55; (m)-BFPC28; (n)-BWCA82; (o)-BWCA55; (p)-BWCA28; (q)-CFA2; (r)-CBA12; (s)-CBA22. 137
Figure 5.3 Plots of mass loss, DTA and corresponding gas evolution profiles with temperature (when heated at 10 ℃/min in 12.5% O2/He) for El Cerrejon coal, pine and blended ash samples: (a)-PPA1; (b)-PPA2; (c)-WS1; (d)-WWP1; (e)-PCC1; (f)-PCC2; (g)-PCC3; (h)-CA82; (i)-CA55; (j)-CA28; (k)-BFPC82; (l)-BFPC55; (m)-BFPC28; (n)-BWCA82; (o)-BWCA55; (p)-BWCA28; (q)-CFA1; (r)-CFA2; (s)-

CBA11; (t)-CBA12; (u)-CBA21; (v)-CBA22. Refer to Table 5.1 for sample designation. D, H, F refer to deformation, hemisphere and flow temperatures. 150
Figure 5.4 Plot of experimental hemisphere temperatures (HT) and peak endotherm temperatures (STA) for various fuels compared with the results by Baxter. 151
Figure 6.1 Values for different numerical indices at various El Cerrejon coal 1/pine ratios, with ashing temperatures: (H)-800 ℃; (L)-550 ℃. Indices: 1, AI Kg/GJ; 2: Ra/b /10; 3: Sx; 4: Fs/1000 (℃). Oblique-lined fill signifies ash produced by blending the fuels then ashing; Hatched fill signifies blended fuel ash (ash produced separatedly then blended). 158
Figure 6.2 Values for different numerical indices at various El Cerrejon coal 2/wheat straw ratios, with ashing temperatures: (H)-800 ℃; (L)-550 ℃. Indices: 1, AI Kg/GJ; 2: Ra/b/10; 3: Sx; 4: Fs/1000 (℃).....160
Figure 6.3 Values for different numerical indices at various pilot scale test ash from different collection point and re-burned ash refer to Table 3.5~Table 3.6 and 4.7 for sample designation. Indices: 1, AI Kg/GJ; 2: Ra/b; 3: Sx/100; 4: Fs/1000 (℃). 161
Figure 6.4 The change of viscosity with temperature for ash from different fuels based on the Watt-Fereday viscosity model, calculated by Equation 6.7; for comparison the Streeter model by Equation 6.13 is shown, applied to the pine.....166
Figure 6.5 The change of viscosity with temperature for different ash samples based on the modified Watt-Fereday viscosity model, calculated by Equation 6.8; for comparison the Streeter model by Equation 6.13 is shown, applied to the pine.....168
Figure 6.6 The change of viscosity with temperature for different ash samples based on the modified Watt-Fereday viscosity model, calculated by Equation 6.8; for comparison the Streeter model by Equation 6.13 for lignite is shown, applied to the pine. 170
Figure 6.7 The change of viscosity with temperature for different ash samples based on the modified Watt-Fereday viscosity model, calculated by Equation 6.8; for comparison the Streeter model by Equation 6.13 for lignite is shown, applied to the pine. 171
Figure 6.8 The change of viscosity with temperature for different ash samples based on the modified Watt-Fereday viscosity model, calculated by Equation 6.8; for comparison the Streeter model by Equation 6.13 is shown, applied to the bottom ash (CBA21). 173

Figure 6.9 The change of slag mass fraction in non-gas phase with increase in temperature for each coal/pine ratio as calculated by FactSage. Temperatures: 1, 500 ℃; 2, 600 ℃; 3, 700 ℃; 4, 800 ℃; 5, 900 ℃; 6, 1000 ℃; 7, 1100 ℃; 8, 1200 ℃; 9, 1300 ℃; 10, 1400 ℃; 11, 1500 ℃; 12, 1600 ℃; 13, 1700 ℃; 14, 1800 ℃. Solid and dashed line represents the lower and upper limits of the measured deformation temperature range (by ash fusion test) for the different blends. 175
Figure 6.10 Stable solid phases in equilibrium with the slag phase for 100%El Cerrejon coal1—PCC2.....179
Figure 6.11 Stable solid phases in equilibrium with the slag phase for 80% El Cerrejon coal1 and 20% pine co-combustion—BFPC28.....179
Figure 6.12 Stable solid phases in equilibrium with the slag phase for 50% El Cerrejon coal1 and 50% pine co-combustion—BFPC55……...……180
Figure 6.13 Stable solid phases in equilibrium with the slag phase for 20% El Cerrejon coal1 and 80% pine co-combustion—BFPC82.....180
Figure 6.14 Stable solid phases in equilibrium with the slag phase for 100% pine—PPA1. 181
Figure 6.15 The change of slag mass fraction in non-gas phase with increase in temperature for each El Cerrejon coal 2 / wheat straw ratio as calculated by FactSage. Temperatures: 1, 500 ℃; 2, 600 ℃; 3, 700 ℃; 4, 800 ℃; 5, 900 ℃; 6, 1000 ℃; 7, 1100 ℃; 8, 1200 ℃; 9, 1300 ℃; 10, 1400 ℃; 11, 1500 ℃; 12, 1600 ℃; 13, 1700 ℃; 14, 1800 ℃. Solid and dashed line represents the lower and upper limits of the measured deformation temperature range (by ash fusion test) for the different blends. 182
Figure 6.16 Stable solid phases in equilibrium with the slag phase for 100% El Cerrejon coal 2—PCC3.....186
Figure 6.17 Stable solid phases in equilibrium with the slag phase for 80% El Cerrejon coal2 and 20% wheat straw co-combustion—BWCA28. 186
Figure 6.18 Stable solid phases in equilibrium with the slag phase for 50% El Cerrejon coal2 and 50% wheat straw co-combustion—BWCA55. 187
Figure 6.19 Stable solid phases in equilibrium with the slag phase for 20% El Cerrejon coal 2 and 80% wheat straw co-combustion—BWCA82. 187
Figure 6.20 Stable solid phases in equilibrium with the slag phase for 100% wheat straw-- WS1. 188
Figure 6.21 The change of slag mass fraction in non-gas phase with increase in temperature for 100% white wood pellet as calculated by FactSage. Solid and dashed

line represents the lower and upper limits of the measured deformation temperature range (by ash fusion test) for the 550 ℃ white wood pellet ash (WWP1). 189
Figure 6.22. Stable solid phases in equilibrium with the slag phase for white wood pellet. 190
Figure 6.23 The change of slag mass fraction in non-gas phase with increase in temperature for each PACT ash samples as calculated by FactSage. Temperatures: 1, 500 ℃; 2, 600 ℃; 3, 700 ℃; 4, 800 ℃; 5, 900 ℃; 6, 1000 ℃; 7, 1100 ℃; 8, 1200 ℃; 9, 1300 ℃; 10, 1400 ℃; 11, 1500 ℃; 12, 1600 ℃; 13, 1700 ℃; 14, 1800 ℃.....192
Figure 6.24 Stable solid phases in equilibrium with the slag phase for original ash of CFA1. 193
Figure 6.25 Stable solid phases in equilibrium with the slag phase for re-burned ash of CFA2.....193
Figure 6.26 Stable solid phases in equilibrium with the slag phase for original ash of CBA11. 194
Figure 6.27 Stable solid phases in equilibrium with the slag phase for re-burned ash of CBA12. 194
Figure 6.28 Stable solid phases in equilibrium with the slag phase for original ash of CBA21. 195
Figure 6.29. Stable solid phases in equilibrium with the slag phase for re-burned ash of CBA22. 195
Figure 7.1 (a) Variation of values for different numerical indices for different El Cerrejon coal 1 / pine ratios, and **(b)** Composition (wt%) of main inorganics in the ash (expressed as oxides) with ashing conditions: (H)-800 ℃; (L)-550 ℃. 200
Figure 7.2 (a) Variation of values for different numerical indices for different El Cerrejon coal 2 /wheat straw ratios, and **(b)** composition (wt%) of main inorganics in the ash (expressed as oxides) with ashing conditions: (H)-800 ℃; (L)-550 ℃. 201
Figure 7.3 Comparison between Fs and temperature when slag mass fraction ≥0.75 during phase change (FactSage model of Figure 6.9, Figure 6.15, Figure 6.21, and Figure 6.23) of different ash samples.....205

Chapter 1 Introduction

1.1 Background

In the past century, the main energy resources were fossil fuels such as coal, petroleum, and natural gas. However, the burning of coal, natural gas, and oil for electricity and heat is the largest single source of global greenhouse gas (GHG) emissions. Since the energy crisis from fossil fuels has become a challenge in this century, biomass energy has become a key contender for low carbon electricity, heat, gas and oil. The statistics from the IPCC presented in **Figure 1.1 (a)** shows that about 26% GHG was generated by energy supply process in 2007 [1]. Also the Carbon Dioxide Information Analysis Centre (CDIAC) also reported the 2008 global CO_2 emissions from fossil fuel combustion and some industrial processes (million metric tons of CO_2), as presented in **Figure1.1 (b)** [2].

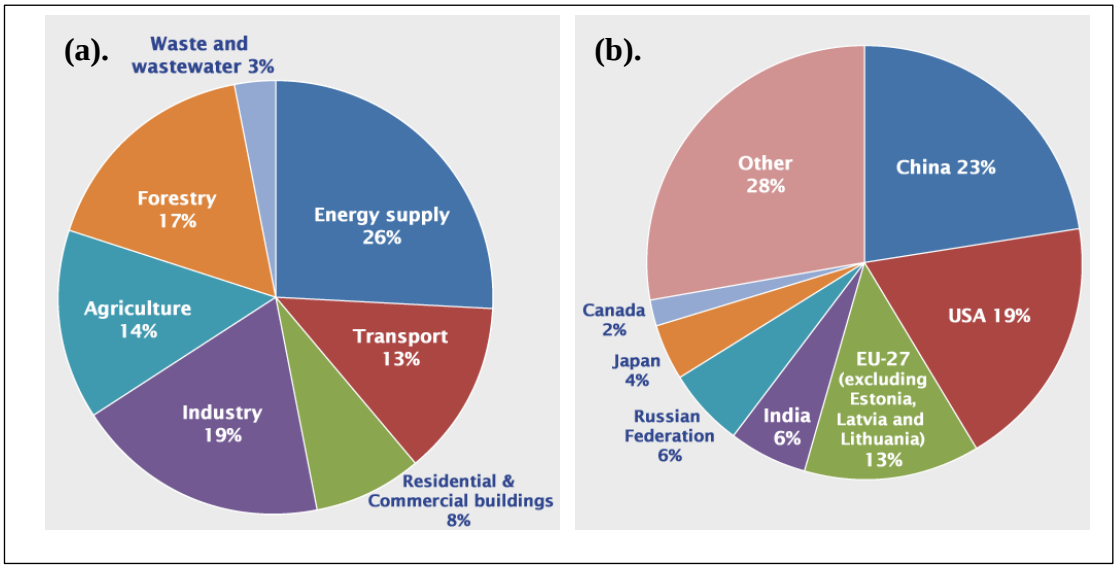

Figure 1.1 Global Greenhouse Gas Emissions: (a). by different sources and (b). in different countries [1, 2]**.**

To reply to the climate challenge and fossil fuel crises, the European Union has set up their own binding legislation for climate and energy which is called the "20-20-20" targets for 2020. This measure aims to achieve a 20% reduction in EU greenhouse gas emissions from the 1990 levels, thus raising the share of the EU energy consumption produced from renewable resources to 20% and with a 20% improvement in the EU's energy efficiency. According to the report in 2014, the average emissions (excluding LULUCF and international aviation) are expected to be about 23 % lower than the 1990 levels over the second commitment period from 2013 to 2020 on average [3].

A long-term policy plan has been formulated as the roadmap to encourage EU members to develop and utilize their resources in a sustainable way which can assist to build up a low-carbon economy. As the seen in **Figure 1.2**, the EU 2050 target announced an 80% decrease of GHG from 1990 levels through UK domestic reductions. Particular steps were measured in some important sectors such as power generation, industry, transport, buildings and construction, agriculture, etc. [4].

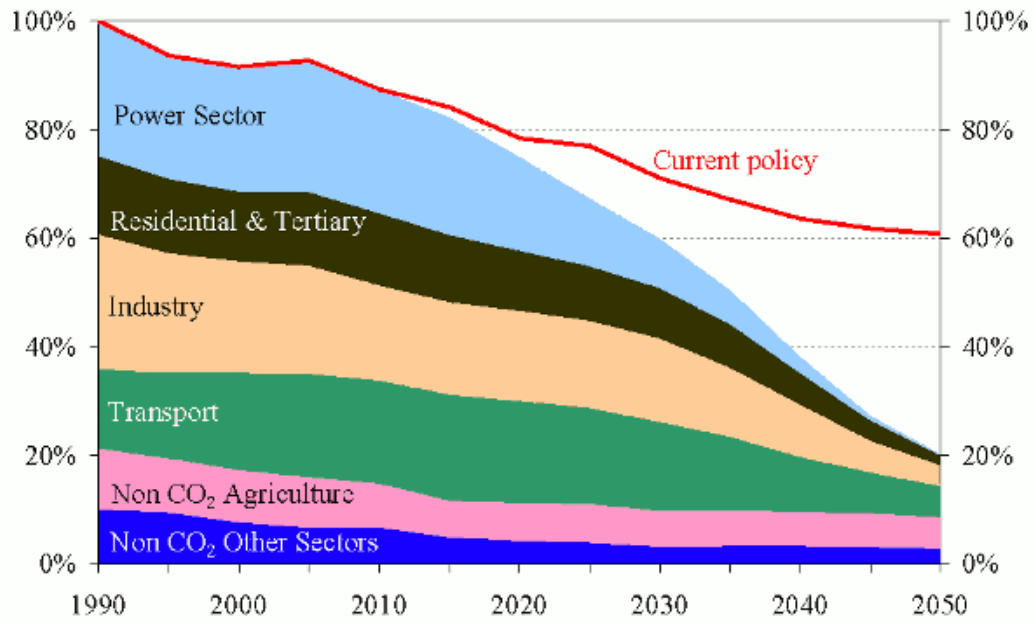

Figure 1.2 The UK versus EU GHG emission targets for different sources of GHG. The UK current policy outcome is shown [4].

Since the sharp decline of the fossil fuel reserves and aggravated serious environment issues, from the fossil energy resources, biomass has attracted attention by all countries of the world. In the growing process of biomass, photosynthesis dominates the carbon fixation and storing of energy. Specialists have calculated the CO_2 emission value during combustion and gasification processes, which generates low net CO_2. The huge existing biomass resources are widely used as a potential renewable energy with many advantages that include: lower sulphur; lower net CO_2 emission than traditional fossil fuel, and a sustainable resource, if well-managed. Thus biomass is classified as a green energy.

Biomass is a source of sustainable materials and fuels. Biomass energy can be mainly generated from those renewable or recycled organic materials, such as woods, wood waste, straws, agricultural crops and their residues or waste by-products, municipal solid waste, animal wastes, waste from food processing, and aquatic plants and algae. The major organic components are the lignocelluloses, which should be grouped into cellulose, hemicelluloses, lignin and extractive [5].

According to the statistics and forecasts by the world energy council [6], increasing consumptions of about 34.4% for coal and 3.6% for biomass throughout world from 2011 to 2020 were reported. As a rough estimate, the reserves of biomass (about 220 billion oven-dry tones) can support about 4500EJ energy, which is about 10 times the energy consumption for the whole world each year [7]. Most of biomass has been widely used in the pulp and paper industries, where residues from production processes are combusted to produce steam and electricity.

The statistical data shows that the amount of consumed of biomass accounted for approximate 11.7% of the EU final energy consumption by the late 1990s. Up to 2007, about 10% primary energy was provided by traditional biomass. Meanwhile, about 470EJ energy was generated by the combustion of biomass. According to the budget, approximately 150~400EJ/yr energy can be exploited through the application of biomass, thus equals to 25% of the total energy requirement in 2050 [8].

1.2 Current biomass energy policy in UK

To achieve the greenhouse gas (GHG) reduction target of 80% by 2050, the UK government plans to exploit bio-energy and energy crops as a part of the energy resource to support the UK's renewable energy strategy. Under European Union targets by 2020, the UK must increase their production of energy from renewable sources to 15% of the total energy requirement and this is still a challenge for the current industry of transport, heating and electricity generation [9].

As the UK is located in a special geographic position，which is a sovereign state located off the north-western coast of continental Europe, the limited land resources cannot satisfy vast natural resources of biomass. Compared with other EU countries, the UK faces a fierce shortage of above ground biomass forest resources and agricultural waste. To meet the indigenous energy requirement, the UK Government has encouraged the growing of energy crops, which is projected to bring substantial economic benefits [10]. To avoid the side effects on food yield and price, short rotation coppice (SRC) willow and miscanthus were considered to be the main potential biomass feedstock which can be produced at a commercial scale in non-arable lands. Based on the biologists' research, both SRC willow and miscanthus have

about 20 years' plantation lifetime, during this period these crops can be harvested several times with low nutrient requirements and few pests or disease. As perennial crops, SRC willow and miscanthus have many inherent advantages, such as cost-efficient investment for soil cultivations, fertilizers and agrochemicals, etc., thus the sustainability of these energy crops is increased. Until today, the agronomy of these energy crops is in the initial stages. There are many agronomic limitations for optimum growth, such as the expensive cultivation process, some progress with respect to these hindrances was achieved by the UK's Energy Crops Scheme [11].

The legally binding targets for carbon reductions were proposed by the UK Government to address the urgent climate change crisis, which was caused by the huge combustion of fossil based fuels [12, 13]. The UK Government drafted a development plan to increase the percentage of energy from renewable resources to achieve the renewable energy target. For the 2020 targets, the electricity generated by renewable resources was increased from 5.5% in 2009 to 15% in 2013, but this is only equivalent to about half of its goals (around 30%) by 2020; heat from green energy will be increased from a negligible quantity in 2009 to 12%; transport energy form bio-fuels will reach 10% from 2.6% in 2020 [14]. About 2.2 Mha of energy crops are in the plan for achieving the target by 2030. Most of that indigenous biomass will be cultivated and harvested in the UK [15]. According to the UK government reports, a 16% increase in the existing cultivation area has been achieved in mainland UK. Further, approximately 7500 ha of miscanthus and 6200 ha of SRC willow currently has been planted and this has not achieved the previous budget, which was limited at 1Mha non-food crops.

There are some risks to add the energy crops cultivation, such as the effect on the environment and natural heritage. The sustainability of biomass energy for electricity

and heat faces many difficult challenges to keep supplying as the demand in increases. Given the predicted impacts on climate change, it is worth increasing the investment on the development of infrastructure and industrial plant to deliver the sustainable energy scheme [16].

1.3 Current biomass energy application

In the past 100 years, most of the electricity, heat and domestic energy have been generated by the combustion of coal, oil and natural gas. As a market report, annual biomass energy generation had achieved about $2x10^5$ GWh and the installed biomass power capacity had reached 39GW in the entire world in 2004 [17]. From the 2015 Ecoprog market report, until the middle of 2014, approximately 3050 active pure biomass power plants in the world wide had increased the bio-electricity generation capacity to 49.5 GW [18]. To reduce the pressure on fossil fuel use, the use of pure biomass or in combination with coal, for energy generation is undertaken. Furthermore the co-combustion power system of coal with biomass could support the policies of GHG reduction, which contributes less emission of carbon dioxide (CO_2), nitric oxide (NO_x) and sulphur dioxide (SO_x).

Biomass may have the potential to partially replace coal, even almost entirely, to be combusted in power generating plants. According to the investigation of biomass, especially the economic and environmental advantages of the biomass properties, co-firing of coal with biomass is encouraging, although the extent of the use depends on the government policies at the time. But under the current technologies, the immediate use of biomass as a successor to fossil fuel is not ideal. This is due to the differences between the physical and chemical characteristics which affect a number of factors, including the input the biomass fuel into traditional boilers, which is a challenge.

Currently, biomass is always converted into large quantities of secondary energy carriers such as electricity, gaseous, liquid and solid fuels, heat, etc.. Generally, the conversion technologies are classified into thermal, chemical and biochemical processes as shown in **Figure 1.3**.

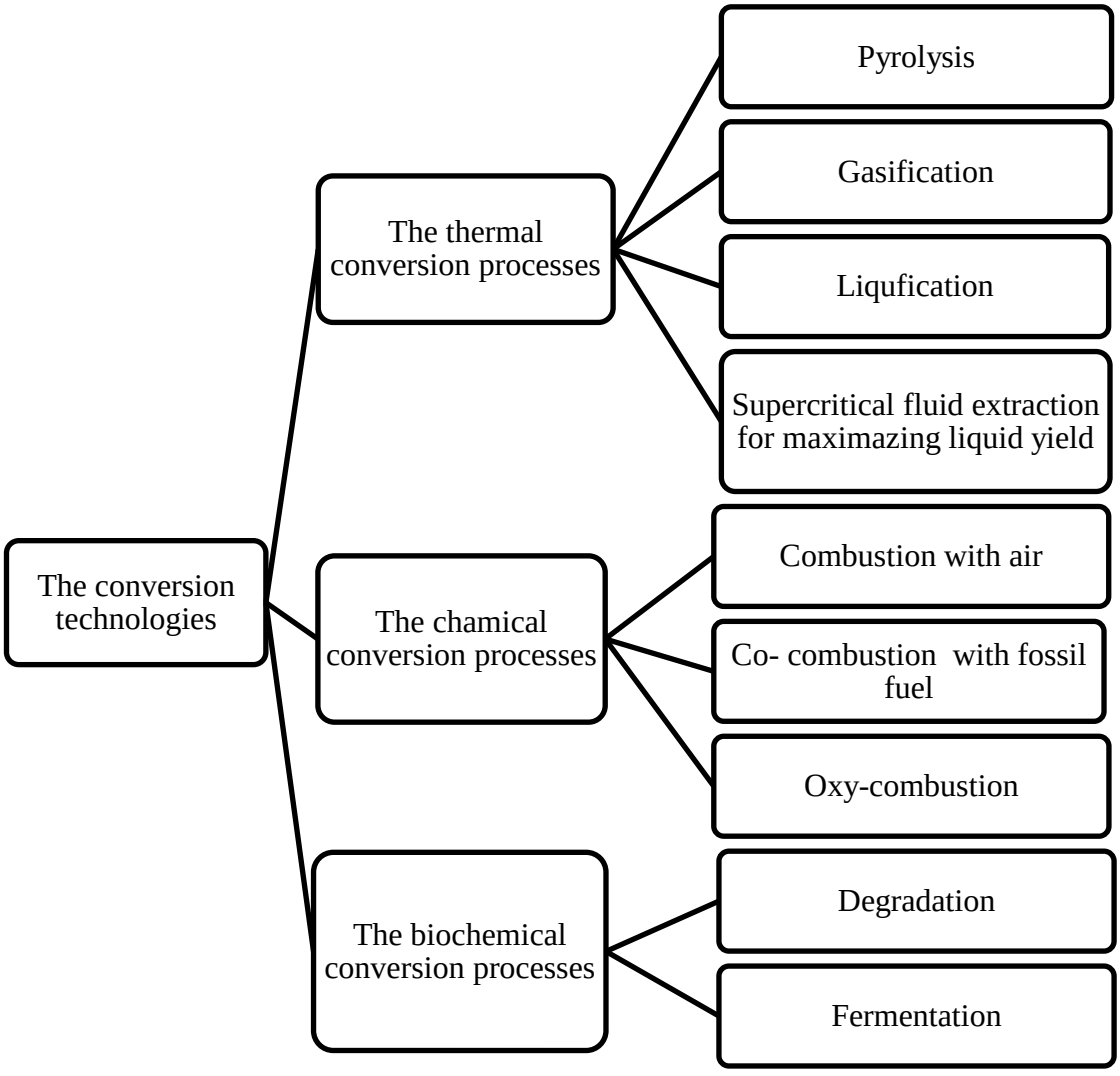

Figure 1.3 Schematic of the classification of the conversion of biomass application technologies.

Combustion of biomass can be divided into three segments: pure biomass combustion with air, co-combustion with fossil fuel and oxy-combustion. In general combustion and co-combustion with fossil fuels are the most important and mature technologies available nowadays for biomass utilization, but there also need to be improvements in the efficiency, emission and cost for further exploitation. [19]

In the complex process of biomass combustion, consecutive heterogeneous and homogeneous reactions will occur. The main processes consist of drying, devolatilization, gasification, char combustion, and gas-phase oxidation. Further, the time control is crucial in each reaction as and some control parameters are chosen based on the fuel size and properties, temperature and combustion conditions. [20]

1.4 Ash deposits problems of high percent biomass combustion

Biomass fired, and/or co-fired power plants have been developed around the world because of the worsening environment and severe energy crisis. However, there exist a variety of intractable ash-related issues that occur during the combustion process, which are barriers for the further popularization and application of biomass combustion [21]. Scientists have illustrated those different planting environments, harvest seasons and parts of the different biomass show changeable ash contents and compositions [22, 23]. Thus its composition is variable. Also different types of biomass show different inorganic components. As reviewed in previous studies, the most popular woody biomass have low silica and low potassium but high calcium content; agricultural residues have high silica, high potassium and low calcium content; animal residues have high phosphorus and high calcium content. All the above reasons constitute the changeable ash composition related to the uncertain ash issues. [24-27]

According to Nussbaumer [28], in general, biomass combustion can be operated with the feedstock, which has water content up to a maximum of 60%. The constituents of S and N in the fuel are related to the formation of the pollutant and the in-organics to the formation of the deposits, corrosion and ash. Relevant constituents in the biomass are nitrogen, which contribute to the NO_x and ash components (e.g. K and Cl as a source of KCl) that lead to particulate emissions. The herbaceous biomass such as straw, miscanthus, switch grass, etc., can have higher contents of S, K, Cl, etc., that lead to higher emissions of particulates, and increased ash, corrosion, and deposits. Some toxic pollutants, such as heavy metals and chlorine compounds, should be destroyed during the combustion of contaminated biomass [29].

The existing technologies for pure biomass combustion show additional problems due to the low melting point of the biomass ash, which can cause severe deposition problems. Currently, the problems are observed during biomass combustion in both dedicated systems and when pulverized coal in firing power plant is observed. The inorganic content of the biomass contributes to the ash particles which may stick on the heat transfer surfaces, and the superfluous ash may accumulate on the inside wall to form deposition that can cause slagging in the boilers and also; induce fouling in the convective pass. Because the abundant deposits easily agglomerate and sinter, the ash deposition is considerably harder and often cannot be removed using traditional methods, e.g. by shedding or soot blowing from the boiler and tubes. Sometimes, the facilities need to be turned off for cleaning. Even then, sometimes manual cleaning cannot achieve a good property. This, then, remains a key challenge in biomass combustion: How can our understanding deliver quantitative information about deposit formation and the strength and degree of the fusion on the heat transfer surface [30].

Figure 1.4 shows ash deposits from different boiler regions. According to Weber [31], generally, slagging takes place in the hottest parts of the boiler whilst the fouling occurs as the flue gases and ash particles cool down. i.e. The ash deposition in combustion chamber can, be classified into slagging deposits and fouling deposits.

The slagging deposits are identified as the hard deposits which are chemically active at high temperatures and these are partially or completely molten. During this process the original chemical and physical structures of the ash particles undergo substantial changes. These deposits are always observed in the regions of the boiler which are directly exposed to flame radiation, such as the furnace walls and the pendant super heaters, and they are difficult to remove by soot blowing.

The fouling deposits are identified as the deposits which are formed in lower temperatures regions, normally in the boiler regions which are not directly exposed to flame radiation. These particles are transported to the convection regions in where the heat transfer process is dominant, and their original physical and chemical structures do not change.

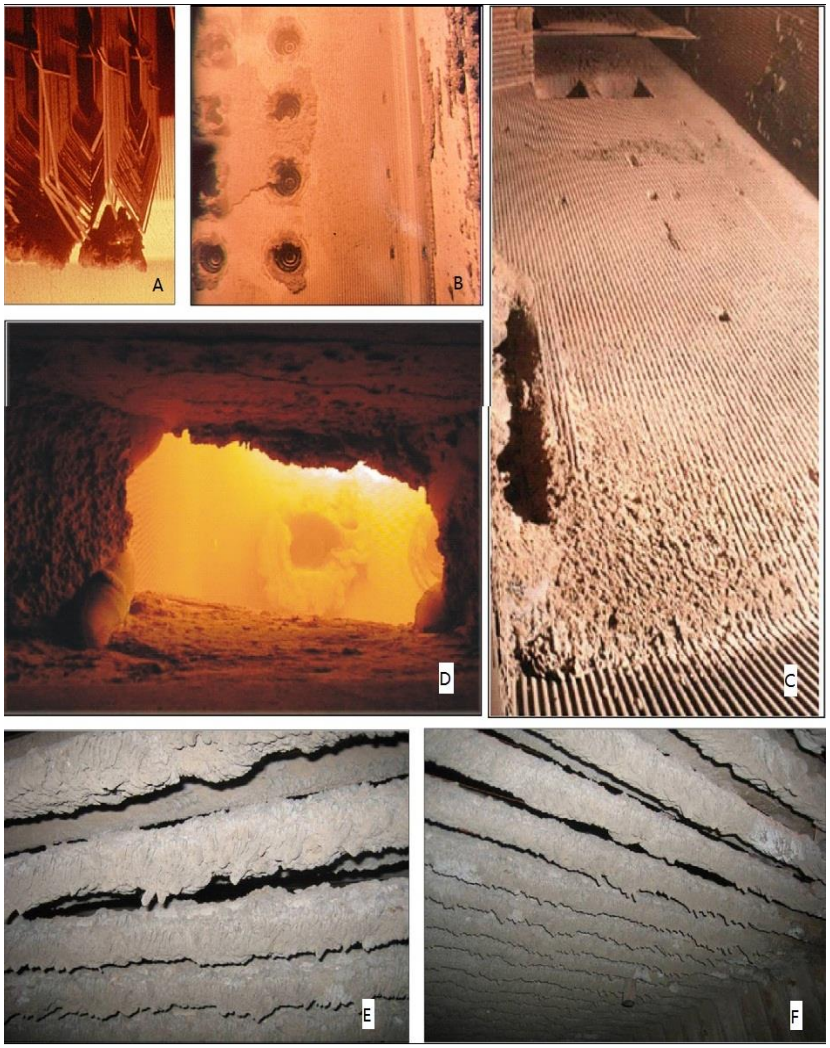

Figure 1.4 Examples of ash deposits in different boiler regions, A: superheater; B: burner region and boiler walls; C: boiler walls; D: burner quartz; E,F: superheater tubes in the waste incinerator [31].

In previous studies [32], the deposition behaviour of the fossil fuels was analysed by chemical fractionation and also thermodynamic equilibrium calculations. To understand the related biomass ash issues, mathematical modelling has been developed to predict the formation of the depositions and the understanding of the process, which can assist in the optimization of the operating parameters. The aim is to optimize the performance of the planned plants as a function of the input fuel composition, plant dimensions and operating conduction; a positive reference can

support the boiler designer to consider the effect of a change in the fuel composition on the operation of the plant, or the effect of a shift in the load on the operating conditions and output performance.

1.5 Thesis Aim

The aim of this thesis is to gain a fundamental understanding of ash behaviours of biomass and biomass-coal blends for the composition of complicated deposits which are formed under different temperatures during combustion. The ash fusion process is described by an ash fusion test, and the specific melting point is used to compare with the calculated indices to judge the reliability of the traditional predicting method. These data for the deposits composition and properties are included in the thermodynamic model to predict the ash deposition at specific temperatures. The estimated results could be associated with the experimental ash fusion test to describe the deposition forming process. Similar methods are repeated in large scale tests, which can assist in knowing the deposition forming process in practice.

Specific objectives are:

- To select a coal and a number of biomass which are of interest to the industry.
- To characterise the fuels, and in particular to fully characterise the ash.
- To validate and compare the main methods of ash characterisation, namely X-ray fluorescence and wet chemical analysis.
- To characterise the melting behaviour of the ash from coal/biomass blend, using the ash fusion test and STA-MS.
- To compare results from traditional slagging and fouling indices with those from both the modelling and laboratory tests.
- To model slag formation using FactSage, a thermodynamic model.

Chapter 2 Literature Review

Today, biomass is mainly used for heat and electricity generation along with bio-fuel production. To improve the heat value and conversion efficiency, before combustion or gasification, some pre-treatment processes are required to optimize the characteristics of biomass in a similar way. Despite the continuing search for alternate sources of energy, whether they are other fossil fuels or non-fossil fuels such as biomass, there is little doubt that coal combustion will remain an important source of energy throughout the 21st century. Many coal combustion and gasification technologies and equipment are used in the biomass application technologies, which saves costs for the exploitation of biomass energy [32].

Comparing biomass with coal combustion helps to understand biomass performance and related issues in power plants. Thus the literature review will study and summarize the coal and biomass combustion and co-combustion technologies. Some previous experimental work and slagging prediction indices will be introduced to understand the effect of high percentages of biomass causing deposition problems during pure combustion or co-firing. Some popular combustion modelling tools will also be reviewed to provide suggestions for the prediction of slagging and fouling potential during biomass combustion and co-firing.

2.1 Coal combustion technologies

Coal is used as a major and stable supply of energy. Coal combustion provides the majority of consumable electricity in the world. Pulverised coal firing has been used as a bulk source of energy for generating power in utility boilers for almost a century and provides the dominant technology. Its hazardous and risky extraction procedures

as well as environmental pollution have not been neglected. In the late 1940s the developed nations began to undertake coal research based on scientific principles to ensure the most efficient use of the world's primary energy resource represented by coal. With empirical relationships based on the principles of physics and chemistry for coal utilization, sulphuric and nitrogen oxides with carbonized products can be minimized by using clean coal combustion technologies, such as Fluidized Bed Combustion (FBC), Oxy fuel pre-post combustion (OFPC). Some of these advanced technologies have been directly used to provide efficiency improvements. As it is required to control the pollutants produced during the combustion of coal, the constantly accumulation of scientific knowledge for boiler designs is growing [33].

2.1.1 Pre-treatment of coal

Coal preparation is the first step after coal mining as a pre-treatment for improving the quality of coal. Size reduction and cleaning are important for handling, processing and improving quality to satisfy combustion requirements in power plants. Some of the current coal preparation methods also help to improve the technologies for biomass pre-treatment.

- *Reducing coal size*

Size reduction of run-of-mine coal is an important step to make sure these fuels are utilized efficiently for power generation, production of coke, as well as other industrial uses such as the production of synthetic fuels. Reducing the size of coarse coal is required to the pre-determined maximum size of particle for coal utilization is required. The major steps in reducing coal size are breaking, crushing, and screening [34]. There are four types of equipment used for size reduction of run-of-mine coal: (1) rotary breakers, (2) roll crushers, (3) hammer mills, also called ring mills, (4) impactors, and (5) tumblers. It is necessary to screen the irregular sized coal before

crushing, so that only oversized coal will be crushed to reduce power consumption in the crusher and it is also important to pass these large size coals past a magnetic separator to remove tramp iron from the flow, which might damage the crusher [35]. Similar to some biomass wastes, wood chips and crop residues, large amounts of irregular small sized coals are generally wasted during excavation and cleaning activities, which leads to a loss of valuable energy matter and potential environmental problems. [36-39]

- *Coal cleaning*

Run-of-mine coal generally has mineral matter of the order of 5 to 40 wt% and sulphur of the order of 0.2 to 0.8 wt% depending on the geologic conditions and mining technique used. Coal cleaning helps to remove inorganic impurities such as alkali metals, heavy metals, sulphurs, and nitrogen for more efficient and environmentally safe utilization of coal [42, 43]. Current commercial coal cleaning methods are invariably based on physical separation as chemical and biological methods tend to be too expensive. Generally, froth flotation, flocculation, oil agglomeration and enhanced gravity separators are mainly used to clean crushed and pulverized coals [44-46]. The general coal pre-treatment process could be described in **Figure 2.1** [47].

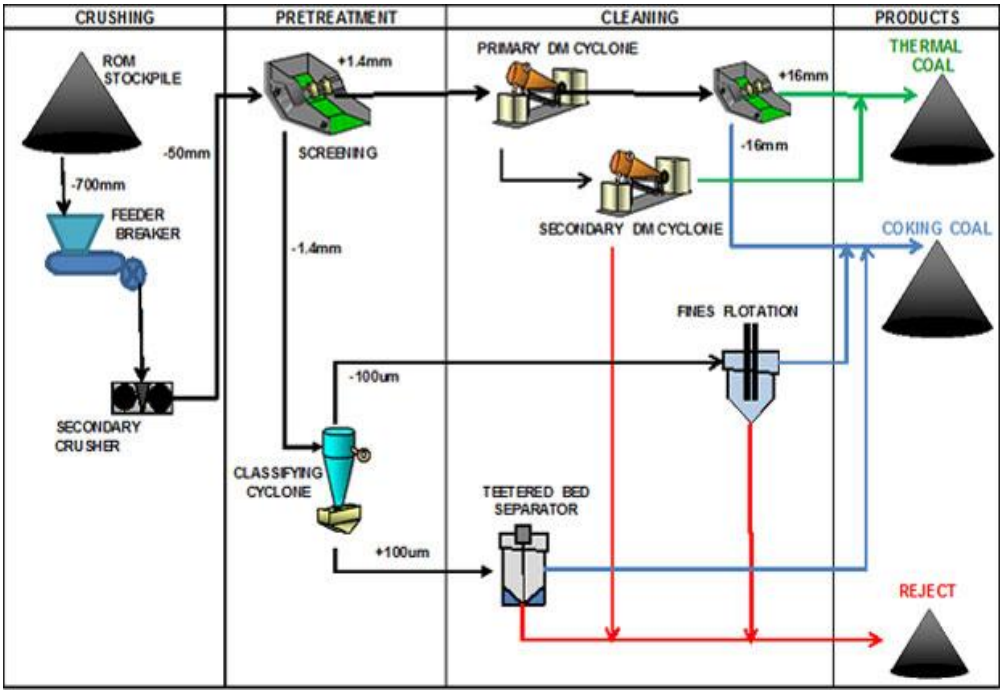

Figure 2.1 Coal sizing and cleaning processes [47].

- *Coal drying*

The presence of water in coals is generally in three forms:

- Inherent moisture contained in the internal pores of the coal substance, including water associated with the mineral impurities;
- Surface moisture wetting the external surfaces of the coal particles in which adsorption may play a small part;
- Free water held by capillary forces in the interstices between the coal particles.

According to Karthikeyan's study [48], the water content of a coal reduces its heating value, increases the costs from handling difficulties and extra-weight of transportation, and decreases the yields of carbonization producing and affects other conversion processes. Moreover, loss of volatile organic compounds (VOC) during the coal drying process at high temperatures also reduces fuel calorific value and simultaneously promotes the risk of fire from the combustion of volatile organic

compounds. The concepts of drying at lower temperature or by using a slight vacuum environment to minimize the loss of volatile organic compounds were mentioned, but non-ideal drying rates are the concerns for worried by such approaches. Reduction of the water content has been some mature techniques. As the moisture exits in different states, different methods must be chosen for moisture removal as listed in **Table 2.1** [48].

Table 2.1 Different types of moisture in coal and methods for removal [48].

Category	Location	Common name	Removal techniques
Interior adsorption water	Micropores and microcapillaries each coal particles	Inherent moisture	Thermal or chemical
Surface adsorption water	Particle surface	Inherent moisture	Thermal or chemical
Capillary water	Capillaries in coal particles	Inherent moisture	Thermal or chemical
Inter-particle water	Small crevices found between two or more particles	Surface moisture	Mechanical or thermal
Adhesive water	Film around the surface of individual or agglomerated particles	Surface moisture	Mechanical or thermal

2.1.2 Coal combustion process

The chemical principle of coal combustion can be described as an exothermic reaction stimulated by artificial initiation and spontaneous propagation. The physical processes involved in combustion are principally those that involve the transport of matter and the transport of energy. The conduction of heat, the diffusion of chemical species, and

the bulk flow of the gas all follow from the release of chemical energy in an exothermic reaction. As the particle temperature increase in the furnace, the organic matter of coal begins to volatilize and a large amount of carbon and mineral compounds are retained and combined to form char which will combust with the oxidant. Although the knowledge of coal combustion has been accumulated for a century, the general mechanism of pyrolysis processes are not universally accepted and forecasted by any models [49].

Due to the complexity of coal molecular structure, the main body of coal is usually described by individual carbon atom, hydrogen atom, nitrogen atom and sulphur atom, which can react with oxygen. In direct combustion, the reactions actually consist of a series of oxidations of different elements in coal. There are some uncertain and irregular reaction mechanisms which are caused by the nature heterogeneous pyrolysis performance between solid and gaseous phases. Several stoichiometric reaction equations are listed in **Table 2.2**. The carbon part of coal is usually oxidized in two ways, producing either carbon monoxide or carbon dioxide. The final purpose of coal combustion is simply to achieve the most transformation of original elements in coal and their intermediate products from primary reactions to the form of stable oxides. Sometimes, coal carbon is not completely oxidized and it may react with moisture to produce hydrogen. Then, further oxidization of those combustible compounds is also treated as secondary oxidizing stage. Unfortunately, the formation of nitric and sulphuric oxides cause serious environmental problems and requires removal from any product gas streams [50].

Table 2.2 Basic reactions during coal combustion [50].

$2C_{Coal} + O_2 \rightarrow 2CO$	$C_{Coal} + O_2 \rightarrow CO_2$
$2CO + O_2 \rightarrow 2CO_2$	$H_{Coal} + O_2 \rightarrow H_2O$
$C_{Coal} + H_2O \rightarrow CO + H_2$	$N_{Coal} + O_2 \rightarrow NO_X$
$S_{Coal} + O_2 \rightarrow SO_X$	$2H_2 + O_2 \rightarrow 2H_2O$
$2C_{Coal} + O_2 \rightarrow 2CO$	$2C_{Coal} + O_2 \rightarrow 2CO$
$C_{Coal} + 2H_2O \rightarrow CO_2 + H_2$	$CO + 2H_2O \rightarrow CO_2 + 2H_2$

Coal pyrolysis cannot be simply determined as individual chemical reaction and thermal transport processes, since the volatile matter and coal char combustion process always happen simultaneously, sequentially, or with some overlap. Nevertheless it is usually simplified into three basic stages [51]:

- The release of the volatile matter resulting from de-volatilization.
- Combustion of the released volatile matter.
- Combustion of the remaining char.

In the process of de-volatilization, a variety of combustible products are produced, such as tar and hydrocarbon gases. Those volatiles, organic body and mineral matters are exposed simultaneously in the flame. The complicated thermal phase is difficult to be distinguished and interpreted. Coal combustion performance is very sensitive and easily affected by specific properties of coal type, coal rank, physical properties (particle size, moisture content) and operating conditions. In the injecting process of pulverized coal, coal powders are transferred into furnace in with a dense stream of

hot air. The particles on the outside surface of the hot stream are heated rapidly in the presence of high levels of oxygen, while particles in the centre parts of the stream are heated relatively slowly within an anaerobic environment. Drying is also a particular de-volatilization process, as the moisture on the particle surface cannot be easily removed by simple pre-treatment nor prevented during the storage stage. During pulverized coal combustion, the injected hot fuel streams are heated rapidly, the direct particle-to-particle contact is assumed as a chain reaction especially on fluidized-bed combustion [52].

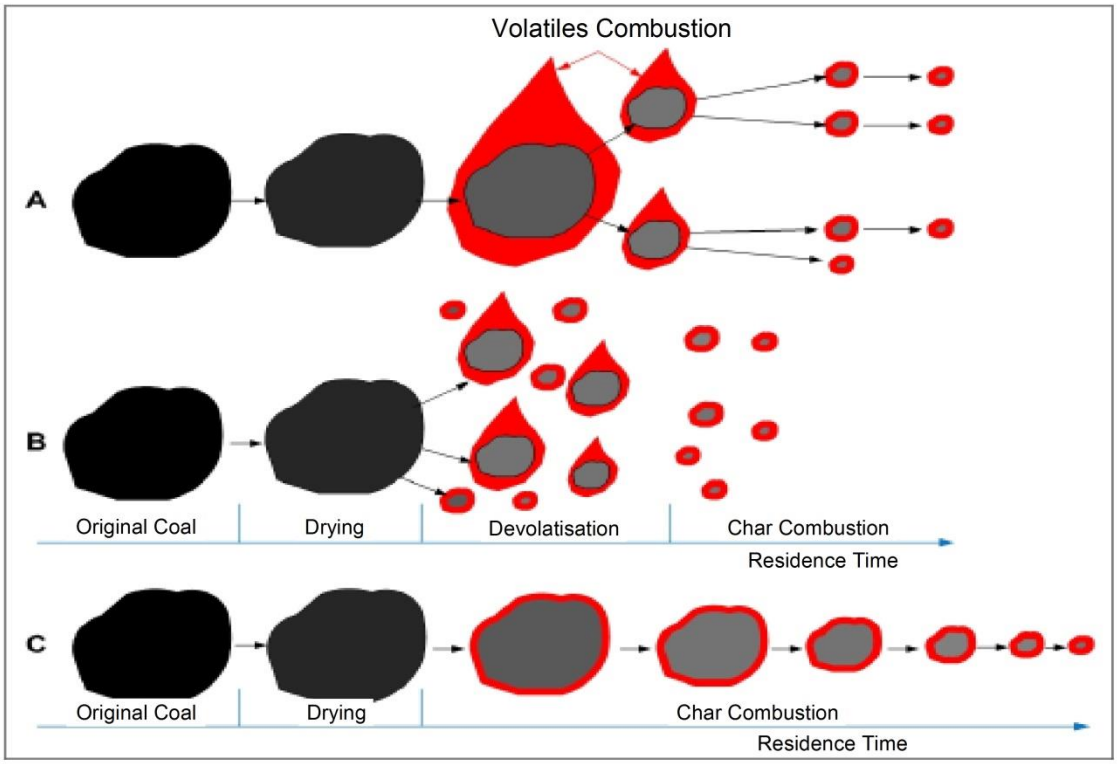

Figure 2.2 General coal combustion processes [53].

Process A: Where coal combustion in pulverised fuel (PF) with high volatile content.

Process B: Where coal with high volatile content and low mineral matter in bubbling fluidized bed combustion (BFBC).

Process C: Where coal with low volatile content in circulating fluidised bed combustion (CFBC).

The coal combustion process is summarized and described in **Figure 2.2**. According to Wu's study [53], comparing those three combustion process, the coal combustion efficiency will be affected by the coal size, coal type, volatile content, and combustion temperature and control parameters. In a BFBC process, the coal particle with high volatiles will fracture rapidly with their expulsion in the presence of thermal shock. The efficiency of this BFBC mainly lies on the high volatile and low mineral matter

fuels to achieve very high carbon burnout. The PF and CFBC technologies are more expensive than BFBC due to the more complex facilities and operations.

The physical characteristics shown in coal the devolatilizing process under given set of conditions are dependent on the heating conditions, and will be influenced by chemical characteristics of the original coal. When the oxidizing temperature is in the range of 400℃ to 1000℃, coking and non-coking bituminous coals, subbituminous coals, and lignite tend to show some degree of plastic behaviour and adhesion to other particles [54]. The production of volatile tar is diffusion-controlled in the initial stages of the thermal decomposition of coal, and the yield of tar is varied by heating conditions. Under different reacting temperature and with different chemical properties of coal, primary tar will own different composition and characters. Secondary oxidizing reactions also play an important role in the overall coal combustion process. Under low heating rates condition, primary tar will hardly escape from the pores in char particles and participate in secondary char-forming processes. High heating rates will help to develop primary tars, and cracking and ring condensation reactions will promote the secondary oxidizing stage [55]. After the de-volatilization process, the produced char with a porous structure start to react with oxidant on the particle surface. The porous structure expands the surface area for reactions and enhances the penetration of reactant species into the char particle. The predominant parameters which will vary the thermal decomposition of char can be summarized as: the extent of physical detachment of volatile species from the coal matrix, the volatile compounds yield from the organic core, the volatilizing rate and rate of volatile escape from pores in the char particle. If the volatile components are able to be detached from char instantaneously, the forming reaction of volatile compounds will dominate the thermal decomposition process [56-57].

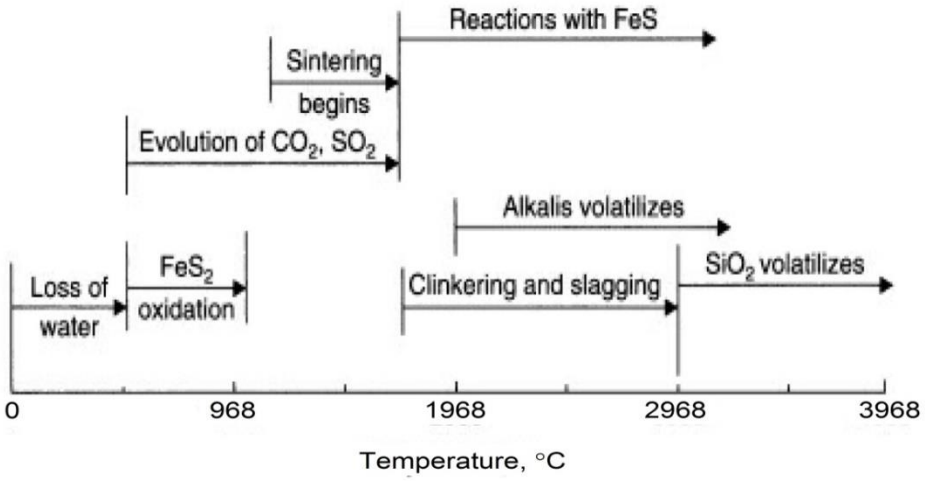

Figure 2.3 Changing of mineral phase during coal combustion [58].

Inorganics also devolatilise at high temperature as shown in **Figure 2.3**. This can lead to objectionable stack emissions, coal ash and volatile inorganic material generated by thermal alteration of mineral matter in coal and will adversely affect heat transfer processes by fouling the heat-absorbing and radiating surfaces. It may also influence the performance of the combustion system by causing corrosion, and operating procedures must therefore provide for effective countering of all these hazards [58].

2.1.3 Coal combustion systems

Coal combustion is a mature technology and widely used in a range of applications that vary from domestic fires to large industrial furnaces and utility boilers. The coal is burned to convert the chemical energy of the coal into thermal energy, after which the sensible heat in the products of combustion then can be converted into steam that can be converted into shaft horsepower [59]. Most coal fired power plants crush coal bulks into fine powder by pre-treatment and fed them into a combustion unit where coal is burned. Heat from coal burning is used to generate steam that is used to spin one or more turbines to generate electricity. During the coal firing technology

developing process, various systems have been designed to fit the purpose of converting coal to power and, as might be expected, the design of such systems varies with the nature of the coal feedstock [60].

Coal combustion may be achieved using pulverized coal in entrained systems, or as sized particles in fixed or slowly moving beds; larger pieces may, in certain instances, also be used. Nowadays the fixed- and slowly-moving bed combustors usually employ a mechanical stoker to feed the coal, and a grate to support the coal particles as well as to admit air for the combustion process [61]. Pulverized coal combustion involves grinding the feed coal to approximately <150 μm and injecting the powdered coal into the combustor from either wall-mounted burners or corner-mounted (tangential) burners. Combustion takes place within a few seconds at flame temperatures up to 1500 ℃. This parameter is also important for observing ash behaviours in deposition studies. Supercritical pulverized coal combustion is a variation that seeks to improve thermal efficiency, from the typical values of up to about 40% for pulverized coal combustion to 43–47% in supercritical systems through higher steam temperatures and pressures [62-63].

To adapt for more kinds of fuel, a fluidised bed boiler was designed for particles of different sizes. At still higher upward air velocities, an important change occurs; the bed becomes very turbulent with rapid mixing of the particles. Bubbles, similar to those in a briskly boiling liquid, pass through the bed and the surface is no longer well defined but becomes diffused. A bed of solid particles in this state is said to be 'fluidised', because it has not only the appearance, but also some of the properties, of a boiling fluid. The operating limits are set, on the one hand, by the minimum air / gas velocity needed to keep the particles fluidised and, on the other hand, by the maximum velocity that can be used before an excessive quantity of bed particles are

blown out of the bed containment box [64-66]. The basic structure and combustion process are illustrated in **Figure 2.4** [67]:

A fluidised bed of solids behaves in many ways like a liquid and has important characteristics [67]:

- The fluidised bed obtains its adaptive level. A fluidised bed of solids in a container retains a level surface if it is tilted from the horizontal position.
- A fluidised bed in one container transfers the same level to another connected container.
- With intensely stirred, the solid particles in a fluidised bed will always be rapidly mixed.
- The floating or sinking of solid particles in a fluidised bed occurs according to their density, as in a liquid.

One of the characteristics of a fluidised bed is the rapidly and uniformly transfer of heat which is in contrast to heat transfer through stationary particles slowly from one layer to another in fixed beds [68]. In contrast to stationary particles in beds, hot particles in a fluidised bed will not cause large temperature difference, but quickly transfer the heat to cool surfaces such as boiler tubes. This provides a continuous supply of heat on the transfer surface [69]. The stability of fluidized bed boiler is also influenced by the pressure drop, the minimum fluidization velocity and ash separation [70].

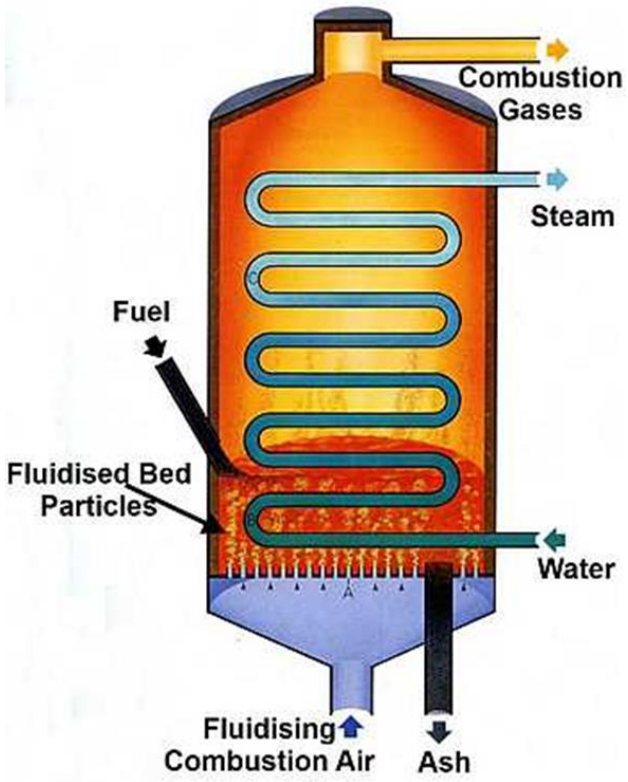

Figure 2.4 The structure of fluidized bed coal combustion boiler [67].

Ishida [71] proposed the concept of chemical looping combustion (CLC), which can be described as a solid oxygen carrier based on transferring oxygen from air to fuel [72]. The interconnected fluidized bed reactor as one type of CLC system was the most widely approved reactor system which is consisted of a fuel reactor (FR) and an air reactor (AR) [73-74]. These two reactors play different roles in the CLC process; firstly the oxygen carrier is reduced in the fuel reactor by the fuel to form unburned matter and then re-oxidized by the air when circulated to the air reactor [75]. In contrast to normal combustion, the total heat in the CLC process consists of two chemical reactions (in FR and AR). Combining the above fluidized bed design and the chemical looping combustion concept, the diagram of a circulating fluidized bed (CFB) boiler for coal combustion is shown in **Figure 2.5** below [76]:

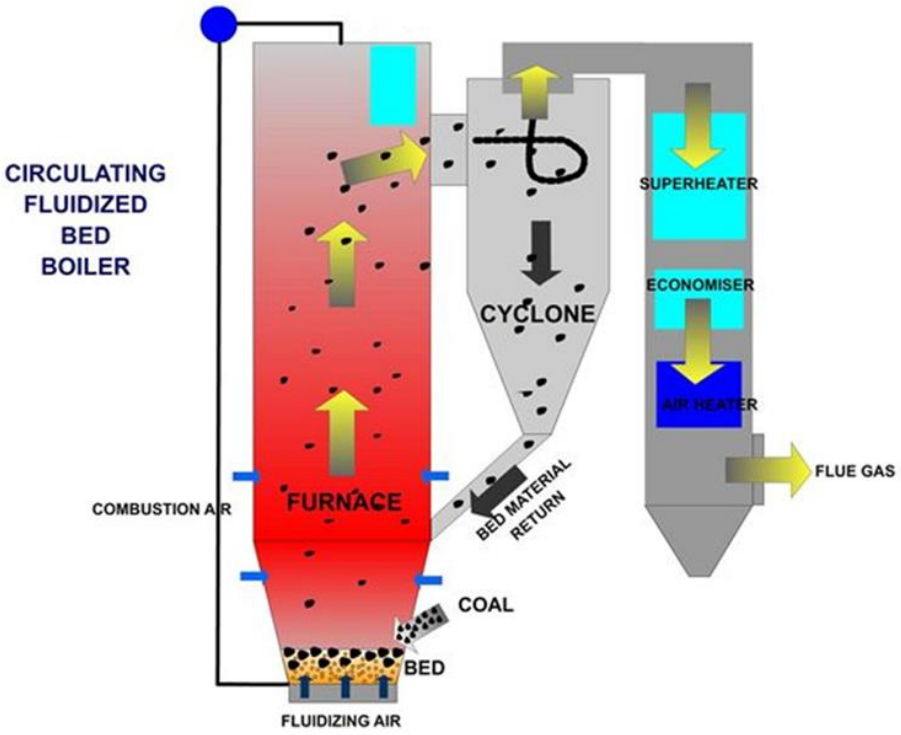

Figure 2.5 The structure and combustion process of CFB system [76].

2.1.4 CO_2 capture and coal oxy-combustion

Compare to about 37% of coal combustion efficiency in last century, the advanced modern coal power plant can achieve approximately 50% of efficiency with at least 650 kg of CO_2 emission per 1 MWh of electricity generation, which is over 30% less than the older plants operating today. Arduously, as the continuous increasing of global electricity consumption, only the improving of power generation efficiency is hardly keeping up with the accelerated increasing CO_2 emissions [77]. According to Skorek-Osikowska's study [78], focus on improving the controlling parameters of the coal-fired power plants is not an ideal method of controlling the carbon dioxide emission. Thus, at present, it is commonly believed that a significant reduction of the

anthropogenic emission of greenhouse gases in the power sector can only be achieved by integrating plants with carbon dioxide capture and storage installations. Three carbon capture methods have been developed to solve the current CO_2 emission risks as: capture after post-combustion process, capture by separation of CO_2 between pre-combustion and formal combustion process, and oxy-combustion within an oxygen atmosphere [79]. The dominant oxy-combustion technology is better than the other two CO_2 capture methods (post-combustion and pre-combustion capture) with less consumption of energy in the process of CO_2 capture installation required. It is also cost less to develop new equipment and easily fit out this technology into existing systems (by retrofitting) because it uses most of the existing machines and plant equipment [80].

The principle of oxy-combustion technology is based on fuel combustion in an atmosphere of pure oxygen without the influence of nitrogen. The expected flue gas of carbon dioxide and water vapour always inevitably mixed nitrogen, argon, oxygen or sulphur dioxide in a real combustion situation, which due to the purity of the oxygen produced is not 100% or the leakages in the installation [81]. Although the advantages of oxy-combustion have been noted, this technology is still not adopted at present in large scale commercial power plant due to the high energy consumption for the production of pure oxygen [82]. Currently, the main technologies for oxygen supplements in most of present power plants rely on cryogenic installations. Vacillatingly, the reasonableness of such energy-consuming production of pure oxygen used for oxy-combustion (which aims to reduce CO_2 emissions from the energy sector) still waits to be proved [83-84].

The laboratory studies of developing oxy-combustion technologies in existing power plants may save approximately 35% costs than present implementing capture methods.

Compared to other methods, the greater advantages of oxy-combustion technology can help to reduce the size of the boiler and fittings in the future. The high efficiency technology of oxy-combustion helps to save flue gas recirculation process and remain the temperature in whole combustion process [85].

2.1.5 Coal combustion issues

There are still some unavoidable issues in present coal combustion technologies, such as the combustion efficiency and environment problems. Although mature coal combustion technology has been used for centuries, the influence of efficiency and environmental issues caused by practical parameters, mineral matters, sulphur content, and moisture content still exist [86].

From experience, the increasing rank of coals with higher heat value doesn't give higher reactivity as expected. From a environmental perspective, low volatile content coals (anthracite) also show poor burning properties than high volatile coals (bituminous). The grinding process will contribute to higher reactivity but a high unit surface area of coal particles will enhance the retained moisture content even after drying process [87-88].

Another important factor of coal combustion process is the soot, which could be observed above the flames in the pyrolysis or combustion process. The formation of soot normally can attribute to fuel rich oxidation, sublimation of volatile metals, and suspended solid particles. Heat transfer is an important factor of coal-fired power furnace operation, it is mainly limited by conduction, convection, and radiation. In the combustion process, the small particles (an average size around 50 μm) always are coerced by rising primary air in traditional wall-fired, swirl-stabilized or pulverized coal combustor and transported into the furnace from a pulverized coal burner. Under an operating condition of combustion the formation of soot is not only an

environmental issue, but also a waste of energy. In the staged combustion process, especially by using the low NO_x burner, the intensive fuel region is rapidly heated and the hot particles are activated by the recirculating hot gases and the heat radiation from the combustor walls and hot flame in the combustor [89].

Slagging and fouling are the main reasons of the ash deposition which influence the heat transfer efficiency, cause corrosion on the surface of furnace, burner and water-wall tubes, and block the gas flow path. The slagging is mainly generated by condensation of fusion fly ash from the high temperature radiant region in the furnace and when they come across the lower temperature heat transfer surfaces and refractory surfaces. The fouling is hardly indicated but always be observed in the high temperature section of heat convection, which are produced by ash deposition, volatiles and sulfureted ash [35, 90].

2.2 Biomass combustion technologies

Biomass thermal application including combustion, co-combustion, gasification and pyrolysis are designed to achieve reduction in greenhouse gas and pollutants emissions. In ancient times, biomass such as wood and straw were mainly used as a combustion feedstock. Since the beginning of 18th, fossil fuels were widely used as industry developed. Nowadays, because of the shortage of the fossil fuel and climate change, humans again have examined the utilization of biomass materials. As the combustion technologies were improved, even wet biomass feedstock with up to 60% moisture content are able to be fired. Unfortunately, herbaceous biomass contains more nitrogen, sulphur, potassium, chlorine and microelements etc. and so the combustion of herbaceous biomass contributes more emissions of NOx, particulates, corrosion, ash, deposits, and GHG compared with wood. As an advantage, wood is more suitable for combustion for ~~household~~ energy and industry scale due to its low content of ash and low N (i.e it contributes less NOx emission). There are rich wood resources such as in forests, urban waste wood and demolition wood. While wood is as well suited for household heating as for larger plants, herbaceous biomass is restricted for larger plants. The same is true for urban waste wood and demolition wood. [91-94]

2.2.1 Pre-treatment of biomass

Without a treatment, biomass always has a low energy density; low bulk density, high moisture content and difficult morphology that make the biomass application have low efficiency and high costs. During the application process, biomass can also absorb moisture that seriously affects the storage of the biomass with decay and decomposition. All of these effects will deteriorate the properties of biomass for combustion and gasification.

To promote the energy conversion efficiency of biomass during the thermal process, pre-treatment of biomass is necessary. Generally, the pre-treatment methods are classified as physical, chemical, biological and combinatorial pre-treatment.

- Physical treatment of biomass

According to a previous study by Palmowski [95], the possible physical methods to optimize the available specific surface area of biomass are classified into coarse size reduction, chipping, shredding, grinding and milling. Moreover, comminution of biomass into small particles is effective to reduce both the degree of polymerization (DP) and cellulose crystalline. Generally, the original physical treatment of biomass can be identified as the harvesting and preconditioning process, which can cut the biomass into coarse size and reduce the unnecessary residues from land. Furthermore coarse size pre-treatment, chipping, is more effective for reducing the transportation costs. Grinding and milling can cut the mass into smaller particle size, which are important processes to improve the characters of the feedstock, making pelletizing easier.

According to Cadoche's study [96], the energy requirement for the mechanical comminution process is very high. However, Bougrier [97] indicated that it is economical to comminute biomass into small particles at industry scale, which can improve the yield of bio-fuel, such as biogas, bio-ethanol, bio-hydrogen, etc.

- Chemical pre-treatment of biomass

Chemical pre-treatment is mainly used prior to biological conversion and can be divided into acidic, alkaline and neutral pre-treatments. In Fengel's report [98], acids, alkali, organic solvents, and ionic liquids can modify some properties of the biomass. For example, the alkali can change the internal shape of the biomass and make it swell.

If the internal space of the biomass is expanded, the degree of polymerization and cellulose crystallinity will be decreased; this affects the structure of the cellulose and hemicelluloses by breaking the linkage. According to Chandra [99], alkali is less effective for lignin than cellulose and hemicelluloses, so alkali is always used to treat the low lignin content biomass. Acid solution is also introduced to hydrolyze biomass. Diluted acid such as sulphuric acid, hydrochloric acid, and phosphoric acid are generally used in the pre-treatment of biomass to break the hemicelluloses structure into small monomers. Chemical pre-treatment is recognized as an economical and effective method to optimize the biomass performance during biological reactions.

- Biological pre-treatment of biomass

Biological pre-treatment uses fungi to hydrolyse the biomass into carbohydrate. The hydrolytic enzyme is capable of degrading lignin, hemicelluloses, and polyphones into a series of monosaccharide or polysaccharide. By fermentation those carbohydrate can be converted into bio-fuel or biogas. In Hatakka's [100] report, white- and soft-rot fungi are introduced to degrade lignocelluloses material, and it has proved to be an effective biological method. The relevant reactions and process can be described as:

(1) Lignocelluloses $\xrightarrow{\text{Fungi \& heat}}$ monosaccharide $\xrightarrow{\text{Fermentation}}$ degradation products and by- products (glucose) (**Reaction 2.1**)

(2) Glucose: $C_6H_{12}O_6 \xrightarrow{\text{Enzyme}} 2C_2H_5OH + 2CO_2$ (**Reaction 2.2**)

While biological pre-treatment of biomass can give good yield of bio-fuels with low auxiliary energy cost, the period of the biological degradation process is very long.

- Combinatorial pre-treatment of biomass

Combinatorial pre-treatment methods can be composed of physical pre-treatment, chemical pre-treatment and biological pre-treatment. The biological pre-treatment with long-term internal reaction is suggested for the beginning of the combinatorial pre-treatment process in the storage space. Secondly, the chemical pre-treatment of biomass is more suitable to be operated before the physical pre-treatment of biomass. There are also other pre-treatment technologies, which can be involved in this process, such as physicochemical pre-treatment. This physicochemical pre-treatment technique can be classified into a variety pre-treatment technologies such as steam pre-treatment, liquid hot water pre-treatment, wet oxidation pre-treatment, ammonia fibre/freeze explosion, ammonia recycle percolation, aqueous ammonia retreatment, organic pre-treatment, inorganic-liquids and cellulose solvent-based lignocelluloses fractionation pre-treatment. The physicochemical pre-treatment of biomass is based on chemical and physical properties to modify the biomass structure.

All of these pre-treatment techniques are focused on the development of the chemical and physical properties of biomass. The improvement of the characteristics can promote the combustion and gasification of biomass with good thermodynamic performance approaching those of fossil materials. In summary, the pre-treatment concept is in order to achieve a reduction of moisture content, decreasing both the degree of polymerization (DP) and cellulose crystallinity, and improving the available specific surface areas which are key factors in conversion to liquid fuels, as well as in gasification and combustion process. Chemical and biological reactions degrade the complicated and high molecular weight compounds into more active ingredients with

higher energy density. Considering some safety and economic factors, certain pre-treatment of biomass (e.g torrefaction) is expected to improve the stability for storage and reduce the transport costs. Although many advantages of the pre-treatment technologies are illustrated, the high cost and potential pollution from the pre-treatment itself are not neglected. Recently, torrefaction is introduced as another advanced pre-treatment method as well. Torrefaction of biomass is a mild pyrolysis process like cooking or roasting in the absence of air, which can decrease the mass of the biomass by up to 30%. It is proposed as an effective way to improve the energy content, which hides in the solid by removing the moisture. Torrefaction is usually operated in the range of 230~290℃, however it is an energy consuming process [101].

2.2.2 Biomass combustion process

Combustion is a major utilization of biomass for energy generation. The biomass combustion technologies are divided into general combustion, co-combustion and oxy-combustion. To improve the fuel economy, the associated combustion conditions and combustion furnace have been developed with high combustion efficiency.

Biomass combustion is a typical thermodynamic process involved with multiple phase change and chemical reactions. The whole combustion process is composed of consecutive heterogeneous and homogeneous reactions. Biomass energy is exploited through the thermal process involved with drying of the materials, liquefaction, gasification then combustion of the organic compounds, char combustion and a series of oxidation reactions. Each reaction depends on the physical shape and size, operating temperature, biomass characters, and combustion conditions. According to a previous wood combustion experiment by Baxter [102], the relationship between combustion of batch small wood particle and combustion time, and derivative relationship between volatile and char combustion are shown in **Figure2.1**. As the

temperature increases, the combustion reaction speeds up as seen in the mass loss with time curves. The volatile and char content are important data to judge the combustion efficiency.

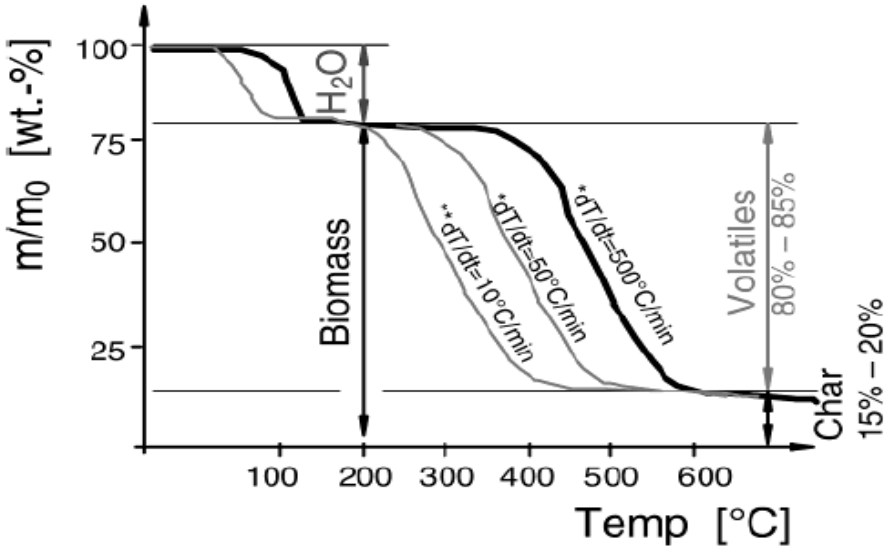

Figure 2.6 Relationship between biomass consumption speeds by combustion associated with the temperature change from thermo-gravimetric analysis (TGA) [102].

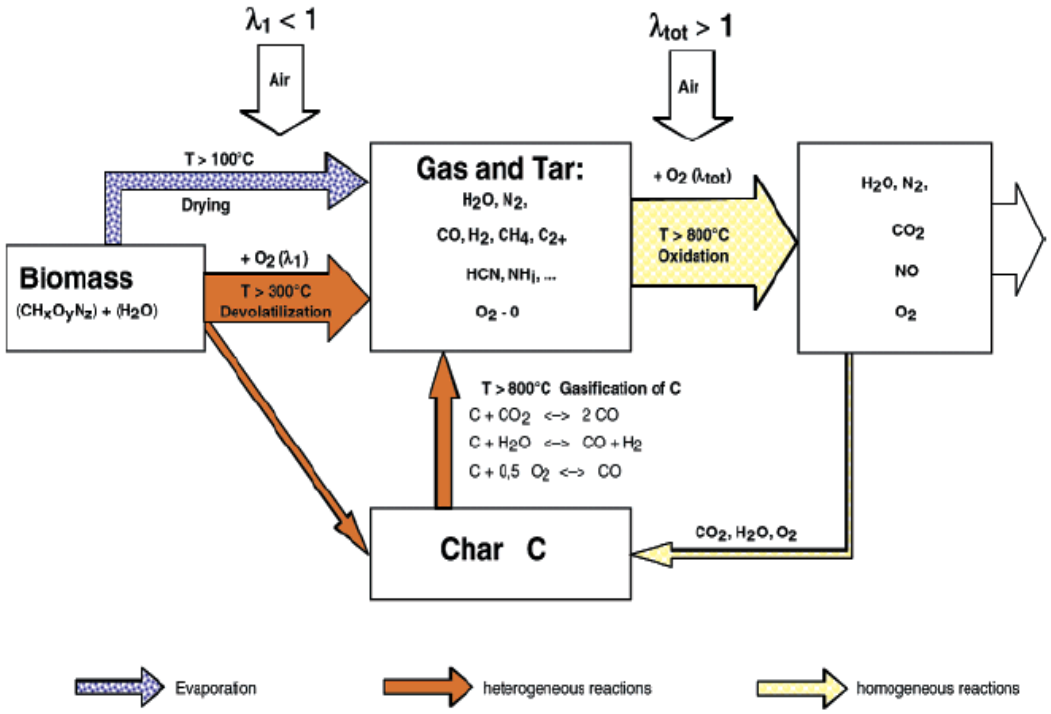

Figure 2.7 General Combustion process with air [103].

- General combustion with air

General combustion with air is widely used today. **Figure 2.7** summarises the reaction sequence and in automatic combustion systems the consecutive reactions are operated in different zones in the furnace above the grate [103]. The main reactions during two-stage combustion of biomass with primary air and secondary air are described in the **Figure 2.7**. To optimize the general combustion technologies and achieve high efficiency and low emission, the design of the furnace is of significant important. After the ignition, the combustion process is operated by the parameter of input air ratio λ. According to Nussbaumer [93], if we assume the average composition of biomass materials such as wood, straw, or similar material to be $CH_{1.44}O_{0.66}$ without the effect of other lesser elements such as N, Cl, metals, etc, the general combustion reaction can be described as the equation below:

$CH_{1.44}O_{0.66} + \lambda 1.03\ (O_2 + 3.76N_2) \longrightarrow$ intermediates (C,CO,H_2, CO_2, C_mH_n, etc.)

$\longrightarrow CO_2 + 0.72H_2O + (\lambda\text{-}1)O_2 + \lambda 3.87N_2$ -439kJ/kmol (**Reaction 2.3**)

2.2.3 Biomass combustion system

To achieve high efficiency, the structure and function of the boiler furnace is more important and has a broad space for development. Nowadays, based on the different characters of the biomass feedstock, there are various boilers designs. The utilization of biomass energy by combustion can be used for district heating in developing countries, but in the UK it is mainly used for electricity generation. The maximum energy yield can achieve up to 50 MWth. The energy converted principle of combined heat and power production (CHP) with biomass is based on steam cycles (Rankine cycle), and organic Rankine cycles (ORC). The heat from combustion raises hot and high pressure stream to operate steam turbines and steam engines to get power outputs in the range of 0.5~10 MWe or higher in the case of power generation in large plant [104]. Stirling engine is a typical power generation engine, and has10 kWe to 100 kWe power capacity. Nowadays, the electricity and heat generation are mainly depending on further applications of co-combustion with coal [105]. The present equipment is related to BFB, CFB, cyclone, and stoker boilers, some of them are shown below in **Figure 2.8. ~ Figure 2.11.**

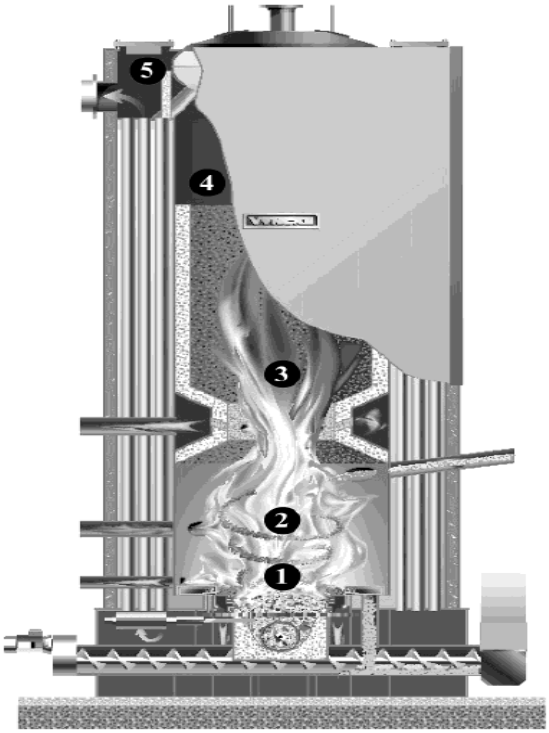

Figure 2.8 Combination of under stoker furnace with entrained flow reactor for air and fuel staging. The operation process is arranged of (1) Feeding of primary fuel and primary air;(2) Reduction zone;(3) Injection of secondary fuel and consecutively tertiary air;(4) End of post combustion chamber, flue gas exit to convection part and cyclone [104].

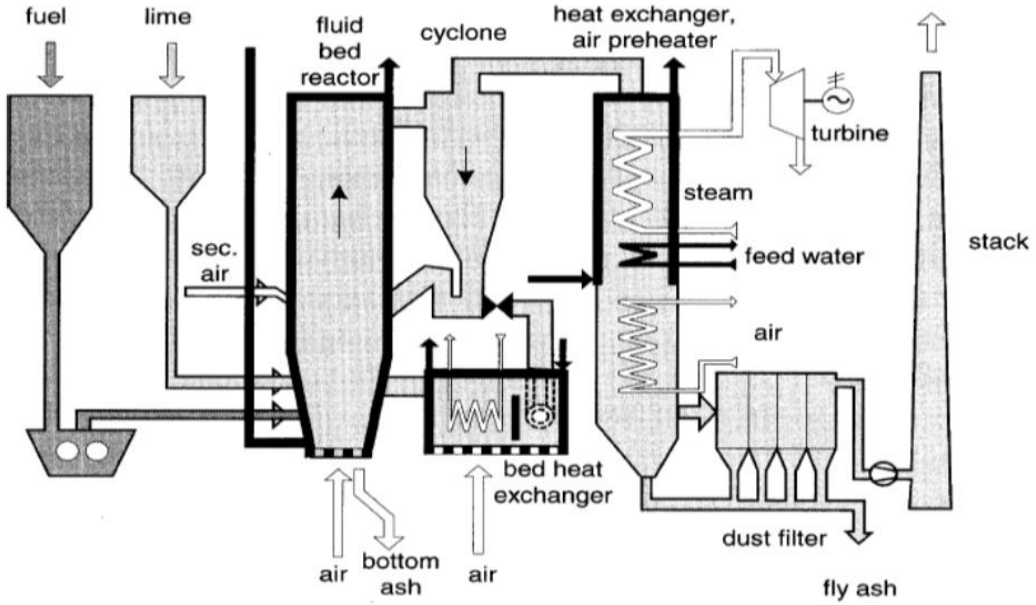

Figure 2.9 CFB plant with steam boiler for co-combustion [104].

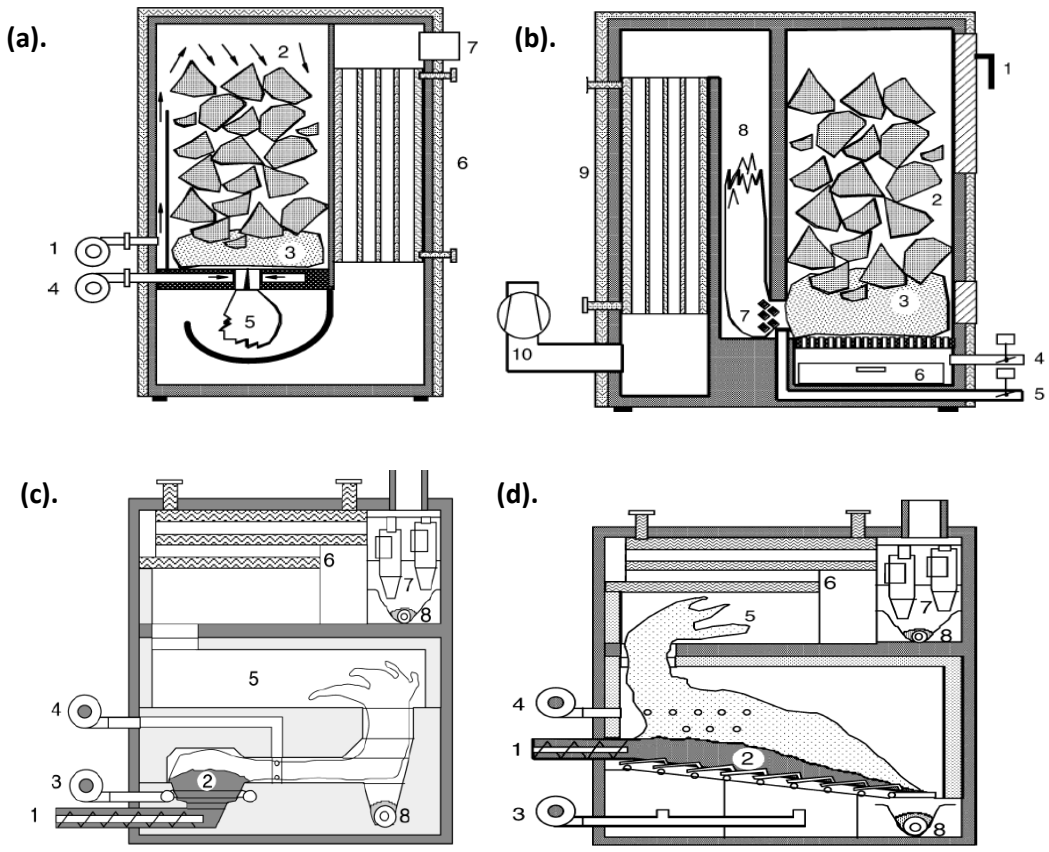

Figure 2.10 Typical boilers for biomass combustion [105]

(a).: Downdraft boilers with inverse combustion of biomass and enrich air flow:(1) Primary air, (2) fuel hopper, (3) glow bed, (4) secondary air, (5) post combustion chamber, (6) heat exchanger, (7) chimney.

(b).: Downdraft boilers with inverse combustion of biomass and enrich air flow:(1) Fuel inlet, (2) fuel hopper, (3) glow bed, (4) primary air, (5) secondary air, (6) ash bin, (7) mixing zone, (8) post combustion chamber, (9) heat exchanger, (10) chimney.

(c).: Under stoker furnace with primary and secondary air, mixing zone, and post combustion chamber. (1) Screw feeder, (2)under stoker zone with glow bed, (3) primary air, (4) secondary air, (5) post combustion chamber, (6) heat exchanger, (7) cyclone, (8) ash removal.

(d).: Moving grate furnace with primary air in two stages in the grate and secondary air. (1) Screw feeder, (2) moving grate, (3) primary air, (4) secondary air, (5) post combustion chamber, (6) heat exchanger, (7) cyclone, (8) ash removal.

2.2.4 Biomass co-combustion and Oxy-combustion

- *Biomass co-combustion with fossil fuel*

Co-combustion of biomass promotes a substitution of fossil fuels and a net reduction of CO_2 emissions. Today, co-firing is a favoured technology to respond to the energy crisis with CO_2 reduction. In developed countries, co-firing is developed to achieve low carbon targets. As the properties of biomass are not as good as fossil fuels, co-utilization of biomass was studied to maintain the power generation capacity. The advantages shown by co- combustion of biomass with fossil fuels are lower costs, better combustion efficiency, and low emissions. However biomass materials own the content of alkali metals, which can be oxidized to generate alkali compounds, which contribute to fly ash and particles which are hard to remove. During co-combustion of typical biomass with fossil fuels such as coal, the alkali composition can react with the acid ions (SO_3^-, NO^-, Cl^-.) which may contribute slag, bottom ash, pollutants which generate soluble compounds. Because lower Fuel-N and Fuel-S, the emission of SO_x and NO_x can be reduced dramatically with lower specific costs and higher combustion efficiency. However, some potential risks such as deposit formation on the walls of the boiler and corrosive by-product should not be neglected, especially alkali metals, which will be deposited during large scale use of biomass. Different with other bottom ash from pure fossil fuel combustion, the ash from co-combustion is more easily removed by washing and absorption. According to previous research, the suitable mass mixture ratio of biomass and fossil fuel is 9:1. The popular co-combustion can divided into direct co-firing, indirect co-firing and parallel combustion. [106]

***Direct co-firing*:** Here the prepared biomass is mixed with fossil fuel and directly fed into the boiler or furnace. Because of the different structures of the boiler, such as

fluidized bed, grate, or pulverized combustion, sometimes the biomass and fossil fuel will be fed into boiler separately. Before combustion, drying, grinding, or tramp metal removal should process the biomass.

***Indirect gasification co-firing*:** The indirect co-firing process consists of gasification of biomass. The product gas is fed as fuel into a fossil fuel boiler furnace. Indirect co-firing is suggested because of the high efficiency.

Parallel combustion: Parallel combustion consists of a separate biomass boiler. There is a shared steam cycle in both indirect and parallel combustion.

- *Biomass Oxy-combustion*

The oxy-combustion concept is at a researching stage, and the developing technologies are not yet demonstrated on an industrial scale. Oxygen concentration has an important effect on the second stage of combustion of biomass. For example, in straw oxy-combustion, in the first stage of the firing, most of hydrocarbon C-O, HO, C-H bonds are broken, and only low concentrations of volatiles are consumed during the thermal decomposition process. [107]. Most of these functional groups are resolved by activation energy. Thus, the oxidization process in the first stage is weak and the oxygen concentration provides little effect. At the second stage of oxy-combustion, as the concentration of C-C bonds is increasing, the combustion of hydrocarbon fragments is promoted by the high concentration of oxygen. Most of the C–C can be oxidized to CO and C–O bonds. So the concentration of oxygen has more effect on the second pyrolysis process [108]. The oxy-combustion owns the advantages of high oxidation efficiency of the char which results in the reduction of emission and less bottom ash.

2.2.5 Biomass combustion issues

The combustion efficiency and composition of emission and ash are related with operating temperature, time, and turbulence. To achieve complete burn out, the mixing ratio of combustible gases and air is a major factor, the temperature required is around 850℃, and residence time should be controlled to ≥0.5s. The potential composition of emission and ash after the combustion can be classified into different types:

(1) Un-burnt pollutants such as CO, C_XH_Y, PAH, tar, soot, un-burnt carbon, H_2, HCN, NH_3, and N_2O;

(2) Pollutants from complete combustion such as NOx (NO and NO_2), and CO_2;

(3) Bottom ash and contaminants such as ash particles (KCl, etc.), SO2, HCl, PCDD/F, Cu, Pb, Zn, Cd, etc.

Biomass combustion contributes to high emissions of particulates which are mainly smaller than 10 μm (i.e., particulate matter PM10) with a high share of submicron particles (PM1) [109]. According to Brunner's study [110], the particle composition, which is mainly consisted of K, S, Cl, Zn and Ca, and the particle size, are related to the combustion conditions. According to Oser [111], if complete burn-out is achieved , the ash components in the fuel, such as the salts of K, Cl, S, Ca, Na, Si, P, Fe, and Al, can be converted by an oxidation process through vaporization into the gas phase and form the bottom ash or grate ash. The particles in the vapour also can form deposits on the furnace wall. As a result, the combustion of biomass should be improved to reduce the emission content of toxic pollutants such as heavy metals and chlorine compounds.

In biomass-fired power plants, ash-related problems are still inevitable during combustion. **Figure 2.11** describes the formation process of alkali-induced slagging and silicate melt-induced slagging [112]. In a circulating fluidized bed (CFB) or a grate furnaces, the high-alkali and high-chlorine content of biomass combustion presents the rapidly and uncontrollable growth of deposits on heat transfer surfaces. The alkali-induced slagging commonly occurs on the surface of superheater and the silicate melt-induced slagging concentrated on the surface of water wall. The hard and compact deposition layer reduces the heat transfer efficiency of the boiler [113-117]. Furthermore, the complicated alkali/chlorine compounds in the deposits on tube surfaces contribute to corrosion which may cause leaking or damage of the tubes [118]. Serious agglomeration from fused or partly-fused ash may cause the defluidization and unscheduled shutdown of the entire power plant when biomass combustion in a CFB [119-121].

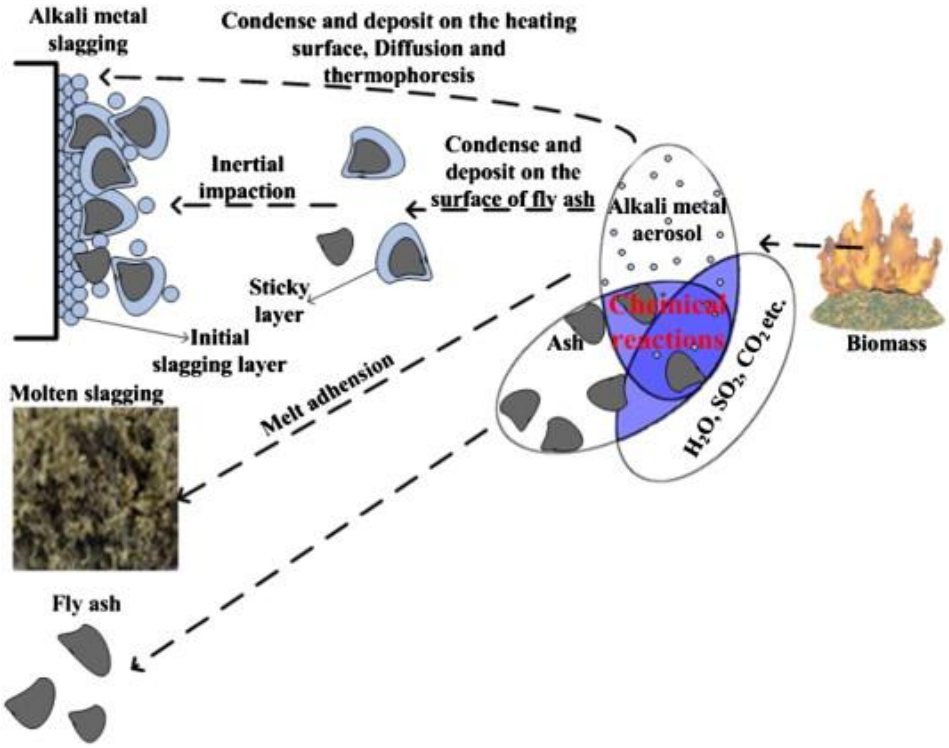

Figure 2.11 Forming mechanism of biomass ash deposition [112].

2.3 Ash composition in combustion

During the combustion of biomass or co-firing with coal, ash deposition causes a variety of problems. Because the ash sticks on the surfaces of the superheater, burner area and boiler walls, burner quartz and superheater tubes, the increased temperature in the boiler contributes to the superheated steam and the rate of heat transfer is decreased, that makes a huge waste of energy. The sticky deposits may enhance the corrosion on the surface of radiant superheaters tubes, which may also damage the steel materials. Additionally, the shedding of the bulk ash deposition may break the ash hopper. During the combustion process, the deposits may block heat transfer tubes and may aggravate gas velocity, which enhances excessive fouling in the convective areas and more corrosion happens. Some of the deposits on the burner "eyebrows" also can distort the burner aerodynamics which may cause problems with flame stability and ignition. [122]

2.3.1 Inorganic compounds in biomass ash

For the application of biomass in direct combustion and co-firing with coal, common issues concern the composition of biomass ash**.** The composition of sub μm and super μm particles has been widely studied. The main consistent of the inorganic products are metallic oxide and, mineral salts. Those fine particles mainly contain the elements of K, Cl, S, Na, and Ca and the coarse particles mainly contain the elements of Ca, Si, K, S, Na, Al, P, and Fe. A detailed review of the scientific literature, including more than 600 mostly peer-reviewed references and data compilations has been conducted to systematize the results obtained for composition and properties of biomass and biomass ash. These results provide a sound foundation for an initial database that can be used for phase characterization and subsequent classification and sustainable exploitation of biomass ash. It was also found that serious problems related to phase

investigations of biomass ash occur and some of them are similar to those determined for chemical and phase studies of biomass. But these data have their boundaries. Few of the studies were applied in a large scale test to prove their credibility. According to those studies, ash forming matters in biomass fuels can be classified into four types: (1) water soluble salts, (2) elements associated with the inorganic materials of the biomass, (3) mineral included in the fuel structure, (4) inorganic material added to biomass from extraneous sources [123-125]. For example, those chemical analyses of the compounds in the ash of several of typical biomass fuel are listed in **Table 2.3**.

In the combustion and gasification of biomass, the inorganics play an important role in the thermodynamic reactions. Inorganics are found in all streams, tar, char, bottom ash, grate ash, even in the deposit on the furnace wall. Since the quantities of inorganics are not the same in different biomass, the compositions of the inorganic compounds are variable under different operating conditions. Although the advance and benefits of biomass technologies are widely presented, the drawbacks of the technical problems relating to the inorganic contents of the biomass fuels can never be neglected during the process of energy generation [126]. The most serious risks are the nitrogen and ash components, which widely distribute in relevant constituents in biomass. NO_X, and particulate emissions are certainly caused by the application of biomass.

Many problems, such as slagging, fouling, bed agglomeration, aerosol, ashes, etc caused by the inorganic components of biomass fuels are obviously obstacles in the application of bio-energy. The inorganic materials have always been observed adhering to reactors as deposits under different temperature or fluidizing air inlets [26]. High chlorine and high alkali fuels can be particularly problematic.

The existence of the inorganic fraction of biomass may cause several problems during combustion and gasification. The formation of particles (aerosol and fly ash) in biomass combustion has resulted in sediment generation (slagging and fouling) on the super heater tube, so as to reduce the heat transfer efficiency of the water / steam system, and may result in corrosion of the super heater tubes [127]. These problems may cause costly shutdowns of combustion units. The heavy metals existing in the ash, such as mercury, have also been a concern in the combustion and gasification of coal process. While mercury has a lower concentration in biomass the problem may still exist. The formation of fine inhalable particles enriched in toxic metals or gaseous emissions is also a concern.

Table 2.3 Analysis of biomass ashes in main oxides [123-125].

Biomass	**CaO**	**K_2O**	**P_2O_5**	**MgO**	**SiO_2**	**Al_2O_3**	**Fe_2O_3**	**TiO_2**	**Na_2O**	**SO_3**
Manure	13	12.3	5.5	4.5	42	6	1.9	0.2	4.9	-
Sewage sludge	19–52	0.1–3	2–17	0.5–3	5–31	2–13	1–15	0.1–0.7	0.1–0.5	0.5
RDF	12.7	1.7	1.4	1.7	51	15.2	5.1	2	5	2.5
Sunflower shell	15.8	35.6	4.8	6.1	29.3	2.9	2.1	0.1	1.5	1.3
Switchgrass	5–16	1–15	2–5.5	1.5–5	57–70	0.4–0.5	0.4–0.6	<0.1	0.1–0.5	2–3
Cotton stalks	16.4	30	-	5.2	8.4	0.8	0.5	-	2	-
Poplar	47.2	20	5	4.4	2.6	0.9	0.5	0.3	0.2	2.7
Pine	49.2	2.5	0.3	0.4	32.5	4.5	3.5	0.4	0.4	2.5
Wheat straw	4–6	7–25	3–4	2–4	48–78	0.5–2	1–2	-	0.2–1.0	-
Bagasse	1.9	3.5	-	2.2	54	15.3	14.8	3.5	0.9	-
Cotton gin trash	7–16	11–13	-	3–8	23–41	4.3	2–3	-	-	-
Olive kernel	22.9	9.2	2.4	3.8	45.0	7.0	6.2	-	0.9	1.6

The numerous processes related to ash formation are listed in **Table2.4** below. The detailed phase transformations during biomass combustion are complex and not discussed here. According to Vassilev [128] the ash formation and behaviors of inorganic and organic compounds in the biomass heating process can be identified by complementary methods: optical microscopy, XRD (X-ray diffraction) and DTA-TGA (Differential thermal analysis and Thermogravimetric analysis). Some observations with temperature range were introduced as: (1) fragmentation of particles was observed under 500°C; (2) agglomeration occurs as initial (700–900°C), significant (700–1100°C) and extensive(700–1300°C); (3)The melting of particles can be observed and described as initial (700°C), extensive (900–1100°C) and complete (1100–1500°C); (4) various new phase crystallizations occur between 500–1500°C; and (5) glass formation process could be identified microscopically in biomass ash between 700–1500°C.

Table 2.4 The formation mechanism of biomass ash [128].

Origin	Formation process	Place of formation	Time of formation	Formation mechanism
Primary	Natural	Biomass	Before and during plant growing, and after plant died	Original phases or minerals that have undergone no phase transformations during combustion
Secondary	Anthropogenic (technical)	Combustion installation	During combustion	New phases generated by solid, liquid and gas reactions among pre-existing and newly formed compounds (amorphization, carbonation, carbonization, coalescence, crystallization, de-carbonation, decomposition, dehydration, de-hydroxylation, destruction, de-sulphation, dissolution, evaporation, fragmentation, hydration, hydroxylation, melting, nucleation, oxidation, polymorphic transformation, precipitation, re-crystallization, reduction, softening, solid-state reactions, sulphation, vitrification, volatilization, combined conversions, others)
Tertiary	Natural	Transportation facilityand disposal site	During transport and storage of combustion residues	New minerals or phases originated by weathering (amorphization, carbonation, crystallization, de-carbonation, decomposition, dehydration, de-hydroxylation, destruction, de-sulphation, dissolution, evaporation, hydration, hydroxylation, oxidation, polymorphic transformation, precipitation, re-crystallization, solid-state reactions, nucleation, sulphation, vitrification, others)

2.3.2 Inorganic in El Cerrejon coal ash

El Cerrejon coal is one of the fuels investigated in this thesis. The composition of ash deposition and behaviours during El Cerrejon coal combustion are less reported. According to López [129], the El Cerrejon coal has a high proportion (14%) of pyrite and a significant proportion (3.5%) of coquimbite, about 54% of quartz and lower proportions of clay minerals, kaolinite, and illite. Brief summaries of El Cerrejon coal in different literatures are listed in the **Table 2.5**. In the future study, the composition of ash deposition during El Cerrejon coal combustion will be identified using laboratory and large-scale tests.

Table 2.5 Summary of El Cerrejon coal.

Name	Wieland [130]	Barbosa [131]	Nathan [132]	Piñeres [133]	Rincon[134]	Quintero[135]
Proximate and ultimate analysis						
H_2O (%)	1.63(db)	13.0(ar)	N/A	N/A	7.01(ar)	12.0
Volatiles (%)	32.58	37.0	N/A	29.17	36.21	31.5~37.0
Ash (%)	11.79	12.6	N/A	18.53	1.41	4.5~11.5(db)
Fixed-C (%)	54.00	50.4	N/A	50.89	55.37	N/A
C (%)	74.28	66.4(±5.0)	N/A	N/A	75.5	82.4~84.23
H (%)	4.34	4.7(±0.4)	N/A	N/A	5.8	5.53~5.9
N (%)	1.73	1.4(±0.1)	N/A	N/A	1.0	1.3~1.85
S (%)	0.73	0.96(±0.01)	N/A	1.41	0.9	0.4~0.85
O (%)	5.50	N/A	N/A	N/A	N/A	7.73~9.5
Cl	N/A	0.07(±0.0001)	N/A	N/A	N/A	N/A
Ca	N/A	0.23(±0.02)	N/A	N/A	N/A	N/A
K	N/A	0.24(±0.02)	N/A	N/A	N/A	N/A
Na	N/A	0.08(±0.01)	N/A	N/A	N/A	N/A
P	N/A	0.004(±0.0003)	N/A	N/A	N/A	N/A
Fe	N/A	0.64(±0.04)	N/A	N/A	N/A	0.009~0.188mg/kg

Al	N/A	1.29(±0.1)	N/A	N/A	N/A	N/A
Mg	N/A	0.004(±0.0003)	N/A	N/A	N/A	N/A
Ba	N/A	<3.6	N/A	N/A	N/A	N/A
Sb	N/A	<0.07	N/A	N/A	N/A	N/A
Mo	N/A	<22.4	N/A	N/A	N/A	N/A
Se	N/A	<0.21	N/A	N/A	N/A	N/A
As	N/A	<0.73	N/A	N/A	N/A	0.078~23.91mg/kg
Hg	N/A	<0.27	N/A	N/A	N/A	0.004~0.187mg/kg
Cd	N/A	<7.3	N/A	N/A	N/A	0.012~1.41mg/kg
Pb	N/A	<22.8	N/A	N/A	N/A	0.30~4.66mg/kg
Cu	N/A	<9.4	N/A	N/A	N/A	1.49~9.78mg/kg
Ni	N/A	<14.4	N/A	N/A	N/A	0.446~5.6mg/kg
Zn	N/A	36.8	N/A	N/A	N/A	1.01~5.02mg/kg
Cr	N/A	33.5	N/A	N/A	N/A	N/A
HHV(KJ/Kg)	28217.54	N/A	N/A	23644	N/A	28500
LHV(KJ/Kg)	27250.76	24790.00	N/A	N/A	N/A	26900
Ash composition						
Al_2O_3 (%)	27.30	N/A	24.4	N/A	N/A	14.73~42.6
CaO (%)	5.74	N/A	4.9	N/A	N/A	0.94~1.97
Fe_2O_3	5.25	N/A	6.7	N/A	N/A	2.7~11.9
K2O	1.35	N/A	0.13	N/A	N/A	0.03~0.57
MgO	1.67	N/A	1.6	N/A	N/A	0.92~2.22
Na_2O	0.55	N/A	0.05	N/A	N/A	1.2~2.1
P_2O_5	1.22	N/A	0.8	N/A	N/A	0.12~0.22
SiO_2	52.01	N/A	58.6	N/A	N/A	41.2~73.0
SO_3	3.51	N/A	0.6	N/A	N/A	2.1~2.7
TiO_2	1.40	N/A	1.2	N/A	N/A	3.0~3.3
Total	100.00	N/A	99.58	N/A	N/A	N/A

Ash fusion temperature		
IDT (°C)	1264.67	N/A
ST(°C)	1380.33	
HT(°C)	1420.00	
FT(°C)	1464.67	
Indices		
AI	0.079	Fouling probably
$R_{a/b}$	0.18	Low slagging propensity

According to Nathan [132], the crystals in El Cerrejon coal are probably consisted of Mullite,($Al_6Si_2O_{13}$); Amorphous(Al–Fe silicates); Amorphous (Ca–Al–Fe silicates), Quartz, (SiO_2); Portlandite, ($Ca(OH)_2$); Feldspar, (mainly anorthite,); Hematite, (Fe_2O_3); Magnetite, (Fe_3O_4); Anatase, (TiO_2).

2.3.3 Forming mechanism of ash deposition

To study the ash deposition caused by biomass fuels, different compositions of the fuels are selected and tested. It is worthy to note that, compared with coal, biomass contain large amount of alkali metals and chlorine and lower amounts of sulphur. The investigation shows that the ash content of biomass fuels is about 1%-10% on a weight basis, and the alkali content in the ash can be major, for example in the case of wood is up to 15–20%. As a result, relatively large amounts of alkali metals, chlorine and sometimes sulphur are released to the furnace during the combustion or co-combustion of biomass, then ash-related problems such as deposition, corrosion and slagging happens [122].

In the co-combustion of biomass and coal, running slag is more common, the lower melting point of biomass ash under the high temperature of coal combustion

circumstance contributes more high-viscosity slag and deposit on the wall of furnace and tube when it cools in the low temperature area, which may cause significant corrosion. Especially in fluidized bed combustors, biomass ash may cause rapid agglomeration and de-fluidization. The depositions on the surface of the heat transfer surface seriously affect the efficiency of the heat exchange between the hot fuel gas and the water/steam cycle on the other side of the wall [136].

Experience of coal combustion shows limited significance when directly extrapolated to biomass. The strength and the rate of ash deposition become more valuable to study for choosing suitable operating conditions. In previous studies of pulverized coal combustion, the basic patterns related to the ash behaviour of particle transport to the boiler walls, inertial impaction, thermophoresis, heterogeneous reactions and condensation have been sufficiently summarized and described as **Figure 2.12** and **Figure 2.13** [137-139].

Walsh et al. [113] summarize the mechanisms of coal ash deposition rate as below:

(1) The deposition of the sticky particles on the surface,

(2) The deposition of solid particles on the sticky surface,

(3) The erosion of the deposits by solid particles.

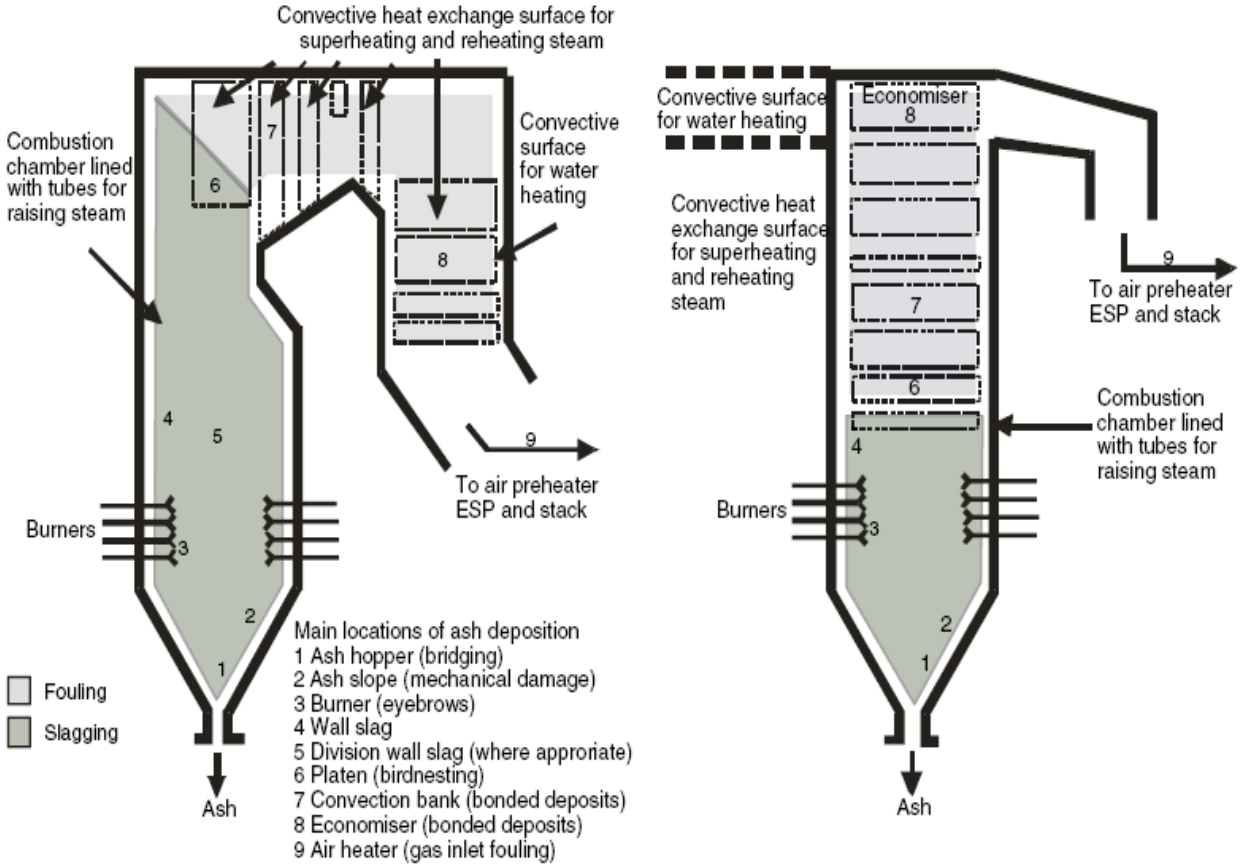

Figure 2.12 Regions of ash related problems in boilers: left — conventional pulverized fuel fired boiler configuration; right — tower boiler configuration [113].

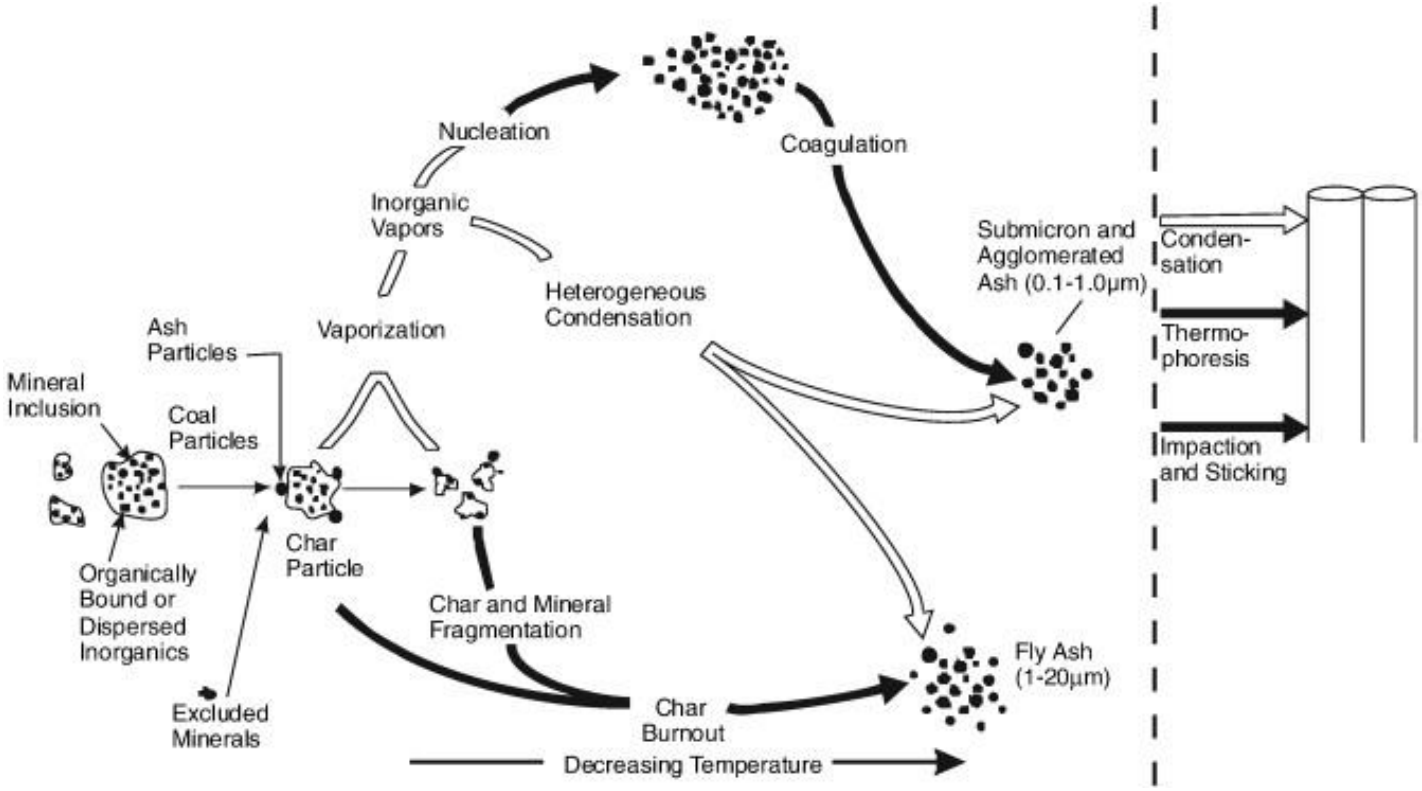

Figure 2.13 The schematic diagram of processes governing the transformation of mineral matter during coal combustion [139].

In the long term struggle to solve biomass combustion issues, the related mechanisms for the formation of alkali-induced slagging and silicate melt-induced slagging are still not explained clearly. The other damage caused by extensive agglomeration and corrosion have not been solved and avoided in effective ways. Even more, there are no standards for re-utilization or disposal of different biomass ash residues to reduce environment stress [140]. Different to other fossil fuels, such as coal, the inorganic composition of biomass is uncertain, by using different planting environments and harvest seasons and selected parts that ash contents and compositions for a particular biomass will be changed. Different types of biomass show different inorganic components. As shown by previous studies, the most popular woody biomass show low silica and low potassium but high calcium content; agricultural residues show high silica, high potassium and low calcium content; animal residues show high phosphorus and high calcium content. All above reasons constitute the changeable ash composition which is related to uncertain ash issues during combustion [26, 141-143]. Wang's study [144] indicates that the sulphates and especially the chlorides are the decisive components which produce ash deposits during biomass combustion in the drop-tube furnace. In his studies, different yields of ash deposits were compared under different extents of the vaporised KCl and SO_2 releasing in high-temperature biomass combustion. The reactions were observed as that a further oxidation of SO_2 contributes the SO_3 to sulphate the KCl which produces the K_2SO_4 and $KHSO_4$ and reduce the concentration of KCl in the gas phase. When the gas temperature decreases, alkali sulphates condense to nanoscale aerosols, $K_2S_2O_7$ and the K_2SO_4 aerosols form the deposits on lower temperature surfaces of heat transfer tubes. Similar results were also observed in many biomass fired power stations. In consequence, the extent of further oxidation of SO_2 becomes an important factor to effect the sulphating

reactions and yields of deposits. For example, in the high-alkali and high-chlorine crop straw combustion, the alkali elements commonly forms the chlorides in the high temperature sections. The chlorides are conducive to produce sulphates with the generation of SO_3 from further oxidation. Different to the straw crop, the low-chlorine content but high-alkali content wood forms NaOH and KOH in high temperature sections. Those alkali hydroxides will still react with SO_2 and SO_3 to form sulphates. According to comparable experiment by using utility furnaces [145-146], the mechanism of alkali-induced slagging formation and growth can be illustrated as that most of K, Na, Cl, and S in fine particles produce KCl and $K_3Na(SO_4)_2$ as nanoscale aerosols, and then the capturing of high Si and Al content coarse particles contribute to the formation of initially slagging layer on the heating surfaces. The re-capturing activities of abundant fine particles, which unable to adhere to the coarse particles, enhance the growth of the slagging layer, as the temperature of old slagging layer decreased by new slagging layer, deposits present stepping levels. The silicate melt-induced slagging were observed in high-silicon content wood combustion, the silicates replace the sulphate to react as the nuclei for the nucleation and condensation. The high content of Si and Al plays the major role as sulphates. **Figure 2.14** [112] describes the alkali-induced slagging formation and growth mechanism as below.

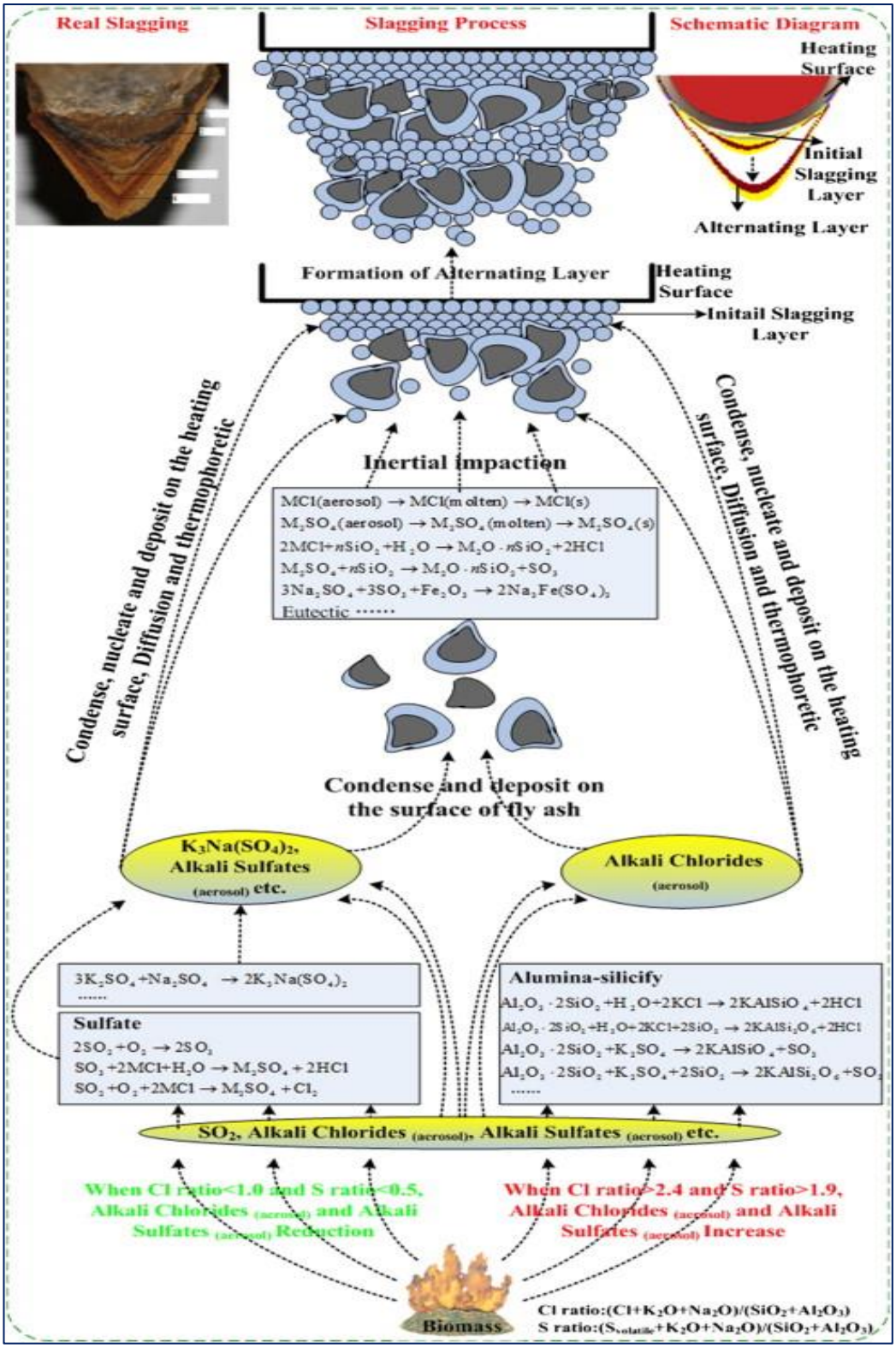

Figure 2.14 Alkali-induced slagging formation and growth mechanisms during biomass combustion. [112]

According to **Table 2.3**, there are a lot of metals (Al, Fe), halogen (Cl),non-metal(S, N, P) and alkali metal(Na, Mg, Zn) involved in the thermal process of biomass combustion. Those inorganics significantly influence the combustion processes.

In a positive aspect, many of those inorganics act as catalysts. According to Alstrup [147], the metal oxides catalysts such as MgO can impair the intermolecular interaction of the complicated polymeric chains. The catalysts can promote dehydration reactions and decomposition of C-C, C-O, C-H compounds. Metal oxides also can play a part in the condensation process and avoid the formation of complicated hydrocarbon with a stable structure. According to Shen [148] about the pyrolysis reaction, the metal catalyst is necessary to lower the activation energy by enhancing breaking of the C-C bond. The positive functions of the metals are related to an encouragement of degradation and decomposition processes. For the combustion process, the metal catalysts can improve the concentrations of the volatile compounds which can be fired easily. During previous research about the combustion of different straw materials, the characteristics of different catalysts were tested for influence in the oxidation reactions.

In summary, during the oxidation process of rice straw biomass combustion and gasification, the inherent metals such as Mg and K could affect the reactions in positive way [149].

However, the inorganics contribute to the formation of particles and aerosols, especially the heavy metals which are identified as toxic emissions. In additions, the existence of alkali and other inorganics enhance slagging, fouling and corrosion, as discussed previously [150].

2.3.4 Composition and crystal structures in ash deposition

There has been a great deal of research aimed at understanding ash behaviours during combustion. As a result, significant information for inorganic matter (various phases and/ or minerals) and, to a lesser extent, organic matter (char, others) identified in biomass ash has been collected and arranged systematically [151]. The behaviour and changes in ash and depositions are associated with the reaction mechanisms and reaction circumstances. For example, according to Vamvuka [152], wood ash material, is mainly composed of Ca-based minerals in the mixture compounds of calcite, anhydrite and dolomite, due to the high natural content of calcium. Particularly, anhydrite could be formed by dehydration of gypsum and/or reactions between calcium and sulphur liberated during fuel combustion:

$$CaSO_4 \bullet 2H_2O \rightarrow CaSO_4 + 2H_2O$$

$$CaO + SO_2 + 0.5O_2 \rightarrow CaSO_4$$

According to Steenari [153], lime was observed in cotton residue ash prepared at 600 ℃, which was probably formed via combustion of calcium organic matter, rather than via decomposition of calcite, which would be transferred at higher temperatures. Other calcium compounds, such as the mixed carbonate fairchildite (olive kernel ash), hedenbergite and hydroxylapatite (olive kernel and cotton residue ashes), occupied a low content per-cent. Kyi [154] studied a range of biomass and found that all the ashes had high contents of quartz, with the exception of vine shoots, (also confirmed by XRF analysis), with smaller contributions from silicates, such as hedenbergite (olive kernel and cotton residue ashes), albite (cotton and forest residue ashes), microcline (cotton residue ash) and clinochlore (paper sludge ash). To study the possible reactions of albite and microcline, the equation mechanisms could be

explained as:

$Na_2SO_4+Al_2O_3•SiO_2+5SiO_2↔2NaAlSi_3O_8+SO_3$ or

$2NaCl+Al_2O_3•SiO_2+5SiO_2+H_2O↔2NaAlSi_3O_8+2HCl$

$K_2SO_4+Al_2O_3•SiO_2+5SiO_2↔2KAlSi_3O_8+SO_3$ or

$2KCl+Al_2O_3•SiO_2+5SiO_2+H_2O↔2KAlSi_3O_8+2HCl.$

Large parts of magnesium (Mg+) compounds mainly exist as periclase, which was identified in many ash samples, and was explained by Koukouzas [155] as it was formed by combustion of magnesia. In paper ash, magnesium is incorporated in talc and clinochlore minerals. Irons compounds (Fe^{2+} or Fe^{3+}) largely exist in forest residue ash in the form of siderite and hematite, which could be produced from oxidation of organic iron or siderite during the combustion process:

$2FeCO_3+0.5O_2→Fe_2O_3+2CO_2$

Minor amounts of alumina-silicates were also observed in many biomass ashes with the exception of vine shoots ash, the aluminium and silicon contents of which are extremely low. The compounds of potassium, which is abundant in agricultural and forest residue ashes, are dominated by carbonates (fairchildite in olive kernel ash), sulphates (arkanite in cotton residue and vine shoot ashes), chlorides (silvite in cotton residue and vine shoot ashes) and K-feldspars (in forest residue ash). The sodium is incorporated within albite (cotton residue, forest residue and waste wood ashes). Finally, the presence of hydroxyl apatite in olive kernel, cotton residue and vine shoots ashes, is most probably associated with the use of fertilizers in agriculture. The mineral phases of the present biomass samples have been also identified and

compared to woody materials of other studies.

The investigation of various crystals and their formation processes can be informed according to the experience of coal and lignite ash chemistry. The calcium, silicon, iron and magnesium minerals could be summarized as the formation of calcite, lime, anhydrite, as well as gehlenite, monticellite (Ptolemais lignite ash) and calcium iron oxide (German lignite ash) in smaller amounts [156-157]:

$Al_2O_3+SiO_2+2CaO \leftrightarrow Ca_2Al(AlSi)O_7$

$CaO+MgO+SiO_2 \leftrightarrow CaMgSiO_4$

$2CaO+Fe_2O_3 \leftrightarrow Ca_2Fe_2O_5$;

$4FeS_2+15O_2+8H_2O \leftrightarrow 2Fe_2O_3+8H_2SO_4$ or

$4FeS_2+11O_2 \leftrightarrow 2Fe_2O_3+8SO_2$

2.3.5 The prediction of biomass ash behaviours

Nowadays, biomass combustion modelling is used to predict gas phase flow and volatile combustion and potential pollutants, etc. [158]. There are many kinds of modelling can be used in biomass combustion analysis. Roman [159] introduced a kinetic model of biomass combustion which is based on Bond Graph methodology. This model focused on calculating the heat generation during the oxidation process. Venturini [160] created a comprehensive computational model to imitate the multi-phase combustion and deposition formation process of biomass. Here, the CFD modelling method was chosen to analyse the wood combustion process. Similar methods were used in Favre's study [161], the gas-phase combustion is simulated as a turbulent combustion, which is predicted based on flow density, turbulence rate and

the chemical effect. The predicted calculation is mainly based on a reduced particle motion equation, the Bassete-Boussinesquee-Oseen (BBO) equation.

About the thermodynamic modelling of combustion, Ross, et.al [162] built up an equilibrium model to predict the concentration of trace metals in the ash and fly ash from co-combustion of coal and biomass in a fixed bed furnace. The trace metal content in the mixture fuels and the ash were classified as: As, Cd, Co, Cr, Cu, Fe, Mn, Ni, Pb, Se, Sn, Tl, V, Zn and Hg. The researchers used the thermodynamic model which is based Gibbs free energy to predict the stability and abundance of metal compounds in the solid and gaseous phases under equilibrium conditions. The modelling of inorganic emissions indicated that there is significant difference between the inorganic emissions from coal and biomass combustion. **Figure2.15** presents the changing curve of the phase distribution of metal concentration over a range of temperatures (600~1400 ℃).

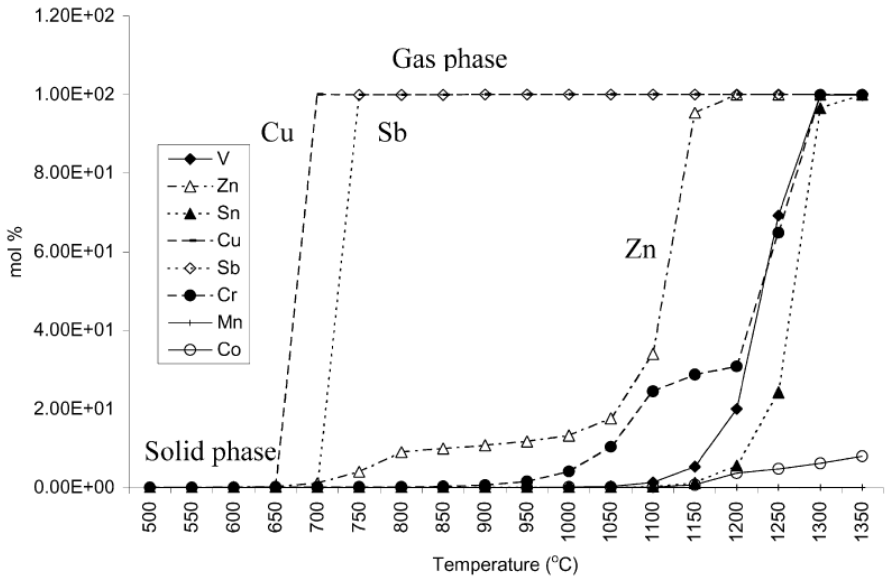

Figure 2.15 Phase distribution of metal species with temperature for Wujek coal [162].

Before 650 ℃, most of the metal species existed in the solid phase. After that the Cu and Sb were volatilized into the gas phase, there are also other volatile metals such as As, Hg, Tl etc. The less volatile metals were oxidized and some of them were mixed into the gas phase at temperature >1000°C. Some non-volatile metals such as Co keep retention in the solid phase even at high temperatures. Through the equilibrium calculation, the performance of the metals can be compared in the curve immediately.

Nowadays, some more modern thermal-balance calculation software has been developed, such as FactSage which is based on Gibbs Free Energy minimization. To evaluate the ash transformation reactions, the combustion temperature, residence time, air input volume and flue gas velocity are needed for building up combustion models. As a consequence of previous studies, the equilibrium conditions are limited by residence time, which effect the interaction and encounters between ash and gases under the combustion of powder or in a pulverized coal-fired (PC) furnace [163-166]. In the studies of ash transformation process, the reaction presents limited predictability. Since previous ash studies, KCl and K_2SO_4 have been noticed to be key compounds of alkali-chlorine/sulphate reactions. K_2SO_4 is mainly formed in a higher gas temperature than KCl [167-169]. According to modeling results, similar results were estimated by both experiment and FactSage simulation calculation [170-171]. In Li' study [172], the $K_2Ca(SO_4)_2$ and $K_3Na(SO_4)_2$ are also predicted in combustion models.

To reduce the drawbacks of ash-related problems during biomass combustion or co-combustion, and propose some reasonable principle for selecting fuel, additives, and types of biomass which will be burned in utility boilers today, current studies pay more attentions on the developments of 'criterion numbers' or 'evaluation indexes', such as the alkali index (K_2O+Na_2O)kg/GJ, (Na+K+2Mg+2Ca)/S ratio,

(K+Na)/(Ca+Mg) ratio and S/Cl ratio [173-176].

2.4 The limitations of previous studies

Some limitations in the previous research works will be summarized and the new research opportunities in this area will be explored

The limitations and problems related to phase investigations of biomass can be summarized as below [155-157,177-179]:

(1) Reliability of online data and previous scientific studies

(2) The long term experience and knowledge of scientific approaches, models and procedures, incomplete data, terms and interpretations which were accumulated in fossil fuel studies may not suitable for many investigations of biomass ash depositions.

(3) The limited description of the specific type, place and manner of biomass ash collection, storage and processing conditions affect the reliable identification and characterization of phases in biomass ash.

(4) The uncertain biomass ash that may contain partially-burnt biomass should always be considered separately from biomass ash generated from natural biomass due to the different origin, composition and potential use.

(5) The lack of generally accepted terminology, classification systems and standards worldwide for the phase composition of biomass ash.

(6) The lack of detailed and complete data sets from simultaneous chemical and phase–mineral analyses for various biomass ashes.

(7) The mineral matter, mineral composition, inorganic matter or inorganics in biomass and biomass ash cannot be clearly and correctly explained by the data from ash yield or the bulk chemical composition.

(8) The common scientific approaches which are used in studying the concentration and behaviour of individual elements (Ca, Cl, K, Na, P, S, Si and trace elements) for

explaining and evaluating different technological and environmental problems have limitations.

(9) The methods for phase and mineral investigations of biomass ash for the identification and quantification of the inorganic and organic phase composition of biomass ash need to be implemented.

(10) Sequential chemical fractionation as an indirect approach cannot be used in distinguishing and identifying the actual modes of occurrence of elements in a multi-component system.

(11) The theoretical equilibrium and stoichiometric calculations of chemical data may not suitable for actual predictions of phases in a multi-component system under non-equilibrium conditions, although they have had some successes.

(12) As biomass ash fusion test is tested under a multi- component system on powder material it cannot have a specific melting point.

(13) Systematic studies about trace elements in biomass and ash, such as Ag, As, Ba, Cd, Cl, Cr, Cu, Hg, Mn, Mo, Ni, Pb, S, Sb, Se, Sn, Th, Tl, U, V and Zn are limited to an initial step of investigation.

Chapter 3 Fuel Analysis and Ash Sample Preparations

In this study, two coal samples (El Cerrejon coal 1 and 2), three biomass (pine, wheat straw, white wood pellet), three ash blends (El Cerrejon coal 1 ash and pine ash in different ash ratios), six fuel blends ash (El Cerrejon coal 1 with pine and El Cerrejon coal 2 with wheat straw in different fuel ratios), pilot scale ash from PACT and their re-burned ashes were tested as described in next few sections and chapters.

3.1 Pretreatment of fuel

The aim of fuel pretreatment is to make the sample suitable for testing. The methods of preparation can be summarized as follows: cutting milling; ball milling and cryogenic milling. Ball mill is a type of grinder which rotates around a horizontal axis which is filled with the media material such as ceramic balls, flint pebbles and stainless steel balls. Through the high speed rotation, the cascading grinding power can cut the rough material into a fine powder. There are many sizes of sieves that can be used for the sifting of the different samples.

Cryogenic milling involves grinding frozen biomass materials; freezing makes the materials weak. The frozen materials can be easily ground into small particle sizes. The cryogens are always chosen as dry ice, liquid carbon dioxide or liquid nitrogen. In this project, the biomass and coal for proximate, ultimate test, and ash fusion test are prepared by ball milling. The samples of the fuel for the C, H, N, S and Cl test are prepared by cryogenic milling. Sieving was used for sifting the samples which are grinded or crushed flour. Those very small holes of the different sieves can separate coarse particles out from the small particles, and present a narrower particle size, fraction for analysis.

3.2 Ultimate and proximate tests

According to the British Standard (DD CEN/TS 15370 – 1:2006), (BS 1016-104.4:1998) and (CEN/TS 14775: 2004), the fixed carbon, H, N, S and Cl contents were tested from the raw fuel materials by using a Flash EA 1112 series analyzer. Oxygen was calculated by difference and the HHV was calculated by the correlation **Equation 3.1** and **3.2**. The ultimate analysis tests the different contents (always in wt%) of the carbon, hydrogen and oxygen (the major components), and the sulfur and nitrogen in the biomass. The carbon determined includes the content in the organic substance in the fuel and any carbonaceous mineral substances. The hydrogen determination includes the organic materials in the biomass and coal and the hydrogen in all moisture associated with the biomass and coal. All the nitrogen is associated with the organic materials in biomass and coal.

The moisture content, volatiles and ash content were determined using a Carbolite MFS furnace. The proximate analysis can be summarized as follows: moisture content (at 105℃); volatile content (at 900℃); fixed carbon content (by calculation) and the ash content (550℃ for biomass, 800℃ for coal) test. The inorganic residue remaining after the combustion is the ash sample. The high heating value (HHV) is based on the energy released during complete combustion of the sample to carbon dioxide and liquid water. Proximate analysis is the most often used analysis for characterizing biomass and coals in connection with their utilization. In this thesis, the ash samples are sieved ≤106μm.

The high heating value (HHV) of the pine wood, wheat straw, white wood pellet and El Cerrejon coal 1 and 2 samples were calculated from their elemental contents on a dry basis using **Equation 3.1** and **3.2**, which were derived by Friedl [180] and Majumder [181]:

$$HHV_{(Dry)}=3.55C^2-232C-2230H+51.2C\times H+131N+20600 \text{ (kJ/kg)} \quad (\mathbf{3.1})$$

$$HHV_{(as\ received)}=-0.03Ash-0.11Moisture+0.33Volatile+0.35Fixed\ carbon \text{ (MJ/kg)} \quad (\mathbf{3.2})$$

In **Table3.1**, all the related biomass and coal samples in this project are listed. The wheat straw has the highest ash content. White wood pellet has highest volatile matter. El Cerrejon coal show highest fixed carbon content. To study ash behaviors of blends with different biomass ratio, the fuel blends reference data in **Table3.2** are calculated based on pure fuel ultimate and proximate results.

Table 3.1 Pure fuel property results from proximate and ultimate tests.

Reference (%)	Pine	Wheat straw	White wood pellet	El Cerrejon coal 1	El Cerrejon coal 2
[a]Moisture	7.73	8.63	6.80	6.63	8.13
[a]Ash	1.67	6.48	1.28	3.83	3.42
[a]Fixed Carbon	17.96	8.46	7.71	41.55	49.16
[a]Volatile matter	72.64	76.42	84.21	47.99	39.30
[b]C	50.29	47.45	51.26	75.94	79.08
[b]H	5.74	5.53	5.99	4.26	4.21
[b]N	0.61	0.58	0.14	1.76	1.43
[b]S	0.48	0	0	0.64	0.32
[b]Cl	<0.3	N/A	N/A	<0.3	<0.3
[b]O*	42.88	46.43	42.61	17.40	14.96
[c;d]HHV MJ/kg	19.97	18.76	20.42	29.54	29.18

[*]By difference; [a]: As received; [b]: Dry basis [c]: Calculated by equation (3.1); [d]: Calculated by equation (3.2); All measurements were in duplicate, and averages are reported.

Table 3.2 Fuel blends properties by calculation.

Reference (%)	80%pine&20%El Cerrejon coal 1	50%pine&50% El Cerrejon coal 1	20%pine&80% El Cerrejon coal 1	80%white wood pellet&20% El Cerrejon coal 2	50%white wood pellet&50% El Cerrejon coal 2	20%white wood pellet&80% El Cerrejon coal 2
[a]Moisture	7.51	7.18	6.85	8.53	8.38	8.23
[a]Ash	2.11	2.76	3.40	5.86	4.94	4.03
aFixed Carbon	22.72	29.83	36.88	16.64	28.87	41.05
[a]Volatile matter	67.66	60.24	52.87	68.97	57.81	46.69
[b]C	55.42	63.12	70.81	50.50	61.22	71.94
[b]H	5.44	5.00	4.56	5.65	5.11	4.57
[b]N	0.84	1.19	N/A	0.71	0.98	1.25
[b]S	0.51	0.56	N/A	0.06	0.16	0.26
[b]Cl	N/A	N/A	N/A	N/A	N/A	N/A
[b]O*	37.78	30.14	1.53	43.07	32.53	21.99
[c;d]HHV MJ/kg	21.94	24.89	0.61	20.84	23.97	27.10

[*]By difference; [a]: As received; [b]: Dry basis [c]: Calculated by equation (3.1); [d]: Calculated by equation (3.2); All results are by calculations; N/A: not available.

3.3 Ash samples preparation

Firstly, all kinds of ash were prepared from the biomass and coal samples according to the British Standard DD CEN/TS 15370-1:2006 and BS 1016-104.4:1998, respectively. The blended fuel ash is based on the mass ratio, and their ash proportions are calculated related to the different ash content in **Tables 3.1** and **3.2**. Under laboratory conditions, the fuel is combusted in air in silica crucibles using a Carbolite MFS furnace. All the pure ash and blend sample reference names, corresponding fuel and ashing conditions are listed in **Tables 3.3.** Blending was done in two ways as shown in **Table 3.4**: In one set of samples, the pure fuels were ashed and then the ashes were blended; in the second set of samples, the fuels were blended, and then the blends were ashed.

Table 3.3 Pure fuel ash sample designations and preparation conditions.

Sample name		Materials (Weight%)	Temperature of preparation °C	Ash ratio Biomass : Coal
Coal	PCC1	100%El Cerrejon coal 1 ash	550℃	0:100
	PCC2	100%El Cerrejon coal 1 ash	800℃	0:100
	PCC3	100%El Cerrejon coal 2 ash	800℃	0:100
Biomass	PPA1	100%Pine ash	550℃	100:0
	PPA2	100%Pine ash	800℃	100:0
	WS1	100%Wheat straw ash	550℃	100:0
	WS2	100%Wheat straw ash	800℃	100:0
	WWP1	100%White wood pellet ash	550℃	100:0
	WWP2	100%White wood pellet ash	800℃	100:0

Table 3.4 Blending fuel ash and ash blends sample designations and preparation conditions.

Sample name		Materials (Weight%)	Temperature of preparation °C	Ash ratio Biomass : Coal
Ash Blends	CA82	Pine ash and Coal ash at fuel ratio of 80%/20%	550℃	63:37
	CA55	Pine ash and Coal ash at fuel ratio of 50%/50%	550℃	30:70
	CA28	Pine ash and Coal ash at fuel ratio of 20%/80%	550℃	10:90
Blending fuel ash	BFPC82	Blended fuels at 80%Pine/20% Coal, then ashed	550℃	63:37
	BFPC55	Blended fuels at 50%Pine/50% Coal, then ashed	550℃	30:70
	BFPC28	Blended fuels at 20%Pine/80% Coal, then ashed	550℃	10:90
	BWCA82	Blended fuels at 80%Wheat straw/20% Coal, then ashed	550℃	95:5
	BWCA55	Blended fuels at 80%Wheat straw/20% Coal, then ashed	550℃	65:35
	BWCA28	Blended fuels at 80%Wheat straw/20% Coal, then ashed	550℃	16:84

Table 3.5 Pilot scale test ash samples.

Reference (%)	CFA1	CBA11	CBA21
[a]**Moisture**	0.56	5.65	6.00
[a]**Ash**	78.82	42.20	13.13
[a]**Fixed Carbon**	0	45.06	77.71
[a]**Volatile matter**	22.69	7.09	3.16
[b]**C**	15.41	46.06	66.73
[b]**H**	0.42	0.09	0.36
[b]**N**	0.19	0.86	1.15
[b]**S**	0.47	0.96	0.30
[b]**Cl**	N/A	N/A	N/A
[b]**O***	83.51	52.03	31.46
[c;d]**HHV MJ/kg**	N/A	N/A	N/A

[*]By difference; [a]: As received; [b]: Dry basis [c]: Calculated by equation (3.1); [d]: Calculated by equation (3.2); All measurements were in duplicate, and averages are reported.

Table 3.6 Re-burned ash of collected pilot scale test ash samples.

Sample name		**Materials**	**Temperature of preparation °C**
Re-burned ash	CFA2	Original CFA1 ash	800℃
	CBA12	Original CBA11 ash	800℃
	CBA22	Original CBA21 ash	800℃

3.4 Ash samples from pilot scale test

To compare with the laboratory work results, the same El Cerrejon coal 2 was also burned in a pilot scale 50kw pulverized fuel unit and the ash from different boiler sections were collected. The air is not preheated. All the process controlling parameters of preheated temperature and flue gas emissions are listed in **Tables 3.7 ~3.10** below. The test facility is located at the UKCCSPACT site in Sheffield. Combustion tests were conducted by Dr. Janos Szuhanszki and the ash samples supplied to Leeds for analysis.

Table 3.7 Experimental parameters for the non-preheated air-firing cases.

	Air
	Non-Preheat
Primary	
Flow (kg/hr)	**60.1 ±0.1**
Temperature(℃)	**18 ±0.1**
Sec/Tertiary	
Flow (kg/hr)	**244.3 ±1.1**
Temperature (℃)	**20 ±0.0**
Purge air	
Flow (kg/hr)	**7.8**
Temperature (℃)	**18**
Fuel	
Coal (kg/hr)	**24.4**
Coal (kW)	**200**

Table 3.8 Flue gas emissions for the non-preheated and preheated cases

	Non-Preheat	
Flue, dry	**Value**	**Error**
O_2 (%)	3.8	± 0.2
CO_2 (%)	15.3	± 0.5
SO_2 (ppm)	291	± 22
NO (ppm)	276	± 17
CO (ppm)	29	± 9

The test facility is shown schematically in **Figure 3.1** and **Figure 3.2**. **Figure 3.1** shows the corresponding observation points, while the combustion temperature profile is listed in **Table 3.9**. The thermocouple locations are set up within the furnace (200mm within and from the inner walls).

Table 3.9 Ashing process controlling parameters

		Air
		Non-Preheat
Temperatures (℃)		
TI-Section1	400	1187
TI- Section 2	900	1215
TI- Section 3	1400	1197
TI- Section 4	1900	1159
TI- Section 5	2400	1101
TI- Section 7	3150	990
TI- Section 8	3650	895
Furnace pressure (mbar)		-0.9

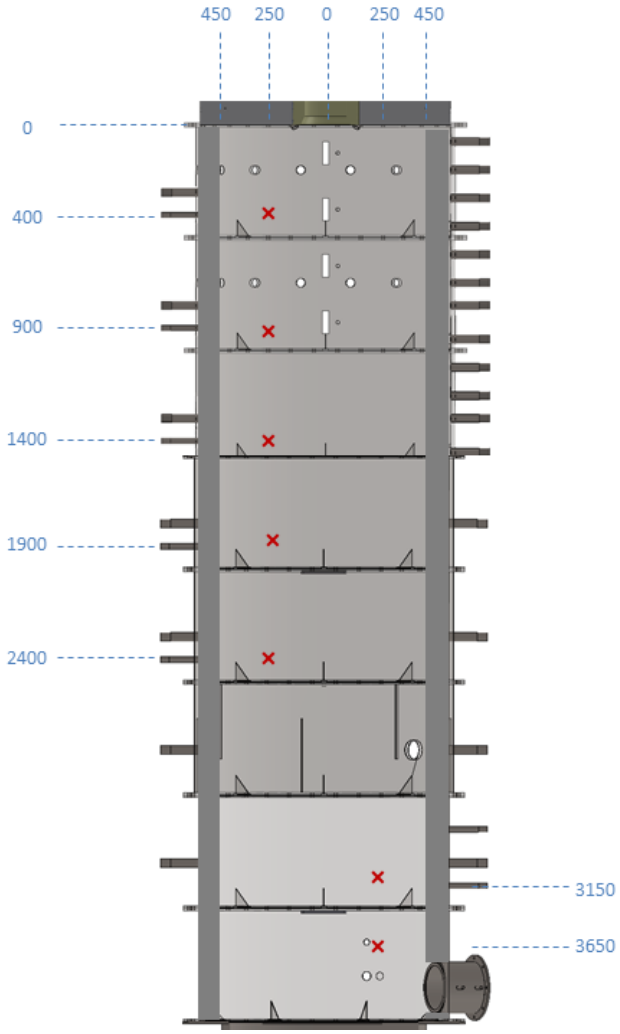

Figure 3.1 Location of the combustion observation locations within the test facility (dimensions in mm).

In **Figure 3.2**, The original fly ash was collected from the bottom of the candle filter and determined as CFA1 (Collection 1), then the original bottom ash from tee section (Collection 2) at the furnace outlet are determined as CBA11 and the original ash samples from the water tray are determined as CBA21 (Collection 3). The ultimate and proximate test results of original collected ash from those 3 different locations are summarized in **Table 3.5**. The re-burned ash and treated conditions are listed in **Table 3.6**. The coal was a Columbian coal from the El Cerrejon region. It was pre-milled in the UK prior to the experimental investigation and stored on site in a 25kg bag.

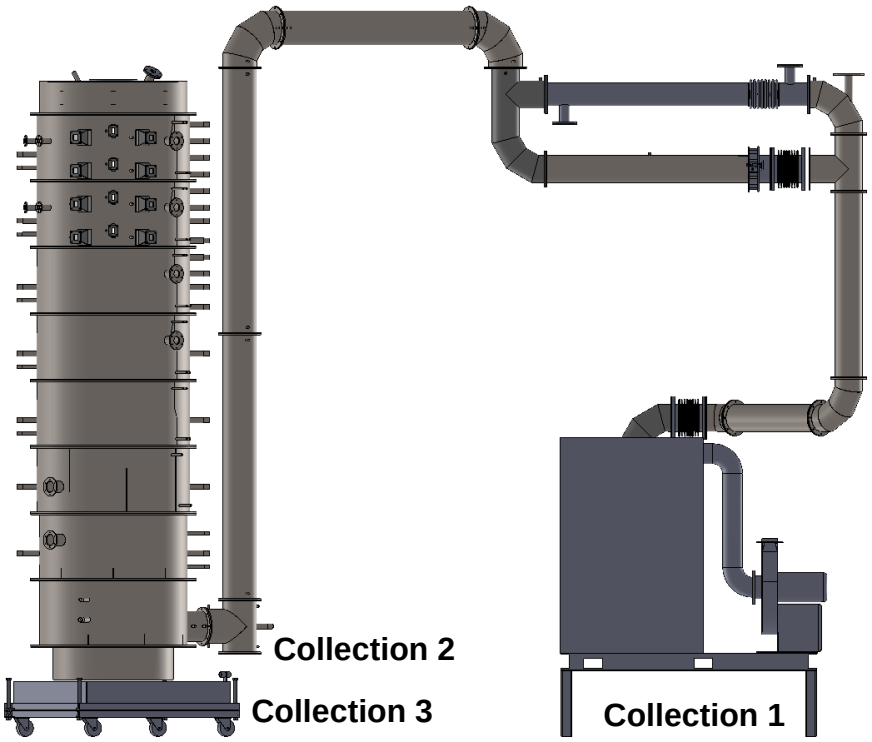

Figure 3.2 Ash collection locations in the pilot scale test.

Table 3.10 Ultimate and Proximate analysis and calorific value data of El Cerrejon coal 2.

Ultimate	**ar**	**dry**	**daf**
C	73.57	78.11	79.31
H	5.04	5.35	5.43
O (by diff.)	11.31	12.01	12.19
N	2.47	2.63	2.67
S	0.37	0.40	0.40
GCV	30.79	32.69	33.19
NCV	29.57	31.39	31.88
Proximate	**ar**	**dry**	**daf**
FC	54.92	58.31	59.21
VM	37.84	40.17	40.79
Ash	1.43	1.52	---
Moisture	5.81	---	---

Chapter 4 Ash Composition Analysis

The inorganic composition of solid fuel is important in relation to the effect on the combustion behaviour in furnaces since it produce corrosion and ash deposition in cooler regions such as heat exchange surfaces. During combustion, the organic matter burns out leaving metal oxides and other inorganics compounds. The understanding of the melting point of these inorganic compounds is important to furnace operations. Also metals act as catalyst to influence the process of pyrolysis. Different types of biomass have different inorganic components which are also affected by the agronomy and harvesting season. The most popular woody biomass contains low levels of silica and potassium and usually have high volumes of calcium. Sometimes agricultural residues also can show high silica, high potassium and low calcium content which depend on the source. [182-187]

4.1 Methodologies of ash composition analysis

The European Standards for the determination of major elements in solid biofuels [188-189] sets out a procedure firstly to produce the biomass ash followed by acid-digestion and then the metal content is determined using spectroscopic analysis. Other analytical techniques for ash analysis commonly reported in the published work include X-ray Fluorescence (XRF) spectroscopy, for example [187] since this is a rapid and convenient method to use. However, XRF spectroscopy is sensitive to other elements which can interfere or obscure the signal produced by other elements. The XRF signal from a particular element in a sample can be influenced by fluorescent emissions by other elements in the matrix, and in which case the abundance of that element may be incorrectly determined although corrections are usually applied. Other factors affect the reliability and accuracy of XRF measurements, including flaws in the sample matrix

and inhomogeneity in the ash solid [184, 186]. However, crucial to the success of the application of this method to biomass is the way in which the ash sample is prepared from the biomass. This applies to other diagnostic methods such as ash melting test methods [190].

4.1.1 X-Ray Analysis

Chemical analysis of major elements in ashes was conducted, using two methods: X-ray fluorescence spectrometer (XRF); and identified by wet chemical analysis by using AA240FS of VARIAN fast sequential atomic absorption spectrometer. The wet chemical analysis was operated follow the steps described in Section **4.2**. Mineralogical analysis of ashes was conducted by using X-ray diffraction (XRD) (model D8), with application of Cu kα radiation and graphite monochromator (U=35 kV, I=35 mA). The XRD scans were performed between 2 and 70 2θ°, with a step size of 0.0330°/s. A software system DIFFRAC plus Evaluation by Bruker XS and the JCPDS database were used for data processing and identification of crystalline components.

4.1.2 Wet Chemical Analysis

Wet chemical analysis is using the traditional chemical method to test fuel and ash composition. The main process can be divided into two steps: solution preparation and measurement.

The first step is to prepare solution:

Solution A: Weigh 1.5g of sodium hydroxide into a nickel crucible, cover with a nickel lid and heat to melt the sodium hydroxide. Allow cooling before proceeding to the next step

Weigh by difference approximately 0.05g of the sample accurately to 4 decimal places and transfer to the cold sodium hydroxide melt. Place into a furnace set at 650°C for 10min. Remove and allow cooling.

Add about 25ml of water and place on a steam bath for 30min. Pour the contents of the crucible into a 600ml beaker containing 400ml of water and 20ml of 1:1 HCl. With a rubber policeman remove any residue from the crucible and wash into the beaker. Do not allow the nickel crucible to come into contact with the acid.

Transfer the solution to a 1000ml volumetric flask; dilute with distilled water to the mark, and mix. Store the solution in the plastic bottle marked A.

Solution B: Weigh approximately 0.4g of the sample accurately to 4 decimal places into the 60ml polypropylene beaker. Take it to the fume cupboard and add 2ml of distilled water; swirl then add 10ml of hydrofluoric acid. Place on a steam bath until all the HF has been evaporated.

To the dry residue add 10ml. of hydrochloric acid, replace the lid and place the poly beaker back on the steam bath for 10min. After which remove from the bath and pour approx. 30ml. of distilled water into the beaker and allow cooling. Transfer the contents of the beaker - washing out well - to a 400ml Pyrex beaker and place on a hot plate set to 200℃ to evaporate to dryness. Remove the beaker from the hotplate the increase the heat to 300℃. Allow the beaker to cool before adding 5ml of 1:1 H_2SO_4. Place back on the hotplate and allow fuming for 10mins. Remove from the hotplate and allow cooling then adding 5ml of concentrated HNO_3 cover with a watch glass and heat for 15min allow cooling then adding distilled water to the 200ml mark and place back on the hotplate ant turn down to 250℃. Leave for 30 minutes. After cooling the solution is transferred to a 250ml volumetric flask and made up to volume and is finally stored in a plastic bottle.

Solution C: Weigh approximately 0.2g of sample accurately to 4 decimal places and transfer to a 60 ml polypropylene beaker. Add 2ml of distilled water swirl then add 10ml. of HF and evaporate to dryness on a water bath. When all the HF has evaporated,

wash the residue into a nickel crucible and evaporate once again. Add 2g of potassium hydroxide and fuse at dull red heat, over a Bunsen for 5 minutes. Allow to cool, and then add 20ml of water and place back on the water bath for 1 hour. Wash the contents of the crucible into a 250ml volumetric flask; add 20ml of 1:1 HCL and make up to the mark.

Testing processes are described as below:

(1) %SiO_2:

The **Solution A** is tested by a spectrometer for the silica content. Pipette 10ml aliquot of sample **Solution A**, 10ml of each standard solution, and blank solution into separate 100 ml volumetric flasks. Dilute to 50 to 60 ml with water and mix. Add 1.5 ml ammonium molybdate solution with a measuring pipette, mix and let stand for 10 minutes. Pipette 4ml tartaric acid solution, followed immediately by 1 ml reducing solution, into the first flask, mixing during the additions. Dilute contents of this flask immediately to the mark and mix before proceedings to the next flask. Let each solution stand for one hour, then determine its absorbance at 650nm using the blank solution as reference. The calculation equation is:

$$\%SiO_2=\frac{A1\times C\times V1xV3\times d}{A2\times W\times 10^4\times V2}$$

*A1=Absorbance of sample; A2=Absorbance of standard; C=concentration of standard mg/L; V1= aliquot of standard(L); V2=aliquot of sample(L); V3=original volume(L); W=weight in g; d=dilution factor =10

(2) %P_2O_5:

The **Solution B** is tested by a spectrometer for the phosphorus content. Pipette two separate 5ml aliquots of sample **Solution B** into separate 50mlvolumetric flasks. Pipette 25ml of the phosphorous working standard (which is diluted by using standard P_2O_5 solution from 200mg/L to 20mg/L) into a third 50 ml flask and add 10 ml of

molybdovanadate solution to flask one of the sample flasks and the standard flask. The other sample flask is the blank and has no reagent added. Make all three solutions up to the mark and shake. Leave the solutions for 30 min and then measure the absorbance at 430nm. Zero the instrument for each sample with the blank. The calculation equation is:

$$\%P_2O_5=\frac{Abs\times C\times V1\times V3}{Abt\times W\times 10\times V2}$$

*Abs = Absorbance of sample; Abt = Absorbance of standard; C = Concentration of standard mg/ml; V_1 = Aliquot of standard; V_2 = Aliquot of sample; V_3 = Volume of sample flask; W = Weight of sample in g

(3) %CaO

The CaO is tested by titration of **Solution B**. Pipette 25ml of sample **Solution B** and 25ml of the blank solution into separate 500ml Erlenmeyer flasks. Add 20 drops of concentrated HCl, 5ml of the triethanolamine solution, 5ml ammonium hydroxide, and 10ml potassium hydroxide solution in that order, mixing after addition of each reagent. Dilute with water to about 300ml. Add approximately 40mg calcine indicator and titrate with standard EDTA (0.01M) solution until the colour changes from a green fluorescence to purple. Observe the colour change in diffused light. The calculation equation is:

$$\%\ CaO=\frac{E\times V1\times V2\times 100}{V3\times W}$$

*E = milli-equivalent; V1 = liter volume; V2 = original volume (from **Solution B**); V3 = pipette volume (25ml); W = weight g

(4) %Fe_2O_3; %Al_2O_3; %MgO; %MnO; %K_2O; %Na_2O

The %Fe_2O_3; %MgO; %MnO; %K_2O; %Na_2O (**Solution B**) and %Al_2O_3 (**Solution C**) are tested by Atomic Absorption Spectrophotometer (AAS). The units used in AAS are ppm (parts per million), mg $litre^{-1}$ (milligrams per litre) and μ/ml (microgram per millilitre). These units are numerically identical:1ppm=1mg·$litre^{-1}$=1μg·ml^{-1}. The

calculation equation is:

$$\%X=\frac{C\times V\times d}{W\times 10^4}$$

*X=Unknown concentration; C=Concentration of solution by AAS in PPM (mg dm^{-3}); V=Volume of original flask; d=Dilution factor (note: no dilution =1); W=Weight in g

The oxides of $\%Fe_2O_3$; %MgO; %MnO; $\%K_2O$; $\%Na_2O$ and $\%Al_2O_3$can be calculated is:

$$\%X_mO_n=\frac{\%X}{M_X\times m}\times(M_X\times m+M_O\times n)$$

*M_X is the atomic weight of particular element. M_O is the atomic weight of oxygen (always to be 16.00). M and n are the number of atoms.

4.2 A comparative assessment of ash composition analysis

This study compares the results obtained from "wet" chemical analytical techniques with those from XRF analysis. The wet chemical analysis is used to "calibrate" the XRF analysis such that the sample preparation and the absorption and enhancement matrix effects can be corrected for. Subsequent comparison with other samples allows the reliability and accuracy of XRF analysis for biomass ash to be quantified.

Researchers have shown that ash contents and compositions for a particular biomass vary depending on planting environments and harvest seasons as well as selected parts. Different types of biomass show different inorganic components. As shown by previous studies, the most popular woody biomass show low silica and low potassium but high calcium content; agricultural residues show high silica, high potassium and low calcium content; animal residues show high phosphorus and high calcium content. All the above reasons contribute to the changeable ash composition related to uncertain ash issues [128, 151].

In the complex process of biomass combustion, consecutive heterogeneous and homogeneous reactions will happen. The main processes consist of drying, devolatilization, gasification, char combustion, and gas-phase oxidation. The time control is crucial in each reaction as well. Some control parameters are chosen based on the fuel size and properties, temperature and combustion conditions. Determination of the major inorganic elemental content of biomass and biomass ash is important for the analysis of the combustion behaviour of solid biomass fuels in furnaces since they influences corrosion reactions with furnace components and ash deposition on heat exchange surfaces. With increasing temperature, organic matter burns out, and the low melting point substances evaporate, while the high melting point substances are generated [182-183].

4.2.1 The accuracy of XRF test

To develop a new method which can easily help to correct the XRF results to traditional wet chemical analysis results, a number of tests were conducted by both wet chemical analysis and XRF to build up the data relationship. These calibration sets were generated by the technician, Mr. Simon Lloyd and are shown in the **Figure 4.1 (a)~(h)** below.

The correlations between XRF results and wet chemical analysis results are strong with $R^2 \geq 0.9$ in average. Also plotted in the **Figure 4.1(a)~(h)** are the XRF (as X axes) and WCA (as Y axes) results of PPA1 and PPA2 (∗) which distribute around the trend line. In the XRF test, SiO_2 in the ash of coal is in closer agreement to the wet chemical analysis results than the biomass. The Fe_2O_3 and MgO contents form the XRF test also show some differences compared to wet chemical test results. Obviously, if more experimental results could be added, the equations of the linear regression will be enhanced. The connected equations of different oxides are summarized as below:

Al_2O_3:	$Y_{WCA}=1.0222X_{XRF}-0.2417$	$R^2 = 0.9992$
Fe_2O_3:	$Y_{WCA}=0.9789X_{XRF}+0.214$	$R^2 = 0.9830$
CaO:	$Y_{WCA}=1.1816X_{XRF}-1.7141$	$R^2 = 0.9302$
K_2O:	$Y_{WCA}=1.1444X_{XRF}-0.7094$	$R^2 = 0.9167$
MgO:	$Y_{WCA}=1.1825X_{XRF}-0.2009$	$R^2 = 0.9368$
Mn_2O:	$Y_{WCA}=1.0104X_{XRF}+0.0191$	$R^2 = 0.9733$
P_2O_5:	$Y_{WCA}=0.922X_{XRF}+0.1933$	$R^2 = 0.9846$
SiO_2:	$Y_{WCA}=1.027X_{XRF}-1.07$	$R^2 = 0.9975$

(a)

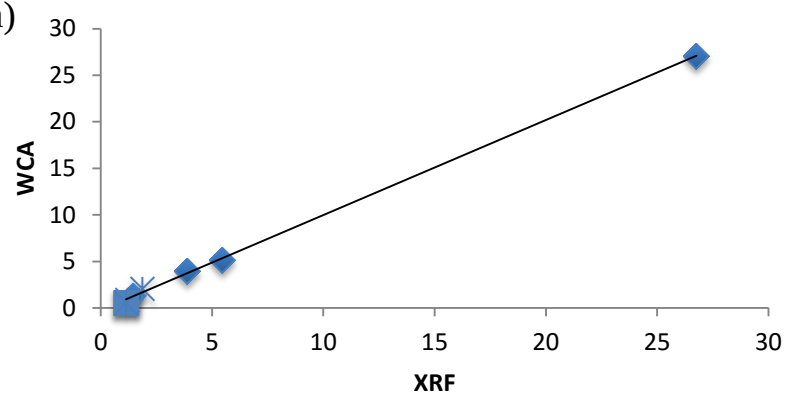
WCA
XRF
0
5
10
15
20
25
30

(b)

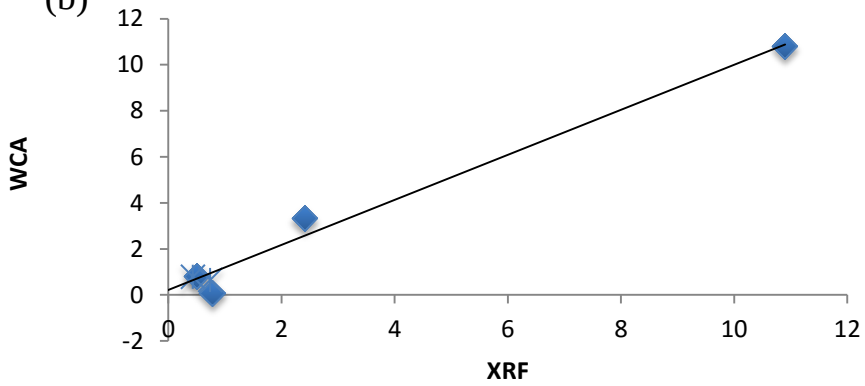
WCA
XRF
-2
0
2
4
6
8
10
12

(c)

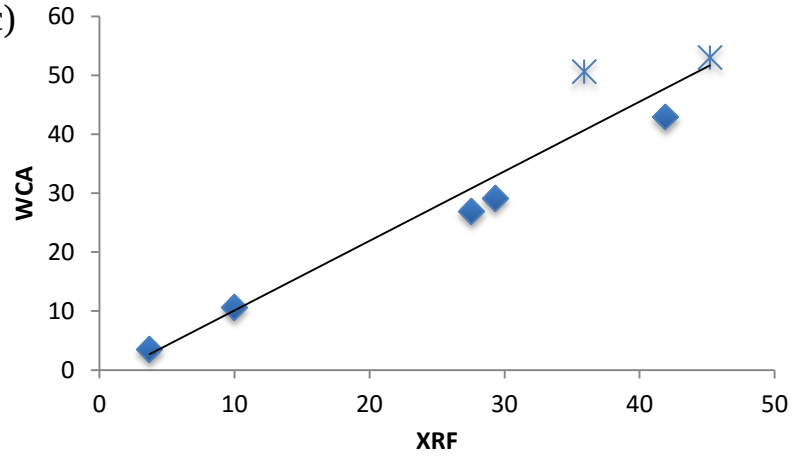
WCA
XRF
0
10
20
30
40
50
60

(d)

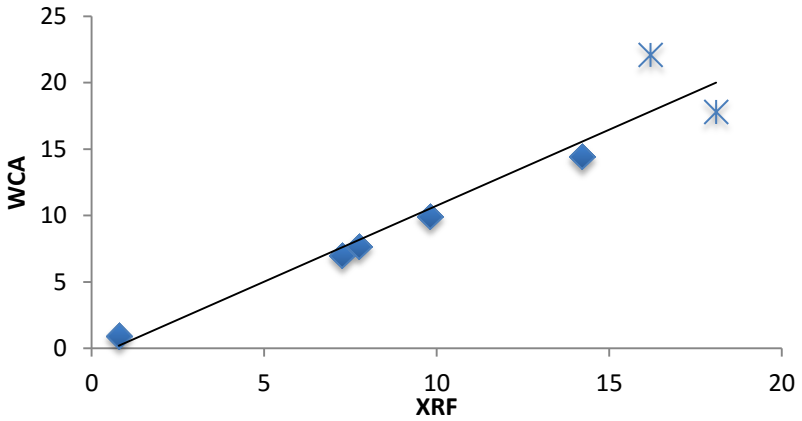
WCA
XRF
0
5
10
15
20
25

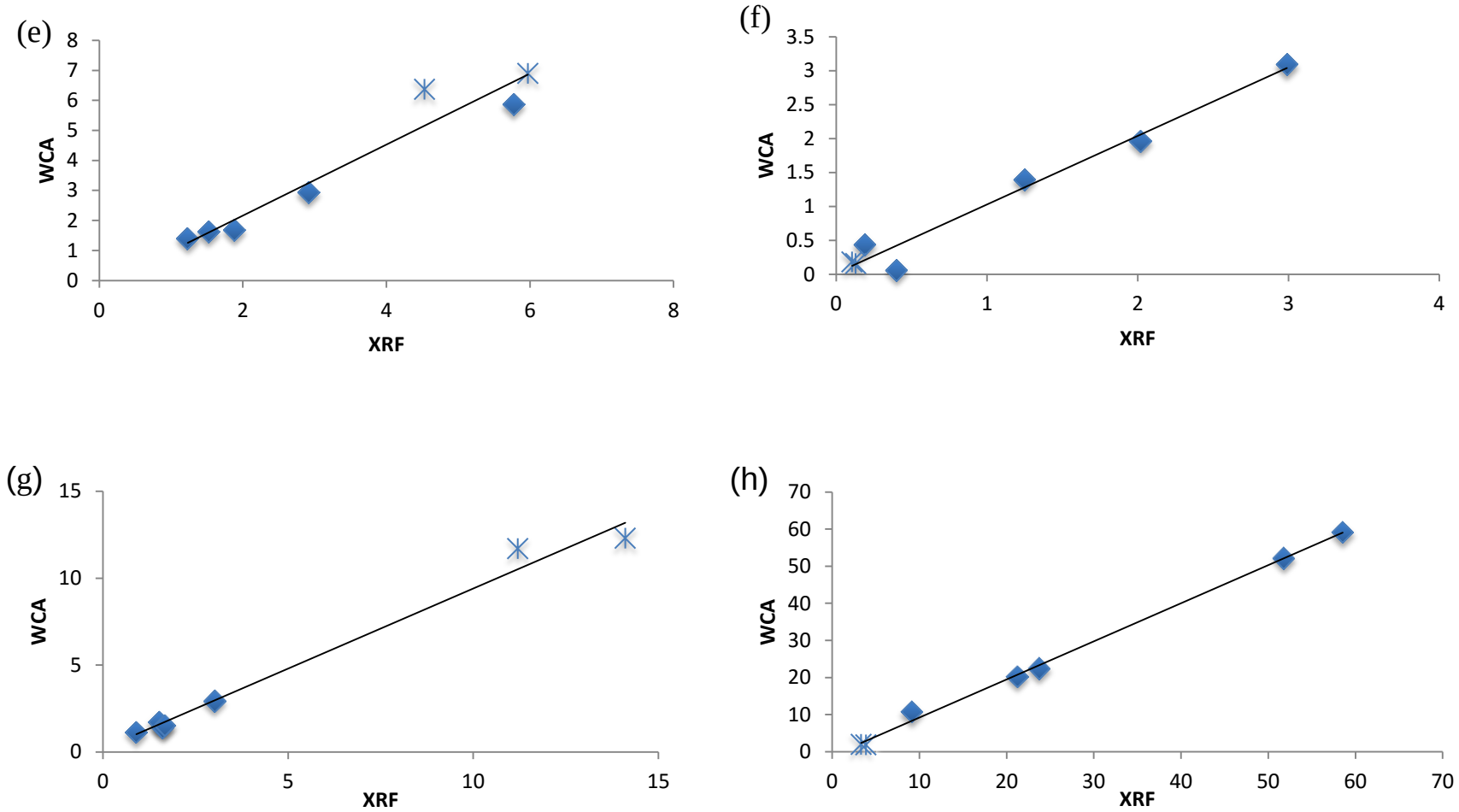

Figure 4.1 The connection between XRF results and wet chemical analysis results: (a)-Al_2O_3; (b)-Fe_2O_3; (c)-CaO; (d)-K_2O; (e)-MgO; (f)-MnO_2; (g)-P_2O_5; (h)-SiO_2. ◆: Calibration data set; ✳:PPA1 and PPA2 data.

4.2.2 A comparison results of ash composition by different testing methods

Twenty solid biomass fuels were selected for this study and these are typical materials used in large scale power plant, many of them being sourced from power plant operators. The selection includes forestry biomass, energy crops, agricultural residues and a torrefied biomass (produced at a temperature of 280°C), thus providing a representative range of differing ash content and composition. The reference names of these sample fuels adopted are given in **Table 4.1**.

Table 4.1 Reference names used for the biomass ash prepared at temperatures of 550/850 ℃.

Biomass	Reference name	Biomass	Reference name
Willow pellet	WP	Rape straw	RS
Mixed Forestry pellets	MFP	White Wood pellet	WWP
Miscanthus A	MA	Pine	PE
SRC Willow	SRCW	Olive Residue	OR
Wheat Straw B	WSB	Miscanthus B	MB
Oatmeal	OAT	Peanut	PEA
Wood	WO	Misc	MIS
Chipped Wood	CW	Straw	STR
Torro Wood	TOR	Wheat Straw pellet	WSP
Alstom Pine<90 μm	ALSM	Black Pellets Znilkas	BPZ

The samples of ash for analysis were prepared from portions of the raw materials following the European Standards [188-189]. They were reduced to <0.2mm particle top size using a Retzch cutting mill and ash samples were produced in crucibles in an electric furnace at a temperature of 550 °C and heated for 14 h. Since a considerable amount of ash sample was required, biomass samples of about 100 g were used in a crucible which was stirred every 1h. In order to reduce these samples completely to ash without leaving any unburned carbon they were further heated. Two methods were used: (i) in the first batch (Case 1) the temperature was raised to 850°C in 2h and the sample was stirred every 0.5h, and (ii) a second batch of ashes from five biomass (Case 2) were prepared from five biomass samples by heating to a temperature of 815°C for 2h whilst stirring every 0.5h. The resulting ashes were manually ground and sieved to

<106µm.

A sample of each ash was prepared as above for wet chemical analysis by acid digestion. Two analyte solutions were produced named as Solution A and Solution B. Solution A is from the reaction of ash with sodium hydroxide at 650°C to produce sodium silicate which is dissolved in HCl to give silicic acid in solution. The analyte is used only for the determination of silicon content. Solution B is prepared from acid digestion by hydrofluoric, hydrochloric, sulphuric and nitric acid sequentially. The content of ten major inorganic elements were quantified using the analytical methods summarised in **Table 4.2**.

Table 4.2 Wet chemical analytical methods for the major elements in the ash analysis.

Element	**Analyte**	**measurement method**
Sodium	Solution B	AAS
Magnesium	Solution B	AAS
Aluminium	Solution B + KCl	AAS
Silicon	Solution A + ammonium molybdate + reducing agent to give silicomolybdic complex (blue)	Spectrophotometer at 650nm
Phosphorous	Solution B + molybdovanadate to give vanadomolybdophosphoric complex (yellow)	Spectrophotometer at 430nm
Potassium	Solution B	AAS
Calcium	Solution B + triethanolamine	Titration with EDTA
Titanium	Solution B + hydrogen peroxide to give pertitanic complex (yellow)	Spectrophotometer at 430nm
Manganese	Solution B	AAS
Iron	Solution B	AAS

The XRF results were compared against the wet chemical analysis results for the same ash samples and it should be noted that the major difference was in that the melt preparation stage is unique to the XRF technique. Sample discs were prepared and the results were obtained using the XRF method for **Cases 1** and **2**.

- **Case 1**

In the case of the first batch (**Case 1**), samples of ash for XRF analysis were fused into solid glass discs for insertion in to the XRF analyser. These consisted of 0.5g of standard or sample (ground to <106 μm), 5.0g of flux and 0.05g lithium bromide. A melt was produced using a melt at 1200°C for 12 min in a Pt/Au crucible and was cast as a disc in a mould. The samples were analysed using an X-Thermo ARL Advant XP sequential X-ray fluorescence spectrometer. This method was applied to twenty biomass samples which had been ashed at 550°C and then increased temperature to 850°C with 50°C/30mins. The results obtained from the wet chemical analysis and XRF test are presented in **Table 4.3**.

Table 4.3 Tested inoganic oxides of different biomass ashes composition (%). **Case 1**: Ash samples prepared in two stages at 550°C then 850°C; Samples fused into glass disc at 1200°C.

		Al_2O_3	CaO	Fe_2O_3	MnO	MgO	K_2O	P_2O_5	SiO_2	TiO_2	Na_2O
WSB	XRF	0.232	10.149	0.239	0.129	1.021	11.746	2.207	46.639	0.471	0.270
	WCA	0.570	14.500	0.040	0.050	0.850	15.900	0.460	45.100	0.150	0.470
MB	XRF	0.138	8.541	0.288	1.770	2.506	7.854	4.953	46.659	0.464	0.983
	WCA	0.410	11.400	0.080	0.400	1.890	11.700	1.180	63.600	0.150	0.680
SRCW	XRF	0.504	45.013	0.490	0.143	2.399	11.311	8.389	6.492	0.494	1.112
	WCA	1.520	49.800	0.150	0.070	1.730	15.700	2.050	7.900	0.080	1.210
OR	XRF	0.584	8.360	0.458	0.000	2.413	33.034	3.523	5.192	0.477	2.170
	WCA	1.860	11.300	0.240	0.020	2.190	46.500	0.940	8.500	0.070	0.890
PE	XRF	0.413	39.153	0.370	0.120	4.787	11.131	9.742	2.496	0.486	1.391
	WCA	0.700	36.300	0.700	0.100	3.900	14.700	10.100	4.500	0.000	0.800
MA	XRF	0.442	8.311	0.397	0.074	1.654	10.961	3.721	40.794	0.473	2.189
	WCA	1.010	10.700	0.160	0.030	1.530	18.500	0.980	43.400	0.080	0.810
WWP	XRF	3.074	25.535	1.905	3.409	5.896	10.605	3.634	18.029	0.606	2.485
	WCA	2.880	27.300	2.130	3.200	6.410	15.300	4.500	21.200	0.240	2.060

MFP	XRF	4.476	21.244	2.786	2.080	4.275	6.422	1.847	26.446	0.684	2.310
	WCA	5.280	22.500	3.560	1.780	4.690	8.400	1.650	34.800	0.430	2.780
RS	XRF	0.544	51.142	0.408	0.002	1.958	6.617	3.419	9.786	0.479	1.876
	WCA	0.630	53.000	0.440	0.040	2.300	11.700	3.620	9.700	0.050	2.490
WP	XRF	4.216	18.455	3.401	0.133	1.754	4.449	2.706	35.101	0.686	1.589
	WCA	4.740	20.200	4.260	0.150	2.240	5.900	2.990	41.700	0.360	1.660
PEA	XRF	3.743	5.129	1.871	0.210	2.539	10.874	2.996	23.692	0.832	0.234
	WCA	8.368	7.876	2.932	0.266	3.319	19.317	0.001	22.733	0.004	0.890
OAT	XRF	0.198	1.775	0.511	0.147	2.008	8.433	6.983	31.406	0.468	0.384
	WCA	1.689	19.128	0.938	0.067	2.128	17.969	0.001	29.643	0.000	2.902
MIS	XRF	0.439	8.537	1.792	0.112	1.114	6.265	2.423	32.386	0.487	0.619
	WCA	1.293	12.220	2.355	0.154	2.052	10.454	0.001	30.539	0.001	1.326
WO	XRF	3.610	14.568	2.633	1.569	2.817	4.923	1.537	21.567	0.654	0.864
	WCA	0.696	3.721	0.669	0.182	2.589	13.893	0.003	20.421	0.001	0.803
STR	XRF	0.560	13.320	0.740	0.027	1.229	10.336	3.208	22.481	0.493	0.825
	WCA	7.234	19.938	3.768	1.819	3.897	7.954	0.000	21.217	0.002	2.866
CW	XRF	2.782	26.269	2.485	4.062	2.751	5.678	2.786	19.322	0.656	1.481
	WCA	5.190	26.880	3.320	3.090	2.930	7.680	2.920	22.440	N/A	N/A
WSP	XRF	0.360	8.376	0.345	0.071	1.139	10.258	1.494	46.501	0.478	0.582
	WCA	1.330	10.650	0.090	0.440	1.610	14.440	1.720	59.140	N/A	N/A
TOR	XRF	1.823	28.488	1.231	0.077	5.272	7.129	1.683	17.760	0.912	0.515
	WCA	3.940	29.180	0.090	1.400	5.860	9.920	1.400	20.330	N/A	N/A
ALSM	XRF	1.008	34.219	1.140	0.110	2.843	6.712	8.503	10.822	0.534	0.536
	WCA	1.103	34.985	0.876	0.135	3.563	12.562	10.516	11.807	N/A	N/A
BPZ	XRF	0.665	42.308	1.213	0.779	1.570	5.331	1.805	9.214	0.496	1.139
	WCA	2.060	42.950	0.650	1.960	1.680	7.000	1.530	10.750	N/A	N/A

The calibration equation of the XRF results which via corresponding wet chemical test results for 20 different types biomass ash are summarized in **Figure 4.2**. The average deviation for all results is ± 0.68 percentage. The relationships from XRF results to wet chemical test results can be described as: $Y_{[WCA]} = 1.0943X_{[XRF]} + 0.3745$, and $R^2 = 0.9369$ where $Y_{[WCA]}$ is the wet chemical analysis result, $X_{[XRF]}$ is the XRF result and R^2 is the linear regression coefficient. It should be noted that R^2 is not ideal for the conversion of the XRF results to the WCA results.

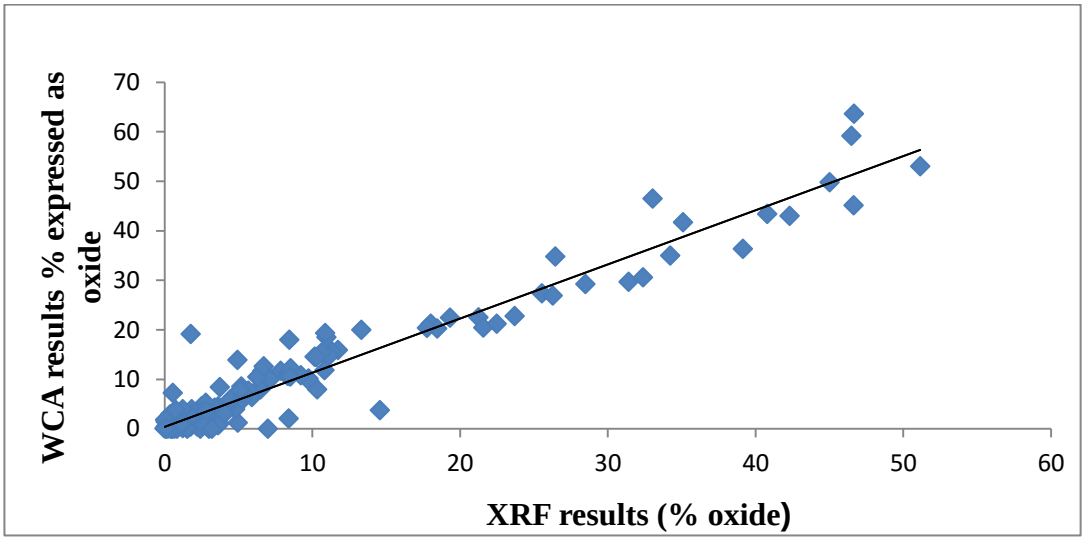

Figure 4.2 The calibration of XRF results by wet chemical analysis results—**Case 1**.

- **Case 2**

Because the XRF sample preparation needs a fusion temperature of about 1200°C, the effect on the biomass ash composition can be observed. According to Niu [183], different ashing rates in different ashing temperatures lead to different ash compositions, which affect the ash fusion characteristic (AFC). Therefore, it is essential to establish an appropriate standard to distinguish the biomass AFC. It appears that the fusion characteristics of the biomass ash depend on the high-temperature molten material, rather than simply on the proportion of elements in ashes. Niu [183] reports

that with increasing ashing temperature, the relative content of K_2O drops, while MgO, CaO, Fe_2O_3 and Al_2O_3 rise, and Cl is nearly zero at 815°C with a slight rise at 600°C.The major factor determining the biomass AFC is its own high-temperature molten material which provides a supporting effect of a skeleton structure; i.e. ash composition is not determined simply by the proportion of elements in ashes prepared at different temperatures.

These ashes were also characterised by using a Netzsch 449C Jupiter Simultaneous Thermal Analyser (STA), coupled to a Netzsch QMS 403C Aeolos Quadrupole Mass Spectrometer. This involves the simultaneous application of thermogravimetry (TG) and differential thermal analysis (DTA), which monitors the temperature difference between the sample and an inert reference material. Here 10 mg of ash was heated from room temperature to 1400°C at 10°C/min under a gas flow rate of 80 ml/min of 12.5% O_2 in He. The gases evolved were transferred via a heated fused silica capillary to a mass spectrometer; the monitored species were H_2O, CO, CO_2, K and KCl.

To identify the effect of the molten temperature of different types of biomass ash, five ash samples prepared at 550°C were also analysed using a Simultaneous Thermal Analyser (STA). Plots showing the mass loss upon heating of ash samples in the STA, different gas evolution profiles are presented in **Figure 4.3 (a)~(e)** as WWP, OR, SRCW, MB and WSB. The mass loss curves are complex with gradual mass losses up to the final temperature of 1400°C. Melting in the STA is characterized by the DTA curve becoming endothermic which are not shown. Notable in many samples is formation of CO and CO_2 at 700°C which is due to the combustion of residual carbon in ash. Carbonate decomposition are observed in **Figure 4 (b)** and **(d)** at temperatures ≥1000°C.

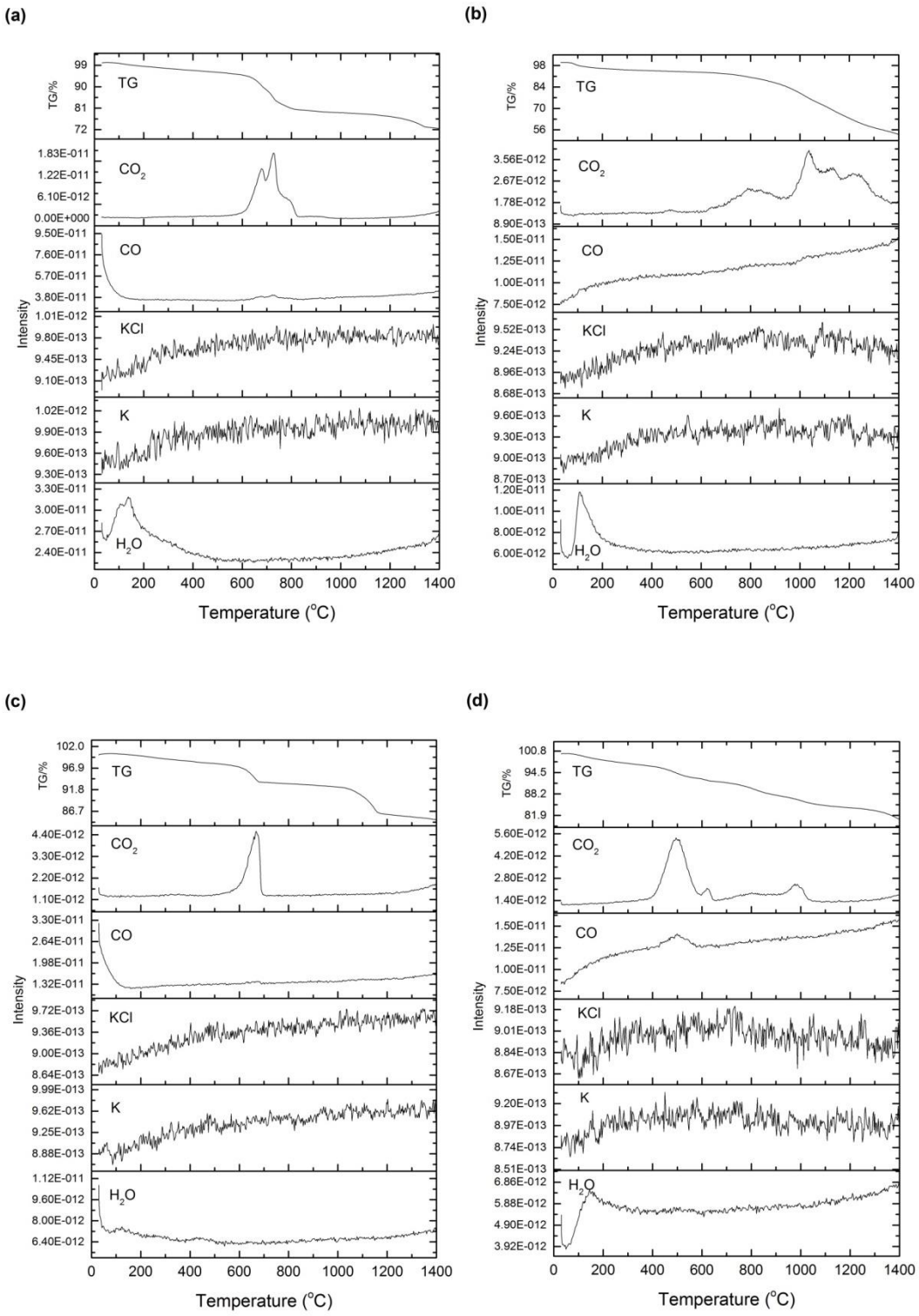
(a)
(b)
(c)
(d)
TG/%
TG
CO2
CO
KCl
K
H2O
Intensity
Temperature (°C)

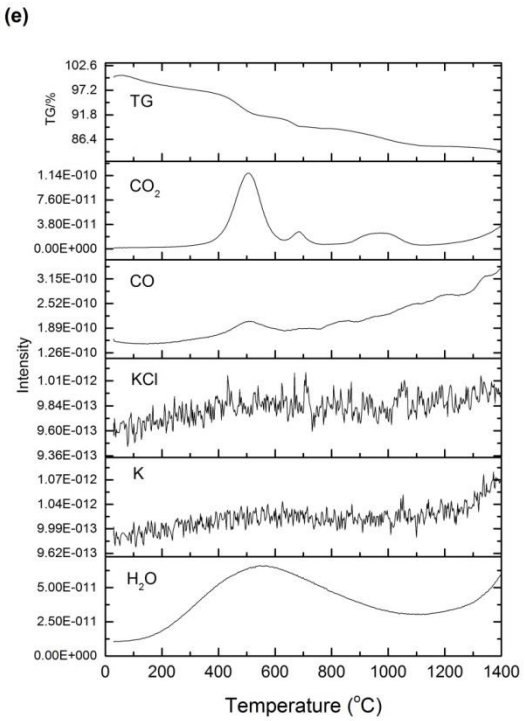

Figure 4.3 (a)-(e) Properties of five different biomass ash fusion properties by STA-MS: (a) White wood pellet (WWP); (b) Olive residue (OR); (c) SRC Willow (SRCW); (d) Miscanthus B (MB) and (e) Wheat straw (WS).

This study does suggest that the ashing temperature of biomass should be higher than the European standard in order to remove residual carbon and deliver a more suitable ash for the measurement.

In this case of the second batch (**Case 2**) the XRF calculation software employed a coal standard ash. Five different biomasses were ashed under 550°C and then the furnace temperature was increased to 815°C with 50°C/30mins. The XRF sample preparation procedure followed the previous steps but changing the flux was decreased to 4.5g and the fusion temperature was decreased from 1200°C to 1100°C. After 9 min the sample was poured into the mould. The calibration results from wet chemical test and XRF which had an average deviation of ± 0.23 % are listed in **Table 4.4**.

Table 4.4 Tested inorganic oxides of ash composition results for biomass ash and standard coal ash at 815 ℃. **Case 2**: Ash samples prepared in two stages at 550°C then 815°C; Samples fused into glass disc at 1100°C.

Samples	**Ref**		**SiO_2%**	**K_2O%**	**Fe_2O_3%**	**Na_2O%**	**MgO%**	**MnO%**	**Al_2O_3%**	**CaO%**	**P_2O_5%**	**TiO_2%**
White Wood Pellets	MWWP	WCA	24.655	10.768	2.501	2.406	8.643	2.668	4.820	27.488	2.581	2.518
		XRF	23.140	11.392	2.426	1.661	8.541	2.939	3.272	26.327	3.313	0.597
Olive Residue	MOR	WCA	9.420	32.931	0.666	1.117	4.642	0.038	1.840	13.057	4.210	0.489
		XRF	9.351	33.719	0.668	0.837	4.666	0.009	1.253	13.439	5.277	0.489
SRC willow	MSRCW	WCA	7.208	9.587	0.537	1.535	3.024	0.174	1.092	53.362	8.956	1.543
		XRF	6.602	10.729	0.520	0.901	3.242	0.183	0.582	55.103	10.576	0.491
Miscanthus	MMB	WCA	53.742	7.825	0.265	0.849	2.940	1.533	0.196	9.643	4.918	0.626
		XRF	52.724	8.423	0.338	0.575	2.740	1.908	0.223	9.435	5.195	0.458
Wheat Straw	MWS	WCA	52.343	12.083	0.197	0.460	1.610	0.127	0.350	10.847	2.273	1.406
		XRF	52.068	12.477	0.252	0.589	1.159	0.144	0.275	11.090	2.309	0.472
ASRM 010-2 coal ash	Coal ash	WCA	52.489	0.847	9.387	1.688	0.590	0.148	18.705	2.147	1.575	1.408
		XRF	39.607	0.826	9.420	0.535	0.984	0.214	17.849	2.665	1.462	1.404

The calibration equation for the XRF results with the corresponding wet chemical test results for the biomass ash samples, is summarized in **Figure 4.4**.

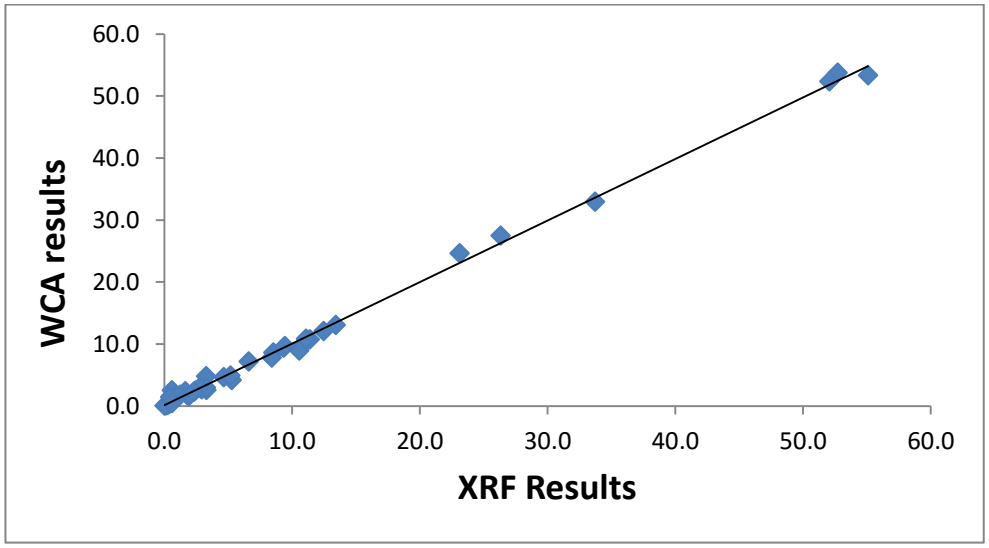

Figure 4.4 The calibration of XRF results by wet chemical analysis results—**Case 2**.

The relationships can be described as: $Y_{[WCA]} = 0.9927X_{[XRF]} + 0.1314$, where $R^2 = 0.9971$. Clearly this equation shows a good value for the mean deviation R^2.

There have been several concerns about the accuracy of the XRF test method if low temperature (550^{o}C) biomass ashing is used and different metal oxides show different reliabilities. This arises because of unburned carbon that may be present resulting from the way the samples are prepared. The XRF method was compared with results obtained by employing wet chemical analyses. Previously eight correlation equations were obtained with highest reliability of Al_2O_3 for 550°C biomass ash. To simplify this calibration for all types of metal oxides, and enhance the suitability of the ash composition for XRF anlysis, the thermal performance of different biomass ash was examined by STA-MS.

An average ashing temperature 850°C was suggested, which can achieve the removal of unburned carbon with little loss of other alkali metals. The calibration of XRF results

by wet chemical analyses for 20 different biomass ash samples at temperatures of 850°C can be expressed by the equation [Wet chemical result] = 1.0943 [XRF] + 0.3745 where R^2 = 0.9369. The reliability of this calibration is still not ideal due to the high fusion temperature of the XRF sample pellet. To avoid these errors the XRF ash sample preparation temperature was decreased to 815°C (based on the miscanthus ash thermal properties). Five different kinds of biomass were ashed under the 815°C condition. The XRF calculation software was calibrated by using standard coal ash produced at the same temperature as that was used for these five biomass ash composition tests. The correlation equation becomes $Y_{[WCA]}=0.9927X_{[XRF]}+0.1314$ with $R^2=0.9971$.

4.3 Ash composition of biomass ash, coal ash and co-firing ash

In this project, ash samples prepared as in **Chapter 3** were tested by XRF analysis, which were fused into solid glass discs for insertion in to the XRF analyser. These consisted of 0.5g of standard or sample (ground to <100 μm), 5.0g of flux and 0.05g lithium bromide. A melt was produced using a melt at 1200°C for 12 min in a Pt/Au crucible and was cast as a disc in a mould. The samples were analysed using an X-Thermo ARL Advant XP sequential X-ray fluorescence spectrometer. Those concerned ash samples were also tested by wet chemical analysis follow the steps described in previous studies. The results obtained from the wet chemical analysis and XRF test are presented in **Table 4.5~4.7**. According to **Chapter 3**, in **Table 3.3~3.6**, the El Cerrejon coal 1 were ashed at 550°C and 800°C as PCC1 and PCC2, the El Cerrejon coal 2 was ashed at 800°C as PCC3, the pine, wheat straw and white wood pellet were ashed at 550°C and 800°C as PPA1(550°C), PPA2(800°C), WS1(550°C), WS2(800°C), WWP1(550°C), WWP2(800°C) respectively. The El Cerrejon coal 1 and pine ash blends and their fuel blends ash were ashed at 550°C as CA28, CA55 CA82, BFPC28,

BFPC55, and BFPC82 respectively. The El Cerrejon coal 2 and wheat straw fuel blends ash were ashed at 550°C as BWCA28, BWCA55, and BWCA82 respectively. The pilot scale ashes from PACT are CFA1, CBA11, and CBA21. Their re-burned ashes at 800°C are CFA2, CBA12, and CBA21 respectively.

Table 4.5 Inorganic oxides components of El Cerrejon coal 1 and 2 ash, pine ash, wheat straw ash and white wood pellet ash blend.

Sample	SiO_2%	P_2O_5%	K_2O%	MgO%	Na_2O%	Fe_2O_3%	CaO%	Al_2O_3%	TiO_2%	MnO%	C%	H%	N%
[1]PCC1	41.81±0.41	0.27±0.01	0.93±0.06	1.34±0.02	1.85±0.05	12.38±0.01	4.87±0.01	21.07±0.02	1.17±0.00	0.00±0.00	0.32	0.10	0.10
[2]PCC1	41.90	0.22	0.97	1.54	1.99	14.20	5.03	23.30	1.04	856ppm	N/A	N/A	N/A
[1]PCC2	44.69±0.02	0.34±0.01	0.96±0.04	1.40±0.12	2.30±0.02	13.34±0.05	4.59±0.44	22.44±0.38	1.69±0.01	0.00±0.00	0.19	0.00	0.00
[2]PCC2	43.30	0.23	0.86	1.56	2.47	14.80	5.14	23.10	0.99	750ppm	N/A	N/A	N/A
[1]PCC3	54.45±0.05	0.35±0.02	1.21±0.02	1.49±0.01	2.19±0.06	16.76±0.26	2.46±0.12	21.13±0.01	1.22±0.00	0.10±0.02	0.33	0.04	0.00
[2]PCC3	43.40	0.31	1.36	1.76	1.13	22.00	3.78	23.00	1.06	877ppm	N/A	N/A	N/A
[1]PPA1	3.87±0.06	11.32±0.04	16.68±0.20	4.53±0.23	1.29±0.03	0.50±0.00	48.86±0.01	1.21±0.04	0.00±0.00	0.12±0.05	7.24	0.00	0.00
[2]PPA1	1.87	11.70	22.10	6.37	1.31	0.82	50.60	0.85	506ppm	0.16	N/A	N/A	N/A
[1]PPA2	3.33±0.04	14.43±0.07	18.66±0.26	5.96±0.03	1.60±0.08	0.43±0.00	50.74±0.20	1.14±0.02	0.00±0.00	0.11±0.03	1.97	1.10	0.00
[2]PPA2	1.98	12.30	17.80	6.90	0.99	0.79	53.00	0.52	561ppm	0.18	N/A	N/A	N/A
[1]WS1	59.73±1.47	1.43±0.04	15.83±0.07	1.70±0.00	2.56±0.21	0.10±0.02	9.93±0.05	0.48±0.05	0.14±0.00	0.11±0.06	6.68	0.49	0.14
[2]WS1	56.20	1.29	18.40	1.28	4.26	0.29	12.70	0.48	974ppm	0.13	N/A	N/A	N/A
[1]WS2	20.38±2.41	2.66±0.03	16.82±0.97	10.43±0.00	2.97±0.07	2.18±0.12	13.75±0.12	3.10±0.01	0.27±0.05	2.65±0.01	3.00	0.26	0.06
[2]WS2	N/A	N/A	N/A	N/A	N/A	N/A	N/A	N/A	N/A	N/A	N/A	N/A	N/A
[1]WWP1	26.89±0.03	2.87±0.01	14.27±0.13	9.06±0.01	1.89±0.03	1.73±0.17	19.89±0.06	3.91±0.24	0.27±0.00	2.14±0.10	4.59	0.21	0.00
[2]WWP1	23.80	2.94	20.80	8.97	1.38	4.49	27.00	5.16	0.26	2.56	N/A	N/A	N/A
[1]WWP2	20.38±0.11	2.66±0.00	16.82±0.15	10.43±0.11	2.97±0.05	2.18±0.05	13.75±0.47	3.10±0.03	0.27±0.02	2.65±0.08	1.26	0.39	0.00
[2]WWP2	25.30	2.65	19.80	8.69	1.94	3.99	26.60	5.48	0.22	2.42	N/A	N/A	N/A

[1]: Test by wet chemical analysis; [2]: Test by XRF; [3]: By calculation

Table 4.6 Inorganic oxides components of blending fuel ash and ash blends.

Sample	SiO_2%	P_2O_5%	K_2O%	MgO%	Na_2O%	Fe_2O_3%	CaO%	Al_2O_3%	TiO_2%	MnO_2%
[3]**CA82**	18.86	7.29	10.91	3.38	1.66	5.22	32.60	9.01	0.62	0.08
[3]**CA55**	32.40	3.64	5.69	2.34	2.00	9.48	17.91	16.05	1.18	0.04
[3]**CA28**	40.72	1.41	2.49	1.70	2.20	12.09	8.89	20.38	1.53	0.01
[2]**BFPC82**	17.40	6.79	12.8	4.46	2.07	5.96	32.80	8.19	0.49	0.164
[2]**BFPC55**	29.30	3.18	7.76	2.80	1.32	11.00	17.60	14.90	0.74	0.107
[2]**BFPC28**	37.90	1.07	2.92	1.96	1.93	13.20	8.93	19.90	0.94	956ppm
[2]**BWCA82**	57.30	1.69	16.90	1.76	1.78	3.01	11.70	3.78	0.22	0.14
[2]**BWCA55**	51.80	1.06	12.90	1.49	1.33	7.85	9.32	8.97	0.41	0.12
[2]**BWCA28**	48.20	0.57	6.51	1.71	0.98	13.90	6.46	16.80	0.72	0.12
[3]**BWCA82**	59.47	1.38	15.10	1.69	2.55	0.93	9.55	1.51	0.19	0.11
[3]**BWCA55**	57.91	1.06	10.78	1.63	2.44	5.85	7.35	7.60	0.51	0.11
[3]**BWCA28**	55.29	0.52	3.54	1.53	2.25	14.10	3.65	17.84	1.05	0.10

[1]: Test by wet chemical analysis; [2]: Test by XRF; [3]: By calculation

Table 4.7 Metal oxidant components of Cerrejon coal ash from PACT.

Sample	SiO_2%	P_2O_5%	K_2O%	MgO%	Na_2O%	Fe_2O_3%	CaO%	Al_2O_3%	TiO_2%	MnO_2%	C%	H%	N%
[1]**CFA1**	31.10±0.11	0.10±0.01	0.15±0.01	23.60±2.43	1.74±0.01	5.99±0.02	1.20±0.01	3.64±0.02	0.14±0.02	0.12±0.01	15.41	0.42	0.19
[1]**CFA2**	29.92±0.61	0.05±0.01	0.18±0.01	30.87±0.02	2.32±0.02	7.87±0.06	1.44±0.04	4.99±0.05	0.20±0.01	0.16±0.02	0.06	0.04	0.00
[2]**CFA2**	41.4	191ppm	0.30	36.80	1.36	10.00	1.91	5.00	0.171	949ppm	N/A	N/A	N/A
[1]**CBA11**	19.83±1.04	0.16±0.12	0.22±0.01	0.58±0.03	1.10±0.01	5.53±0.01	1.92±0.02	8.83±0.58	1.02±0.01	0.11±0.02	46.06	0.09	0.86
[1]**CBA12**	24.70±0.16	0.21±0.02	0.61±0.05	1.25±0.11	2.64±0.15	13.16±0.03	3.63±0.01	18.68±0.93	1.09±0.04	0.16±0.01	0.16	0.03	0.00
[2]**CBA12**	44.40	0.16	0.88	1.46	2.48	15.10	6.55	24.10	1.13	616ppm	N/A	N/A	N/A
[1]**CBA21**	6.94±0.08	0.48±0.02	0.00±0.00	0.35±0.02	0.46±0.01	1.81±0.02	0.78±0.03	2.17±0.04	0.95±0.05	0.14±0.01	66.73	0.36	1.15
[1]**CBA22**	34.55±0.31	0.74±0.06	0.77±0.12	1.02±0.03	2.04±0.06	15.71±0.16	1.98±0.02	22.20±0.13	0.95±0.02	0.30±0.03	0.22	0.05	0.00
[2]**CBA22**	45.10	0.69	1.62	1.45	1.18	14.70	4.45	25.30	0.96	0.20	N/A	N/A	N/A

[1]: Test by wet chemical analysis; [2]: Test by XRF.

The ash composition of the individual fuels and their blends, as determined by both XRF and wet chemical analyses are given in **Table 4.5~4.7**. In the case of the ash blends (CA82, CA55 and CA28), only the ash from the fuel blends (i.e. fuels mixed prior to ashing) were examined by XRF, whilst the composition of the ash blends (i.e. mixed after ashing) were calculated based on the ash compositions of the pure fuels (as analysed by wet chemical methods) and according to the equivalent coal/biomass blend ratio. For example, for a blend of 50:50 (mass of pine/coal) the actual ash ratio is ~30:70. Since the ash contents of pine and coal are 1.67% and 3.83%, respectively, the different ash components are calculated by 30% of the pine ash (prepared at 500 ℃) and 70% of El Cerrejon coal ash (prepared at 800 ℃). To study the properties of El Cerrejon coal 1 and 2 with pine and wheat straw ash during co-firing, the composition of the ashes prepared at both low and high temperatures were compared and some differences were observed. The high temperature ash results in lower C, H and N content, which in turn affects the proportion of metal oxides in the resultant ash analysis. Du et al. [191] used DTA-TGA (Differential thermal analysis and Thermogravimetric analysis) to study pine and a number of other biomass ashes. They showed that laboratory ash produced at higher temperatures results in a lower yield due to decomposition and vaporisation of some of the inorganic components. The ash characteristics thus vary with the preparation temperature as well as by the method of preparation.

4.4 Crystal analysis of ash composition by XRD

To identify the composition of coal and biomass ash and help to explain the inorganic compounds testing results, X-ray scattering techniques (X-ray diffraction) was used to scan the crystals and content in mixture powders. The results will be used to analysis the composition of biomass ash behaviour during combustion and co-combustion. Mineralogical analysis of ashes was conducted by using an X-ray diffraction (XRD) (model D8), with application of Cu kα radiation and graphite monochromator (U=35 kV, I=35 mA). The XRD scans were performed between 2 and 70 2θ°, with a step size of 0.0330 °s and time of 1216s. A software system DIFFRAC plus Evaluation by Bruker XS and the JCPDS database were used for data processing and identification of crystalline components.

4.4.1 El Cerrejon coal ash

Experimentally, ash deposition can be observed at some critical temperature and associated with some particular compounds, which may be contributed by XRD analysis. The peaks of graphs (**Figure 4.5~4.9**) show the different compositions of El Cerrejon coal ash, biomass ashes, ash blends, blending fuel ash and pilot scale combustion ash which were prepared under different conditions, the top plot is the practical test results (e.g. PCC1 ash), and the analysis results are listed below the testing peak. The crystalline mineral species in the samples, which were analysed by PANalytical's HighScore Plus software, are listed in **Table 4.8~4.12** below.

(a)

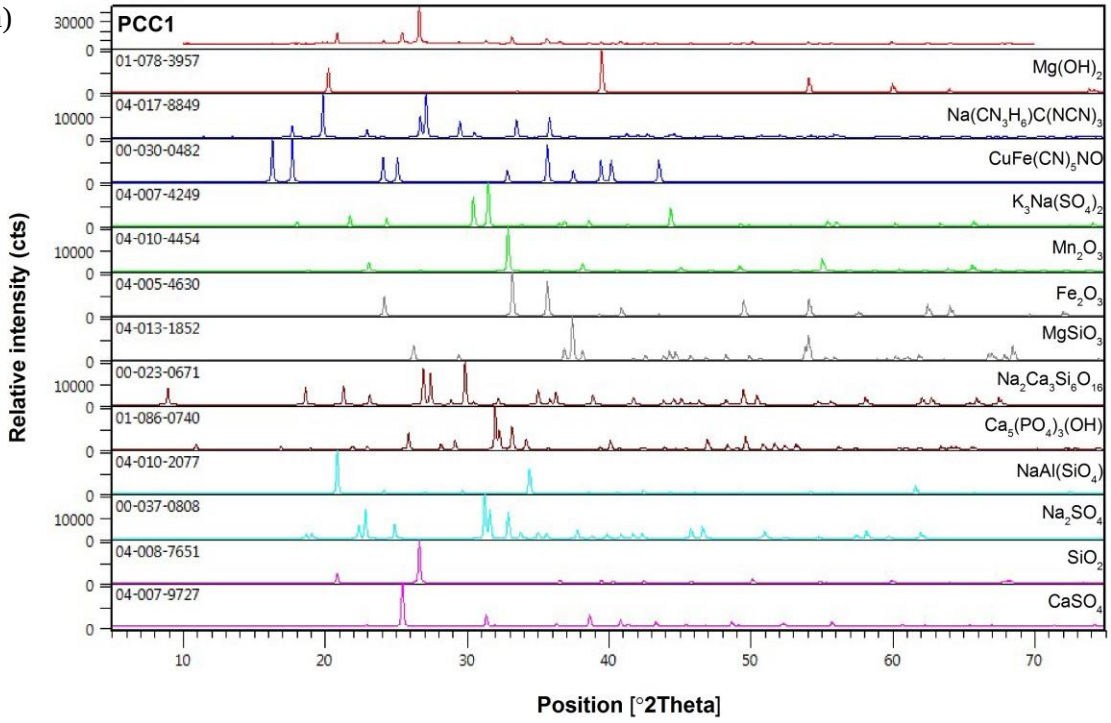
PCC1
01-078-3957
Mg(OH)2
04-017-8849
Na(CN3H6)C(NCN)3
00-030-0482
CuFe(CN)5NO
04-007-4249
K3Na(SO4)2
04-010-4454
Mn2O3
04-005-4630
Fe2O3
04-013-1852
MgSiO3
00-023-0671
Na2Ca3Si6O16
01-086-0740
Ca5(PO4)3(OH)
04-010-2077
NaAl(SiO4)
00-037-0808
Na2SO4
04-008-7651
SiO2
04-007-9727
CaSO4
Relative intensity (cts)
Position [°2Theta]

(b)

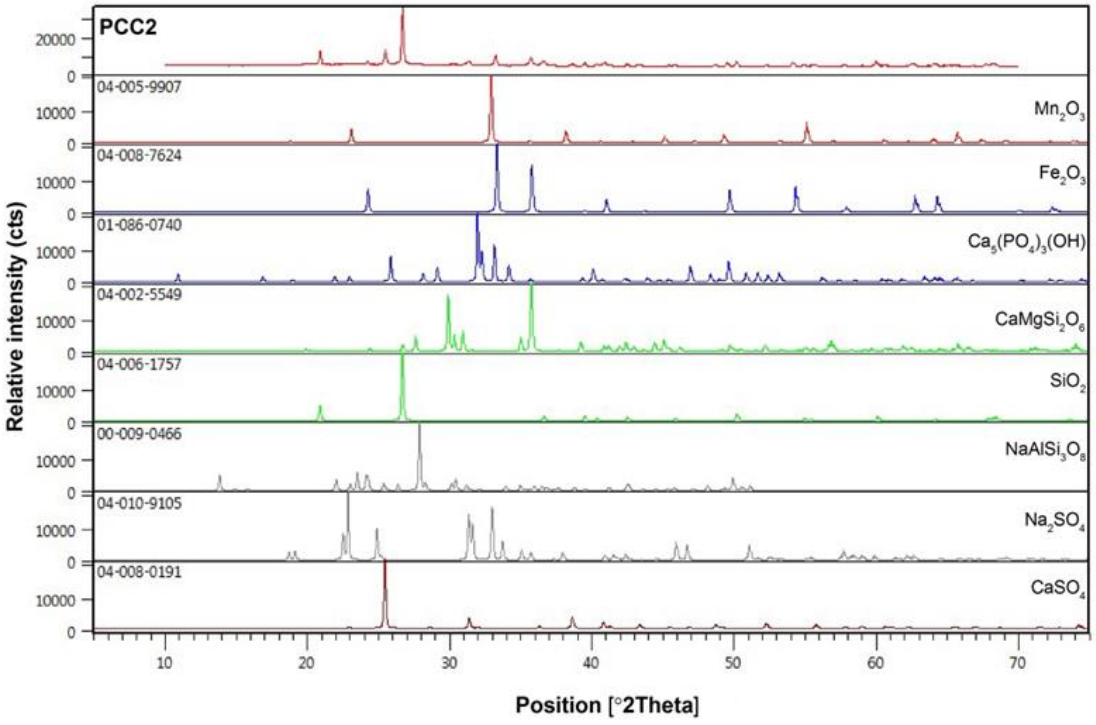
PCC2
04-005-9907
Mn2O3
04-008-7624
Fe2O3
01-086-0740
Ca5(PO4)3(OH)
04-002-5549
CaMgSi2O6
04-006-1757
SiO2
00-009-0466
NaAlSi3O8
04-010-9105
Na2SO4
04-008-0191
CaSO4
Relative intensity (cts)
Position [°2Theta]

(c)

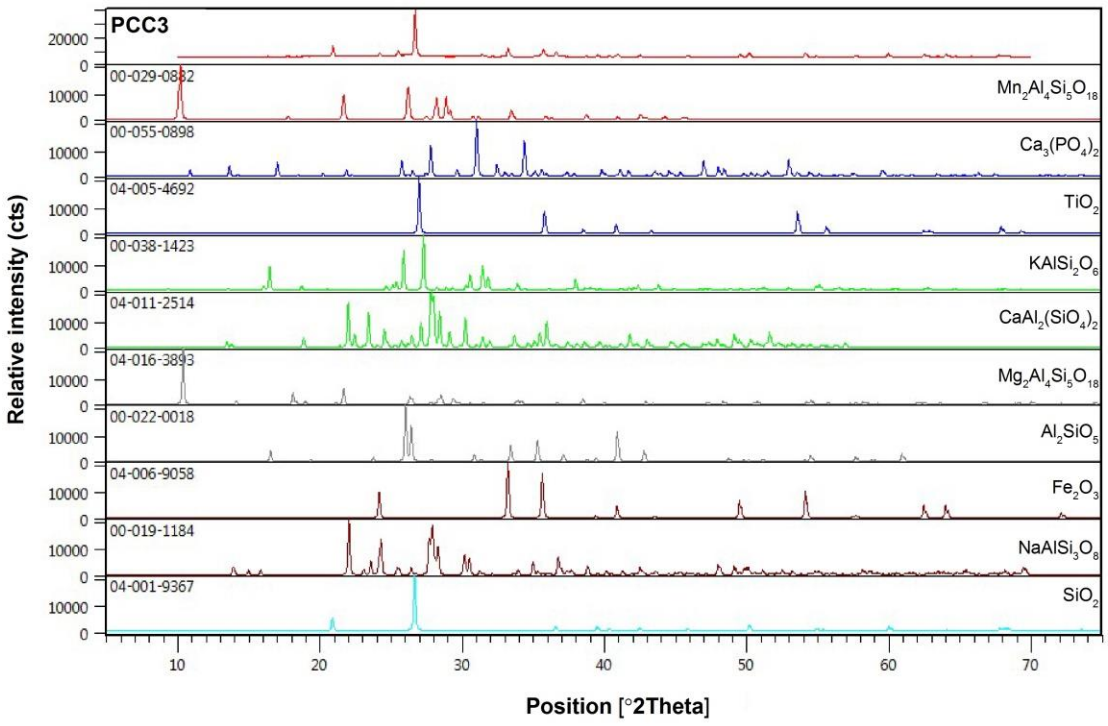

Figure 4.5 (a)~(c). Analysis of El Cerrejon coal 1 and 2 ash mineral compositions: (a) PCC1 (550°C); (b) PCC2 (800°C); (c) PCC3 (800°C).

As observed from **Figure 4.5 (a)~(c)**, the mineral phases and chemical formulas of coal ash are summarized in the **Table 4.8** as below:

Table 4.8 List of El Cerrejon coal 1 and 2 ash mineral compositions.

PCC1(550°C)	PCC2(800°C)	PCC3(800°C)
Chemical Formula	Chemical Formula	Chemical Formula
$Ca(SO_4)$	$Ca(SO_4)$	SiO_2
SiO_2	$Na_2(SO_4)$	$NaAlSi_3O_8$
Na_2SO_4	$NaAlSi_3O_8$	Fe_2O_3
$NaAl(SiO_4)$	SiO_2	Al_2SiO_5
$Ca_5(PO_4)_3(OH)$	$CaMgSi_2O_6$	$Mg_2Al_4Si_5O_{18}$
$Na_2Ca_3Si_6O_{16}$	$Ca_5(PO_4)_3(OH)$	$CaAl_2(SiO_4)_2$
$MgSiO_3$	Fe_2O_3	$KAlSi_2O_6$
Fe_2O_3	Mn_2O_3	TiO_2
Mn_2O_3	-	$Ca_3(PO_4)_2$
$K_3Na(SO_4)_2$	-	$Mn_2Al_4Si_5O_{18}$
$CuFe(CN)_5NO$	-	-
$NaCN_3H_6)C(NCN)_3$	-	-
$Mg(OH)_2$	-	-

If we compare the tested ashes in **Table 4.5**, we observe detection of $CaSO_4$ in the mineral phase for PCC1 and PCC2, even though S was not detected in the coal. The Mn compounds in **Table 4.8** prove the sensitivity of XRF test. The 550°C coal ash shows the existence of unburned carbon that was not present in the 800°C coal ash. Thus for El Cerrejon coal 1 and 2 ashes, as the combustion temperature increase, the mineral phase composition has some changes, including the removal of C and transformation and recombination of the Na, Al, Ca and parts of Si to form some new compounds. Ti compounds were determined as TiO_2 which was not matched in other two coal ash tested peaks. This summary of mineral compositions will be used to calibrate the modelling work in **Chapter 6**.

4.4.2 Pine, wheat straw and white wood pellet ash

(a)

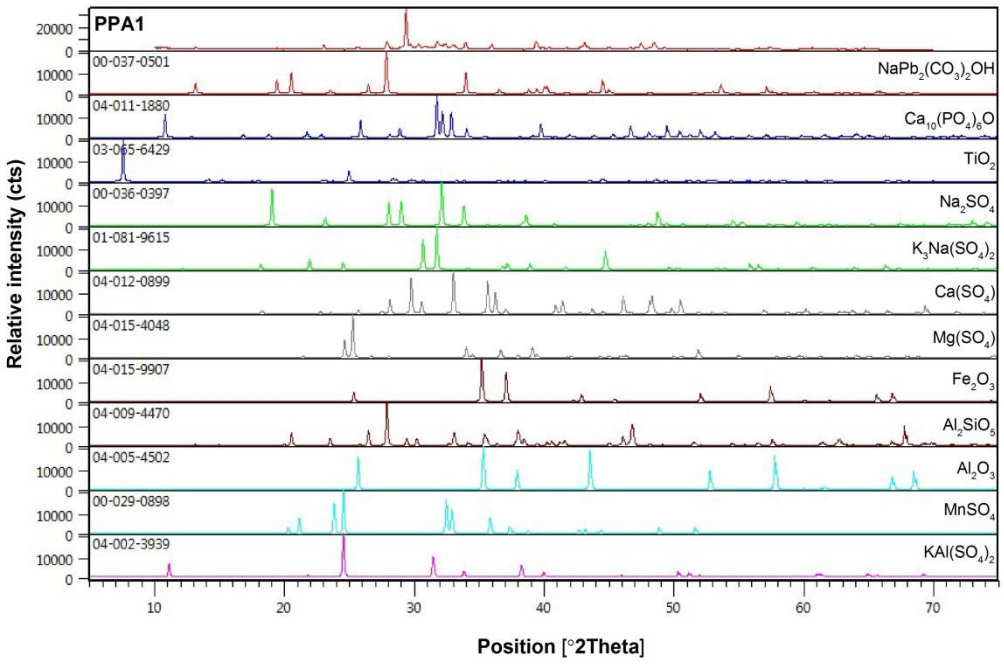

(b)

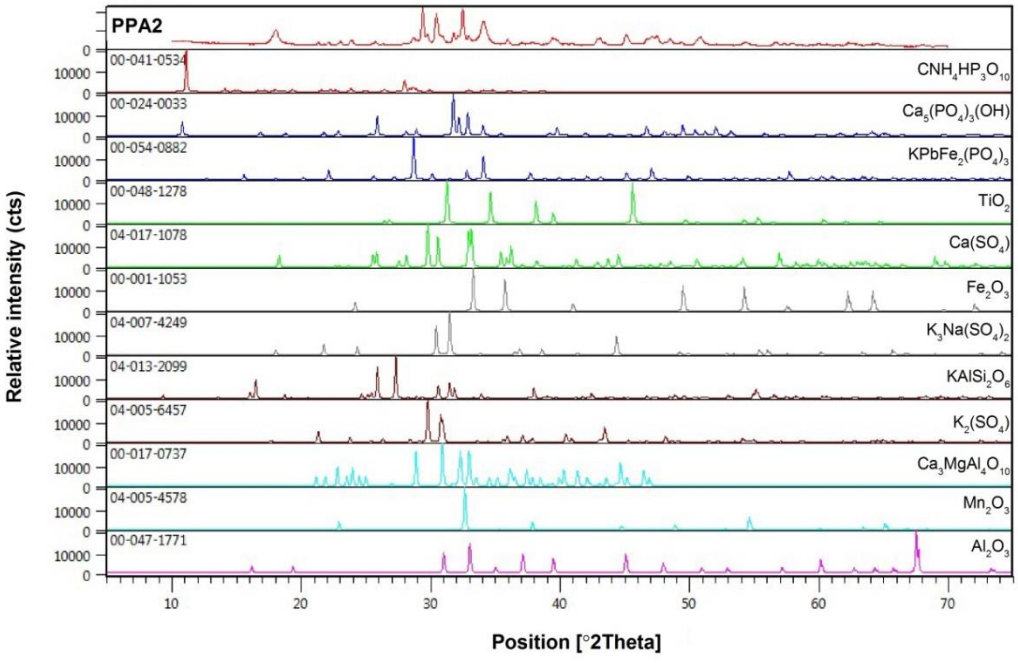

(c)

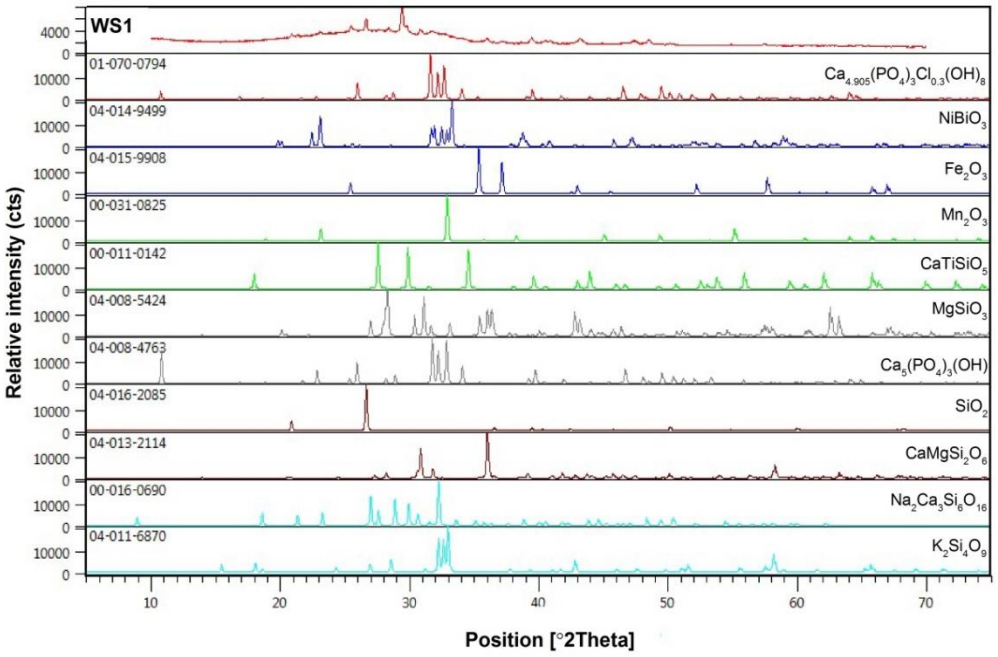
WS1
01-070-0794
$Ca_{4.905}(PO_4)_3Cl_{0.3}(OH)_8$
04-014-9499
$NiBiO_3$
04-015-9908
Fe_2O_3
00-031-0825
Mn_2O_3
00-011-0142
$CaTiSiO_5$
04-008-5424
$MgSiO_3$
04-008-4763
$Ca_5(PO_4)_3(OH)$
04-016-2085
SiO_2
04-013-2114
$CaMgSi_2O_6$
00-016-0690
$Na_2Ca_3Si_6O_{16}$
04-011-6870
$K_2Si_4O_9$
Relative intensity (cts)
Position [°2Theta]

(d)

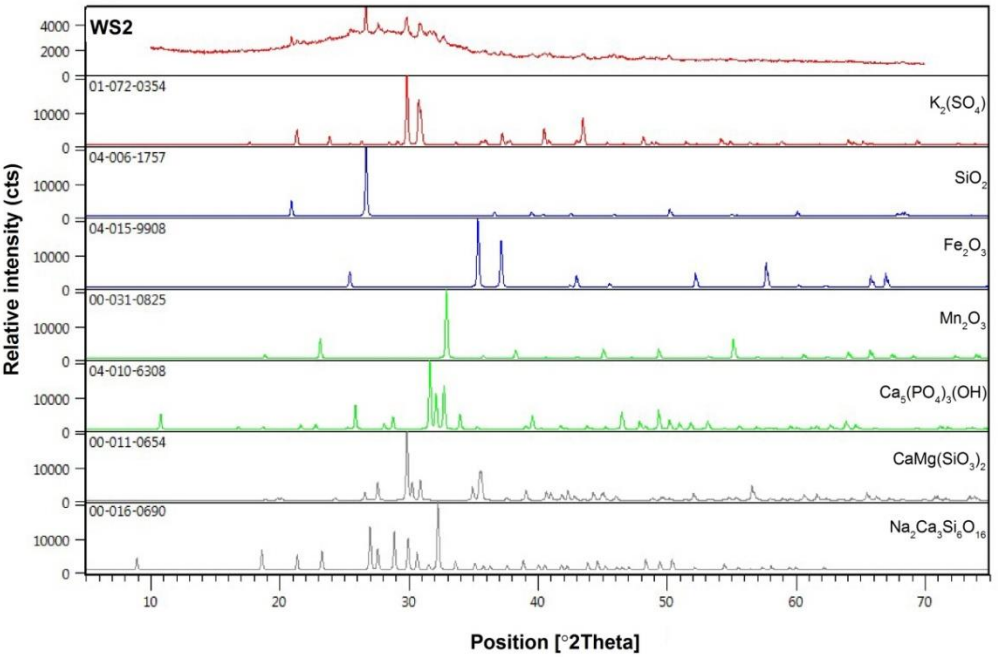
WS2
01-072-0354
$K_2(SO_4)$
04-006-1757
SiO_2
04-015-9908
Fe_2O_3
00-031-0825
Mn_2O_3
04-010-6308
$Ca_5(PO_4)_3(OH)$
00-011-0654
$CaMg(SiO_3)_2$
00-016-0690
$Na_2Ca_3Si_6O_{16}$
Relative intensity (cts)
Position [°2Theta]

(e)

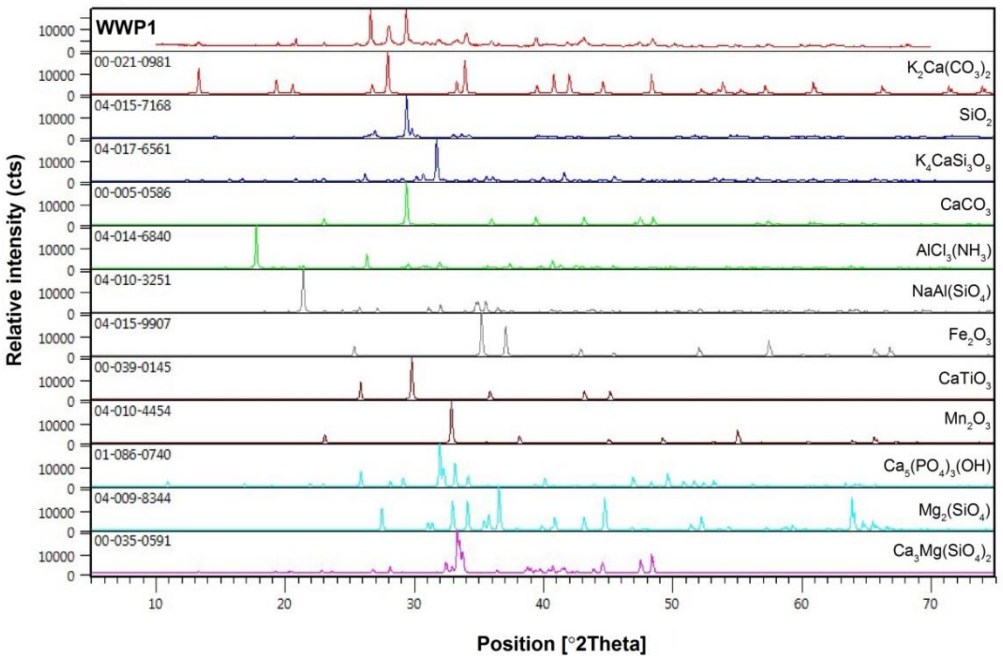

(f)

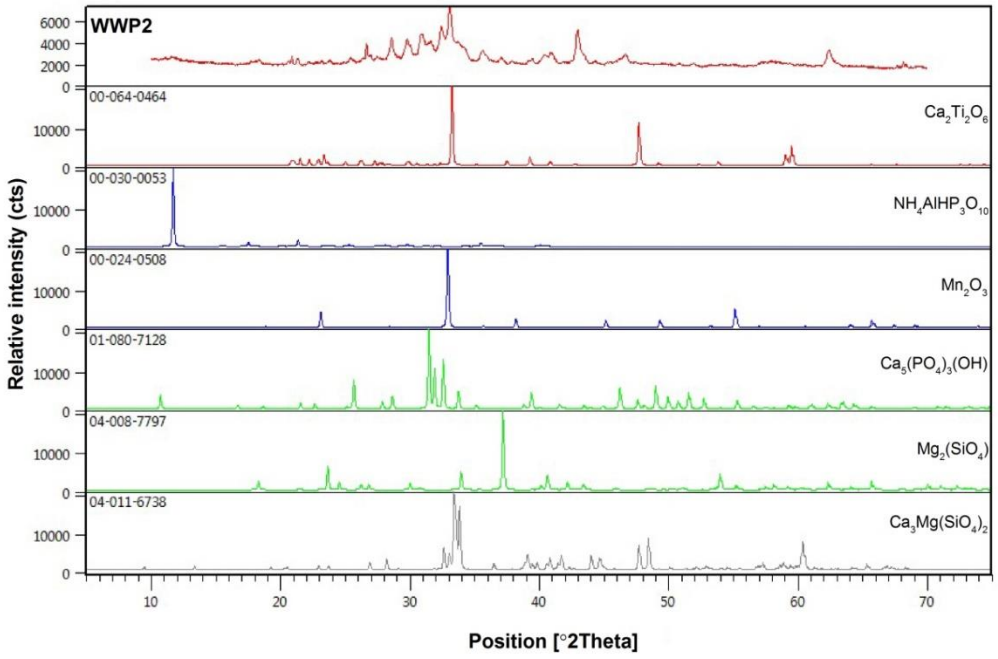

Figure 4.6 (a)~(f) Analysis of different biomass ash mineral compositions: (a) PPA1(550°C); (b) PPA2 (800°C); (c) WS1 (550°C); (d) WS2 (800°C); (e) WWP1 (550°C); (d) WWP2 (800°C).

The XRD traces and analysis of two biomass ashes, pine (PPA) and wheat straw (WS) and white wood pellet (WWP) ashed at 550°C(1) and 800°C (2) are given in **Figure 4.6 (a)~(f)**. The mineral phase chemical formulas of biomasses ashes are summarized in the **Table 4.9.** Comparing the tested inorganic oxides in **Table 4.5**, all of the 550℃ biomass ashes showed the existence of unburned carbon, which was not present in the 800℃ biomass ashes. All the high temperature ashes show mineral composition changes compared to the low temperature ashes. For example, the dominant phosphorus compounds in pine ash show the decomposition process from $Ca_{10}(PO_4)_6O$ to $Ca_5(PO_4)_3(OH)$ with temperature increase. It is notable that the pine ashes contain obviously higher Ca and P compounds and lower Si and Al compounds than wheat straw ash and white wood pellet ash. Comparing the three biomass mineral compositions, pine ash shows a greater tendency to change composition with increasing temperature than the other two biomass ashes.

Table 4.9 List of different biomass ash mineral compositions.

PPA1(550°C)	PPA2(800°C)	WS1(550°C)	WS2(800°C)	WWP1(550°C)	WWP2(800°C)
Chemical Formula	Chemical Formula	Chemical Formula	Chemical Formula	Chemical Formula	Chemical Formula
$KAl(SO_4)_2$	Al_2O_3	$K_2Si_4O_9$	$Na_2Ca_3Si_6O_{16}$	$Ca_3Mg(SiO_4)_2$	$Ca_3Mg(SiO_4)_2$
$MnSO_4$	Mn_2O_3	$Na_2Ca_3Si_6O_{16}$	$CaMg(SiO_3)_2$	$Mg_2(SiO_4)$	$Mg_2(SiO_4)$
Al_2O_3	$Ca_3MgAl_4O_{10}$	$CaMgSi_2O_6$	$Ca_5(PO_4)_3(OH)$	$Ca_5(PO_4)_3(OH)$	$Ca_5(PO_4)_3(OH)$
Al_2SiO_5	$K_2(SO_4)$	SiO_2	Mn_2O_3	Mn_2O_3	Mn_2O_3
Fe_2O_3	$KAlSi_2O_6$	$Ca_5(PO_4)_3(OH)$	Fe_2O_3	$CaTiO_3$	$NH_4AlHP_3O_{10}$
$Mg(SO_4)$	$K_3Na(SO_4)_2$	$MgSiO_3$	SiO_2	Fe_2O_3	$Ca_2Ti_2O_6$
$Ca(SO_4)$	Fe_2O_3	$CaTiSiO_5$	$K_2(SO_4)$	$NaAl(SiO_4)$	-
$K_3Na(SO_4)_2$	$Ca(SO_4)$	Mn_2O_3	-	$AlCl_3(NH_3)$	-
Na_2SO_4	TiO_2	Fe_2O_3	-	$CaCO_3$	-
TiO_2	$KPbFe_2(PO_4)_3$	$NiBiO_3$	-	$K_4CaSi_3O_9$	-
$Ca_{10}(PO_4)_6O$	$Ca_5(PO_4)_3(OH)$	$Ca_{4.905}(PO4)_3Cl_{0.3}(OH)_8$	-	SiO_2	-
$NaPb_2(CO_3)_2OH$	$CeNH_4HP_3O_{10}$	-	-	$K_2Ca(CO_3)_2$	-

4.4.3 Ash blends

The XRDs for the ashed coal-pine blends are given in **Figure 4.7 (a)~(c)**.

(a)

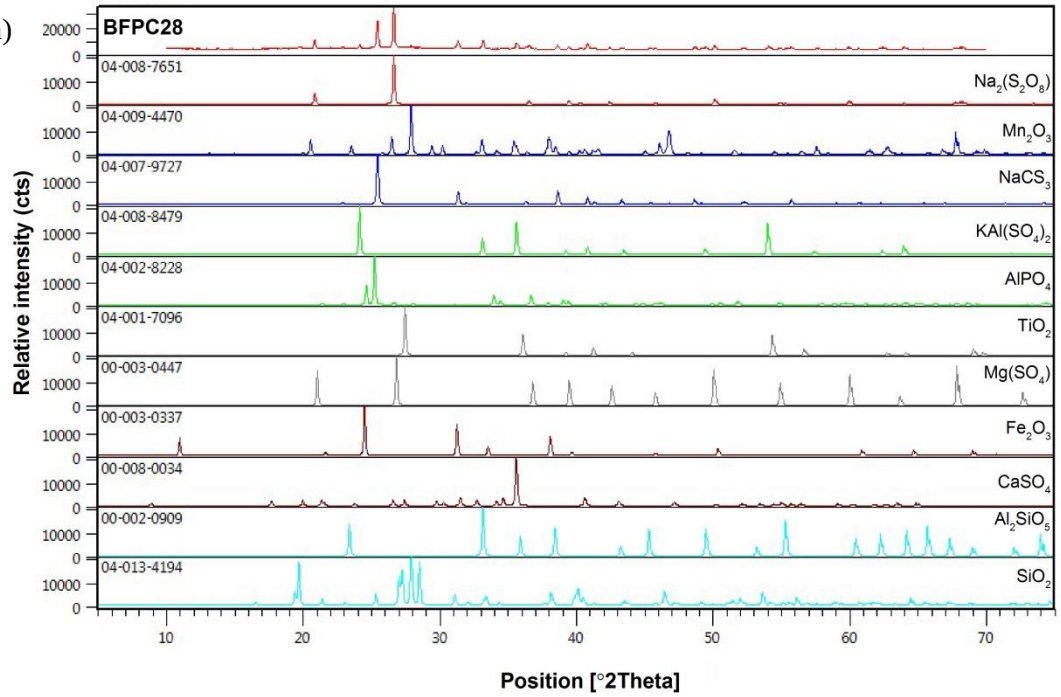

(b)

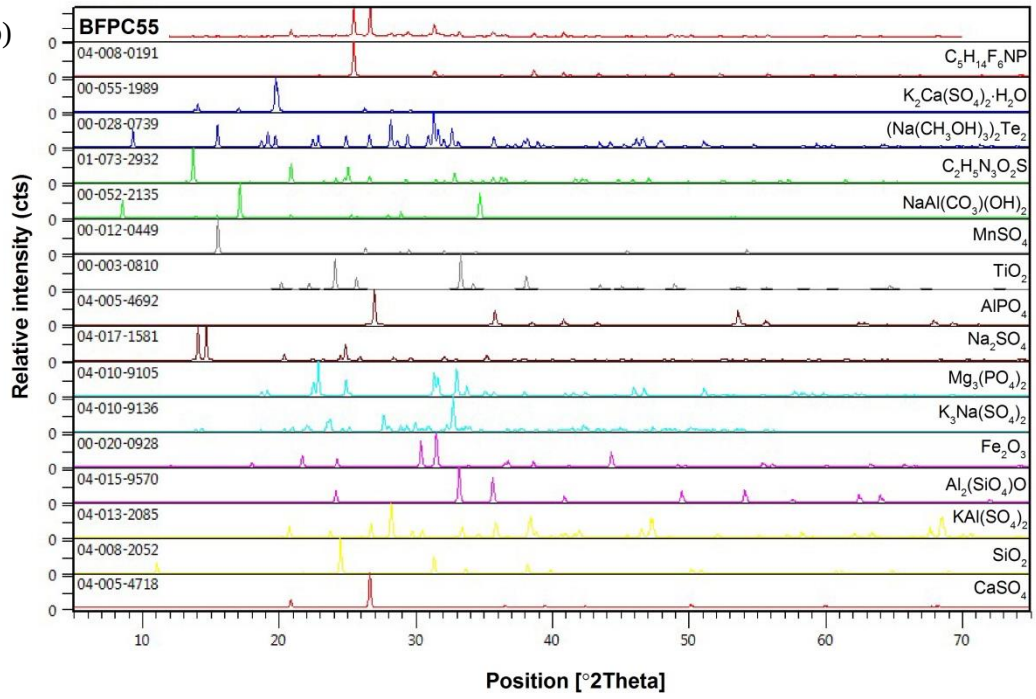

(c)

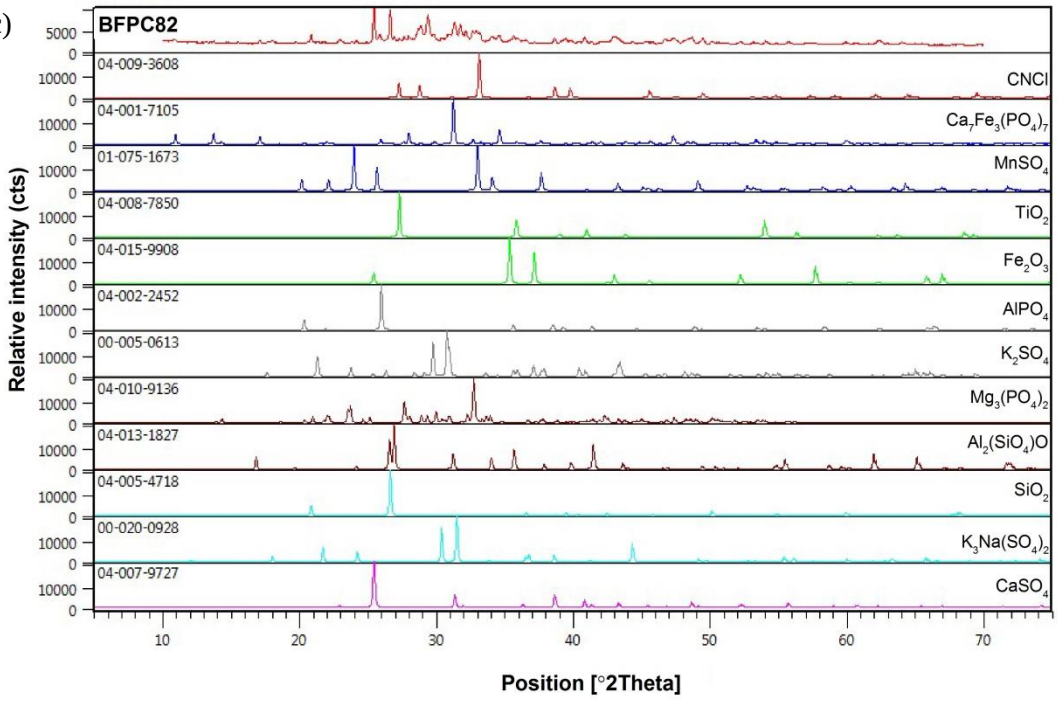

Figure 4.7 (a)~(c) Analysis of El Cerrejon coal 1 and Pine co-firing ash mineral compositions (Ash produced at 550°C from blended fuel).

The mineral phase chemical formulas of those co-fired ashes are summarized in the **Table 4.10**. The pine and El Cerrejon coal 1 co-firing group are as described as in **Chapter 3**. The BFPC55 (fuel ratio is 50/50) shows the most complicated mineral composition. Since all the co-firing ashes were prepared at 550 ℃, all of these ashes contain unburned carbon compounds. The effect of blend ratio can be seen in **Table 4.6**. The dominatant inorganic oxides Si, Fe, Al and Ti compounds decrease with increasing biomass ratio. In contrast, the P compounds, K compounds and Ca compounds increase. When the fuel ratio is 50/50, all the inorganic compounds become an average level and the mineral composition shows the most variety.

Table 4.10 List of El Cerrejon coal 1 and Pine co-firing ash mineral compositions.

BFPC28(550°C)	BFPC55(550°C)	BFPC82(550°C)
Chemical Formula	Chemical Formula	Chemical Formula
SiO_2	$Ca(SO_4)$	$Ca(SO_4)$
Al_2SiO_5	SiO_2	$K_3Na(SO_4)_2$
$Ca(SO_4)$	$KAl(SO_4)_2$	SiO_2
Fe_2O_3	$Al_2(SiO_4)O$	$Al_2(SiO_4)O$
$Mg(SO_4)$	Fe_2O_3	$Mg_3(PO_4)_2$
TiO_2	$K_3Na(SO_4)_2$	K_2SO_4
$AlPO_4$	$Mg_3(PO_4)_2$	$Al(PO_4)$
$KAl(SO_4)_2$	$Na_2(SO_4)$	Fe_2O_3
$NaCS_3$	$Al(PO_4)$	TiO_2
Mn_2O_3	TiO_2	$MnSO_4$
$Na_2(S_2O_8)$	$MnSO_4$	$Ca_7Fe_3(PO_4)_7$
-	$NaAl(CO_3)(OH)_2$	CNCl
-	$C_2H_5N_3O_2S$	-
-	(Na(CH3OH)3)2Te2	-
-	$K_2Ca(SO_4)_2 \cdot H_2O$	-
-	$C_5H_{14}F_6NP$	-

The XRDs for the ashed El Cerrejon coal 2--wheat straw blends are given in **Figure 4.8 (a)~(c)**, together with the XRD analysis results.

(a)

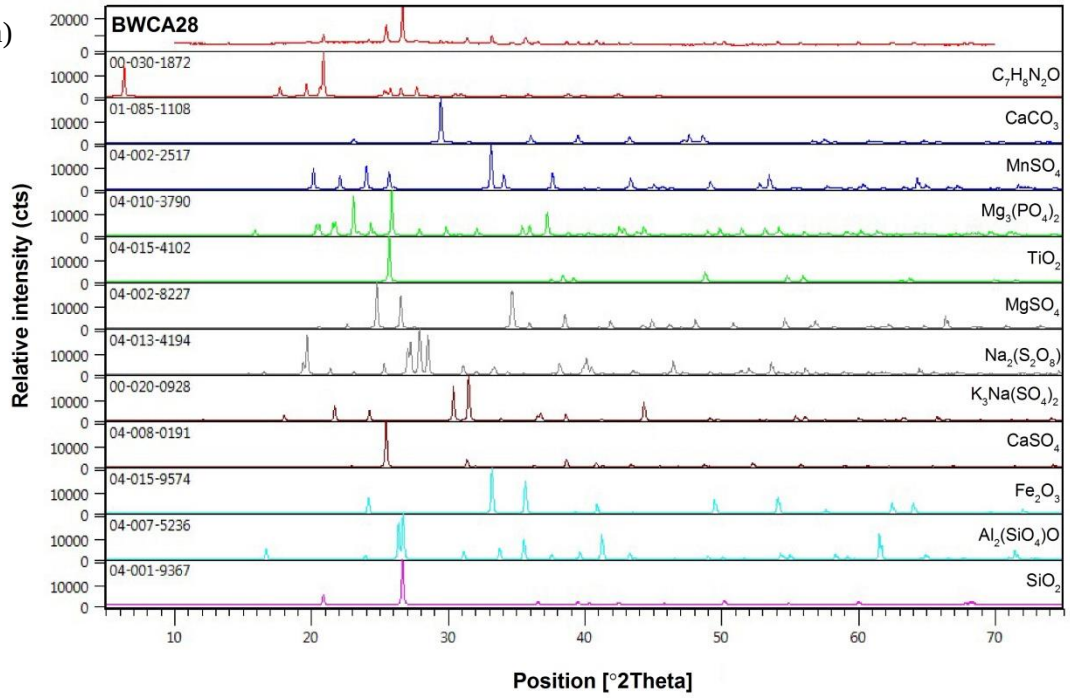
BWCA28
00-030-1872
C7H8N2O
01-085-1108
CaCO3
04-002-2517
MnSO4
04-010-3790
Mg3(PO4)2
04-015-4102
TiO2
04-002-8227
MgSO4
04-013-4194
Na2(S2O8)
00-020-0928
K3Na(SO4)2
04-008-0191
CaSO4
04-015-9574
Fe2O3
04-007-5236
Al2(SiO4)O
04-001-9367
SiO2
Relative intensity (cts)
Position [°2Theta]

(b)

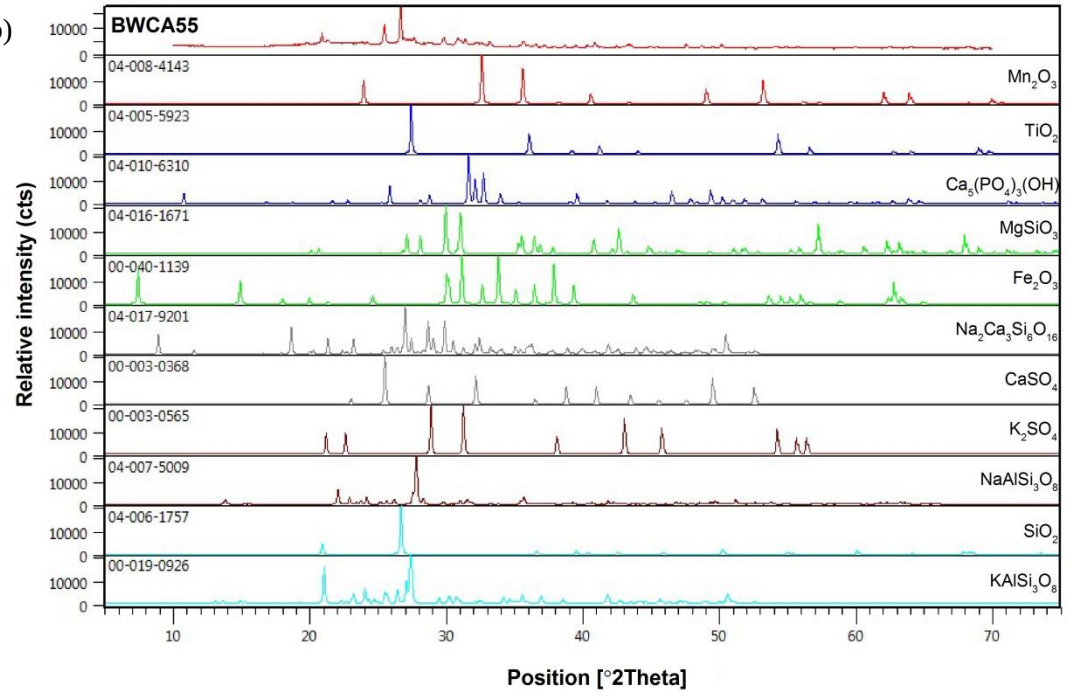
BWCA55
04-008-4143
Mn2O3
04-005-5923
TiO2
04-010-6310
Ca5(PO4)3(OH)
04-016-1671
MgSiO3
00-040-1139
Fe2O3
04-017-9201
Na2Ca3Si6O16
00-003-0368
CaSO4
00-003-0565
K2SO4
04-007-5009
NaAlSi3O8
04-006-1757
SiO2
00-019-0926
KAlSi3O8
Relative intensity (cts)
Position [°2Theta]

(c)

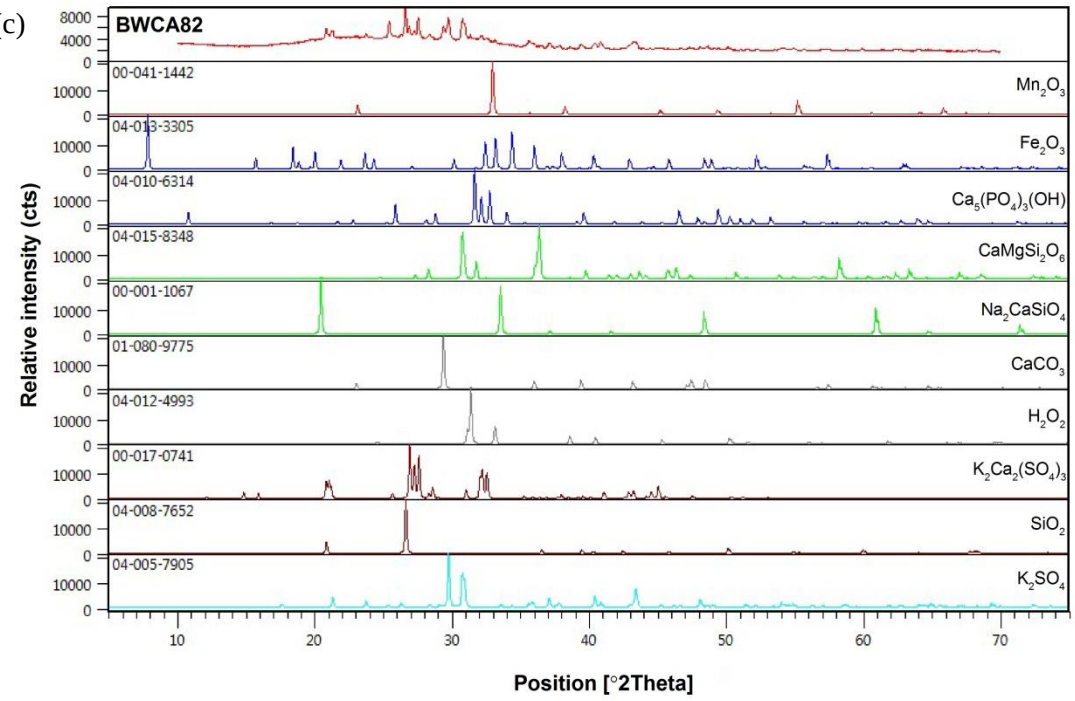

Figure 4.8 (a)~(c) Analysis of El Cerrejon coal 2 and Wheat straw co-firing ash mineral compositions.

The mineral phase chemical formulas of wheat straw and El Cerrejon coal 2 co-firing ash which are prepared as the description in **Chapter 3** are summarized as in the **Table 4.11** as below. With since the increasing ratio of wheat straw, the co-firing ash shows decreasing Fe, Al and Ti compounds and increasing of P, K and Ca compounds. Different to the BFPC group, in the fuel ratio 50/50 dose not exhibit, the complicated mineral composition but displays a significant content of Si compounds.

Table 4.11 List of El Cerrejon coal 2 and Wheat straw co-firing ash mineral compositions.

BWCA28(550°C)	BWCA55(550°C)	BWCA82(550°C)
Chemical Formula	Chemical Formula	Chemical Formula
SiO_2	$KAlSi_3O_8$	$K_2(SO_4)$
$Al_2(SiO_4)O$	SiO_2	SiO_2
Fe_2O_3	$NaAlSi_3O_8$	$K_2Ca_2(SO_4)_3$
$Ca(SO_4)$	K_2SO_4	(H_2O_2)
$K_3Na(SO_4)_2$	$CaSO_4$	$Ca(CO_3)$
$Na_2(S_2O_8)$	$Na_2Ca_3Si_6O_{16}$	Na_2CaSiO_4
$Mg(SO_4)$	Fe_2O_3	$CaMgSi_2O_6$
TiO_2	$MgSiO_3$	$Ca_5(PO_4)_3(OH)$
$Mg_3(PO_4)_2$	$Ca_5(PO_4)_3(OH)$	Fe_2O_3
$Mn(SO_4)$	TiO_2	Mn_2O_3
$Ca(CO_3)$	Mn_2O_3	
$C_7H_8N_2O$		

4.4.4 Pilot scale test ash samples

The XRD patterns of the ash obtained from the PACT facility together with the modelled analysis are given in **Figure 4.9 (a)~(f)**.

(a)

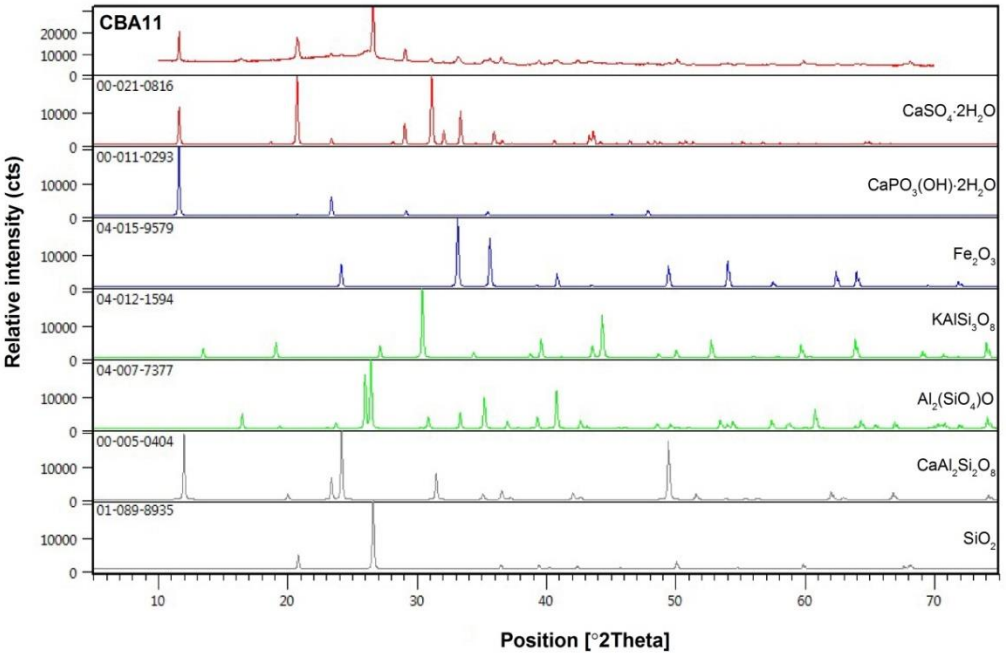

(b)

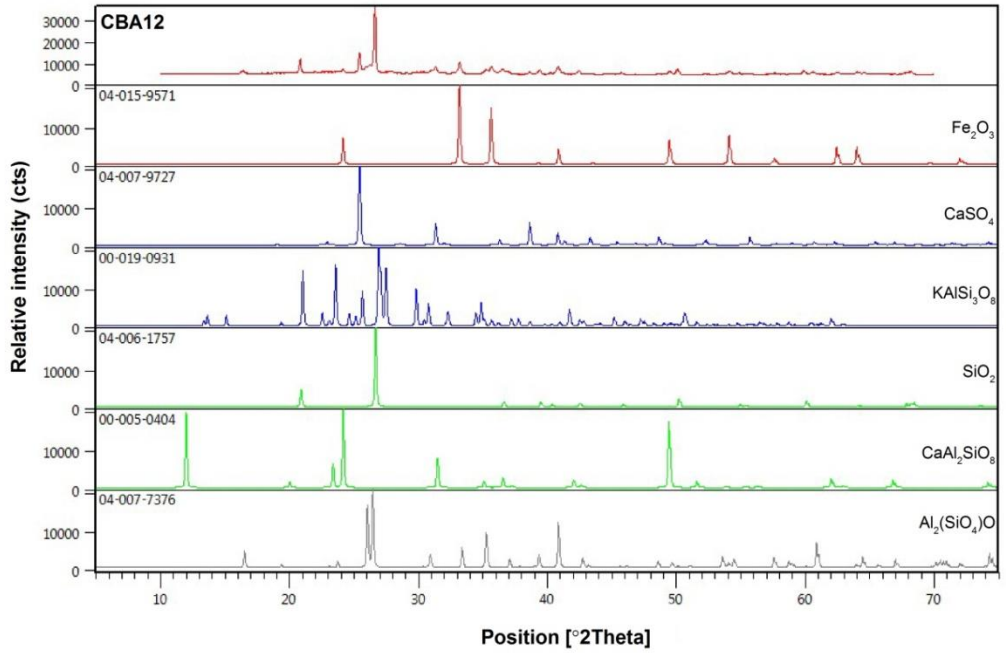

(c)

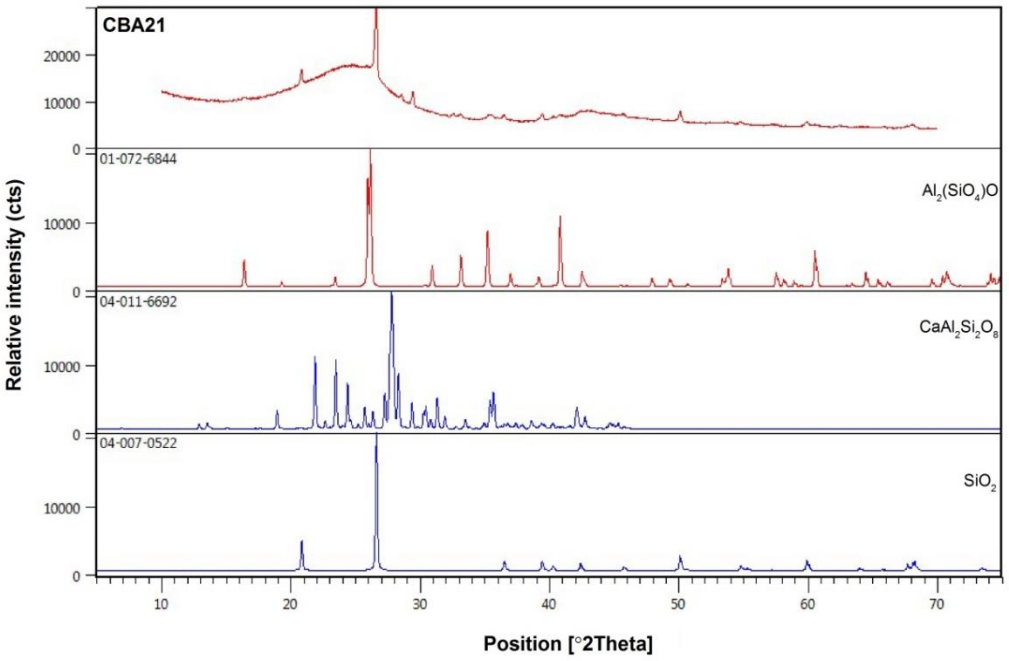
CBA21
01-072-6844
$Al_2(SiO_4)O$
04-011-6692
$CaAl_2Si_2O_8$
04-007-0522
SiO_2
Relative intensity (cts)
Position [°2Theta]

(d)

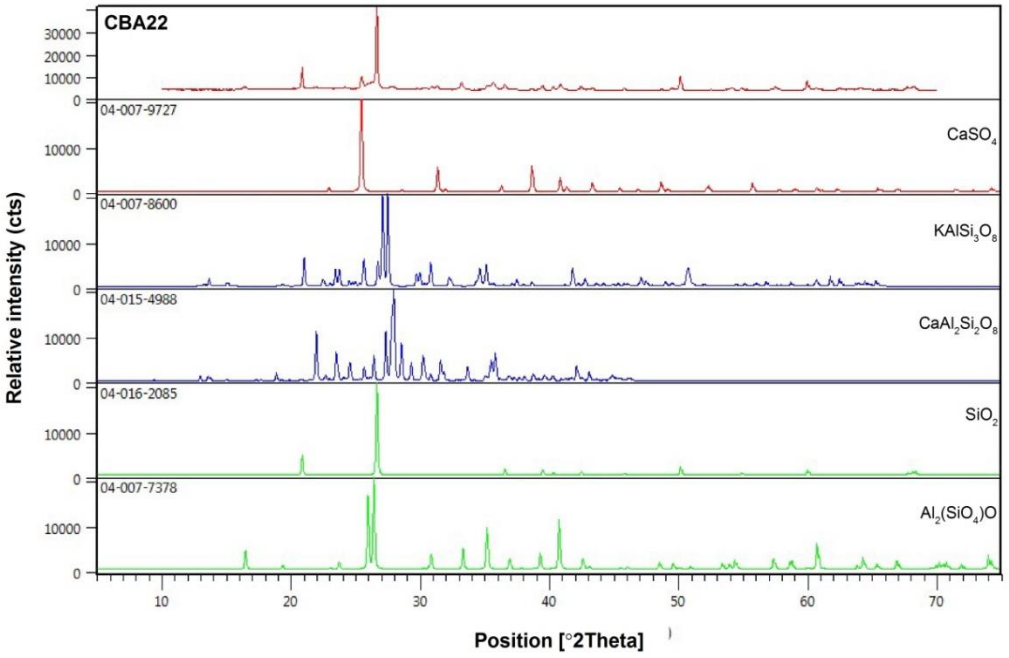
CBA22
04-007-9727
$CaSO_4$
04-007-8600
$KAlSi_3O_8$
04-015-4988
$CaAl_2Si_2O_8$
04-016-2085
SiO_2
04-007-7378
$Al_2(SiO_4)O$
Relative intensity (cts)
Position [°2Theta]

(e)

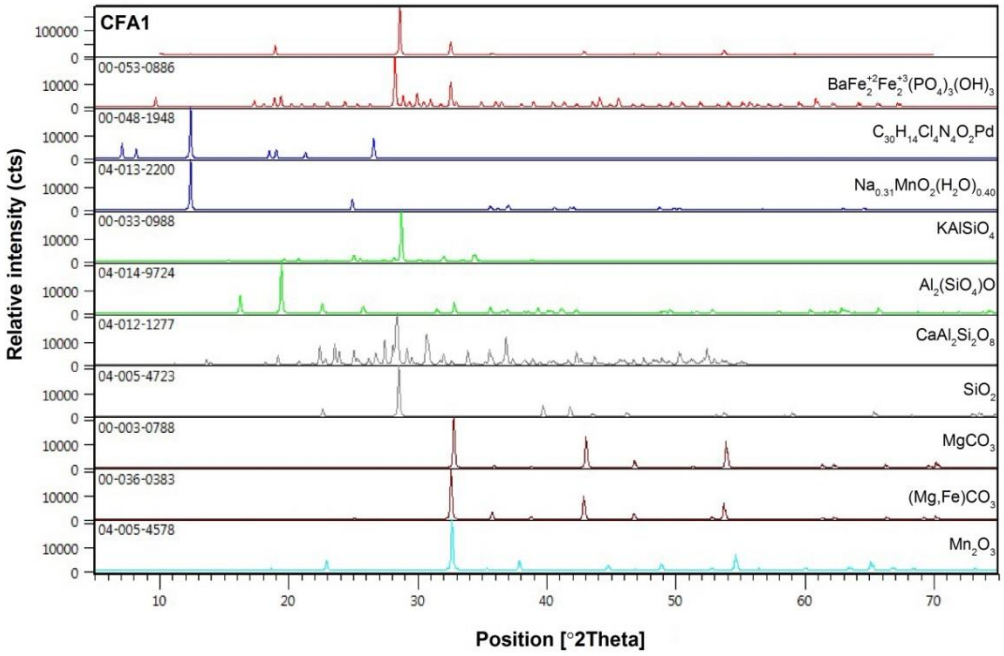

(f)

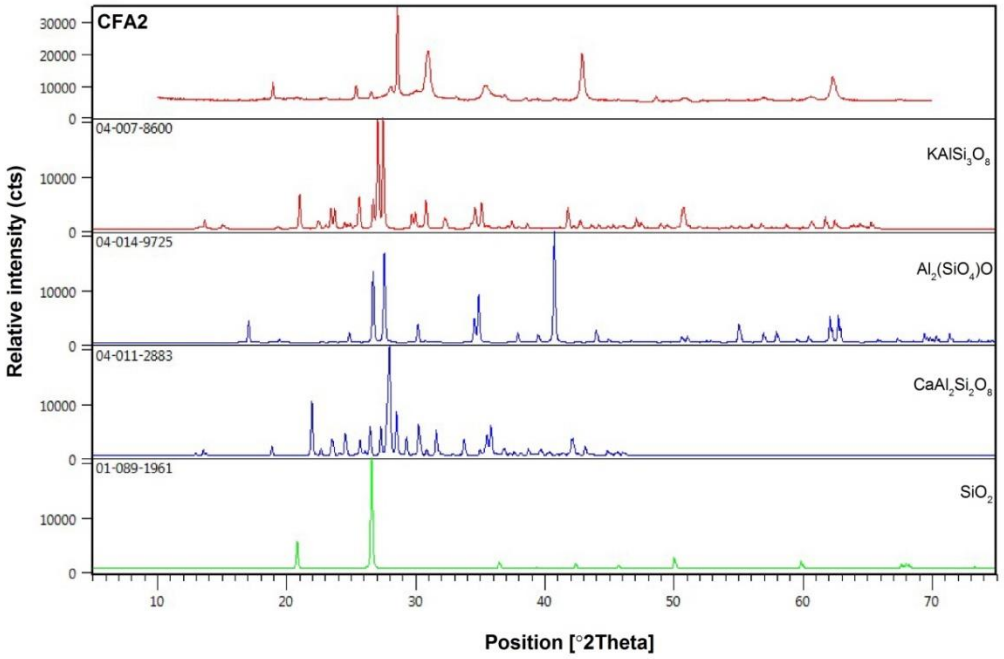

Figure 4.9 (a)~(f) Analysed mineral compositions of El Cerrejon coal 2 ashes from pilot scale combustion and re-burned under 800°C.

Table 4.12 List of El Cerrejon coal 2 combustion ash mineral compositions by PACT.

CBA11	CBA12(800°C)	CBA21	CBA22(800°C)	CFA1	CFA2(800°C)
Chemical Formula	Chemical Formula	Chemical Formula	Chemical Formula	Chemical Formula	Chemical Formula
SiO_2	$Al_2(SiO_4)O$	SiO_2	$Al_2(SiO_4)O$	Mn_2O_3	SiO_2
$CaAl_2Si_2O_8$	$CaAl_2Si_2O_8$	$CaAl_2Si_2O_8$	SiO_2	$(Mg,Fe)CO_3$	$CaAl_2Si_2O_8$
$Al_2(SiO_4)O$	SiO_2	$Al_2(SiO_4)O$	$CaAl_2Si_2O_8$	$MgCO_3$	$Al_2(SiO_4)O$
$KAlSi_3O_8$	$KAlSi_3O_8$	-	$KAlSi_3O_8$	SiO_2	$KAlSi_3O_8$
Fe_2O_3	$Ca(SO_4)$	-	$Ca(SO_4)$	$CaAl_2Si_2O_8$	-
$CaPO_3(OH)\ 2H_2O$	Fe_2O_3	-	-	$Al_2(SiO_4)O$	-
$CaSO_4\ 2H_2O$	-	-	-	$KAlSiO_4$	-
-	-	-	-	$Na_{0.31}MnO_2(H_2O)_{0.40}$	-
-	-	-	-	$C_{30}H_{14}C_{l4}N_4O_2\,Pd$	-
-	-	-	-	$BaFe_2^{+2}Fe_2^{+3}(\,PO_4)_3(OH)_3$	-

The mineral phase chemical formulas of these pilot scale combustion ashes (which are prepared as the description in **Chapter 3**) are summarized in the **Table 4.12**. These ashes (CBA11, CBA21 and CFA1) contain much unburned carbon. Some peaks were complicated to be analysed. After re-burning the ashes at 800°C, the peaks of CBA12 and CBA22 can be more easily clarified. The fly ash has lowest carbon content before re-burn, and the mineral composition is more easily determined. After a re-burn, the compounds in the CFA2 were lost. Compared to PCC3 in **Table 4.8**, SiO_2, $CaAl_2Si_2O_8$, $Ca(SO_4)$, Fe_2O_3 and Al_2SiO_5 can be found as similar compositions.

4.5 Summaries

Results presented in this chapter concern firstly, the analysis of the inorganics present in solid fuels and their blends, and secondly the mineral phases present when they are burned, either under laboratory or pilot scale testing conditions. In terms of analysis of inorganics, both wet chemical methods and XRF are used for the ashes under study. Sometimes there is a deviation between the two methods for some elements, and this is most significant when there is high carbon in ash or where vaporisation of volatile inorganics takes place.

A revised method of XRF analysis was developed which gave much better correlation with the wet chemical analysis methods. 815°C was used as the ashing temperature and 1100°C (for 9min) as the glass fusion temperature. This appears to give a good compromise of minimising C in ash without significant loss of volatile metals.

XRD showed complex interactions between inorganics which changed with biomass type, blend ratio and temperature. Results will be used to compare the FactSage modelling results in **Chapter 6**.

Chapter 5 Ash Thermal Properties and Fusion Performance

Ash fusion characteristics are also important parameters for predicting ash slagging and fouling potentials. In this project, ash fusion characteristics are observed from ash fusion tests (AFT). The main stage temperatures were recorded and the change in height of the test piece was also assessed as a measure of change performance. Baxter et al. [192], who used the STA-MS method to characterise biomass ash, found a correlation between the AFT hemisphere temperature and the endotherm (DTA) peak temperatures for Miscanthus ash samples. In this project, the hemisphere temperature of all studied ash observed by AFT were compared with the endotherm (DTA) peak temperatures plotted alongside data from Baxter et al. for comparison purposes.

5.1 Ash fusion properties

Ash fusion tests (AFT) were performed using a digital ash fusion furnace, which has a black and white camera fixed at the front of the furnace to capture images of the ash whilst it is heated at a controlled temperature rate. The ash was prepared according to British standards, as described in DD CEN/TS 15370-1:2006 [190]. The ash was first ground in an agate mortar and a few drops of distilled water were added to make it into a paste. Because addition of water to the ash could leach certain salts from the sample, this was performed drop-wise to minimize the leaching. The ash paste was then pressed into an upright cylindrical stainless steel mould (about 5 mm diameter ~5 mm height). The mold had been coated with a thin layer of petroleum jelly beforehand,

to facilitate the removal of the test piece. Ash test pieces were then heated to 1700℃ at 5℃/min heating rate. Images were collected by the camera at every degree of temperature rise between 555℃ and 1700℃. These tests were performed in an oxidizing atmosphere (air). For a few samples the tests were repeated in a reducing atmosphere (50% mixture of CO/CO_2). Gas flow rates were 50 ml/min. Key stage temperatures, shrinkage starting temperature (SST), initial deformation temperature (IDT), hemisphere temperature (HT) and flow temperature (FT) were determined as shown in **Figure 5.1**.

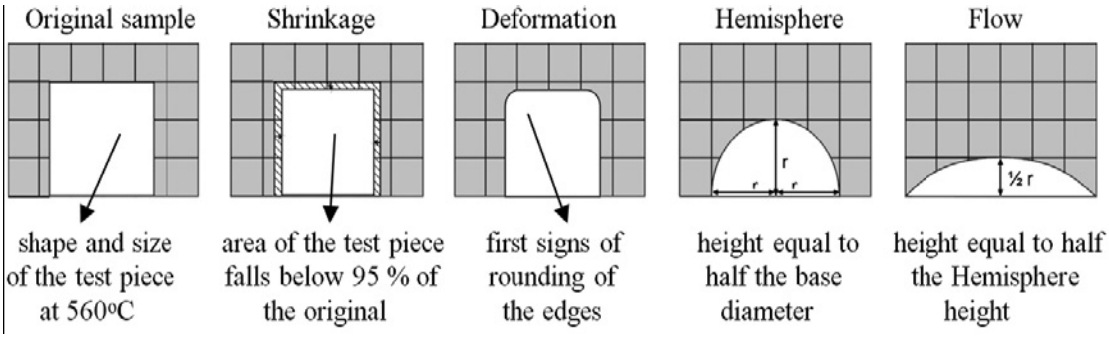

Figure 5.1 Phases in the ash melting process [190].

5.1.1 The ash fusion characteristic temperatures

The ash fusion characteristic temperatures have been summarized in **Table 5.1** for all the ash samples had been studied as below. It can be observed that pine ash (PPA) softens at temperatures between 1350 and 1500 ℃, and this temperature range is higher than that observed for El Cerrejon coal 1 and 2 ashes (PCC). The melting properties of ash blends (CA28, CA55 and CA82) and fuel blend ashes (BFPC28, BFPC55 and BFPC82) show a similar trend; the characteristic temperatures of SST

(start of shrinkage temperature), DT (deformation temperature), HT (hemisphere temperature) generally decrease as the coal ratio increases. It has to be noted that unexpectedly the 50/50 fuel ratio ash (CA55 and BFPC55) results gave the lowest ash fusion temperatures.

Table 5.1 The summary of ash fusion temperatures.

Samples	SST (°C)	IDT (°C)	HT (°C)	FT (°C)
PPA1	1020	1225	1480	1510
PPA2	1085	1285	1495	1515
WS1	855	925	1105	1165
WS2	N/A	N/A	N/A	N/A
WWP1	1225	1245	1290	1295
WWP2	N/A	N/A	N/A	N/A
PCC1	980	1195	1315	1330
PCC2	1005	1205	1360	1375
PCC3	1050	1210	1370	1380
CA82	1170	1210	1320	1335
CA55	1085	1180	1235	1250
CA28	1120	1245	1290	1300
BFPC82	1095	1195	1265	1295
BFPC55	955	1025	1230	1245
BFPC28	1075	1210	1300	1325
BWCA82	815	1010	1195	1225
BWCA55	860	1150	1245	1280
BWCA28	1080	1195	1295	1320
CFA1	N/A	N/A	N/A	N/A
CFA2	1160	1205	1475	1500
CBA11	N/A	N/A	N/A	N/A
CBA12	1060	1220	1335	1345
CBA21	N/A	N/A	N/A	N/A
CBA22	1065	1190	1395	1420

Different to pine ash, the 550°C wheat straw ash (WS1) show lower fusion characteristic temperatures than El Cerrejon coal 1 and 2 ashes. The SST start to be observed below 900°C, the DT is below 1000°C, and even the FT does not reach the SST of coal ash. The addition of straw apparently decreases the fusion characteristic temperatures of El Cerrejon coal 2 ash as observed blending fuel ash BWCA28, 55 and 82. Compare to this coal ash, the blending fuel ash fusion characteristic temperatures decrease and move towards those of pure straw ash as the ratio of straw increases. Even with the addition of 20% straw, the BWCA28 fusion characteristic temperatures are at least 50°C lower than those of PCC3.

Although the ash mineral compositions are different, the 550°C white wood pellet ash (WWP1) shows a similar start of shrinkage temperature to the two coal ashes. The white wood pellet ash fusion process was short-lived and focused on the range between 1200°C and 1300°C from start of softening to flow. There was not more than 50°C between those four stages.

The pilot scale test ash (CFA and CBA) were based on El Cerrejon coal 2. These ashes had high carbon content (CFA1, CBA11 and CBA21), and burn-off during the AFT. Consequently, the large volume of gas can easily break the test pieces if directly tested by AFT. Therefore the ashes CFA2, CBA12 and CBA22 were further ashed at 800°C for 14hrs. The fusion characteristic temperatures reported for the AFT were mainly based on these re-burned ashes. However the fusion processes were also studied by simultaneous thermal analysis for both the original ash and re-burned ash

and this is discussed **Section 5.2**. The AFT of re-burned ashes did not show an ideal regular fusion processes compared to PCC3 and it wasn't always possible to observe fusion characteristic temperatures. The mineral compositions of these ashes from different collecting points (in **Figure 3.2**) were different to the El Cerrejon coal 2 ash, and only the SST of CFA2 from fly ash filter (Collection 1) is very close to PCC3; the DT of the re-burned ashes are generally lower than PCC3; the HT of CBA22 from bottom of furnace (Collection 3) is within 30°C of that for PCC3; the FT of CBA12 from the exhaust gas entrance (Collection 2) is within 50°C of that for PCC3. The influence of different mineral compositions on fusion characteristic temperatures will be studied in **Chapter 7**.

5.1.2 The change in height of AFT samples

These fusion characteristic temperatures are also plotted in **Figure 5.2** along with the height changes of the test piece, according to the method of Pang et. al [193]. The ash test pieces undergo several changes during the test, which include swelling and shrinking. In order to give an insight into the behaviour of the ash during testing, the change in height of the test pieces (relative to the initial height) was estimated from the AFT images and plotted against temperature, as shown in **Figure 5.2** for the pure biomass and coal fuels, ash blends, fuel blends ashes, and ash from PACT, present as : (a) PPA1; (b) PPA2; (c)WS1; (d) WWP1; (e) PCC1; (f) PCC2; (g) PCC3; (h) CA82; (i) CA55; (j) CA28; (k)BFPC82; (l) BFPC55; (m) BFPC28; (n) BWCA82; (o) BWCA55; (p) BWCA28; (q) CFA2; (r) CBA12; (s) CBA22 respectively. From **Figure 5.2 (e)~(g)** it can be observed that coal ash swells at the deformation

temperature. A similar behaviour was also observed for the ash blends with coal ratios of 50% or higher in **Figure. 5.2 (h)~(j)**. In contrast, the pine ash, and the 80:20 blend of pine and coal, shrink at temperatures >800 ℃. Moreover, the shrinking appears to accelerate upon reaching the ash fusion characteristic temperature. Since the shrinking continues until the end of the test it difficult to determine the swelling point with accuracy. Both ash blends and analogous blended fuel ashes behaved similarly, and their behaviours resemble that of pure coal ash as the quantity of coal in the blend increases. Both ash blends and analogous blended fuel ashes behaved similarly, and their behaviours resemble that of pure coal ash as the quantity of coal in the blend increases. This can be seen clearly in **Figure 5.2 (k)~(m)**, when the amount of pine is less than 20% of the blended fuel ash, as its ash behaviour is very close to the pure El Cerrejon coal 1 ash behaviour, and as such it can be more confidently predicted. There were similar findings for wheat straw and El Cerrejon coal 2 which can be observed in **Figure 5.2 (c)**, **(g)** and **(n)~(p)**.

(a)

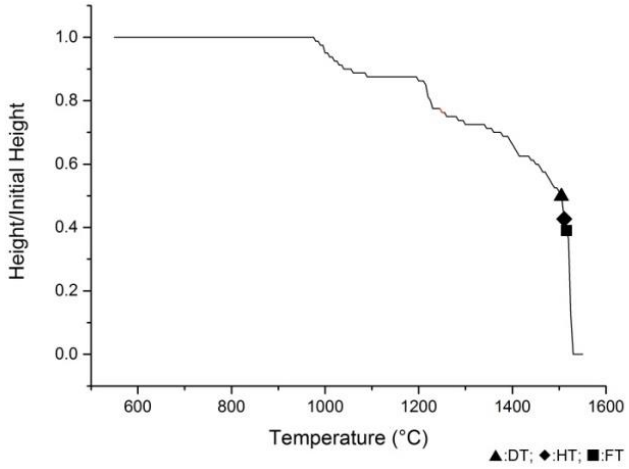
Height/Initial Height
1.0
0.8
0.6
0.4
0.2
0.0
600
800
1000
1200
1400
1600
Temperature (°C)
▲:DT; ◆:HT; ■:FT

(b)

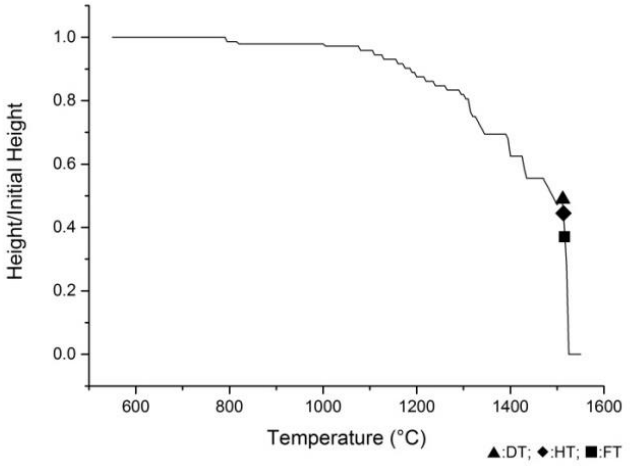
Height/Initial Height
1.0
0.8
0.6
0.4
0.2
0.0
600
800
1000
1200
1400
1600
Temperature (°C)
▲:DT; ◆:HT; ■:FT

(c)

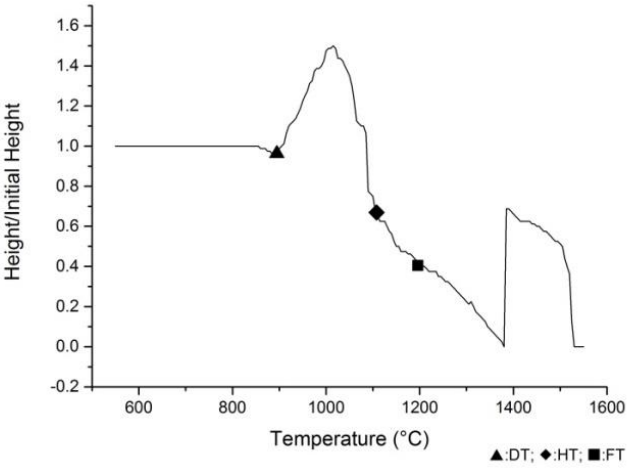
Height/Initial Height
1.6
1.4
1.2
1.0
0.8
0.6
0.4
0.2
0.0
-0.2
600
800
1000
1200
1400
1600
Temperature (°C)
▲:DT; ◆:HT; ■:FT

(d)

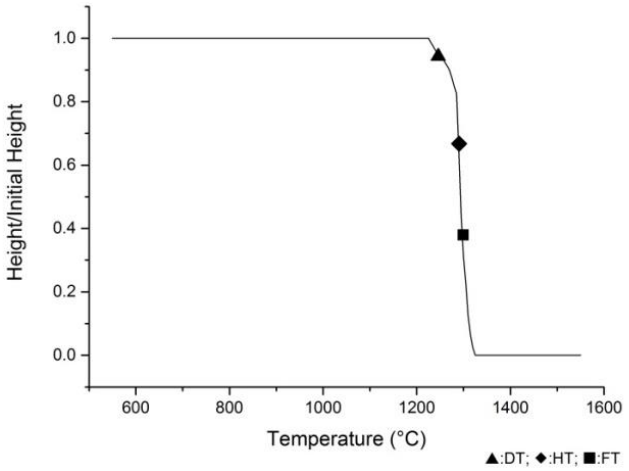
Height/Initial Height
1.0
0.8
0.6
0.4
0.2
0.0
600
800
1000
1200
1400
1600
Temperature (°C)
▲:DT; ◆:HT; ■:FT

(e)

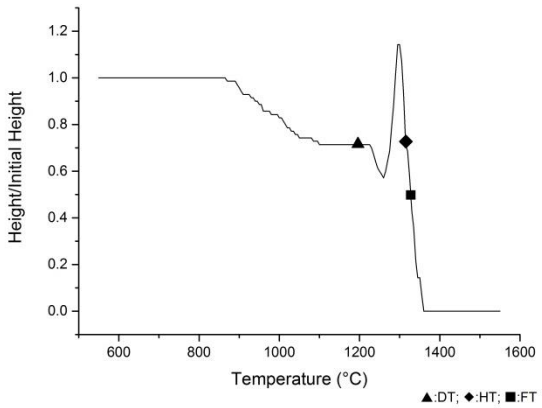
Height/Initial Height
Temperature (°C)
▲:DT; ◆:HT; ■:FT

(f)

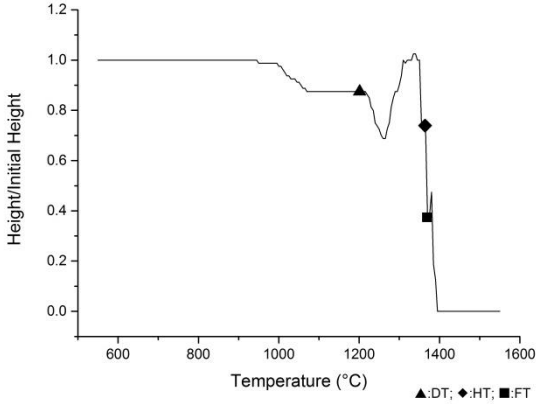
Height/Initial Height
Temperature (°C)
▲:DT; ◆:HT; ■:FT

(g)

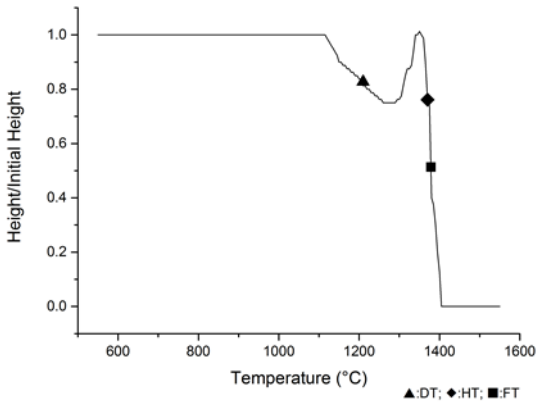
Height/Initial Height
Temperature (°C)
▲:DT; ◆:HT; ■:FT

(h)

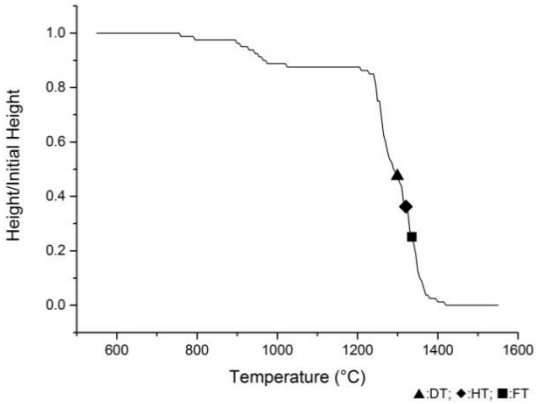
Height/Initial Height
Temperature (°C)
▲:DT; ◆:HT; ■:FT

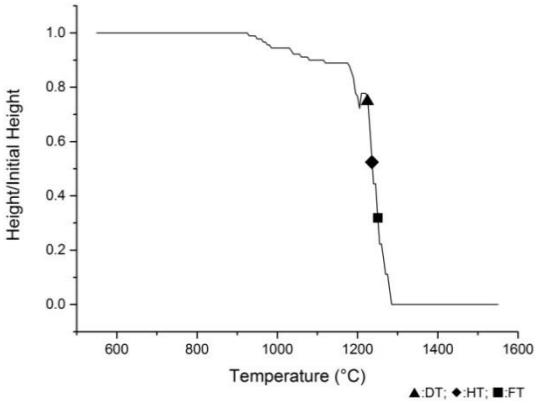
Height/Initial Height
Temperature (°C)
▲:DT; ◆:HT; ■:FT

(j)

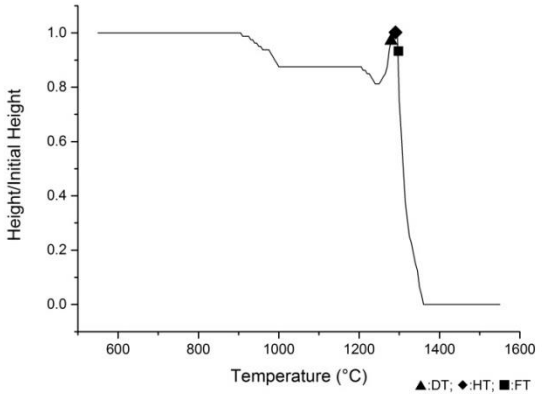
Height/Initial Height
Temperature (°C)
▲:DT; ◆:HT; ■:FT

(k)

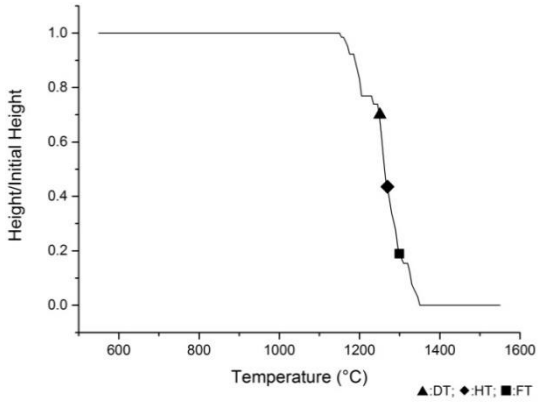
Height/Initial Height
Temperature (°C)
▲:DT; ◆:HT; ■:FT

(l)

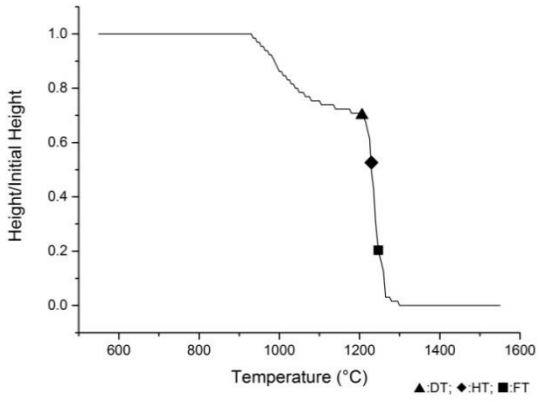
Height/Initial Height
Temperature (°C)
▲:DT; ◆:HT; ■:FT

(m)

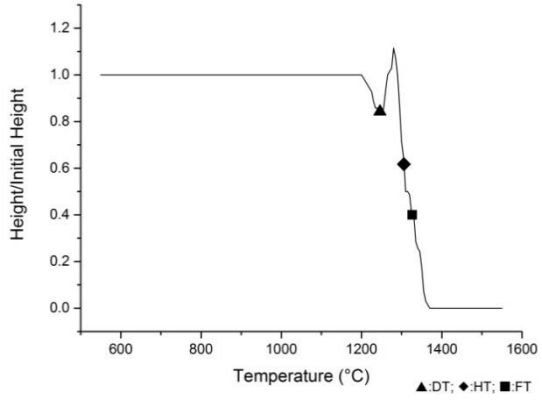
Height/Initial Height
Temperature (°C)
▲:DT; ◆:HT; ■:FT

(n)

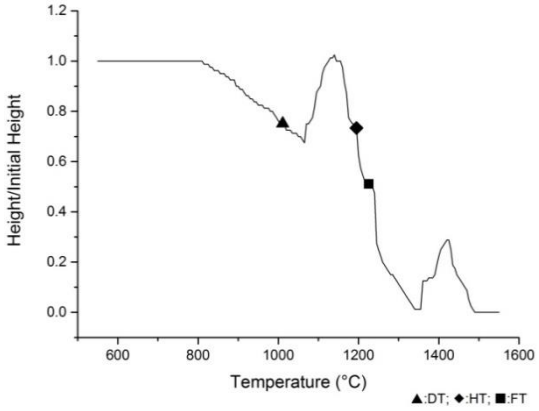
Height/Initial Height
Temperature (°C)
▲:DT; ◆:HT; ■:FT

(o)

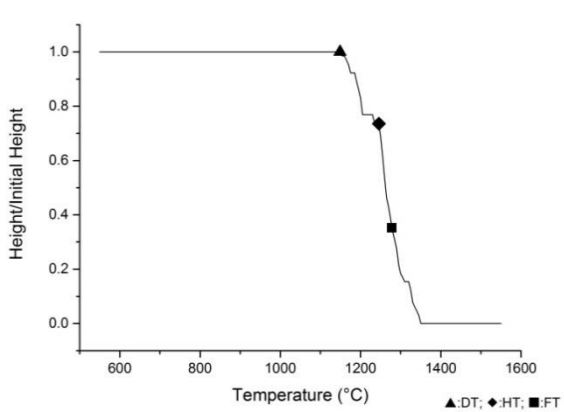
Height/Initial Height
Temperature (°C)
▲:DT; ◆:HT; ■:FT

(p)

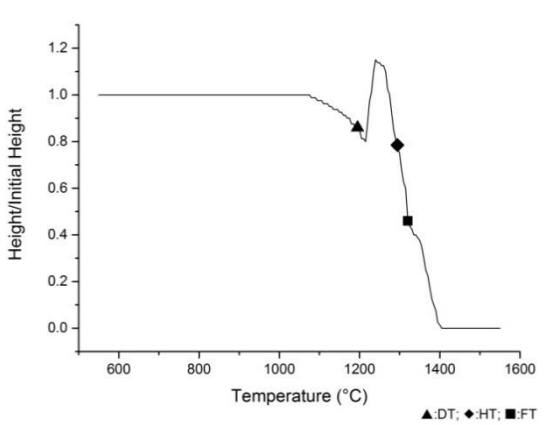
Height/Initial Height
Temperature (°C)
▲:DT; ◆:HT; ■:FT

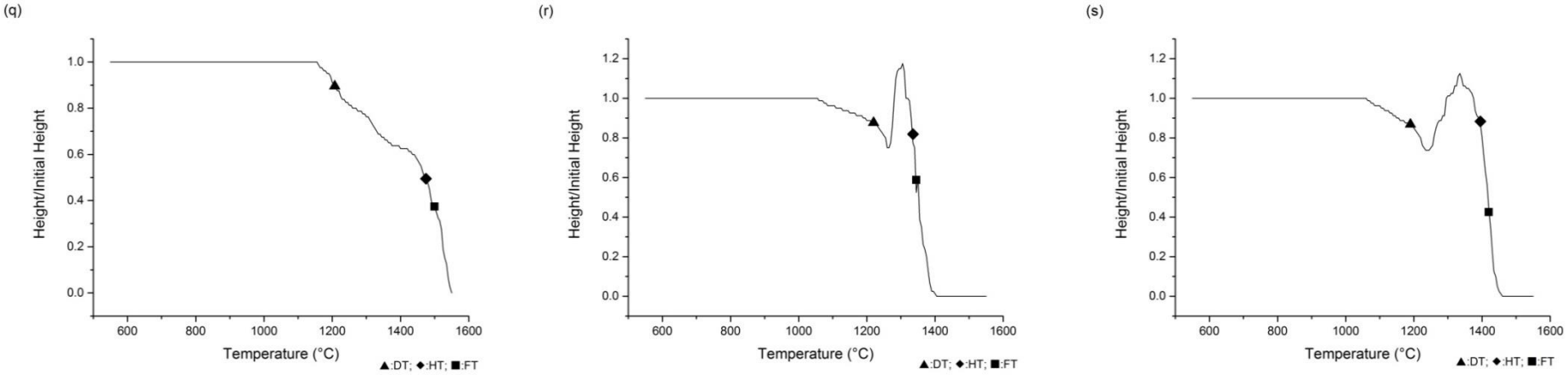

Figure 5.2 Relative deformation of test pieces for different ash during the ash fusion test: (a)-PPA1; (b)-PPA2; (c)-WS1; (d)-WWP1; (e)-PCC1; (f)-PCC2; (g)-PCC3; (h)-CA82; (i)-CA55; (j)-CA28; (k)-BFPC82; (l)-BFPC55; (m)-BFPC28; (n)-BWCA82; (o)-BWCA55; (p)-BWCA28; (q)-CFA2; (r)-CBA12; (s)-CBA22.

5.2 Melting behaviour by simultaneous thermal analysis

A subset of ash samples were also analyzed by using a Netzsch STA (Simultaneous thermal analysis) 449C Jupiter®, coupled to a Netzsch QMS 403C Aeolos Quadrupole Mass Spectrometer. Simultaneous thermal analysis involves the simultaneous application of thermogravimetry (TG) (which measures sample weight loss in a controlled temperature program) and differential thermal analysis (DTA) (which monitors the temperature difference between the sample and an inert reference material). About 10 mg of ash was heated from 30 to 1400℃ at 10℃/min in 12.5% O_2/He. Evolving volatiles were transferred directly into the electron impact ion source of the MS via a heated fused silica capillary. Mass-to-charge ratios (m/z) of monitored gas species were H_2O (m/z 18), C (m/z 12), CO (m/z 28), CO_2 (m/z 44), K (m/z 39), Cl (m/z 35), SO_2 (m/z 64) and KCl (m/z 74). Calibration of temperature and sensitivity was performed according to the standard melting points of five metals (indium, tin, bismuth, zinc and gold), and a buoyancy correction was also applied at the same heating conditions. Ash samples used here were the same samples prepared for ash fusion test.

Plots showing the mass loss upon heating of ash samples in the STA, alongside the corresponding DTA curves and gas evolution profiles are presented in **Figure 5.3** as (a)-PPA1; (b)-PPA2; (c)-WS1; (d)-WWP1; (e)-PCC1; (f)-PCC2; (g)-PCC3; (h)-CA82; (i)-CA55; (j)-CA28; (k)-BFPC82; (l)-BFPC55; (m)-BFPC28; (n)-BWCA82; (o)-BWCA55; (p)-BWCA28; (q)-CFA1; (r)-CFA2; (s)-CBA11; (t)-CBA12; (u)-CBA21; (v)-CBA22 respectively. The mass loss curves are complex with gradual mass losses up to

the final temperature of 1400℃. Melting in the STA is characterized by the DTA curve becoming endothermic from temperatures at and above the deformation temperature.. Comparisons of the endothermic portion of the DTA curve with characteristic AFT temperatures: deformation (DT), hemispherical (HT), and flow temperatures (FT) are marked in **Figure 5.3**, and values are given in **Table 5.1**. In most ash samples the temperatures for the start of melting (as detected by STA) are lower than the deformation temperatures observed in the standard ash fusion test.

For the pine ash (**Figure 5.3 (a)~(b)**), the AFT hemisphere and flow temperatures are closer and are much higher than its deformation temperature. The low temperature pine ash (PPA1) shows peaks for the evolution of CO_2 and CO, which reach a maximum as the temperature approaches the deformation temperature. Compare to PPA1, the high temperature pine ash (PPA2) shows less evolution of CO_2 and CO, which attribute to the removed carbon process with temperature increasing of combustion.

Both of the wheat straw ash (**Figure 5.3 (c)**) and white wood pellet ash (**Figure 5.3 (d)**) show peaks for the evolution of CO_2 due to combustion of unburned carbon. They also show evidence for sulphate decomposition at high temperature.

Figure 5.3 (e)~(g) show the evolution profiles for CO_2, CO, SO_2 and H_2O from the melting of the low temperature coal ash. Moreover, it can be observed that SO_2 evolves at much lower temperatures than the AFT deformation temperature. Similar evolution profiles were observed for the PCC2 and PCC3 ash, which are high temperature ashes, and as such it resulted in lower peak intensity for SO_2 than the

lower temperature coal ash.

Comparison of the pine and El Cerrejon coal 1 ash blends in **Figure 5.3 (h)~(j)** with the ash from the fuel blends in **Figure 5.3 (k)~(m)**, the TGA and DTA curves are very similar to the PPA1 **in Figure 5.3 (a)**, as the ratio of pine increases, but the HT and FT are much closer together and higher than the results from DTA curve. In general, the ash blends with high pine ash ratio show higher fusion temperatures than the high coal ash blends. The behaviour of the 50/50 fuel ratio ash in **Figure 5.3 (i)** is interesting as it results in the lowest characteristic temperatures. The peak for the SO_2 emission shifts to lower temperatures as the El Cerrejon coal 1 ash content in the blend is increase.

Comparison of the wheat straw and El Cerrejon coal 2 blending fuel ash in **Figure 5.3 (n)~(p)** with the ash from the fuel blends (not shown here), indicates that the TGA and DTA curves are very similar to the WS1 **in Figure 5.3 (c)**, as the ratio of straw increases, but the HT and FT are much closer together and higher and the endotherm peak from DTA curve. In general, the blending fuel ash with high straw ash ratio show lower fusion temperatures than the high coal ash blends.

Comparison of original pilot scale test ash and re-burned pilot scale test ash is given in **Figure 5.3 (q)~(v)**. The CFA1, CBA11 and CBA21 show more significant weight loss at around 600°C due to carbon combustion with peaks for the evolution of CO_2 and CO (and water). After 1000°C, the endotherm curves show similar trends in both CFA1 and CFA2 where no gas evolution is detected. The endotherm peaks disappear in CBA11 and CBA21, but they can be observed in CBA12 and CBA22. In **Figure**

5.3 (r), **(t)** and **(v)**, the DTA endotherm curves show more similarity PCC3 (**Figure 5.3 (g)**).

Baxter et al. [191], who used the STA-MS method to characterise biomass ash, found a correlation between the AFT hemisphere temperature and the endotherm (DTA) peak temperatures for Miscanthus ash samples. In **Figure 5.4** the data from the fuel ash and ash blends studied were plotted alongside data from Baxter et al [191]. for comparison purposes. It can be observed that most of the ash samples studied here show higher HT values than the endothermic peak temperature estimated from the STA with the exception of fuel blend ash BFPC82, wheat straw ash (WS1) and fuel blend ash BWCA82, for which both temperatures are close.

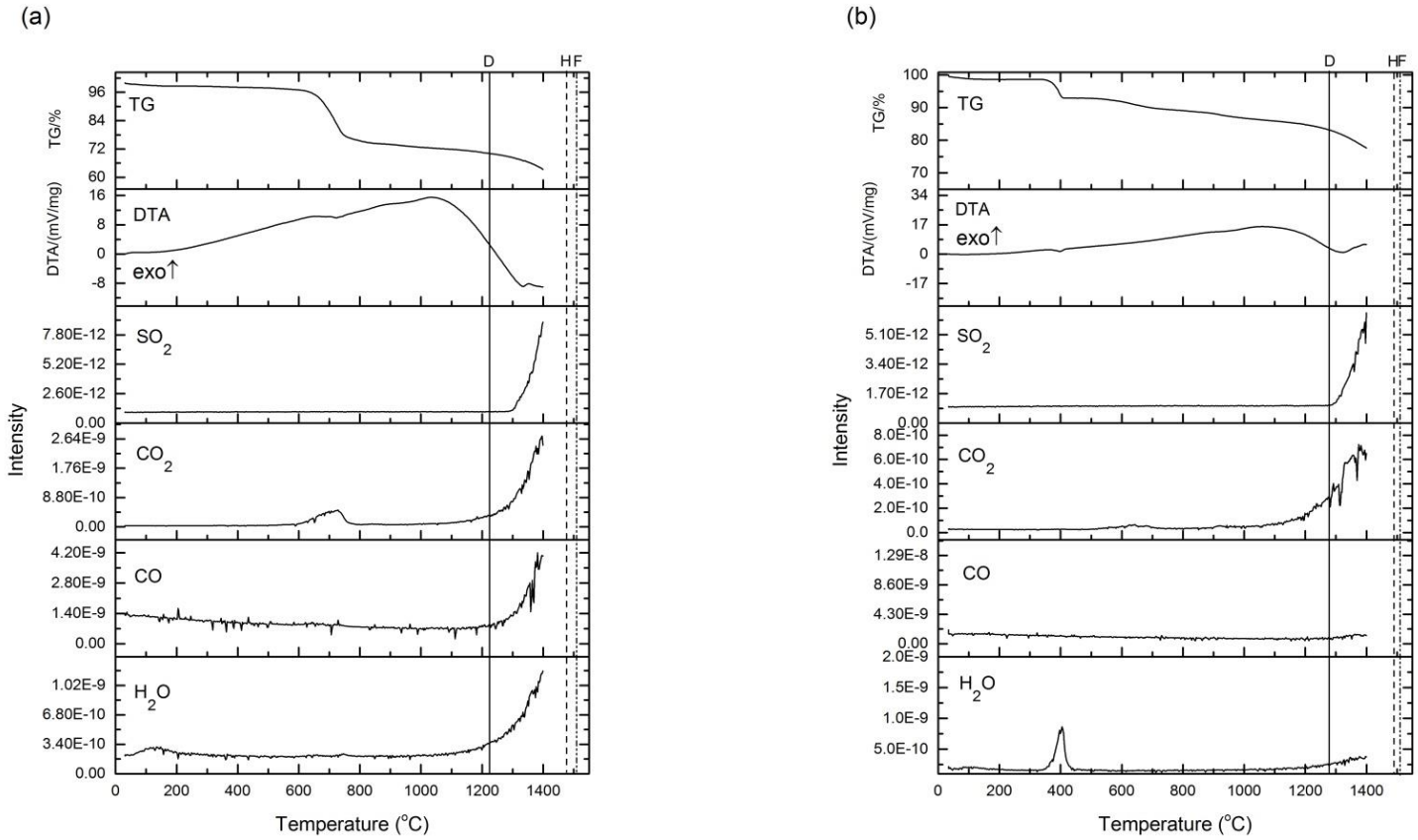
(a)
(b)
D
HF
TG
TG/%
DTA
DTA/(mV/mg)
exo↑
SO2
CO2
CO
H2O
Intensity
Temperature (°C)

(c)

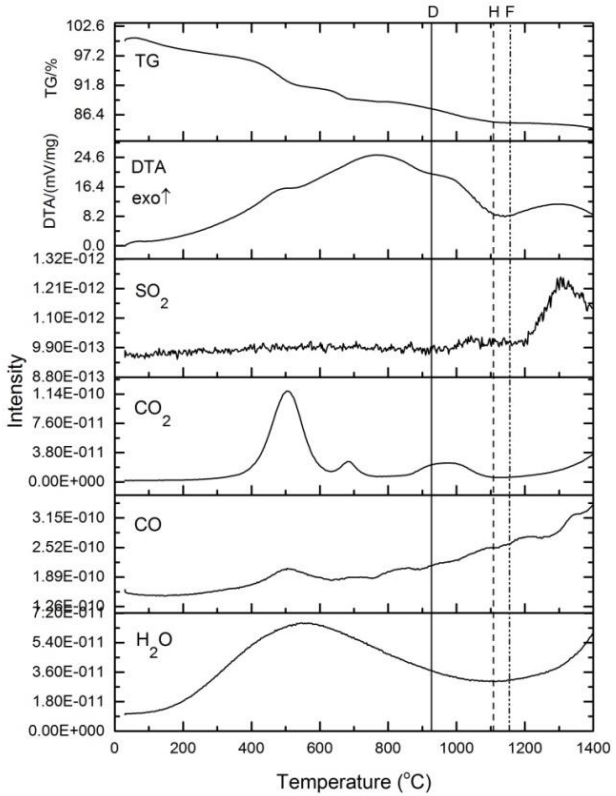
D
H F
TG/%
102.6
97.2
91.8
86.4
TG
DTA/(mV/mg)
24.6
16.4
8.2
0.0
DTA
exo↑
1.32E-012
1.21E-012
1.10E-012
9.90E-013
8.80E-013
SO2
1.14E-010
7.60E-011
3.80E-011
0.00E+000
CO2
3.15E-010
2.52E-010
1.89E-010
CO
5.40E-011
3.60E-011
1.80E-011
0.00E+000
H2O
Intensity
0
200
400
600
800
1000
1200
1400
Temperature (°C)

(d)

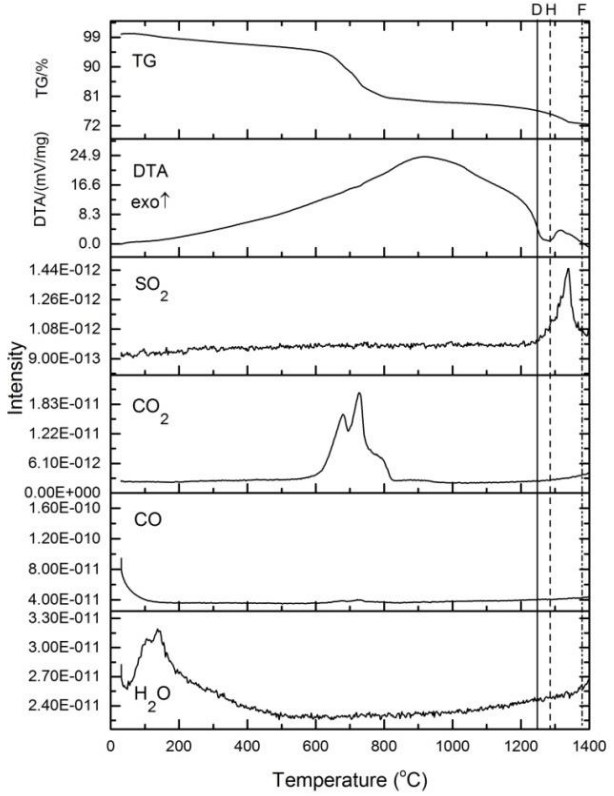
D H
F
TG/%
99
90
81
72
TG
DTA/(mV/mg)
24.9
16.6
8.3
0.0
DTA
exo↑
1.44E-012
1.26E-012
1.08E-012
9.00E-013
SO2
1.83E-011
1.22E-011
6.10E-012
0.00E+000
CO2
1.60E-010
1.20E-010
8.00E-011
4.00E-011
CO
3.30E-011
3.00E-011
2.70E-011
2.40E-011
H2O
Intensity
0
200
400
600
800
1000
1200
1400
Temperature (°C)

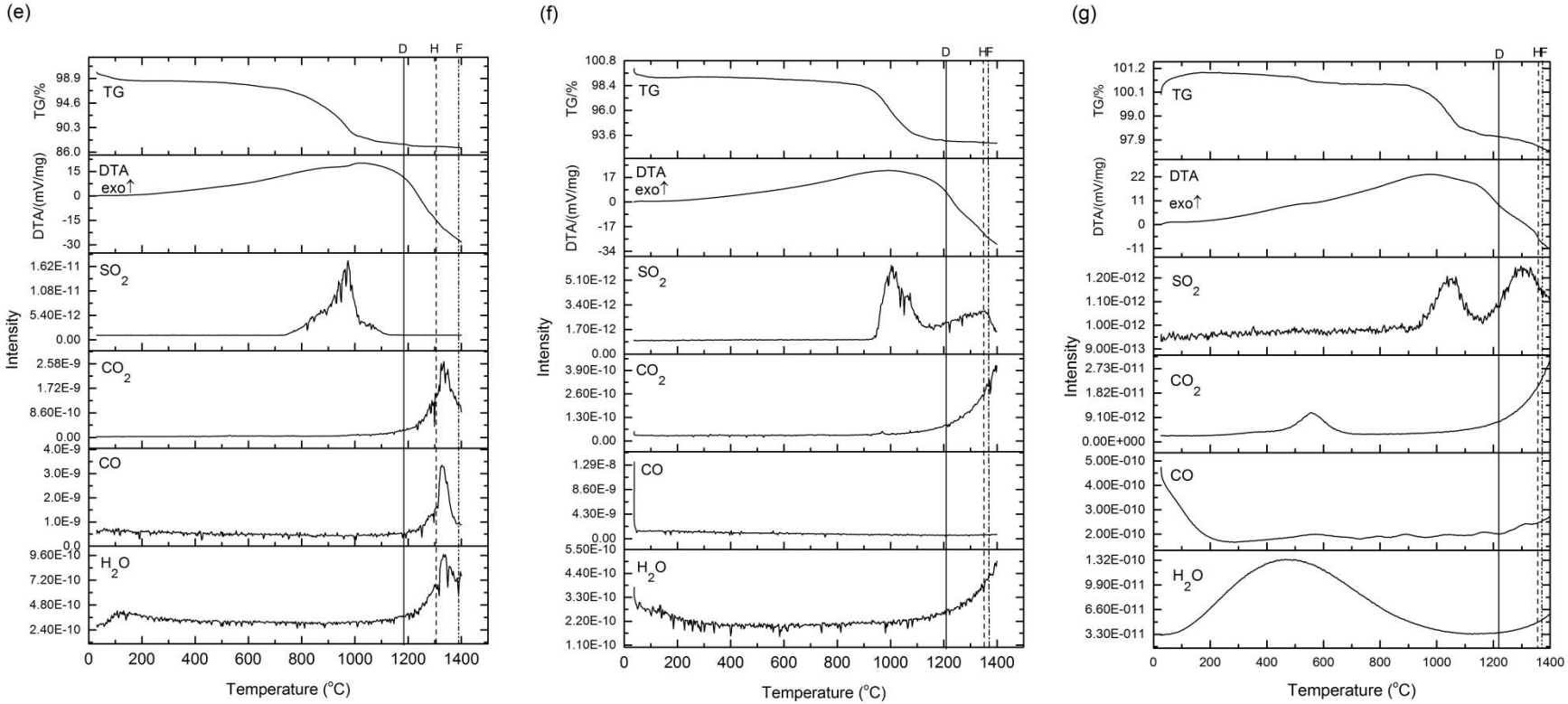
(e)
(f)
(g)
D
H
F
TG/%
TG
DTA/(mV/mg)
DTA
exo↑
Intensity
SO2
CO2
CO
H2O
Temperature (°C)

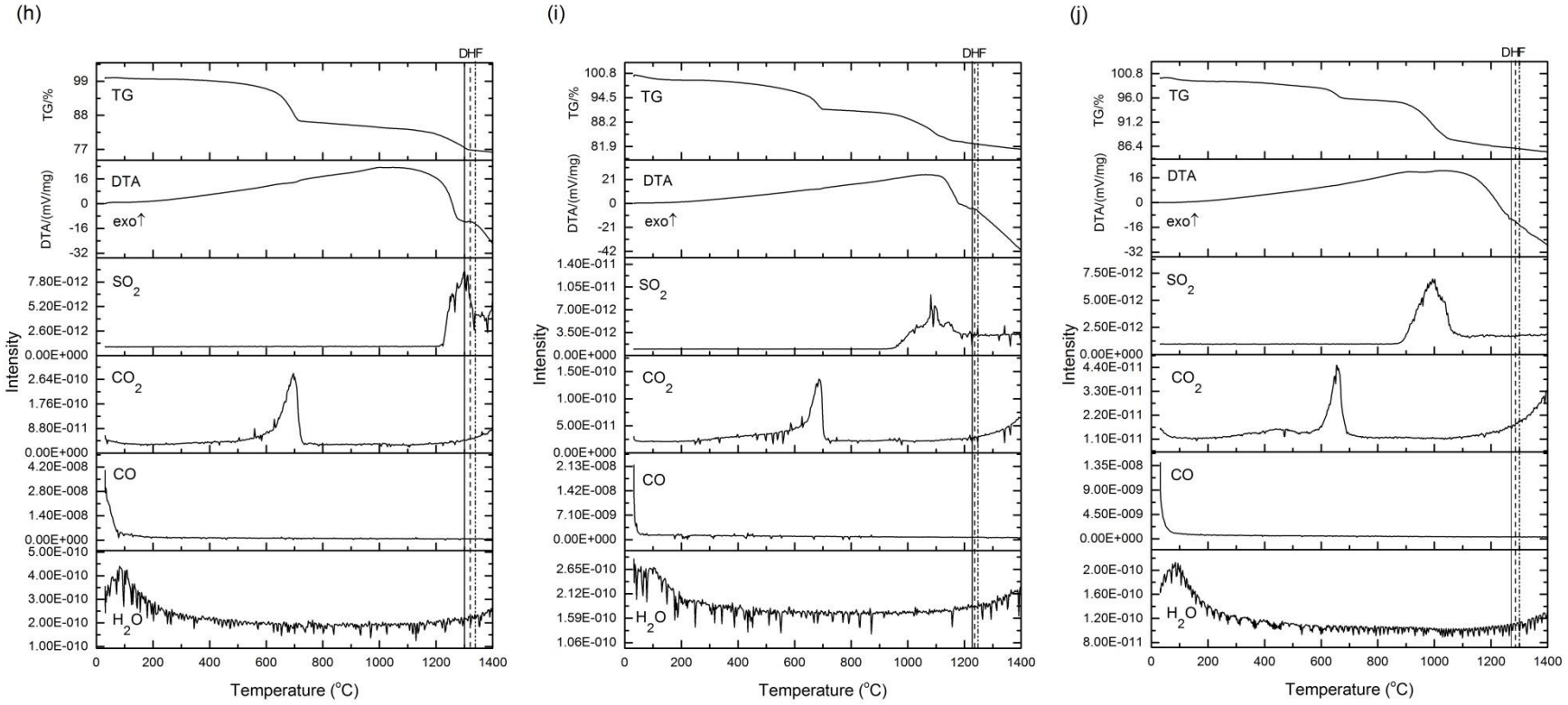
(h)
(i)
(j)
DHF
TG
TG/%
DTA
DTA/(mV/mg)
exo↑
SO2
CO2
CO
H2O
Intensity
Temperature (°C)

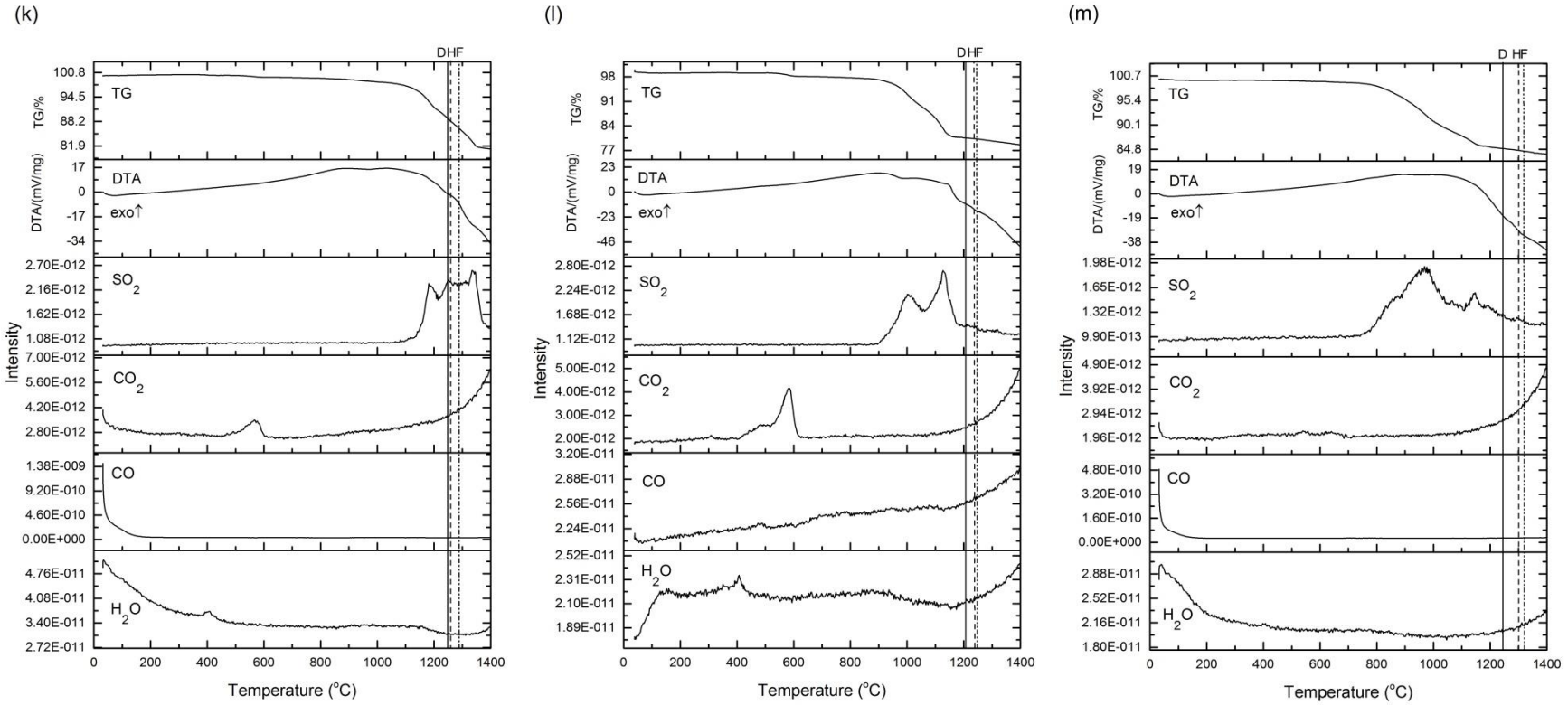
(k)
(l)
(m)
D
HF
TG
TG/%
DTA
DTA/(mV/mg)
exo↑
SO2
CO2
CO
H2O
Intensity
Temperature (°C)

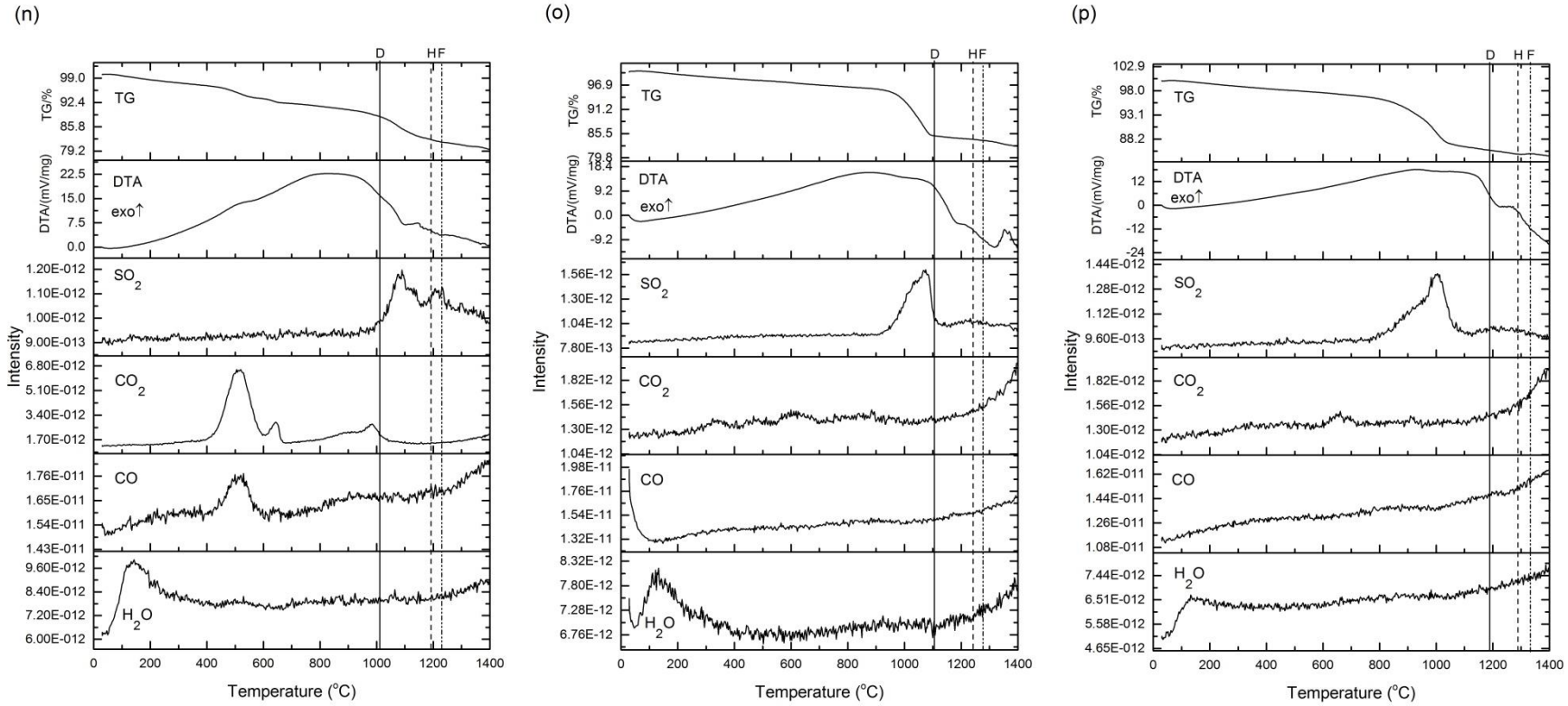
(n)
(o)
(p)
D
HF
TG
TG/%
DTA
exo↑
DTA/(mV/mg)
SO2
CO2
CO
H2O
Intensity
Temperature (°C)

(q)

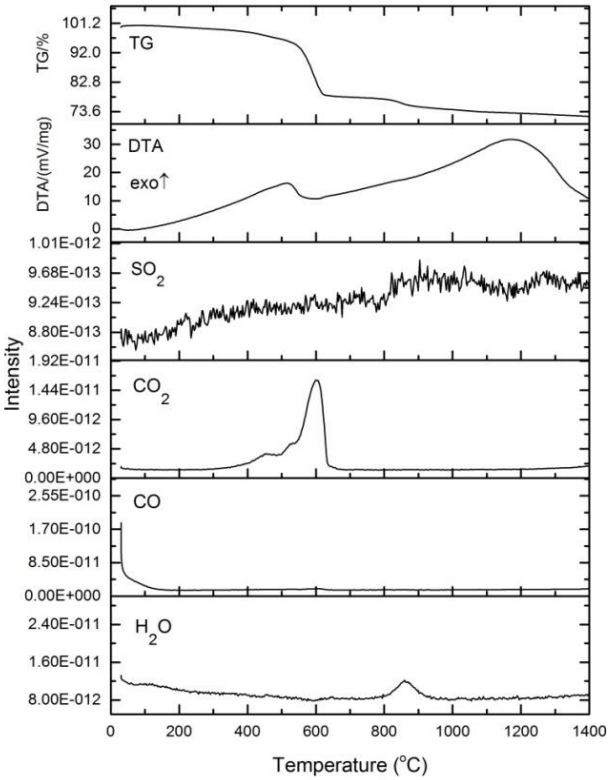
TG/%
101.2
92.0
82.8
73.6
TG
DTA/(mV/mg)
30
20
10
0
DTA
exo↑
1.01E-012
9.68E-013
9.24E-013
8.80E-013
SO2
1.92E-011
1.44E-011
9.60E-012
4.80E-012
0.00E+000
CO2
2.55E-010
1.70E-010
8.50E-011
0.00E+000
CO
2.40E-011
1.60E-011
8.00E-012
H2O
Intensity
0
200
400
600
800
1000
1200
1400
Temperature (°C)

(r)

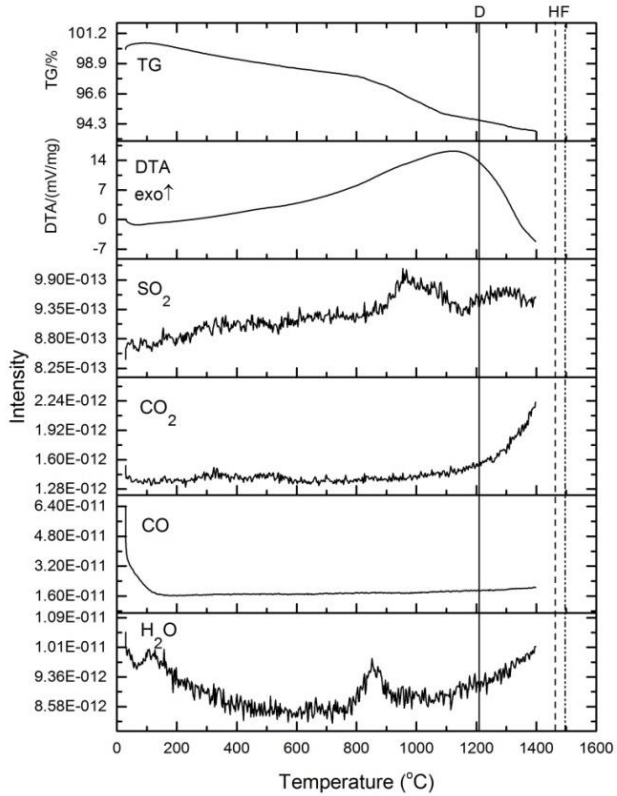
D
HF
TG/%
101.2
98.9
96.6
94.3
TG
DTA/(mV/mg)
14
7
0
-7
DTA
exo↑
9.90E-013
9.35E-013
8.80E-013
8.25E-013
SO2
2.24E-012
1.92E-012
1.60E-012
1.28E-012
CO2
6.40E-011
4.80E-011
3.20E-011
1.60E-011
CO
1.09E-011
1.01E-011
9.36E-012
8.58E-012
H2O
Intensity
0
200
400
600
800
1000
1200
1400
1600
Temperature (°C)

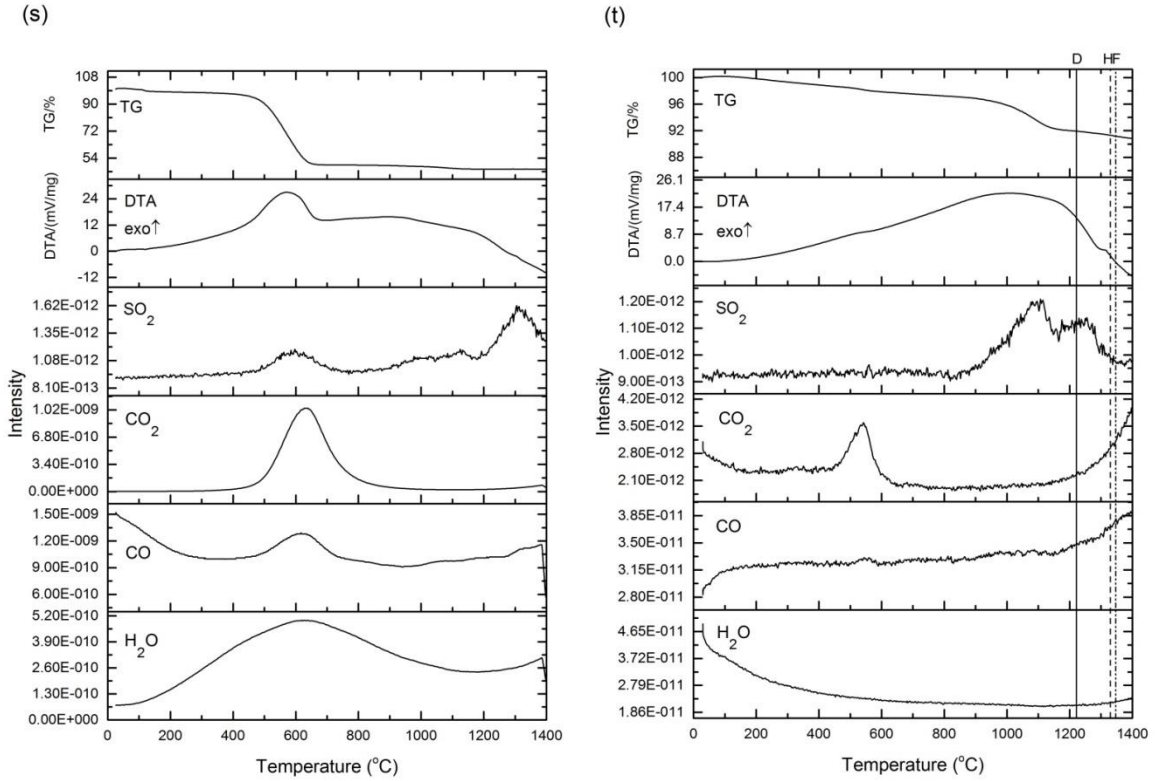
(s)
(t)
TG/%
DTA/(mV/mg)
TG
DTA
exo↑
SO2
CO2
CO
H2O
Intensity
D
HF
Temperature (°C)

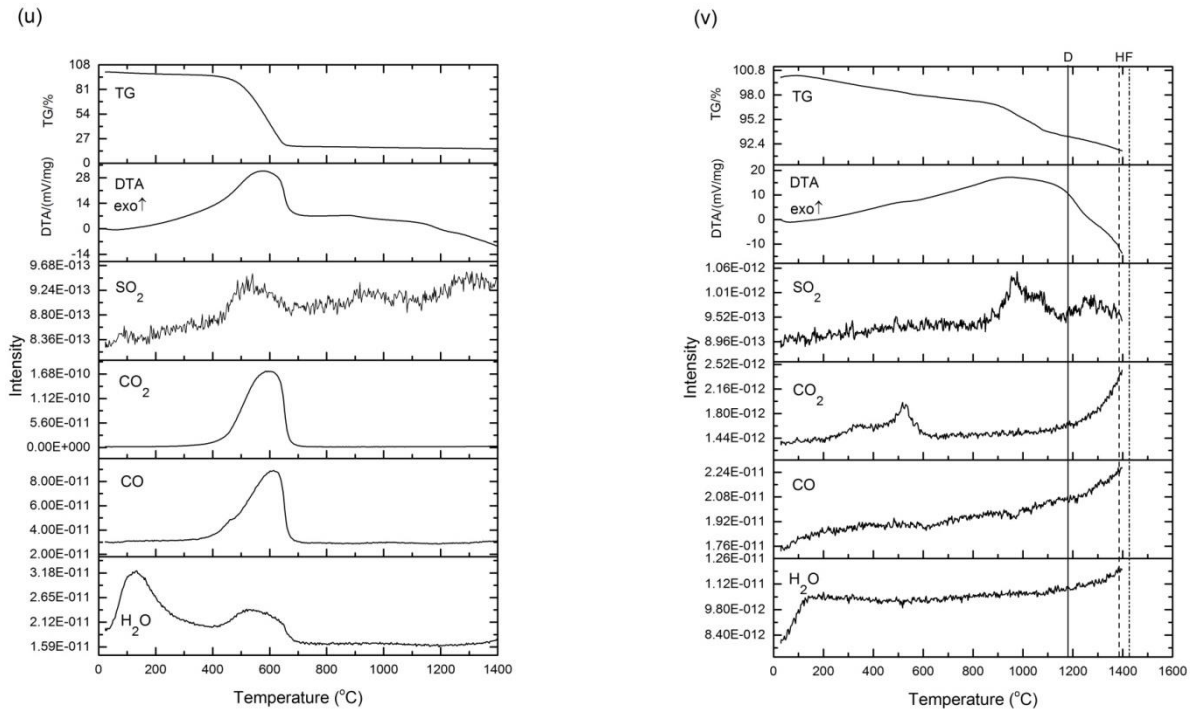

Figure 5.3 Plots of mass loss, DTA and corresponding gas evolution profiles with temperature (when heated at 10 ℃/min in 12.5% O2/He) for El Cerrejon coal, pine and blended ash samples: (a)-PPA1; (b)-PPA2; (c)-WS1; (d)-WWP1; (e)-PCC1; (f)-PCC2; (g)-PCC3; (h)-CA82; (i)-CA55; (j)-CA28; (k)-BFPC82; (l)-BFPC55; (m)-BFPC28; (n)-BWCA82; (o)-BWCA55; (p)-BWCA28; (q)-CFA1; (r)-CFA2; (s)-CBA11; (t)-CBA12; (u)-CBA21; (v)-CBA22. Refer to **Table 5.1** for sample designation. D, H, F refer to deformation, hemisphere and flow temperatures.

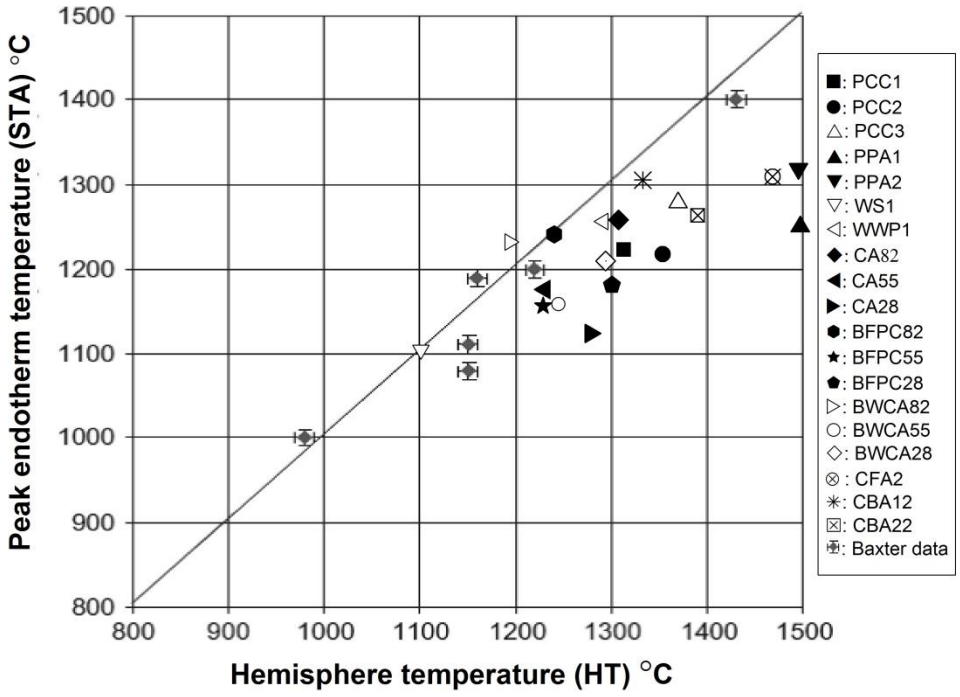

Figure 5.4 Plot of experimental hemisphere temperatures (HT) and peak endotherm temperatures (STA) for various fuels compared with the results by Baxter et al. [192].

5.3 Summaries

The ash fusion characteristics of a range coal and biomass ashes and their blends have been determined. High carbon in ash can make determination of characteristic temperatures difficult due to excessive release of gas causing swelling and even breaking of the ash test pieces. STA-MS can easily identify those samples high in carbon from detection of both rapid weight loss at 600°C and evolution of CO, CO_2 and H_2O. Of the fuels studied (El Cerrejon coal (2 batches), pine, wheat straw, white wood pellets), wheat straw has the lowest fusion temperature and acts to lower the melting temperature of ash when blended with El Cerrejon coal. Pine has the highest

fusion temperature and increases the melting temperature of ash when blended with the coal. Ash produced in pilot scale combustion (of the coal) had very high C in ash and required an ashing step in the laboratory prior to study. These ashes had different fusion characteristics (generally) than the laboratory prepared ashes, possibly due to ash fractionation in the high temperature combustion tests.

Chapter 6 The Prediction of Ash Fouling and Slagging Potential

Slagging refers to molten ash deposition in the furnace region of the boiler where heat transfer is predominantly by radiation [194], while fouling can occur in the convective section of the boiler [195-196]. Ash fusion temperature, ash particle viscosity and ash chemistry are the three most widely used bases for characterizing coal ash deposition and slagging [194]. Most of the existing coal slagging indices use laboratory ash to measure the properties of interest [197], and since they have been established for particular types of coal properties, their use is not necessarily reliable when extended to other types of coal and biomass [198].

One of the aims of this work is to establish whether deposition during co-firing shows the behaviour of two single ashes or a mixture of ash. In particular, the complex chemical nature of the inorganic components of the biomass may result in an increased slagging tendency [199]. Also, biomass has a higher volatile matter and oxygen content and a lower density, ash content and heating value than coal. Therefore, an in-depth understanding of the characteristics of the blended fuels including their deposition tendency is necessary in order to help achieve optimum co-firing efficiency and minimise maintenance costs [200].

Although the ash loading from the biomass may be low compared to that of coal, the composition of the mineral matter within the biomass ash is as broad as that of coal ash and thus creates complex slagging and fouling behaviour. Moreover, it is believed

that the lack of knowledge of the co-firing combustion conditions, as well as the fuel and ash compositions of the biomass fuels, results in poor slagging predictions. Hence, it is a prerequisite to understand the fuel properties and ash behaviour of the coal, biomass and their blends, together with the combustion conditions and potential chemical interactions, before the development of a reliable co-firing slagging tool [201].

6.1 Numerical indices of slagging and fouling

The alkali index was calculated from the quantity of alkali oxides in the fuel per unit of fuel energy (kg alkali/GJ) as given in **Equation 6.1**:

$$AI = \frac{K_2O+Na_2O}{HHV} \text{ (kg/GJ)} \quad (\mathbf{6.1})$$

When the alkali index values are in the range 0.17–0.34 kg/GJ fouling or slagging is considered probable, when these values are greater than 0.34 this indicates that fouling or slagging is virtually certain to occur. [202]

For bituminous coal ashes, the base-to-acid ratio is also an indicator of deposition tendency [197] and can be calculated by the following equation:

$$R_{b/a} = \frac{Fe_2O_3+CaO+MgO+K_2O+Na_2O}{SiO_2+TiO_2+Al_2O_3} \quad (\mathbf{6.2})$$

where each oxide is represented by the mass fraction in the ash (%). As $R_{b/a}$ increases, the fouling tendency of a fuel ash increases. When $R_{b/a}$ <0.5, the fuel shows a low slagging propensity, if 0.5< $R_{b/a}$ <1.0, the fuel shows a medium slagging propensity; when $R_{b/a}$ >1.0, the slagging propensity of the fuel is very high. **Equation 6.2** was

originally developed for use with bituminous coals not biomass. There has been some success in the prediction of slag formation with the use of $R_{b/a}$ or just base percentage for biomass. In a study by Li.et.al [203], this equation was used to evaluate biomass ash slagging tendency, and $R_{b/a}$ has some reciprocal relationship to the deformation temperature. Consequently this equation has been chosen to predict the ash slagging potential from biomass, coal and their blends in this study. The reliability of $R_{b/a}$ for biomass ash and blends will be compared with other methods.

According to McLennen [194], the slagging index (F_S) is based on the initial deformation temperature (IDT) and hemisphere temperature (HT) observed during ash fusion tests, and it is also employed in this investigation to analyse the slagging propensity of the ash samples. The index is defined as:

$$F_S = \frac{4IDT+HT}{5} \ (℃) \qquad \textbf{(6.3)}$$

In this approach, an ash is classified as having a boiler slagging propensity which is low when F_S>1343 ℃; medium when 1232 ℃ <F_S< 1343 ℃; high when 1149 ℃< F_S <1232 ℃; and severe when F_S < 1149 ℃.

For blends with less than 20% biomass, the ash mixture remains predominantly an alumino-silicate, and the pure coal slagging index can be used with caution to predict the slagging potential of such blends [201, 204]. A number of empirical indices which can explain the fouling and slagging behaviour of coals, to some extent, can be found in the literature [130]. In previous studies from Degereji [205, 206], the coal numerical slagging index (Sx) was developed for predicting co-firing slagging

propensity as **Equation 6.4**. A description of the calculation of viscosity, μ, is given in **Section 6.2**.

$$Sx = \gamma/\mathrm{Log}(\mu) \quad \textbf{(6.4)}$$

For pure biomass and coal combustion, the mass of the incoming ash (γ) can be calculated by the ash content and the heating value of the individual fuels as follows:

$$\gamma = \frac{\text{Ash content per kg}}{\text{CV (MJ/kg)}} \quad \textbf{(6.5)}$$

For co-firing, the incoming mass of ash blends and blending fuel ash can be defined by **Equation 6.6**, where x, y, γ_c and γ_b are the ratio of the coal in the blend, the ratio of the biomass in the blend, the mass of the coal ash and the mass of the biomass ash, respectively.

$$\gamma = x\gamma_c + y\gamma_b \quad \textbf{(6.6)}$$

Table 6.1 lists the major components of the ash samples (see **Table 3.3~Table 3.6** in **Chapter 3** for sample designation). The ash samples compositions were determined by WCA, and the ash compositions for the fuel blends were determined by XRF as described earlier (see **Table 4.5~Table 4.7** in **Chapter 4**). For the ash blends, their composition was calculated from the fuel ash compositions according to their ash blending ratio. The slagging and fouling indices are listed in **Table 6.1** and **Figure 6.1~Figure 6.3** are plots of different numerical indices results for different samples.

Table 6.1 The calculation of slagging and fouling index.

Samples	[1]AI	[2]B/A	[3]F_s(°C)	[4]Sx
PPA1	0.15	14.16	1276	-0.38
PAA2	0.17	17.33	1327	-0.38
WS1	0.64	0.50	961	0.55
WS2	0.56	0.69	N/A	0.88
WWP1	0.10	1.51	1254	0.66
WWP2	0.12	1.94	N/A	2.25
PCC1	0.04	0.33	1219	0.65
PCC2	0.04	0.33	1236	0.59
PCC3	0.04	0.31	1322	0.39
CA82	0.12	1.89	1232	1.06
CA55	0.09	0.75	1191	0.43
CA28	0.06	0.44	1254	0.50
BFPC82	0.14	2.23	1209	3.57
BFPC55	0.10	0.90	1066	0.55
BFPC28	0.06	0.49	1228	0.58
BWCA82	0.50	0.49	1047	0.20
BWCA55	0.27	0.42	1169	0.34
BWCA28	0.09	0.34	1215	0.39
CFA1	3.74	0.94	N/A	128.3
CFA2	3.90	1.22	1259	96.1
CBA11	0.81	0.32	N/A	261.7
CBA12	0.84	0.48	1243	43.1
CBA21	0.17	0.34	N/A	-45.1
CBA22	0.14	0.37	1231	3.5

[1]: calculated by Equation 6.1; [2]: calculated by Equation 6.2; [3]: calculated by Equation 6.3; [4]: calculated by Equation 6.4.

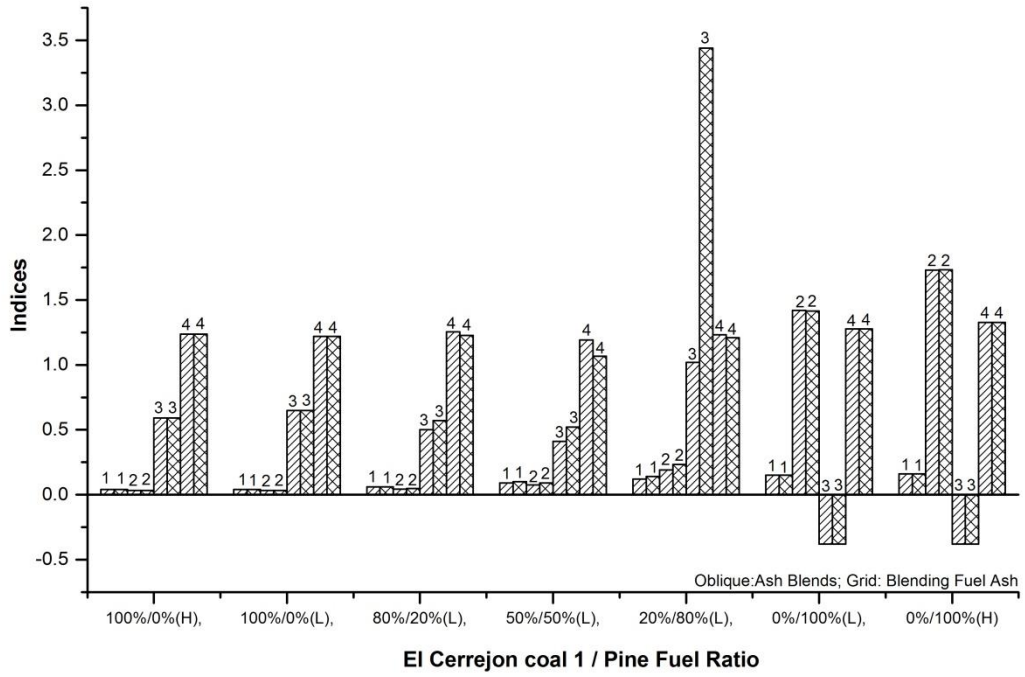

Figure 6.1 Values for different numerical indices at various El Cerrejon coal 1/pine ratios, with ashing temperatures: (H)-800 ℃; (L)-550 ℃. Indices: 1, AI Kg/GJ; 2: $R_{b/a}$ /10; 3: Sx; 4: Fs/1000 (℃). Oblique-lined fill signifies ash produced by blending the fuels then ashing; Hatched fill signifies blended fuel ash (ash produced separately then blended).

The calculated AI indices for all El Cerrejon coal 1/pine fuel ratios are similar for both methods of ash preparation and indicate that all the fuels studied have low fouling potential. However, the calculated base-to- acid ratio, ($R_{b/a}$), indicates that 100% pine ash has high slagging potential, which is not observed in the ash fusion test. The low temperature coal ash PCC1 and the high temperature coal ash PCC2 show low slagging potential. For the ash blends of El Cerrejon coal 1 and pine, increasing the biomass ratio from 20 to 80% increased the ash slagging potential from low to high. In the case of the ash from the fuel blends, a similar trend was also observed BFPC82, which is predicted to have a high slagging propensity; increasing the coal content decreased the slagging

propensity: BFPC55 shows medium slagging propensity and BFPC28 low slagging propensity.

The calculated Fs slagging indices predict that both pure pine ashes (prepared at 550 ℃ (PPA1) and at 800 ℃ (PPA2)) would have low slagging propensities. The El Cerrejon coal 1 ash PCC1 and PCC2 are predicted to have medium slagging potential. However, different predictions for both types of ash blends are obtained from the Rb/a, where the fuel blend ashes, CA55 and BFPC55 show a high slagging propensity according to the AFT. The other ash blends (CA82, CA28, BFPC82 and BFPC28) show high slagging potential.

The calculated values of Sx (at the shrinkage starting temperature, SST) show that because the total amount of ash decreases with the increase of pine ratio as shown in **Figure 6.1**, the slagging potential decreases slowly from 100% coal to 50% coal and 50% biomass. A distinctive feature is a sharp increase when the pine is 80% of the blend. With pure pine the value of Sx shows the lowest slagging potential based on this index. Possibly this refects the crossover point of the Al_2O_3 and K_2O concentrations in the ash.

In **Figure 6.2**, the calculated AI indices for El Cerrejon coal 2 (PCC3) indicates low fouling potential which is similar to El Cerrejon coal 1. In contrast, the wheat straw shows a high fouling potential by AI. As the straw ratio increases the AI indicates an increasing trend. There is low fouling potential for 80% coal/ 20% straw; medium fouling potential for 50% coal/20% straw and high fouling potential for 20% coal/ 80% straw. However, the calculated base-to- acid ratio, ($R_{b/a}$), indicates that 100% wheat straw ash has medium slagging potential, which is not observed in the ash fusion test. The 800°C El Cerrejon coal 2 ash (PCC3) shows low slagging potential which is similar to the two temperatures El Cerrejon coal 1 ashes. For the fuel blends ashes, $R_{b/a}$ indicates high slagging potential for all the BWCA28, BWCA55 and BWCA82 ashes.

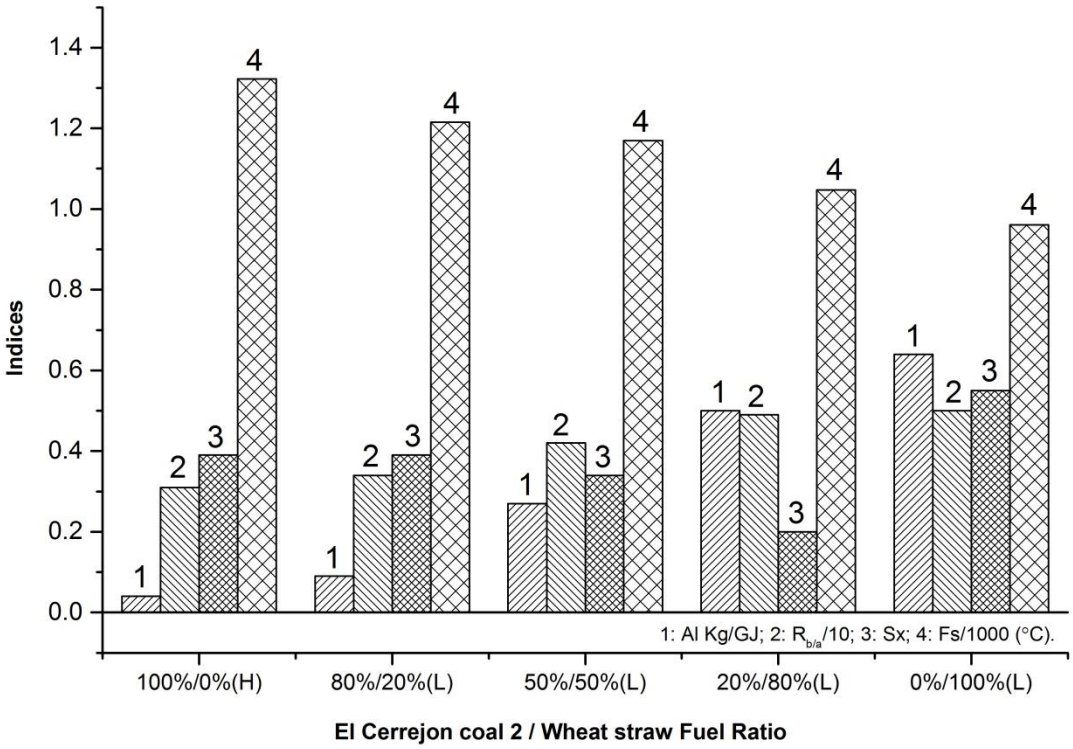

Figure 6.2 Values for different numerical indices at various El Cerrejon coal 2/wheat straw ratios, with ashing temperatures: (H)-800 ℃; (L)-550 ℃. Indices: 1, AI Kg/GJ; 2: $R_{b/a}$/10; 3: Sx; 4: Fs/1000 (℃).

In **Figure 6.2**, the calculated Fs slagging indices predict that wheat straw ash prepared at low temperature (prepared at 550 ℃ (WS1)) would have severe slagging propensity. The El Cerrejon coal 2 ash (prepared at 800 ℃ (PCC3)) is predicted to have medium slagging potential. However, different predictions for fuel blends ashes are obtained from the Rb/a, where the BWCA82 show a severe slagging propensity according to the AFT. The other fuel blends ashes (BWCA28 and BWCA55) show high slagging potential.

The calculated values of Sx (at the shrinkage starting temperature, SST) show that because the total amount of ash decreases with the increase of wheat straw ratio as shown in **Figure 6.2**, the slagging potential decreases slowly from 100% coal to 20%

coal and 80% straw. A distinctive feature is a sharp increase when the straw is 100%. According to **Table 6.1**, with high temperature pure wheat straw ash (prepared at 800 ℃ (WS2)), the value of Sx shows the highest slagging potential based on this index.

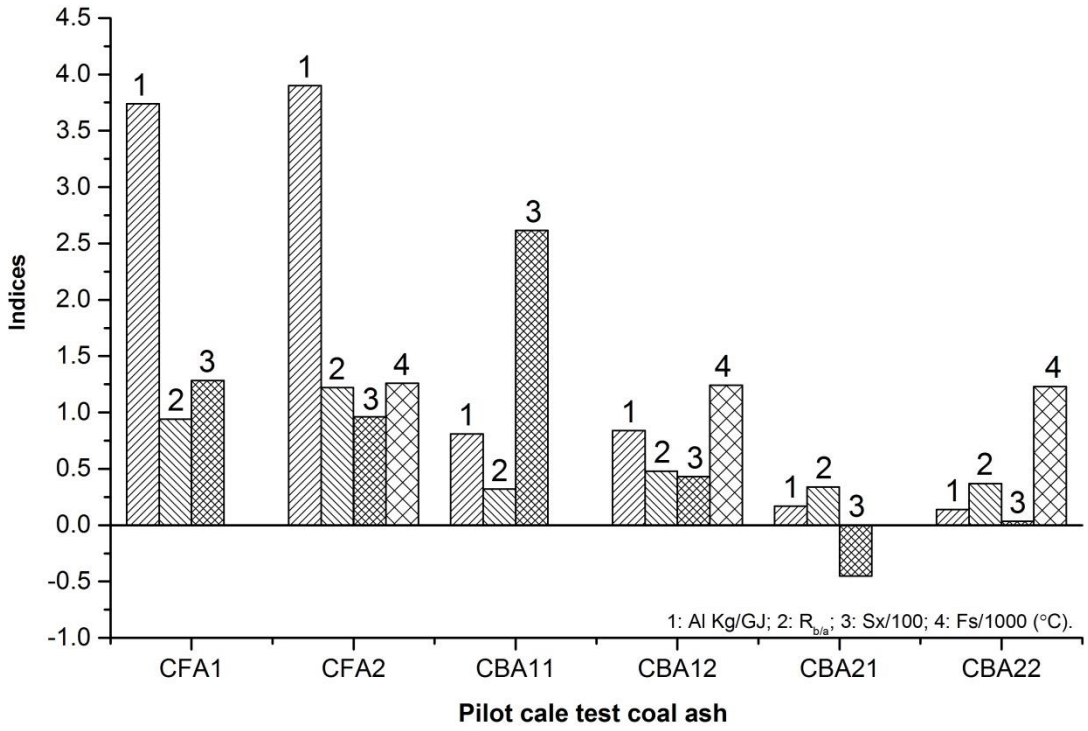

Figure 6.3 Values for different numerical indices at various pilot scale test ash from different collection point and re-burned ash refer to **Table 3.5**~**Table 3.6** and **4.7** for sample designation. Indices: 1, AI Kg/GJ; 2: $R_{b/a}$; 3: Sx/100; 4: Fs/1000 (℃).

Figure 6.3 display the calculated AI indices for some of the ash collected from PACT (CFA1, CBA11) and also the re-burned PACT ash (CFA2, CBA12 and CBA22). These indicate high fouling potential which is different to El Cerrejon coal 2 ash (PCC3). Only the original bottom ash from collection point 3 shows a low fouling potential, similar to the laboratory tested El Cerrejon coal 2 ash (PCC3). The calculated base-to- acid ratio, ($R_{b/a}$), indicate that the fly ash (CFA1) collected from collection point 1 has medium

slagging potential, and the re-burned fly ash (CFA2) has high slagging potential. The other ashes (CBA11, CBA12, CBA21 and CBA22) show low slagging potential which is similar to El Cerrejon coal 2 ash prepared at either temperature.

In this **Figure 6.2**, the calculated Fs slagging indices predict that the re-burned ash from PACT (re-burned at 800 ℃ (CFA2, CBA12)) would have medium slagging propensity, and are similar to PCC3. The re-burned bottom ash (re-burned at 800 ℃ (CBA22)) is predicted to have a high slagging potential.

The calculated values of Sx (at the shrinkage starting temperature, SST) show the following: The re-burned fly ash from collection point 1 (CFA1) and the T-section ash from collection point 2 (CBA11) show deceasing slagging propensity compared to CFA2 and CBA12. In contrast, the bottom ash (collection point 3 (CBA21)) shows increasing slagging propensity after the re-burned process (CBA22). Compared to El Cerrejon coal 2 ash (PCC3 in **Figure 6.2**), the original bottom ash (CBA21) shows lower slagging potential, and the original fly ash (CFA1) shows the highest slagging potential.

6.2 Different viscosity models

With regards to coal combustion, viscosity of ash is an important physical property that affects deposit strength in regions of high temperature (>1100 ℃) and can therefore be used to determine the extent of capture and consolidation of particles on furnace walls with high particle viscosity yielding low slagging potential [207, 208]. The redefined Watt-Fereday viscosity model for coal ashes is as given in **Equation 6.7**, where m and c are the empiric slope and intercept, respectively.

$$\mathrm{Log}(\mu) = \frac{m \times 10^7}{(T-150)^2} + c \quad \text{(Pa s)} \tag{6.7}$$

where: $m = 0.01404294SiO_2 + 0.0100297Al_2O_3 - 0.296285$, and $c = 0.0154148SiO_2 - 0.0388047Al_2O_3 - 0.0167264Fe_2O_3 - 0.0089096CaO - 0.012932MgO + 0.04678$

The viscosity at the softening temperature is defined by the modified Watt–Fereday model [205-206], as **Equation 6.8**. The softening temperatures of both the coal (T_c) and the biomass (T_b), are defined in **Equation 6.9** and **6.10**, respectively, as follows:

$$\mathrm{Log}(\mu) = \frac{m \cdot 10^7}{T_s^2} + c \quad \text{(Pa s)} \tag{6.8}$$

$$T_c = \underline{a}(SiO_2) + \underline{b}(Al_2O_3) + \underline{c}(Fe_2O_3) + \underline{d}(CaO) + \underline{e}(MgO) + \underline{f}(\alpha)] + \underline{g} + 150\ ℃ \tag{6.9}$$

$$Tb = 1.81CaO + 4.2Al_2O_3 - 2.4K_2O + 5.3P_2O_5 + 1017\ ℃ \tag{6.10}$$

and the constants a–g are parameters based on the SiO_2, Al_2O_3 and Fe_2O_3 contents in the ash, as $\underline{a}$=92.55; $\underline{b}$=97.83; $\underline{c}$= 84.52; $\underline{d}$= 83.67; $\underline{e}$=81.04; $\underline{f}$=0.92; $\underline{g}$=-7891.

In **Equation 6.8**, the term T_s for blends can be calculated as **Equation 6.11**. The x and y are coal and biomass fuel ratio in the blends respectively.

$$T_s^2 = xT_c^2 + (y/k)T_b^2 \tag{6.11}$$

The factor k in **Equation 6.12** is calculated from the compound percentages from **Table 5.3** as follows:

$$k = (K_2O + TiO_2)/Fe_2O_3 \tag{6.12}$$

A third viscosity model was tested which was developed based on viscosity measurements on US lignite and subbituminous coal slags [209]. The method follows a

similar procedure to that proposed by Urbain [210] for high silica slags. Here, viscosity is given by:

$$\ln\mu = \ln a + \ln T + \frac{10^3 \cdot b}{T} - \Delta \quad \textbf{(6.13)}$$

Here, $\Delta = m \cdot T + c$ **(6.14)**

Where a and b are defined by the model of Urbain [209] as:

$b_0 = 13.8 + 39.9355\alpha - 44.049\alpha^2$ **(6.15)**

$b_1 = 30.481 - 117.1505\alpha + 129.9978\alpha^2$ **(6.16)**

$b_2 = -40.9429 + 234.0486\alpha - 300.04\alpha^2$ **(6.17)**

$b_3 = 60.7619 - 153.9276\alpha + 211.1616\alpha^2$ **(6.18)**

$b = b_0 + b_1 SiO_2 + b_2 SiO_2^2 + b_3 SiO_2^3$ **(6.19)**

$-\ln a = 0.2693b + 13.9751$ **(6.20)**

$$\alpha = \frac{x_m}{x_m + x_a} \quad \textbf{(6.21)}$$

$x_m = Fe_2O_3 + CaO + MgO + Na_2O + K_2O + MnO + NiO + 2(TiO_2 + ZrO_2) + 3CaF_2$ **(6.22)**

$x_a = Al_2O_3 + Fe_2O_3$ **(6.23)**

From a knowledge of the value of b (SiO_2 is molar ratio of silica in the ash), the fuel is classified as high-silica, intermediate silica or low-silica slag. Then the values of m and c are calculated as follows from the mole fractions of components in the ash:

High-silica slags (b>28):

$$F = SiO_2/(CaO + MgO + Na_2O + K_2O) \quad \textbf{(6.24)}$$

$$10^3 \cdot m = -1.7264 \cdot F + 8.4404 \quad \textbf{(6.25)}$$

$$c = -1.7137(10^3 \cdot m) + 0.0509 \quad \textbf{(6.26)}$$

Intermediate-silica slags (24<b<28):

$$F' = b \cdot (Al_2O_3 + FeO) \quad (\mathbf{6.27})$$

$$10^3 \cdot m = -1.3101 \cdot F' + 9.9279 \quad (\mathbf{6.28})$$

$$c = -2.0356(10^3 \cdot m) + 1.1094 \quad (\mathbf{6.29})$$

Low-silica slags (b<24):

$$F'' = CaO/(CaO + MgO + Na_2O + K_2O) \quad (\mathbf{6.30})$$

$$10^3 \cdot m = -55.3649 \cdot F'' + 37.9186 \quad (\mathbf{6.31})$$

$$c = -1.8244(10^3 \cdot m) + 0.9416 \quad (\mathbf{6.32})$$

According to redefined Watt-Fereday viscosity model (**Equation 6.7**), the variation of viscosity with temperature is illustrated in **Figure 6.4** for El Cerrejon coal 1, pine and their blends samples (see **Table 3.3~Table 3.4** in **Chapter 3**). The Watt-Fereday model predicts decreasing viscosity with increasing temperature for the El Cerrejon coal 1 ash, the 80:20, 50:50 and the 20:80 blends of El Cerrejon coal 1 and pine. It is seen that for pure coal the ash is predicted to have high viscosity up to 1400 ℃, which is related to a low slagging propensity. As the percentage of pine ash in the blend increases, the temperature for slagging decreases, and it is predicted to be around 900 ℃ for the 20:80 coal:pine ash blend. To put the model in some context it can be compared to the glass working point viscosity (when it can be blown), which is 1000 Pa·s, and the glass melting point viscosity, which is 10 Pa·s. It should be noted that using this model, pine ash is predicted to have low viscosity (<0.1 Pa·s) for the entire temperature range. However, the Watt-Fereday viscosity model is an empirical index based on the viscosities of UK bituminous coal ash melts and therefore needs further refinement and validation for high CaO ashes such as pine ash. In comparison, the model by Streeter was also tested for the pine ash (PPA1) (a low silica slag) and the results are given in **Figure 6.4** also. While the model does show decreasing viscosity with temperature

increases, it predicts a highly slagging ash with exceptionally low softening temperature, which was not seen experimentally. This model was developed for lignite and sub-bituminous coals. The results here highlight the need for a more refined and validated viscosity model for biomass ashes.

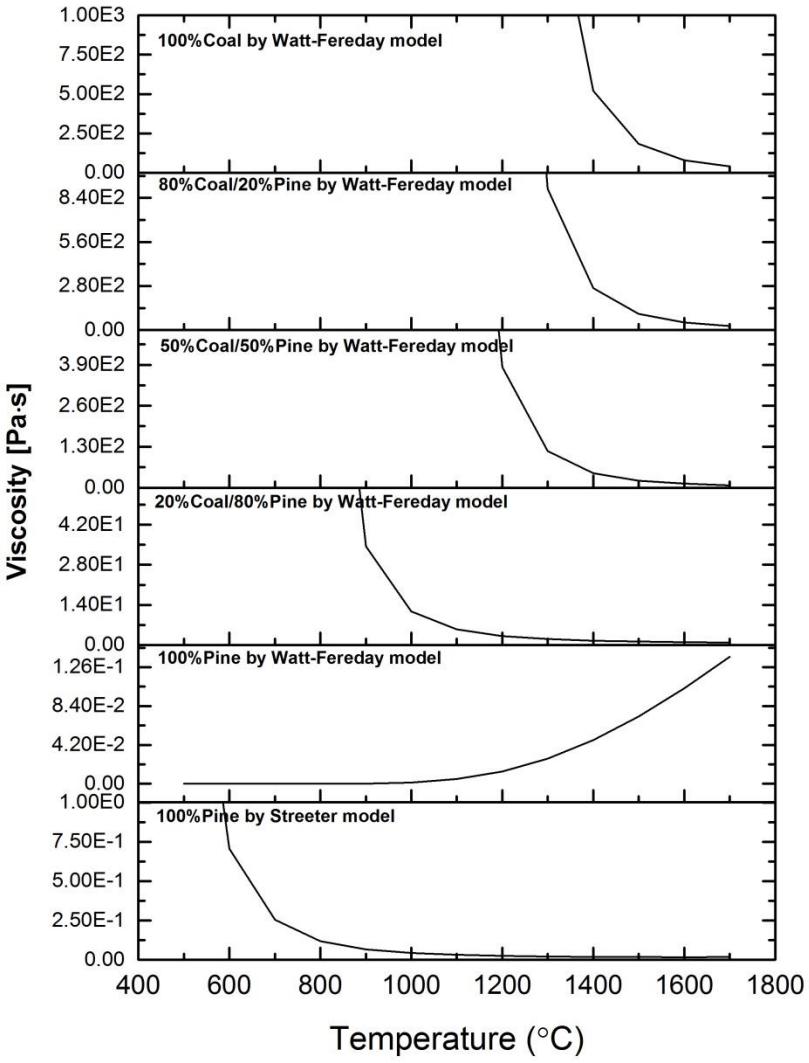

Figure 6.4 The change of viscosity with temperature for ash from different fuels based on the Watt-Fereday viscosity model, calculated by **Equation 6.7**; for comparison the Streeter model by **Equation 6.13** is shown, applied to the pine.

According to modified Watt-Fereday viscosity model (**Equation 6.8**), the variation of viscosity with temperature is compared in **Figure 6.5** for ash produced at two temperatures for El Cerrejon coal 1, pine ashes (PCC1, PCC2, PPA1 and PPA2), ash blends (CA28, CA55 and CA82) and fuel blends ashes (BFPC28, BFPC55 and BFPC82) (see **Table 3.3~Table 3.4** in **Chapter 3 for** sample designation). Both of the two coal ashes are predicted to have high viscosity up to 1400℃, which is related to a low slagging propensity. As the percentage of pine ash in the ash blend and pine ratio in fuel blends increases, the temperature for slagging decreases, and it is predicted to melt at between 650~800°C for the 20:80 coal:pine ash blend and fuel blends ash. Also shown in **Figure 6.5** is prediction of viscosity with temperature for the two pine ashes (PPA1 and PPA2) produced at two temperatures. Both are predicted to have low viscosity (<0.1 Pa·s) for the entire temperature range. In comparison, the model by Streeter was also tested for the two pine ashes (both are low silica slags). Compared to the redefined Watt-Fereday viscosity model (**Equation 6.7**) which is based on the viscosities of UK bituminous coal ash melts, this model does show similar decreasing viscosity with temperature, but it also predicts a highly slagging ash with exceptionally low softening temperature, which was not seen experimentally. The results here highlight the need for a more refined and validated viscosity model for biomass ashes.

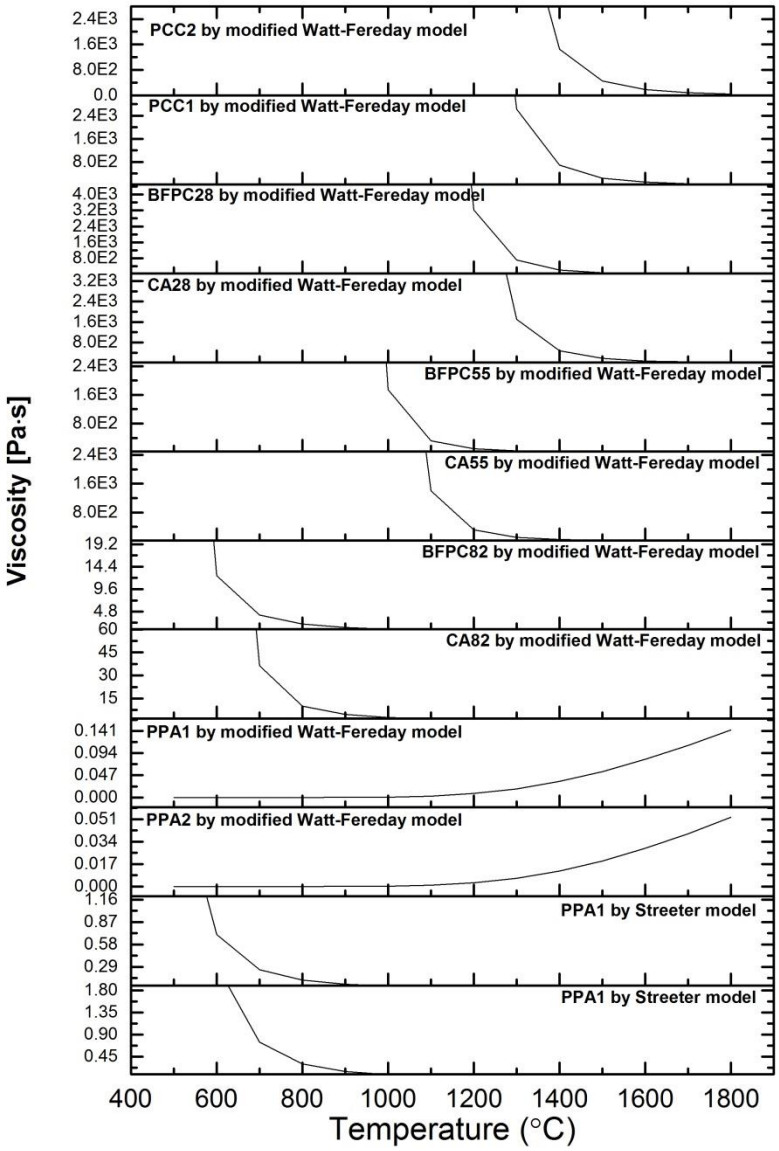

Figure 6.5 The change of viscosity with temperature for different ash samples based on the modified Watt-Fereday viscosity model, calculated by **Equation 6.8**; for comparison the Streeter model by **Equation 6.13** is shown, applied to the pine.

Figure 6.6 compares the viscosity prediction for El Cerrejon coal 2, wheat straw and their fuel blends ashes. The prediction for all the blends containing WS1 arevery similar and there is little difference in the predictions for El Cerrejon coal 2 and pure wheat straw. This is in disagreement with the experimental AFT results. As the ashing temperature increases for wheat straw (WS2), a difference in the softing viscosity predictions is predicted to occur at lower temperatures (~1200°C), but still higher than that observed in the AFT. In comparison, the model by Streeter was also tested for the two wheat straw ashes (WS1 and WS2) (a high silica slag) and the results are given in **Figure 6.6** also. Compared to the glass working point viscosity, the two wheat straw ashes are predicted to have high viscosity for the entire temperature range. While the model does show decreasing viscosity with temperature, it predicts a non-slagging ash which does not replicate the observations in the ash fusion tests.

Figure 6.7 shows viscosity predictions for ash from white wood pellets produced at two temperatures. It also compares prediction from the Watt-Fereday and Streeter models. As the ashing temperature increase to 800°C (WWP2), the temperature for slagging is predicted to decrease substantially. The viscosity at 700C° is predicted to have a viscosity <25 Pa·s (but it still higher than glass melting point viscosity). Compared to modified Watt-Fereday viscosity model, the Streeter model indicates that the two types of ash from white wood pellet are predicted to have high viscosity up to 900℃. A comparison of the predicted ash viscosities with temperature to the measured characteristic temperatures from the AFT is given in **Chapter 6**.

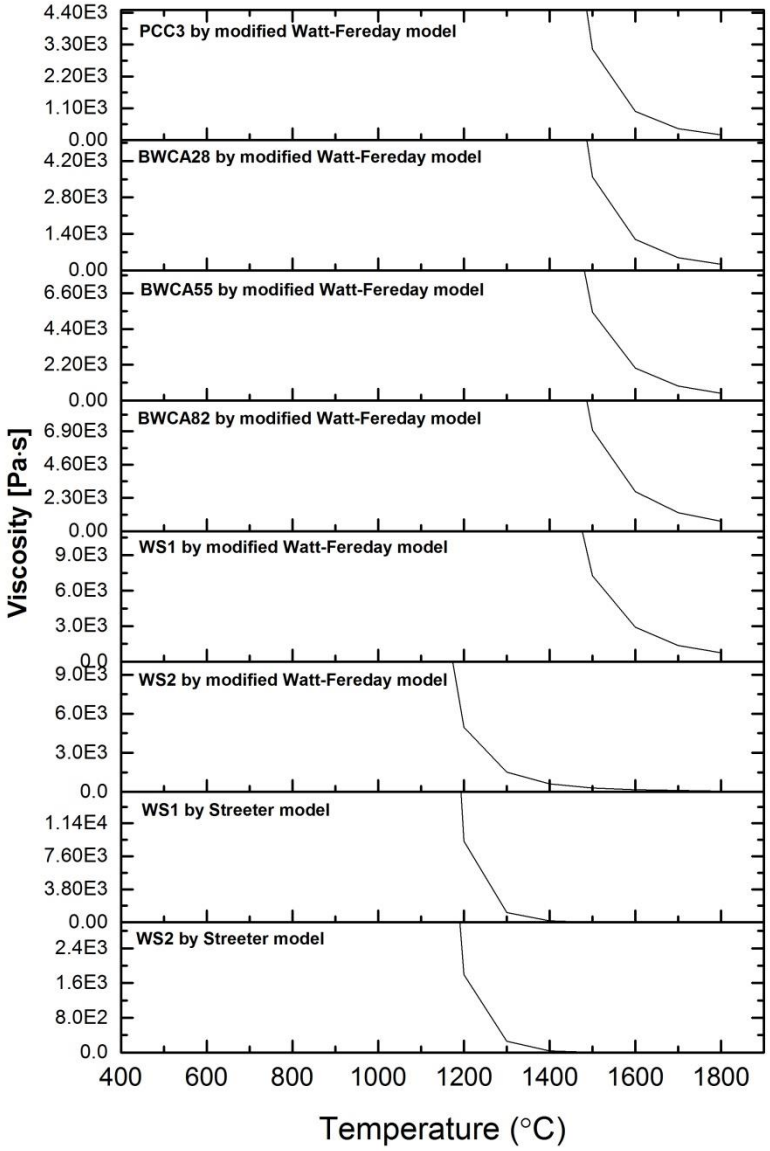

Figure 6.6 The change of viscosity with temperature for different ash samples based on the modified Watt-Fereday viscosity model, calculated by **Equation 6.8**; for comparison the Streeter model by **Equation 6.13** for lignite is shown, applied to the pine.

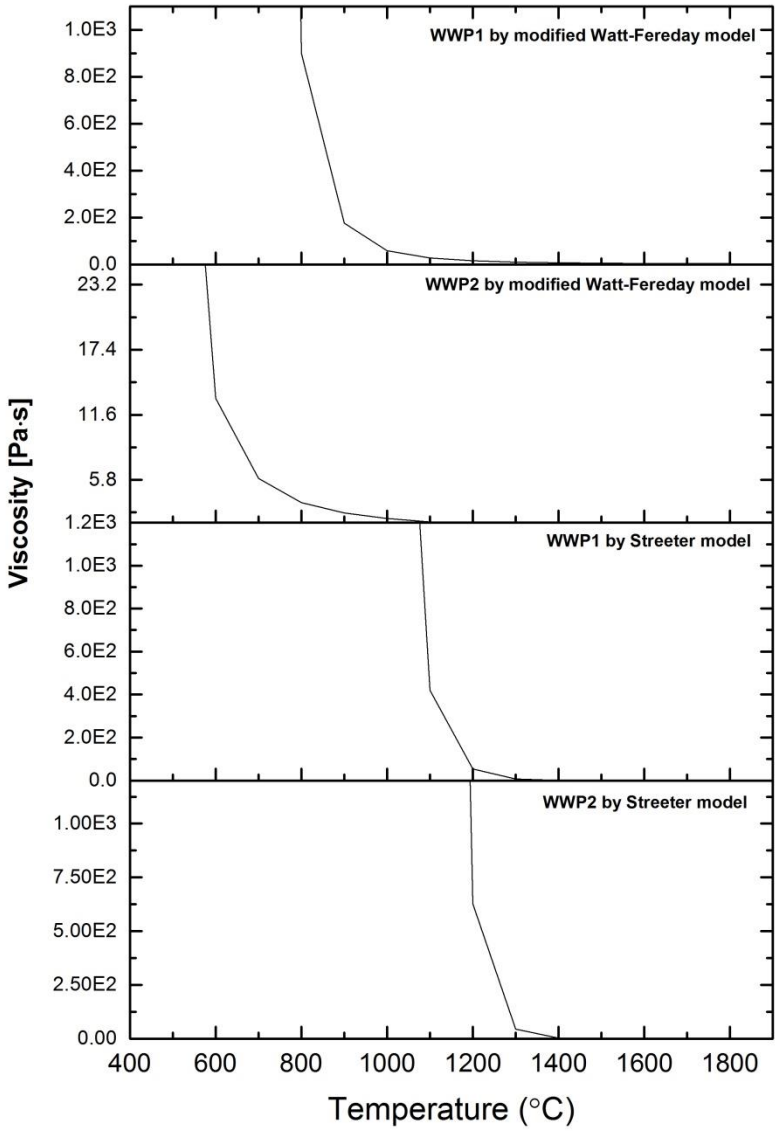

Figure 6.7 The change of viscosity with temperature for different ash samples based on the modified Watt-Fereday viscosity model, calculated by **Equation 6.8**; for comparison the Streeter model by **Equation 6.13** for lignite is shown, applied to the pine.

Predictions of variation in viscosity ith temperature for the ashes obtained from PACT (Some of which were re-ashed) (see **Table 3.5~Table 3.6** in **Chapter 3** for sample designations). The Watt-Fereday model predicts decreasing viscosity with increasing temperature for all those re-burned ashes and original fly ash (CFA1) and T-section ash (CBA11). It is seen that for original fly ash (CFA1) and re-burned fly ash (CFA2) are predicted to have high viscosity up to 900 ℃, which is related to a low slagging propensity. The original Tee section ash (CBA11) and re-burned ash (CBA12) show different predicted viscosity temperature curves whereby, the temperature for slagging increase from around 600°C to 900°C. This model fail for the original bottom ash (CBA21) and predicts low viscosity (<0.2 Pa·s) for the entire temperature range. In comparison, the model by Streeter was also tested for CBA21 and the results are given in **Figure 6.8** also. A similar melting temperature range and slagging tendency are shown for original bottom ash (CBA21) and re-burned bottom ash (CBA22) by Streeter model and modified Watt-Fereday model respectively. Further discussion of viscosity modelling and a comparison with the experimental AFT characteristic temperatures are given in **Chapter 7**.

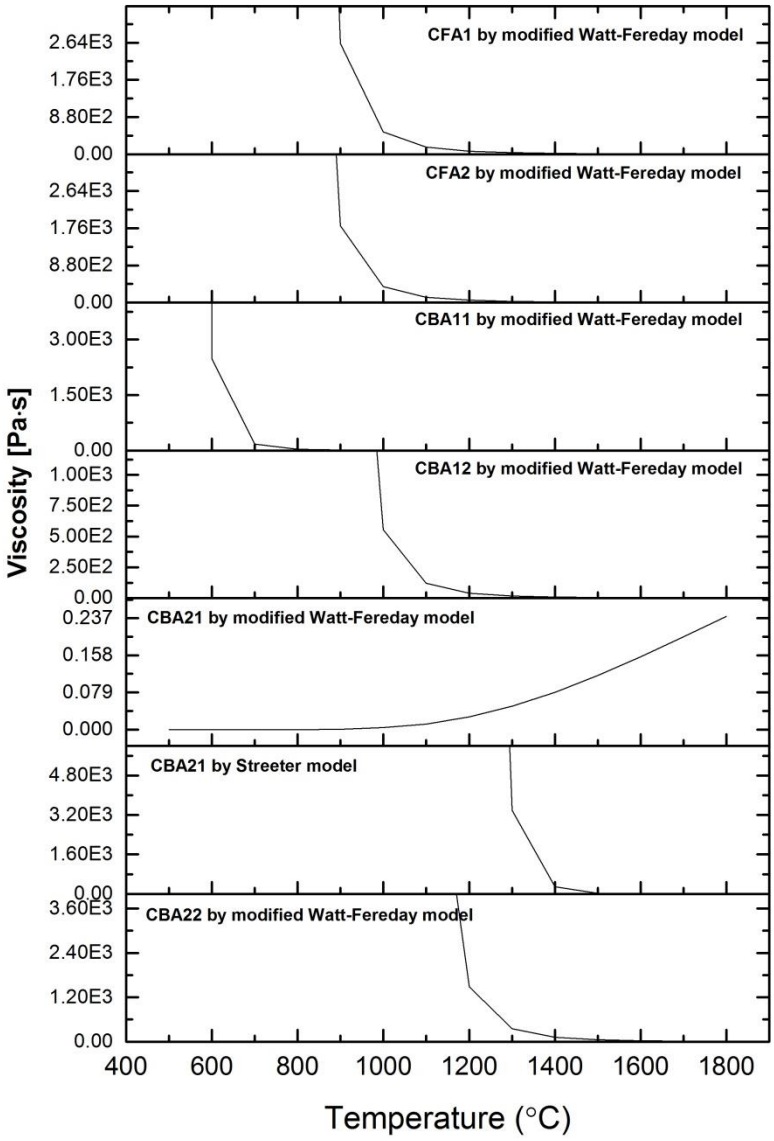

Figure 6.8 The change of viscosity with temperature for different ash samples based on the modified Watt-Fereday viscosity model, calculated by **Equation 6.8**; for comparison the Streeter model by **Equation 6.13** is shown, applied to the bottom ash (CBA21).

6.3 Equilibrium modelling by FactSage

Because of the limitations of the empirical indices in the prediction of slagging and fouling, an equilibrium thermochemical model, FactSage 6.4 [211], was used to predict the formation of slag and to gain further insights into ash behaviour. The proximate and ultimate fuel data were used as inputs. The thermodynamic database was mainly taken from FACTPS and FTOxid, all ideal gas, solid and liquid solutions were calculated from the stoichiometric equations. The reactions took place at a pressure of 1 bar and a residual oxygen content of 6 mol% O_2 in the output, which is typical for a combustion chamber. A temperature range from 500–1800 ℃ was chosen for the reactions between C, O, H, N, S, P, K_2O, Na_2O, SiO_2, CaO, Al_2O_3, Fe_2O_3, MgO, MnO, and TiO_2.

6.3.1 The El Cerrejon coal 1 and pine co-firing model

The modelling results showing the thermal equilibrium phase changes for the ashes from pure pine pine (PPA1, PPA2), El Cerrejon coal 1(PCC1, PCC2) and fuel blends(BFPC28, BFPC55 and BFPC82) with respect to the combustion temperature are presented in **Figure 6.9**.

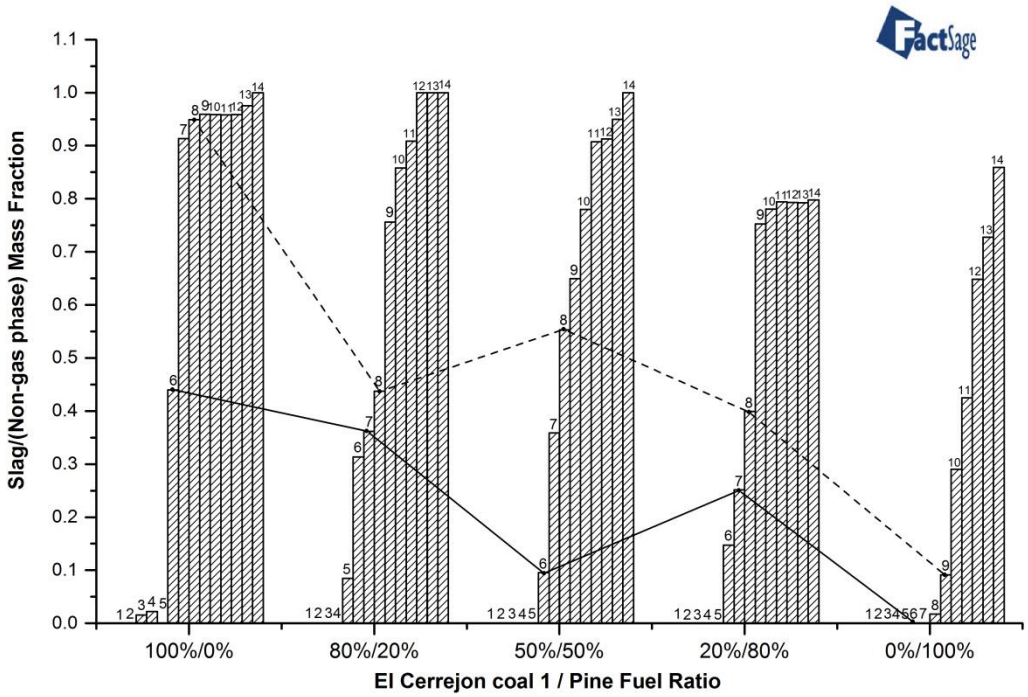

Figure 6.9 The change of slag mass fraction in non-gas phase with increase in temperature for each coal/pine ratio as calculated by FactSage. Temperatures: 1, 500 ℃; 2, 600 ℃; 3, 700 ℃; 4, 800 ℃; 5, 900 ℃; 6, 1000 ℃; 7, 1100 ℃; 8, 1200 ℃; 9, 1300 ℃; 10, 1400 ℃; 11, 1500 ℃; 12, 1600 ℃; 13, 1700 ℃; 14, 1800 ℃. Solid and dashed line represents the lower and upper limits of the measured deformation temperature range (by ash fusion test) for the different blends.

Each bar in the **Figure 6.9** represents the predicted mass fraction of slag for a particular blend at a particular temperature. Also plotted on this figure are the lower and upper limits of the measured deformation temperature ranges, assumed to be represented as the lowest softening temperature (SST) and highest deformation temperature (DT) measured for each El Cerrejon coal 1 and pine blends or pure fuel; the solid and dashed line join these points to give an estimated region for where slagging is observed to occur experimentally.

The first thing to note is that the El Cerrejon coal 1 is predicted to be the most slagging (i.e. has the largest change in slag mass fraction between 1000°C and 1200°C) while the biomass is predicted to be the least slagging and has the lowest change in mass fraction

of slag in this temperature range. The El Cerrejon coal 1 and pine blends are intermediate to these two extremes, and there is a general trend of them becoming less slagging with increasing biomass, although, of these, the 50/50 blend is predicted to have a the largest change in slag mass fraction between 1000°C and 1200°C. These general predictions follow the same trend as the slagging index, Fs, (see **Equation 6.3**) given in **Table 6.1**, which is derived from the experimental ash fusion test results given in **Table 5.1** (see **Chapter 5**).

In the case of pure coal ash, FactSage predicts ca. zero slag at 900^{o}C, 45% slag at 1000^{o}C (near the experimental SST) and this increases to 90% at 1100^{o}C (DT is around 1200^{o}C), so the results are predicting slag at lower temperature than the measured values, but still within about 100^{o}C. For biomass significant slag formation is predicted only at 1200^{o}C and above. Note that the total amount of predicted slag is also much lower for the pine compared to the coal as seen in **Figure 6.9**.

Figure 6.10~Figure 6.14 shows the chemical composition of the predicted species calculated using FactSage for the fuels and fuel blends by different ratios. Note that pine, **Figure 6.14** shows a small propensity of slag formation in terms of g/kg fuel, and this only begins to form at about 1200^{o}C. In contrast, the coal (**Figure 6.10**) displays much higher weight of slag and this is first seen to form at above 900^{o}C. Modelling of the 50/50 blend (**Figure 6.12**) predicts intermediate slagging in terms of g/kg fuel, and a small amount of slag is seen at above 900^{o}C, but this increases significantly at temperatures above 1000^{o}C. The pine slag is mainly predicted as Al_2O_3, the blend slag as a mixture of SiO_2, Al_2O_3 and CaO and the coal slag as a mixture of SiO_2, CaO, and Na_2O. Compared with the study by Rizvi. [212] using a different pine with a lower CaO content than the present work (20wt% compared with 49wt%) there are different predicted results for solid phase change and softening temperature.

Comparison of **Figure 6.10~Figure 6.14** shows that the compositions during the phase changes become more complicated. As the coal ratio increases in these five models the total non-gas phase content increases due to the higher ash content in the fuel. For the solid phase, as the coal ratio increases, Ca mainly exists in $CaSO_4$ and decreases sharply above 700 ℃. In the 50/50 mixture below 900°C, most of the Ca forms $Ca_5HO_{13}P_3$ and $CaAl_2Si_2O_8$ with a decrease in $CaSO_4$. The Si content increases with an increase in coal ratio, and the higher ash content of coal contributes more Si species in the solid phase. With an increase in temperature $KAlSi_2O_6$ and $CaAl_2Si_2O_8$ in the solid phase are decomposed to SiO_2, CaO and Al_2O_3 which are the main slagging components above 900 ℃. Because the amounts of CaO and Al_2O_3 are very close (in **Table 4.5** and **Table 4.6** in **Chapter 4**), after 1500 ℃ these two species have similar content in liquid phase. This is also the case in the 50/50 case; in the 100% coal model, $Ca_5HO_{13}P_3$ in the solid phase remains until 1200 ℃ and changes to $Ca_3(PO_4)_2$ as a solid after 1300 ℃. The differences are in the case for 100% coal where most of the K is replaced by Na and combined with Al and Si oxides. As the SiO_2 in the solid phase decreases above 700 ℃, SiO_2 occurs for the first time in the slag at 800 ℃. After that, because of the decreasing content of $CaSO_4$, Na_2SO_4 and SiO_2 in both solid and liquid phase, these three species react to become $Na_2Ca_3Si_6O_{16}$ as a solid at 900 ℃. As the temperature increases, the $Na_2Ca_3Si_6O_{16}$ and $NaAlSi_3O_8$ in the solid phase react to form $Na_2Ca_2Si_3O_9$ as a solid and SiO_2, CaO and Na_2O as slag at 1000 ℃. Following that, most $Na_2Ca_2Si_3O_9$ and Na_2SO_4 in solid phase are converted into the liquid phase with significant increase of SiO_2, CaO and Na_2O in the slag. Above 1200 ℃, SiO_2 and CaO remain until 1600^{o}C where some of these species are transferred. The reactions as shown by plots in **Figure 6.10~Figure 6.14** are listed as below:

$CaSO_4$(Solid) + Na_2SO_4 (Solid)+SiO_2(Solid)→ $Na_2Ca_3Si_6O_{16}$ (Solid) (900 ℃)

$Na_2Ca_3Si_6O_{16}$(Solid) + Na_2SO_4(Solid) → $Na_2Ca_2Si_3O_9$ (Solid)+ SiO_2(Slag) + CaO(Slag) + Na_2O(Slag) (900~1000 ℃)

$Na_2Ca_2Si_3O_9$ (Solid)+ Na_2SO_4(Solid) → SiO_2(Slag) + CaO(Slag) + Na_2O(Slag) (>1000 ℃)

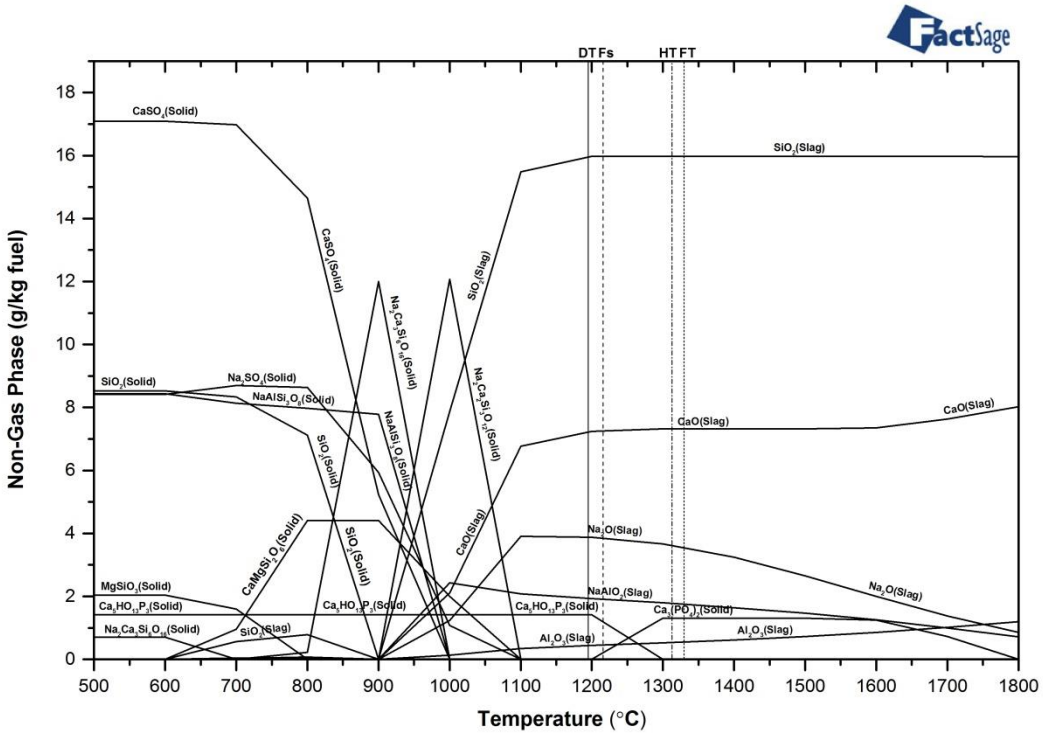

Figure 6.10 Stable solid phases in equilibrium with the slag phase for 100%El Cerrejon coal1—PCC2.

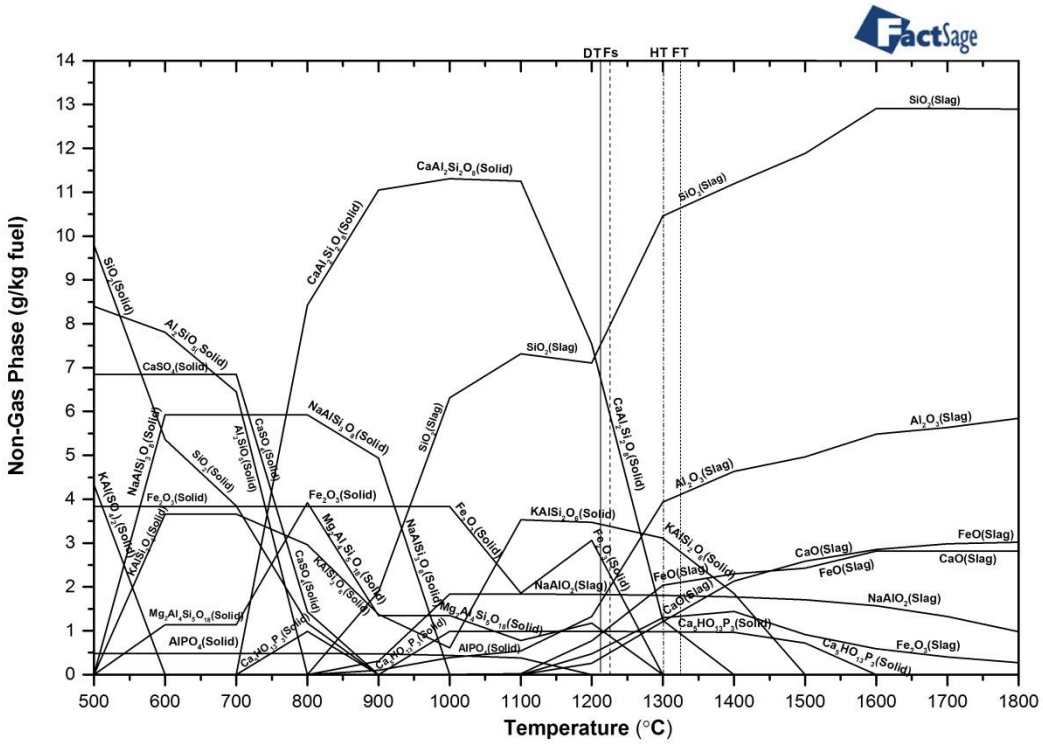

Figure 6.11 Stable solid phases in equilibrium with the slag phase for 80% El Cerrejon coal1 and 20% pine co-combustion—BFPC28.

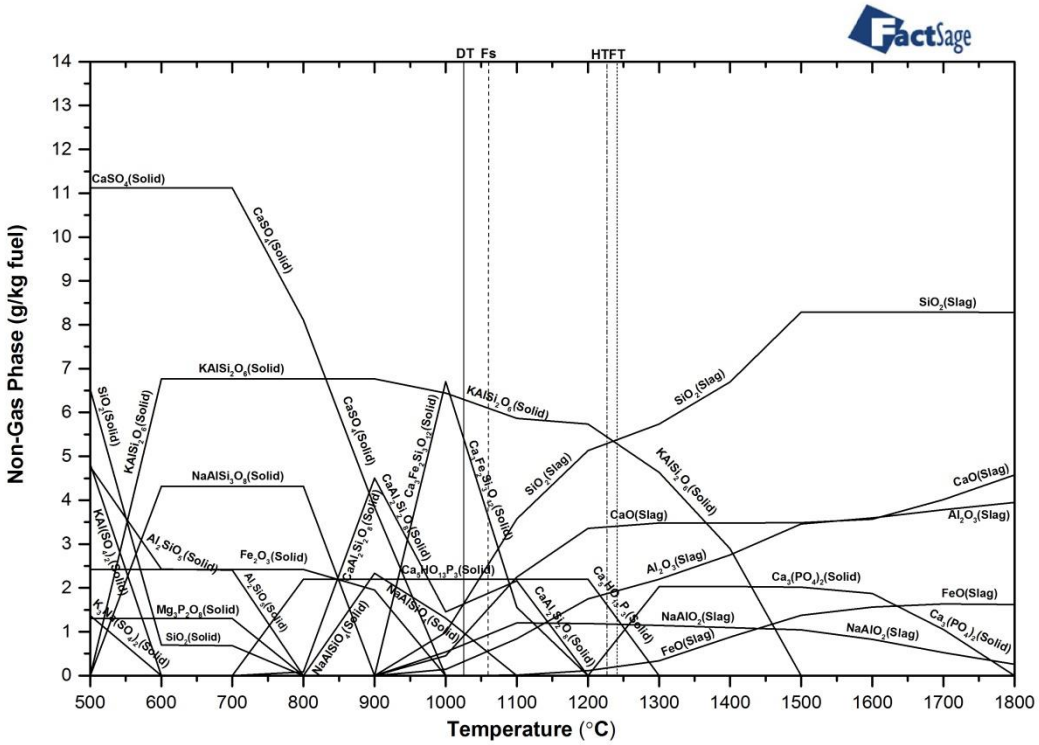

Figure 6.12 Stable solid phases in equilibrium with the slag phase for 50% El Cerrejon coal1 and 50% pine co-combustion—BFPC55.

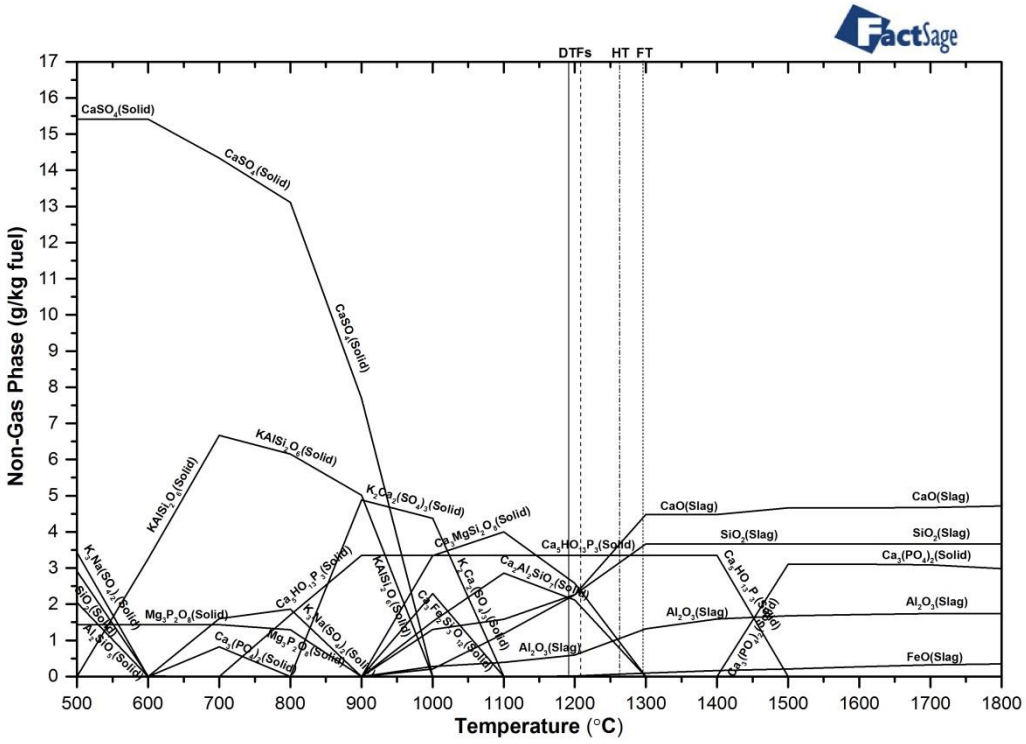

Figure 6.13 Stable solid phases in equilibrium with the slag phase for 20% El Cerrejon coal1 and 80% pine co-combustion—BFPC82.

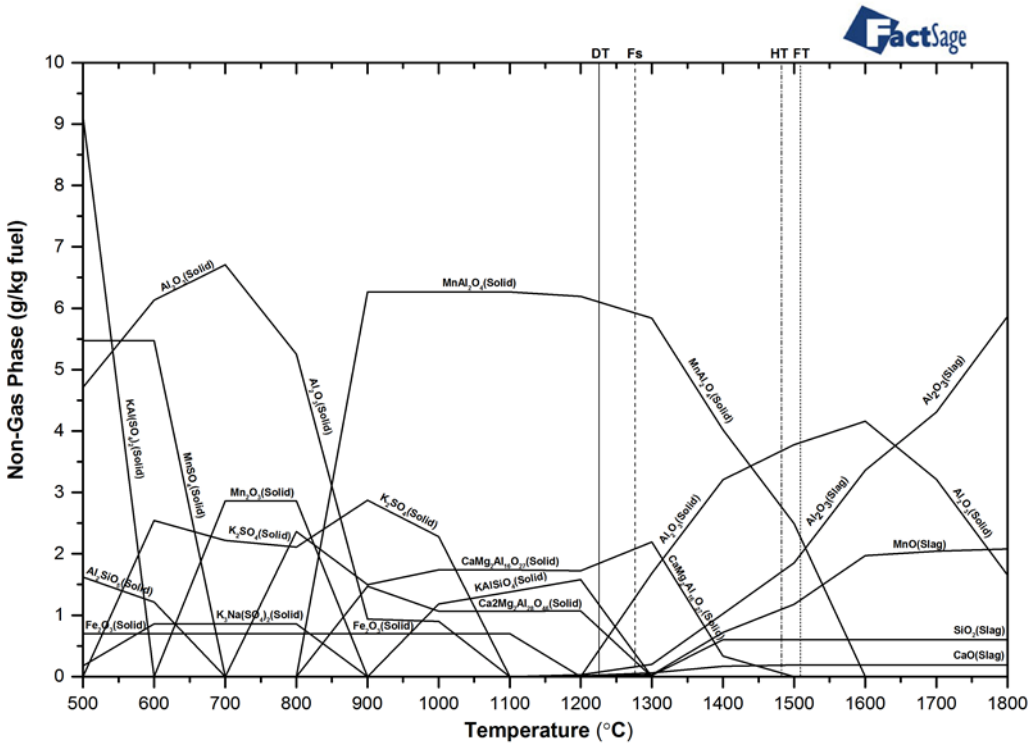

Figure 6.14 Stable solid phases in equilibrium with the slag phase for 100% pine—PPA1.

6.3.2 The El Cerrejon coal 2 and wheat straw co-firing model

As given in **Chapter 3**, the El Cerrejon coal 2 and wheat straw are referred to as PCC3 and WS1, WS2 respectively, and the fuel blend ashes are referred to as BWCA28, BWCA55 and BWCA82 respectively. The modelling results showing the thermal equilibrium phase changes for the ashes with respect to the combustion temperature are presented in **Figure 6.15**.

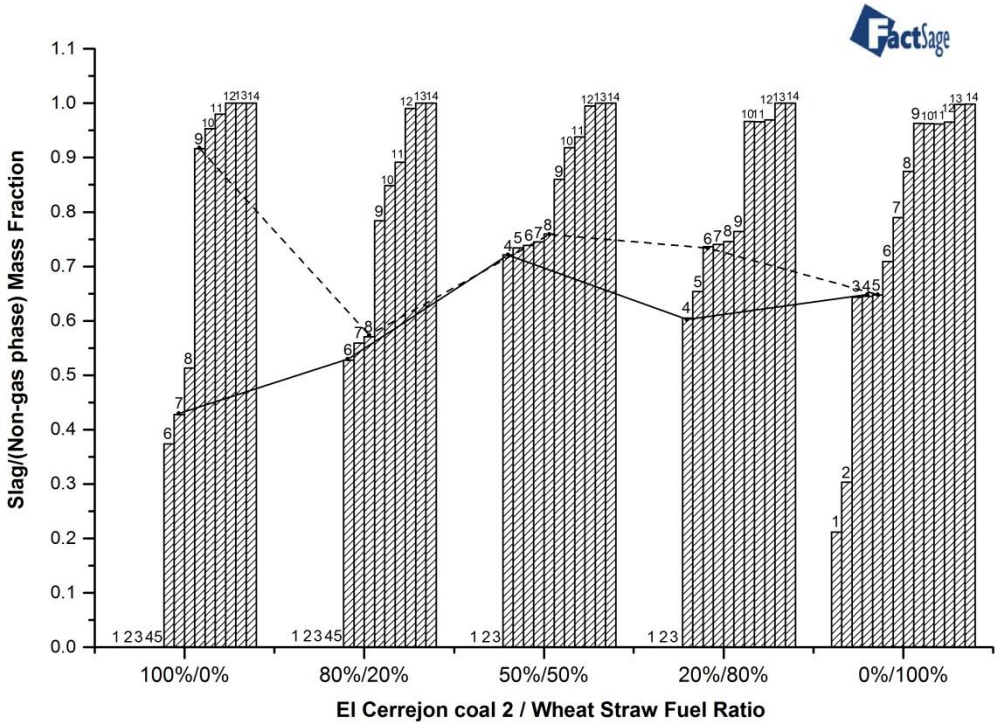

Figure 6.15 The change of slag mass fraction in non-gas phase with increase in temperature for each El Cerrejon coal 2 / wheat straw ratio as calculated by FactSage. Temperatures: 1, 500 ℃; 2, 600 ℃; 3, 700 ℃; 4, 800 ℃; 5, 900 ℃; 6, 1000 ℃; 7, 1100 ℃; 8, 1200 ℃; 9, 1300 ℃; 10, 1400 ℃; 11, 1500 ℃; 12, 1600 ℃; 13, 1700 ℃; 14, 1800 ℃. Solid and dashed line represents the lower and upper limits of the measured deformation temperature range (by ash fusion test) for the different blends.

Each bar in the **Figure 6.15** represents the predicted mass fraction of slag for a particular blend at a particular temperature. Also plotted on this figure are the lower and upper limits of the measured deformation temperature ranges, assumed to be represented as the lowest softening temperature (SST) and highest deformation temperature (DT) measured for each El Cerrejon coal 2 and wheat straw blends or pure fuel; the solid and dashed line join these points to give an estimated region for where slagging is observed to occur experimentally.

The first thing to note is that the pure wheat straw is predicted to be the most slagging at low temperature (i.e. has the largest change in slag mass fraction between 500°C and 700°C) while the pure El Cerrejon coal 2 and 80% coal blends are predicted to be the least slagging in this temperature range. The 50/50 blends are intermediate and have the largest change in slag mass fraction between 700°C and 800°C. These general predictions follow a different trend to the slagging index, Fs, (see **Equation 6.3**) given in **Table 6.1**, which is derived from the experimental ash fusion test results given in **Table 5.1** (see **Chapter 5**) and which shows only a small variation in Fs for WS1 and PCC3.

In the case of pure wheat straw ash, FactSage predicts slag generated from 500^{o}C, about 65% slag at 900^{o}C (near the experimental DT) and this increases to 75% at 1100^{o}C (HT is around 1100^{o}C), so the results are predicting slag at temperature close to the measured values. Note that the total amount of predicted slag is much higher at low temperature for the straw compared to the coal as seen in **Figure 6.15**.

Figure 6.16~Figure 6.20 shows the chemical composition of the predicted species calculated using FactSage for the fuels and fuel blends by different ratios. Note that wheat straw, **Figure 6.20** shows a high propensity of slag formation in terms of g/kg fuel, and this begins to form at about 500^{o}C. In contrast, the coal (**Figure 6.16**) displays a lower weight of slag and this is first seen to form at above 900^{o}C. Modelling of the 50/50 blend (**Figure 6.18**) predicts intermediate slagging in terms of g/kg fuel, and a significant amount of slag is seen at above 700^{o}C. The straw slag is mainly predicted as SiO_2, K_2O and CaO, the blend slag as a mixture of Al_2O_3, FeO, $NaAlO_2$, K_2O, MgO and CaO and the coal slag as a mixture of Al_2O_3, FeO, $NaAlO_2$, SiO_2 and CaO.

Comparison of **Figure 6.16~Figure 6.20** shows that the compositions during the phase changes become more complicated. As the wheat straw ratio increases in these five

models the total non-gas phase content increases due to the higher ash content in the fuel. For the solid phase, as the coal ratio decreases from 100% to 80%, Al mainly exists in Al_2SiO_5 and decreases in the pure coal combustion after 500°C. As the straw ratio increases, in the 50/50 mixture below 600°C, most of the Al mainly exists as $KAlSi_3O_8$, and decomposition to $KAlSi_2O_6$, $NaAlSi_3O_8$ and K_2SO_4 with temperature increase. After 800°C all of these three compounds are decomposed into slag. As the straw ratio increases, the $CaSO_4$ content in the solid phase show increasing content, and when the fuel ratio is 50/50, $Ca_5HO_{13}P_3$ is predicted in the solid phase. When the straw ratio increase to 80% and 100%, low Al content and high Ca content are present in the solid phase and $Na_2Ca_3Si_6O_{16}$, $CaMgSi_2O_6$, $Ca_5HO_{13}P_3$ and $Ca_3Fe_2Si_3O_{12}$ are predicted after 800°C. The Si content increases with an increase in wheat straw ratio, and the higher ash content of straw contributes more Si species in the solid phase. In pure wheat straw, an increase in temperature, $Na_2Ca_3Si_6O_{16}$, $CaMgSi_2O_8$ and $K_2Si_4O_8$ in the solid phase are decomposed to SiO_2, CaO and K_2O which are the main slagging components above 1000 ℃. In the high coal ratio (from 100% to 80%), the main reactions as shown by plots in **Figure 6.16~Figure 6.17** are listed as below:

$SiO_2(Solid) + Al_2SiO_5(Solid) + CaSO_4(Solid) \rightarrow CaAl_2Si_2O_8(Solid) + SO_2(Gas)$ (800 ℃~1200°C)

$CaAl_2Si_2O_8(Solid) \rightarrow SiO_2(Slag) + Al_2O_3(Slag) + CaO(Slag)$ (1100°C~1300°C)

$NaAlSi_3O_8(Solid) \rightarrow SiO_2(Slag) + Al_2O_3(Slag) + NaAlO_2(Slag)$ (900°C)

$Fe_2O_3(Solid) + SiO_2(Solid) + Al_2SiO_5(Solid) \rightarrow Al_2Fe_2O_6(Solid) + SiO_2(Slag)$ (1100°C~1200°C)

$Al_2Fe_2O_6(Solid) \rightarrow Al_2O_3(Slag) + FeO(Slag)$ (>1200°C)

The most complicated phase change of 50/50 fuel ratio co-firing in **Figure 6.18** can be described as the reactions below:

$KAlSi_3O_8(Solid) \rightarrow SiO_2(Solid)+KAlSi_2O_6(Solid)$ (600°C)

$SiO_2(Solid)+KAlSi_2O_6(Solid) \rightarrow SiO_2(Slag)+K_2O(Slag)+Al_2O_3(Slag)$ (800°C)

$NaAlSi_3O_8(Solid) \rightarrow SiO_2(Slag)+Al_2O_3(Slag)+NaAlO_2(Slag)$ (900°C)

$CaSO_4(Solid)+MgSiO_3(Solid) \rightarrow CaMgSi_2O_6(Solid)+SO_2(Gas)$ (900°C)

$CaMgSi_2O_6(Solid) \rightarrow CaO(Slag)+SiO_2(Slag)+MgO(Slag)$ (>1200°C)

$CaSO_4(Solid)+ SiO_2(Solid)+Fe_2O_3(Solid) \rightarrow Ca_3Fe_2Si_3O_{12}(Solid)+SO_2(Gas)$ (900°C)

$Ca_3Fe_2Si_3O_{12}(Solid) \rightarrow CaO(Slag)+FeO(Slag)+SiO_2(Slag)$ (>1300°C)

When the wheat straw ratio increases from 20% to80%, the main reactions as shown by plots in **Figure 6.19~Figure 6.20** are listed as below:

$K_2Si_4O_9(Solid) \rightarrow K_2O(Slag)+SiO_2(Slag)$ (>500°C)

$Na_2Ca_3Si_6O_{16}(Solid) \rightarrow Na_2O(Slag)+CaSiO_3(Solid)$ (900°C)

$CaSiO_3(Solid) \rightarrow CaO(Slag)+SiO_2(Slag)$ (>1100°C)

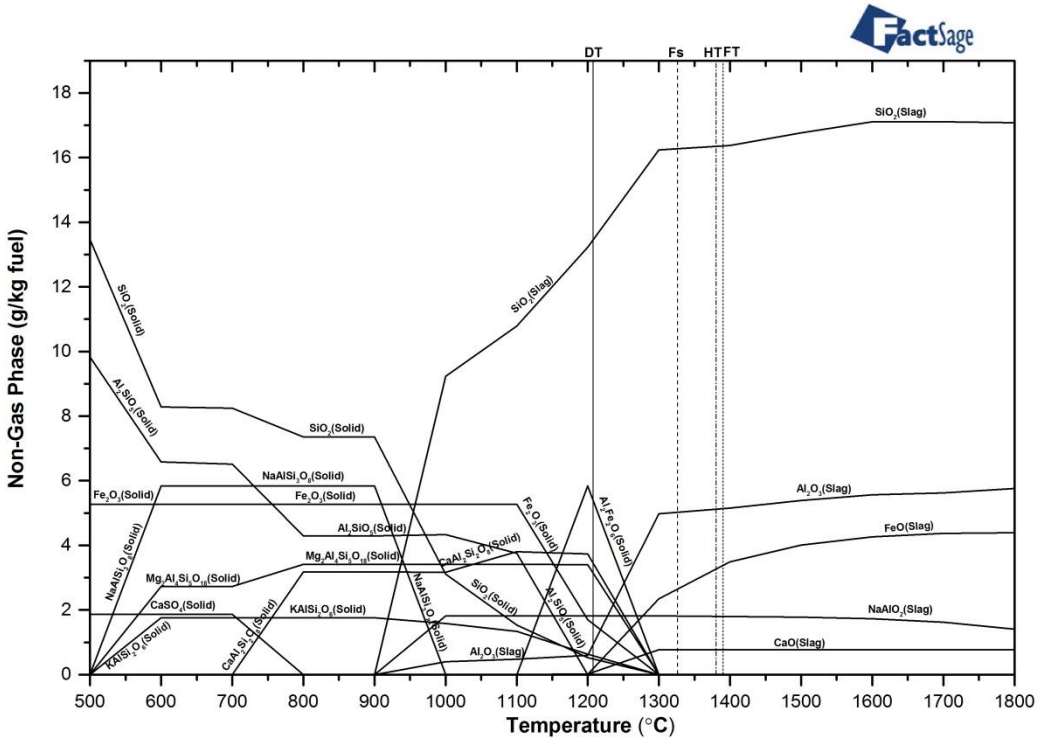

Figure 6.16 Stable solid phases in equilibrium with the slag phase for 100% El Cerrejon coal 2—PCC3.

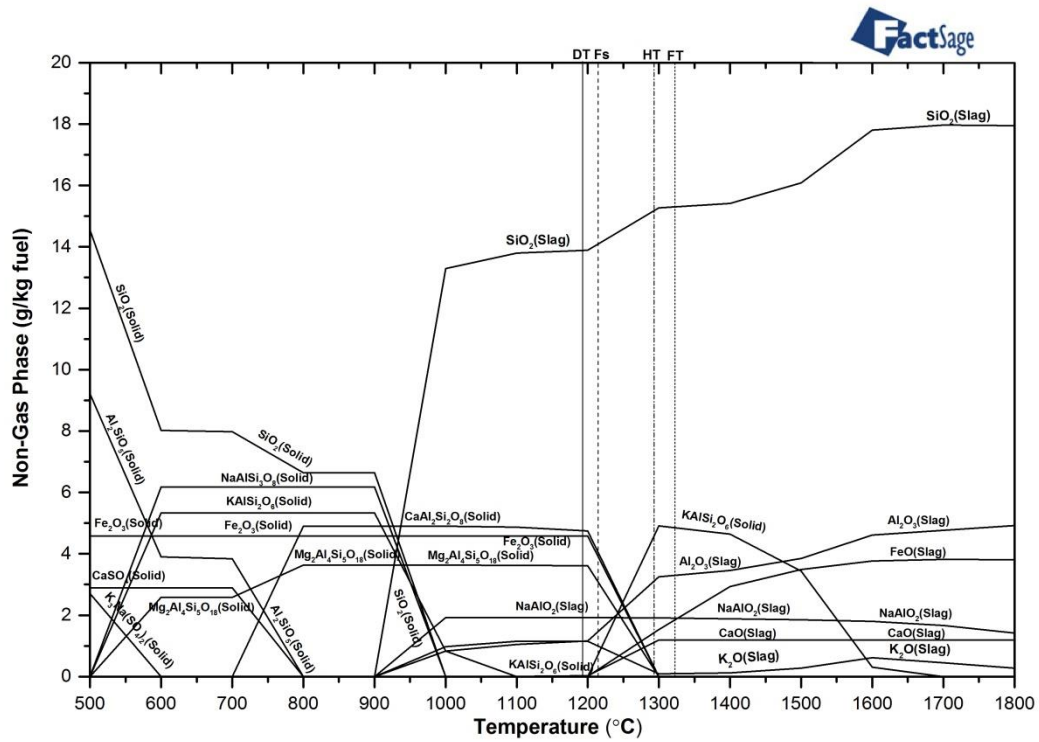

Figure 6.17 Stable solid phases in equilibrium with the slag phase for 80% El Cerrejon coal2 and 20% wheat straw co-combustion—BWCA28.

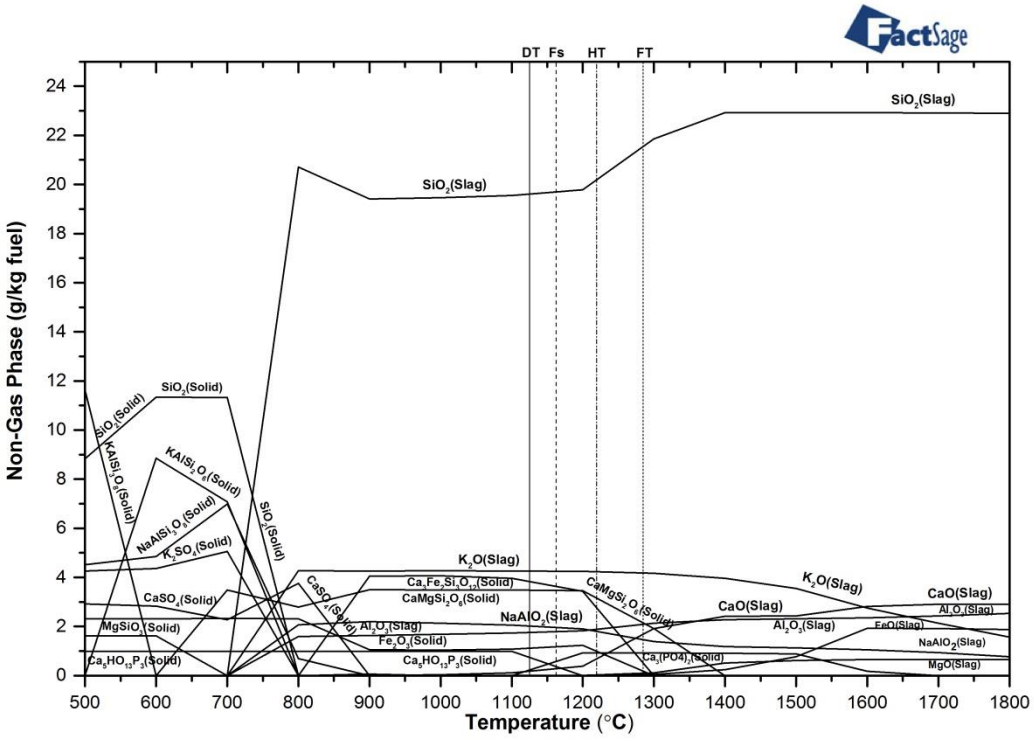

Figure 6.18 Stable solid phases in equilibrium with the slag phase for 50% El Cerrejon coal2 and 50% wheat straw co-combustion—BWCA55.

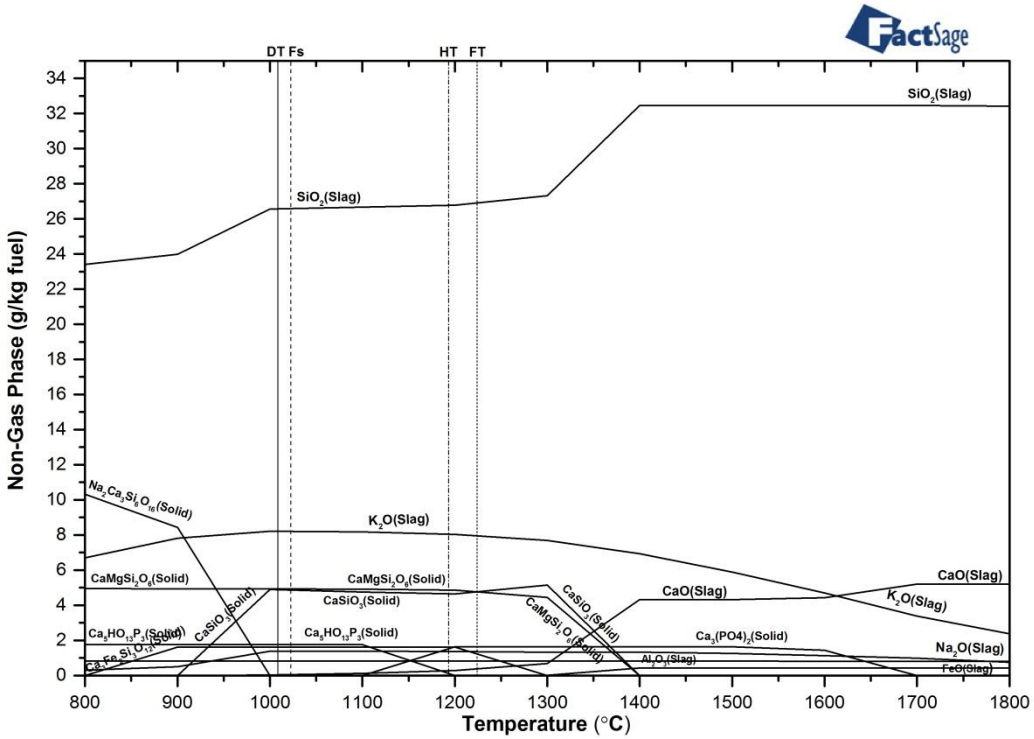

Figure 6.19 Stable solid phases in equilibrium with the slag phase for 20% El Cerrejon coal 2 and 80% wheat straw co-combustion—BWCA82.

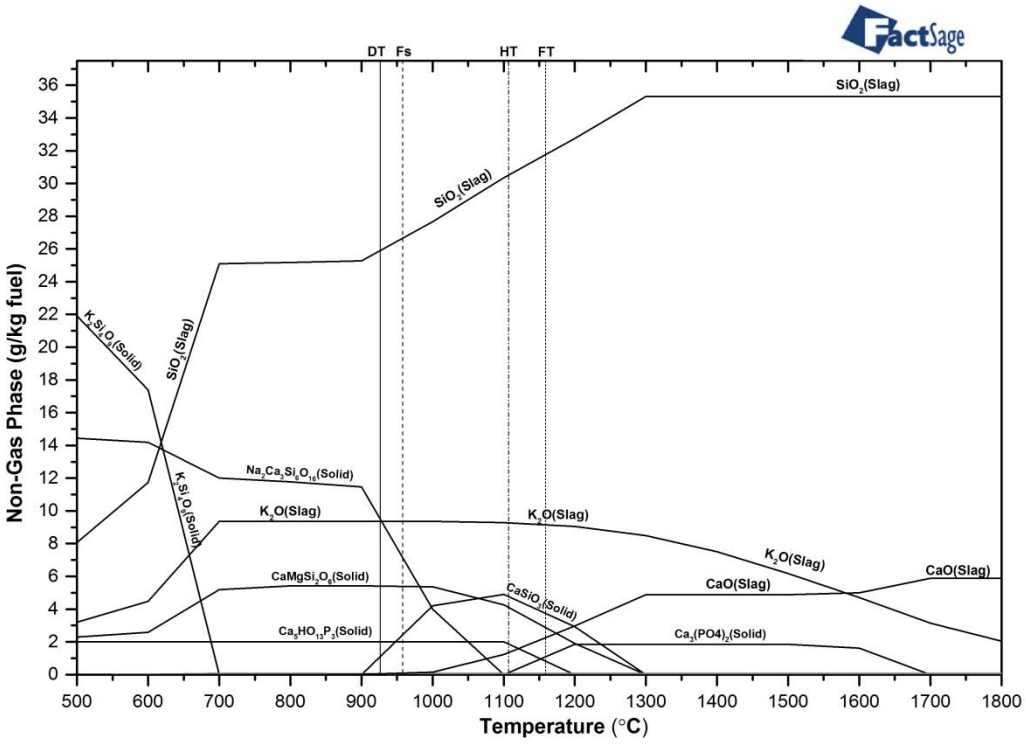

Figure 6.20 Stable solid phases in equilibrium with the slag phase for 100% wheat straw-- WS1.

6.3.3 The white wood pellet pure combustion model

The white wood pellet modelling results showing the thermal equilibrium phase changes for the ashes with respect to the combustion temperature are presented in **Figure 6.21.**

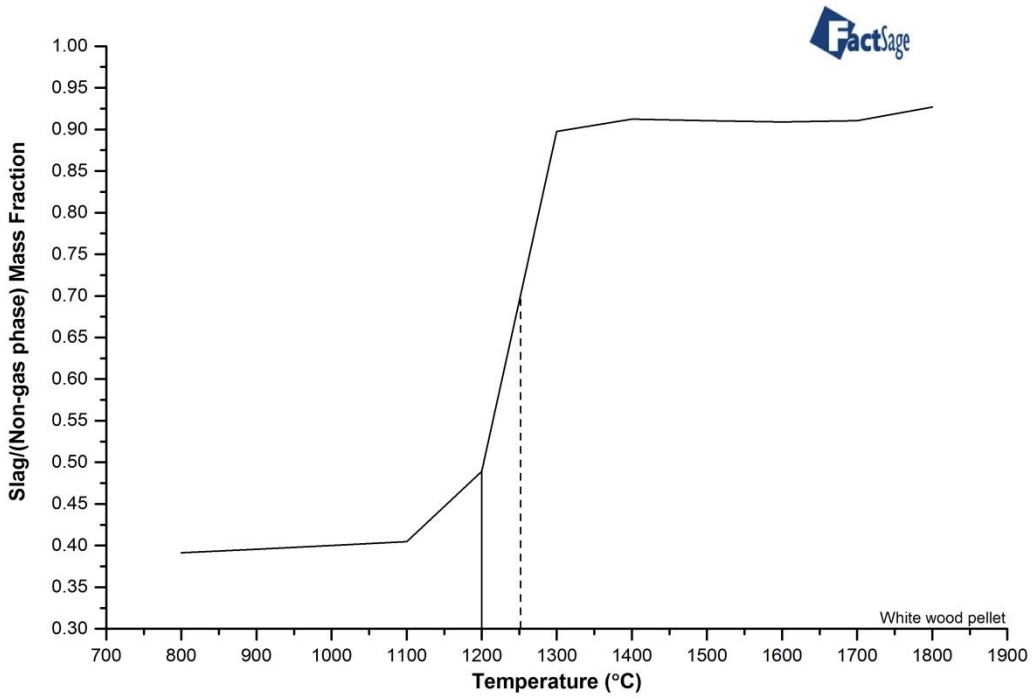

Figure 6.21 The change of slag mass fraction in non-gas phase with increase in temperature for 100% white wood pellet as calculated by FactSage. Solid and dashed line represents the lower and upper limits of the measured deformation temperature range (by ash fusion test) for the 550°C white wood pellet ash (WWP1).

Plotted on this figure are the changes of slag mass fraction in non-gas phase with increase in temperature for 100% white wood pellet as calculated by FactSage. The lower and upper limits of the measured deformation temperature ranges, assumed to be represented as the lowest softening temperature (SST) and highest deformation temperature (DT). The solid and dashed lines show these points to give an estimated region for where slagging is observed to occur experimentally and good agreement is observed. In this model for pure white wood pellet ash, FactSage predicts slag generated

from 800°C (~40%), about 48% slag at 1200°C (near the experimental SST) and this increases to 70% at 1200°C (DT is around 1250°C), so the results are predicting slag at lower temperature than the measured values, although the rapid change in slag production between 800~1200°C is in good agreement.

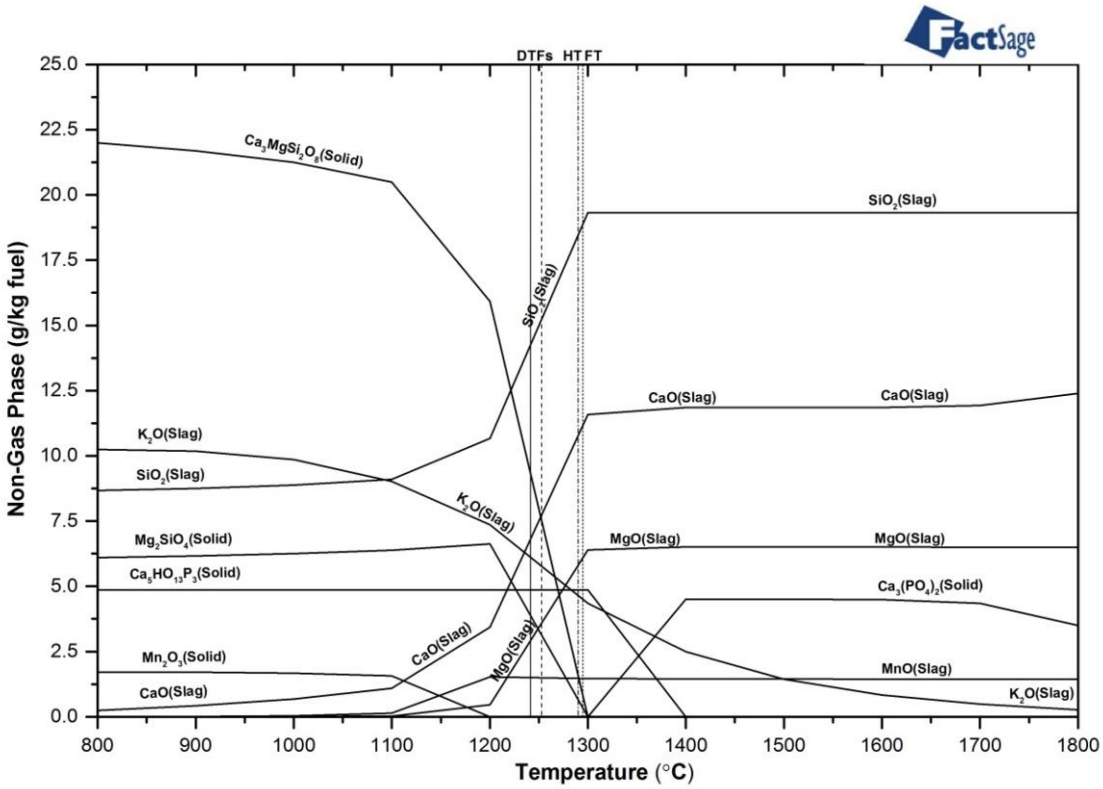

Figure 6.22 Stable solid phases in equilibrium with the slag phase for white wood pellet.

Figure 6.22 shows the chemical composition of the predicted species calculated using FactSage for the pure white wood pellet combustion with air. The slag is mainly predicted as SiO_2, K_2O, MgO, MnO and CaO. The main reactions as shown by plots in **Figure 6.22** are listed as below:

$Ca_3MgSi_2O_8(Solid)+Mg_2SiO_4(Solid)\rightarrow SiO_2(Slag)+CaO(Slag)+MgO(Slag)$

(800°C~1300°C)

And there are minor contributions from:

$Mn_2O_3(Solid) \rightarrow MnO(Slag)$ (1200°C)

6.3.4 The PACT ash thermodynamic equilibrium model

Designations of ash samples from PACT are given in **Chapter 3** (see **Table 3.6~Table 3.6**). The FactSage model was applied to both the original ash from PACT (refer to CFA1, CBA12 and CBA22 and re-burned PACT ash (refer to CFA2, CBA12 and CBA22). The modelling results showing the thermal equilibrium phase changes for the ashes with respect to the combustion temperature are presented in **Figure 6.23**.

For both the original PACT ash and re-burned ash, the slag start to be generated between 1100°C and 1200°C which is within 50°C of the deformation temperature of El Cerrejon coal 2 as deformation temperature in 50°C. The original fly ash from collection point 1 (CFA1) and re-burned fly ash (CFA2) show similar slag generation levels around the measured deformation temperature. A similar performance can be predicted for re-burned T-section ash (CBA12) and bottom ash (CBA22). The re-burned ashes are predicted to have slightly higher slag at 1300~1400°C compared to their original ash counterparts.

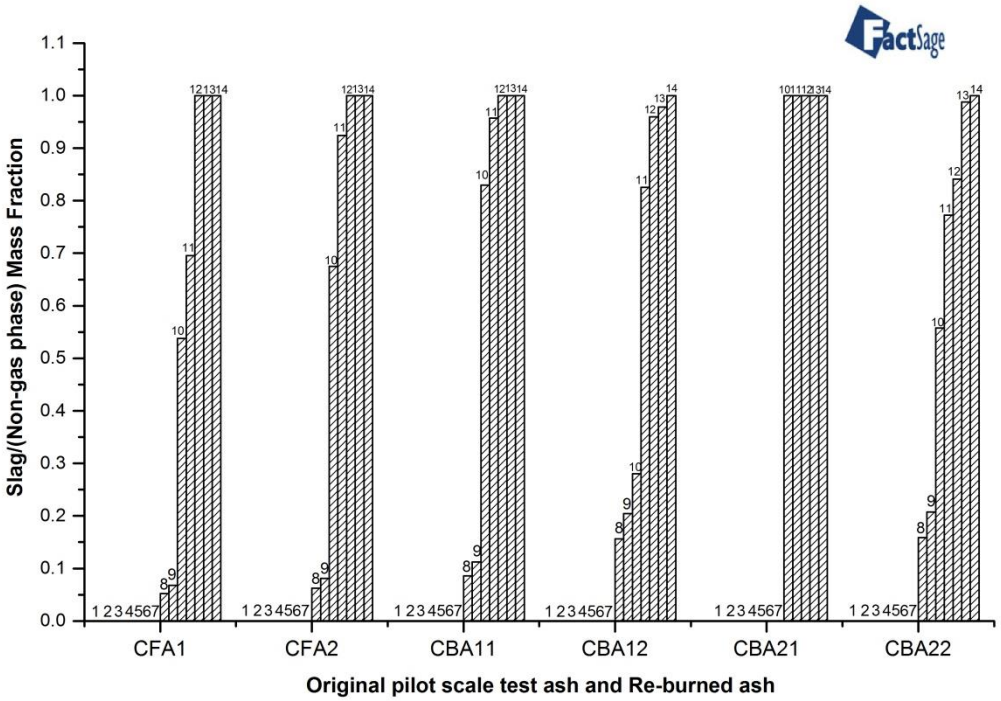

Figure 6.23 The change of slag mass fraction in non-gas phase with increase in temperature for each PACT ash samples as calculated by FactSage. Temperatures: 1, 500 ℃; 2, 600 ℃; 3, 700 ℃; 4, 800 ℃; 5, 900 ℃; 6, 1000 ℃; 7, 1100 ℃; 8, 1200 ℃; 9, 1300 ℃; 10, 1400 ℃; 11, 1500 ℃; 12, 1600 ℃; 13, 1700 ℃; 14, 1800 ℃.

The **Figure 6.24~Figure 6.29** shows the chemical composition of the predicted species calculated using FactSage for the original ash from PACT and their re-burned counterparts. Although they all show different solid content, similar compounds are predicted as SiO_2, $CaAl_2Si_2O_8$, Al_2SiO_5 and $KAlSi_2O_6$. The slag is mainly predicted as SiO_2, Al_2O_3 and CaO. The main reactions as shown by plots in **Figure 6.24~Figure 6.29** are listed as below:

$SiO_2(Solid) + CaAl_2Si_2O_8(Solid) + Al_2SiO_5(Solid) \rightarrow SiO_2(Slag) + CaO(Slag) + Al_2O_3(Slag)$ (>1200 ℃)

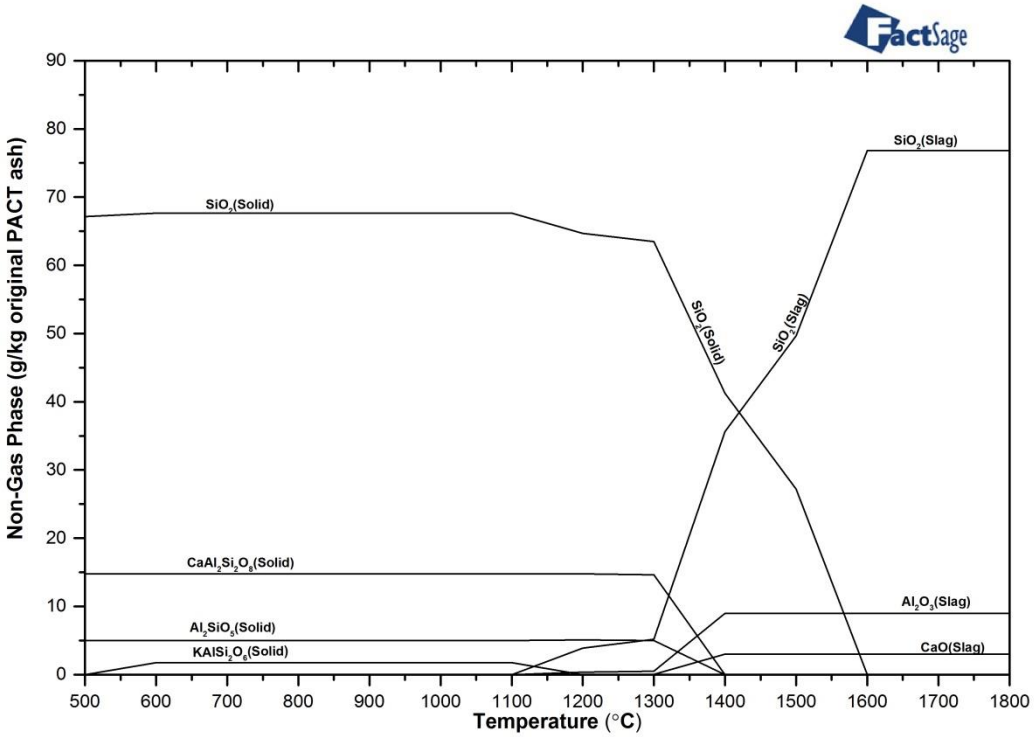

Figure 6.24 Stable solid phases in equilibrium with the slag phase for original ash of CFA1.

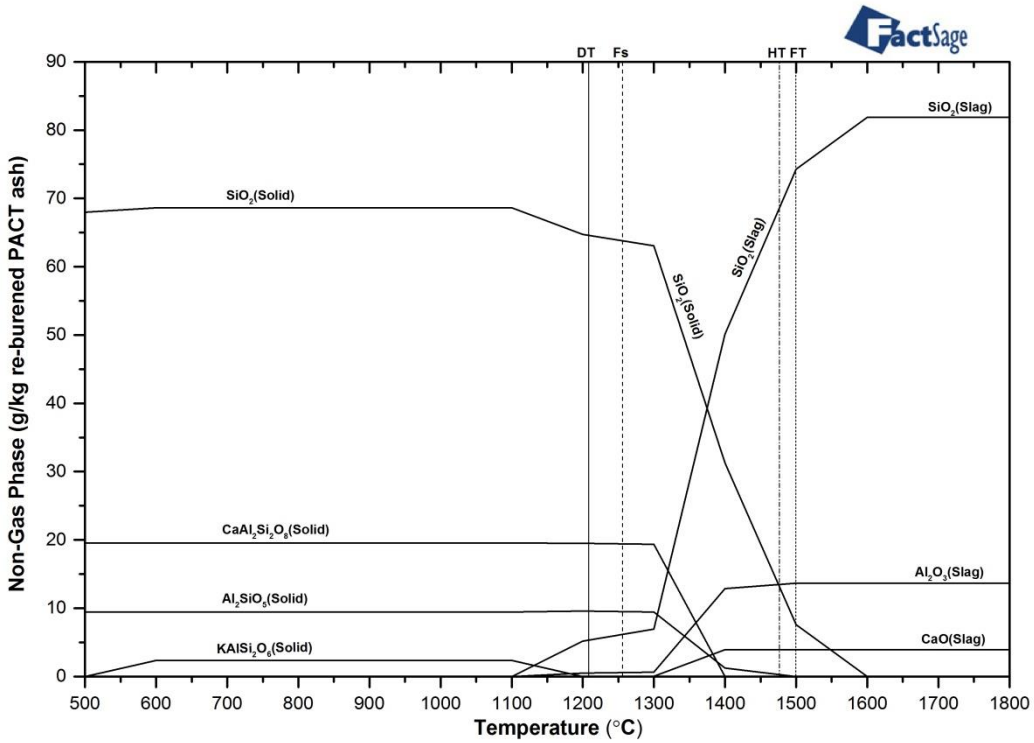

Figure 6.25 Stable solid phases in equilibrium with the slag phase for re-burned ash of CFA2.

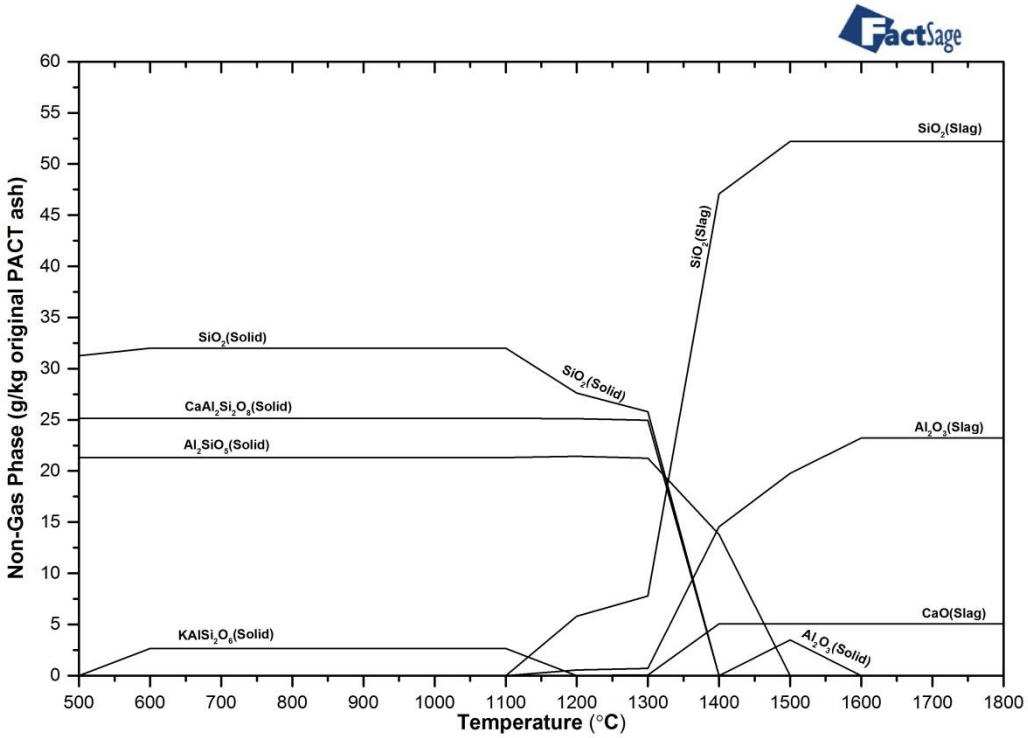

Figure 6.26 Stable solid phases in equilibrium with the slag phase for original ash of CBA11.

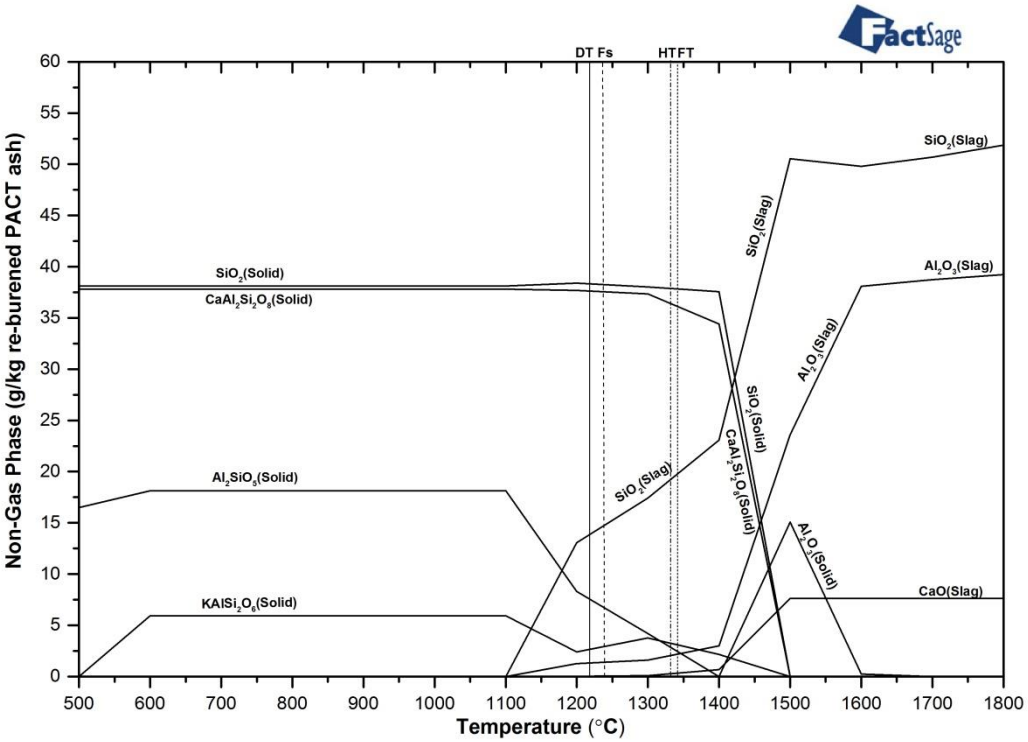

Figure 6.27 Stable solid phases in equilibrium with the slag phase for re-burned ash of CBA12.

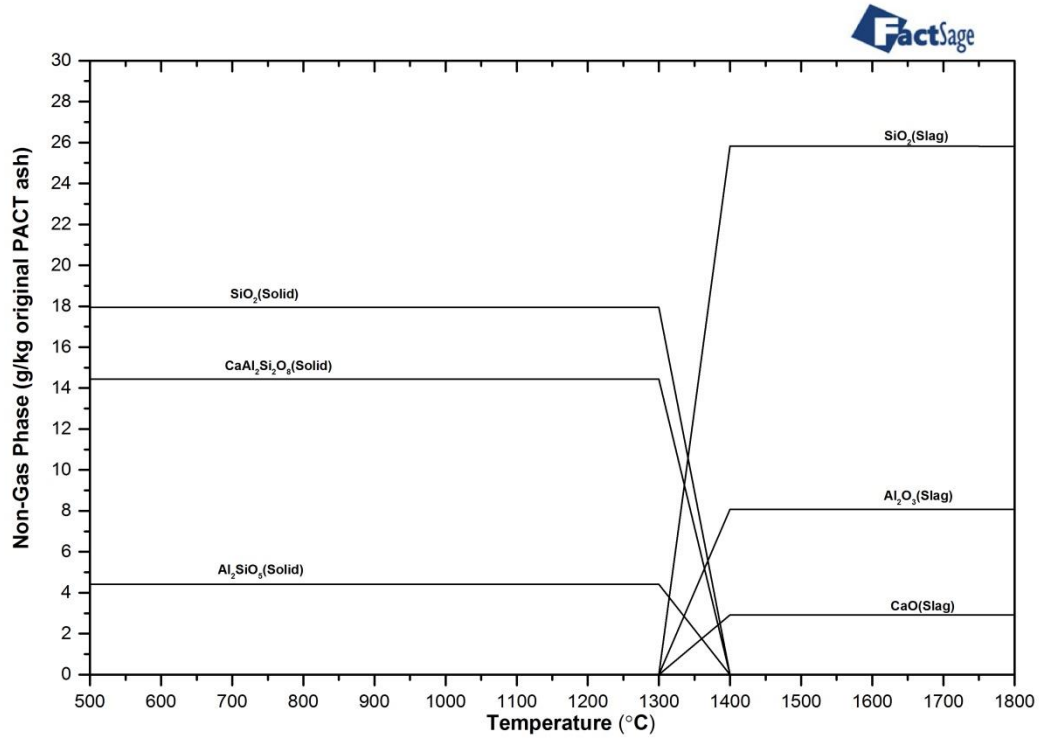

Figure 6.28 Stable solid phases in equilibrium with the slag phase for original ash of CBA21.

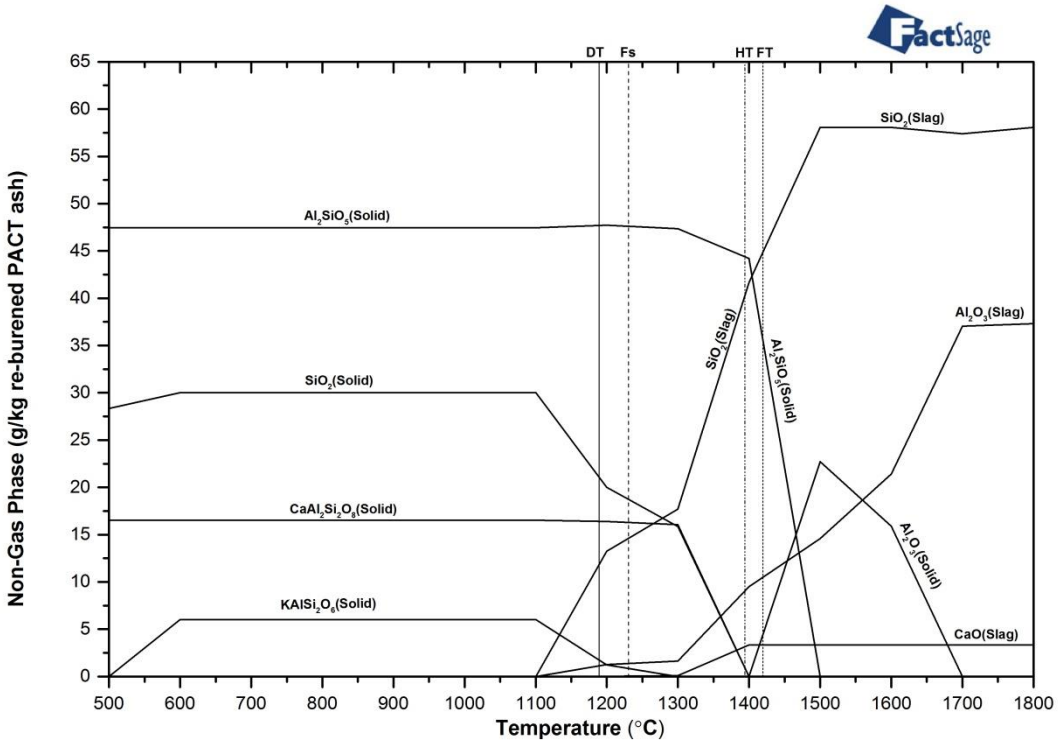

Figure 6.29 Stable solid phases in equilibrium with the slag phase for re-burned ash of CBA22.

6.4 Summaries

Ash viscosity models perform poorly for high biomass blend ratio. This is discussed in more detail in **Chapter 7**. FactSage (equilibrium) modelling fares better than the viscosity model in the prediction of ash slagging from high biomass blends. Comparison of predicted composition and XRD results is given in **Chapter 7**.

Chapter 7 General Discussion

In this study of ash deposition during air firing of high percentages of biomass with coal, ash was characterised by a number of methods for both composition and their behaviours. Full details of these tested fuels and their ashes are given in **Chapter 3** and **Chapter 4**. Ash fusion characteristics were also used to predict ash slagging and fouling potentials in **Chapter 5**. The laboratory results are used to understand the fusion performance and slagging/fouling potential of typical biomass, coal and their blends under different mixing conditions by using numerical indices in **Chapter 6**. Theoretical ash behaviour under boiler conditions is also investigated using the commercial software FactSage and the FACTPS and FTOxid database in **Chapter 6**.

Firstly, a further complication comes from comparing the results obtained here with previous published research because of the large difference in the nature of pine samples from different sources as well as the inaccuraccies introduced by the widespread use of XRF as an analytical tool, at least in the type of samples studied here. X-ray fluorescence (XRF) is a rapid method for testing biomass ash mineral composition. In this work, 20 different types of biomass ash were examined by wet chemical analysis (WCA) methods to determine the principal ash components. These results were compared with the respective results of XRF analysis to assess the reliability of the latter. The correlation between the two methods is summarized by linear regression functions. Although the XRF test for biomass ash prepared at 550°C is quick, evidence is presented here that the accuracy of test is not reliable. Biomass ash prepared using the method set out in the European Standard for biomass ash analysis (at 550 ℃) may be affected by residual unburnt carbon. When ashes are prepared at 550°C and then increased in temperature to 850 ℃ with 50 ℃/30mins (**Chapter 4)** the following calibration equation results: $Y_{[WCA]} = 1.09X_{[XRF]} + 0.37$ with $R^2 = 0.94$. The

reliability is not ideal. Increasing the ashing temperature to 815°C could make the ash composition stable for XRF test. Another equation for 5 different types of biomass ash could be expressed as: $Y_{[WCA]} = 0.99X_{[XRF]} + 0.13$ with $R^2 = 0.9971$. It is shown that the correlation between WCA and XRF is better for biomass ash prepared at the higher temperature (815 ℃).

The role of laboratory tests of solid pulverised fuels is to simulate their behaviour in an industrial combustor. The fuels were characterised by proximate and ultimate analyses and by the determination of their ash composition. The blends were made principally in two ways, by ashing the blended fuels together and then ashing (termed 'blended fuel ash') or by ashing separately and blending the ash from each fuel (termed 'ash blends'). There is a clear physical difference between the two ways of producing blends of ashes. In the first case the mixture of fuels will decompose in a way in which the volatiles and solid matrix of each component can interact with each other and this will influence the final composition. Ash produced independently behave in a similar way to that in a large scale combustor and there could be immediate interaction between the two sets of ash especially if some of the ash melts.

The data obtained were used to calculate indices to determine the slagging and fouling potential of coal-pine and coal-wheat straw and their blends. **Figure 7.1 and Figure 7.2** are plots of values for different numerical indices **(a)** and the main metals, silicon and phosphorus compositions expressed as oxides **(b)** for two different co-firing ratio. In **Figure 7.1** $R_{b/a}$ results indicate that pine wood ash has a higher slagging potential than coal ash, which is not consistent with in the ash fusion measurements. According to **Chapter 5**, though there are some differences in the predictions of the slagging potential from the different approaches, similar ash melting behaviours were observed by the ash fusion tests and STA-MS experimental methods. Pine ash has a higher

shrinkage starting temperature, deformation temperature, hemisphere temperature and flow temperature with a much higher mass loss process than El Cerrejon coal 1 ash. In **Figure 7.1**, during the co-combustion of these two fuels, it was found that higher percentages of pine in the fuel blends resulted in a prediction of increased slagging propensity. In contrast, the ash fusion tests were less conclusive, since the ash fusion temperature was lowest for the 50/50 fuel blend than for any other blend tested here. This may be associated with the contribution of the significant change of SiO_2 and CaO content. The fuel ash blends have different fusion temperatures. Shrinkage and/or swelling were also observed during the ash fusion tests. In **Figure 7.1 (b)**, it's interesting to see that when the CaO content greatly exceeds the Al_2O_3 content, the values of Sx drop significantly. This was also observed in **Figure 7.2** for coal-wheat straw blends. During this simulated co-combustion of El Cerrejon coal 2 and wheat straw, higher percentages of wheat straw in the fuel blends results in increases in $R_{b/a}$ and AI which predict increased slagging and fouling propensities. The 80% wheat straw fuel blends show a decreased slagging potential, which was not observed in the ash fusion test results in **Chapter 5**.

The results indicate that there is very little correlation between the indices ($R_{b/a}$, AI, Sx) and the measured fusion temperatures, represented by Fs. Consequently, more complex modelling is justified and in this work an equilibrium model, FactSage, was tested, as well as some popular ash viscosity models.

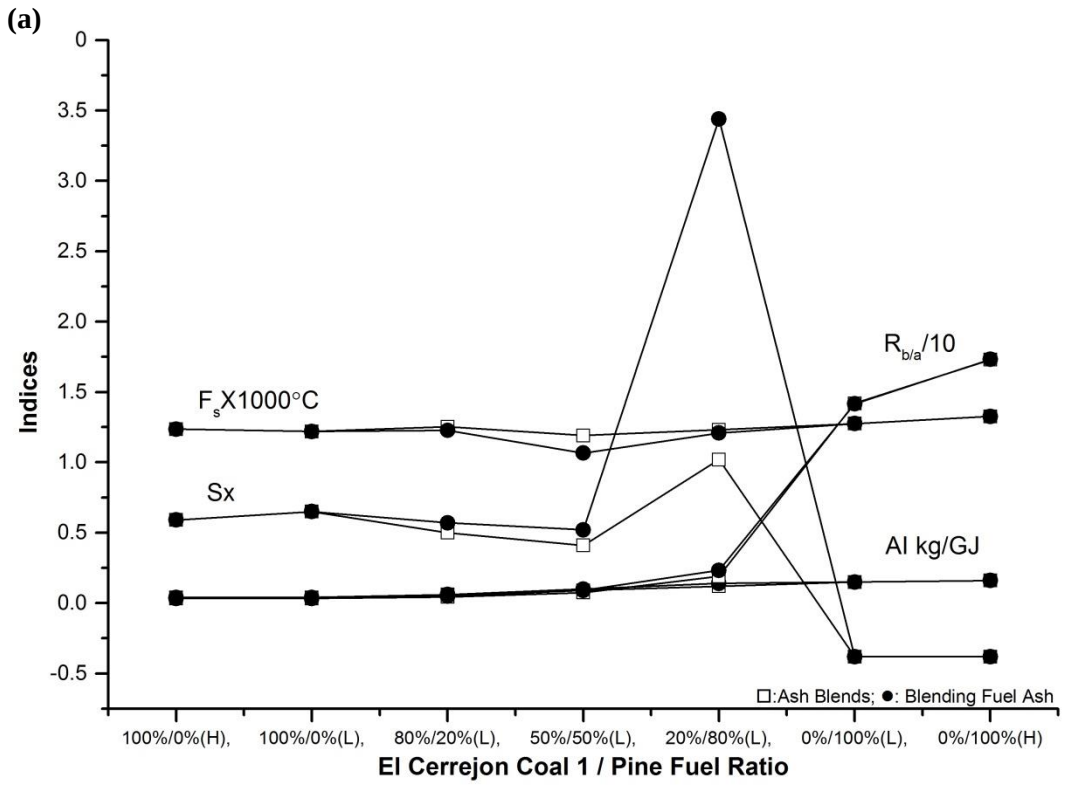

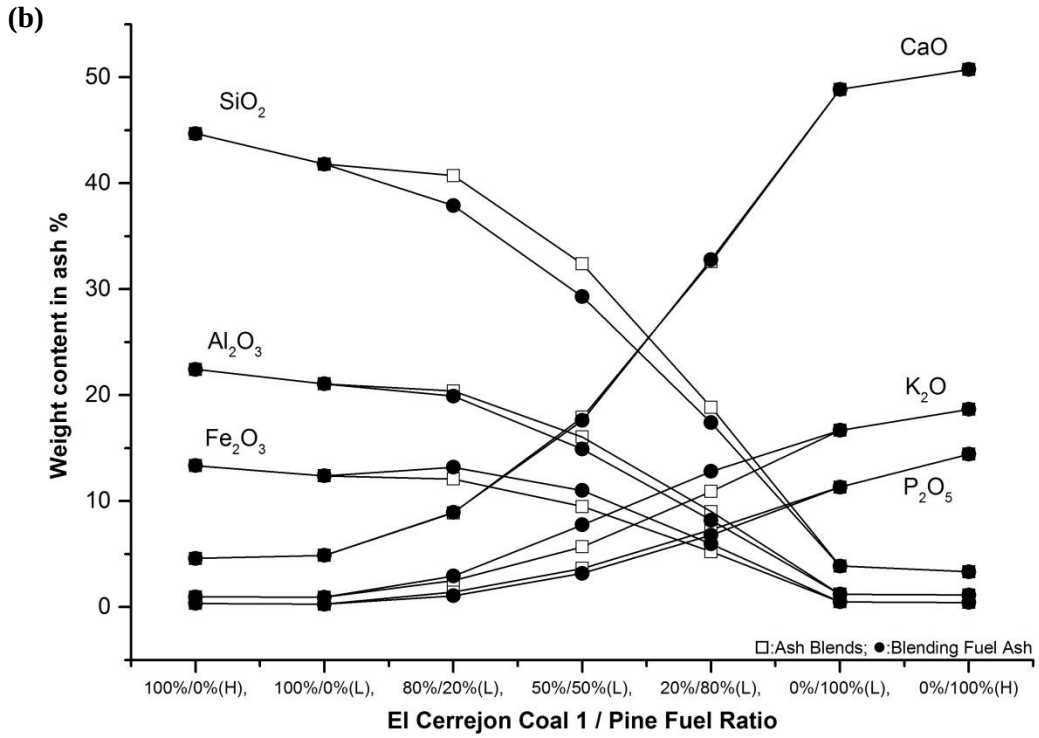

Figure 7.1 (a) Variation of values for different numerical indices for different El Cerrejon coal 1 / pine ratios, and **(b)** Composition (wt%) of main inorganics in the ash (expressed as oxides) with ashing conditions: (H)-800 ℃; (L)-550 ℃.

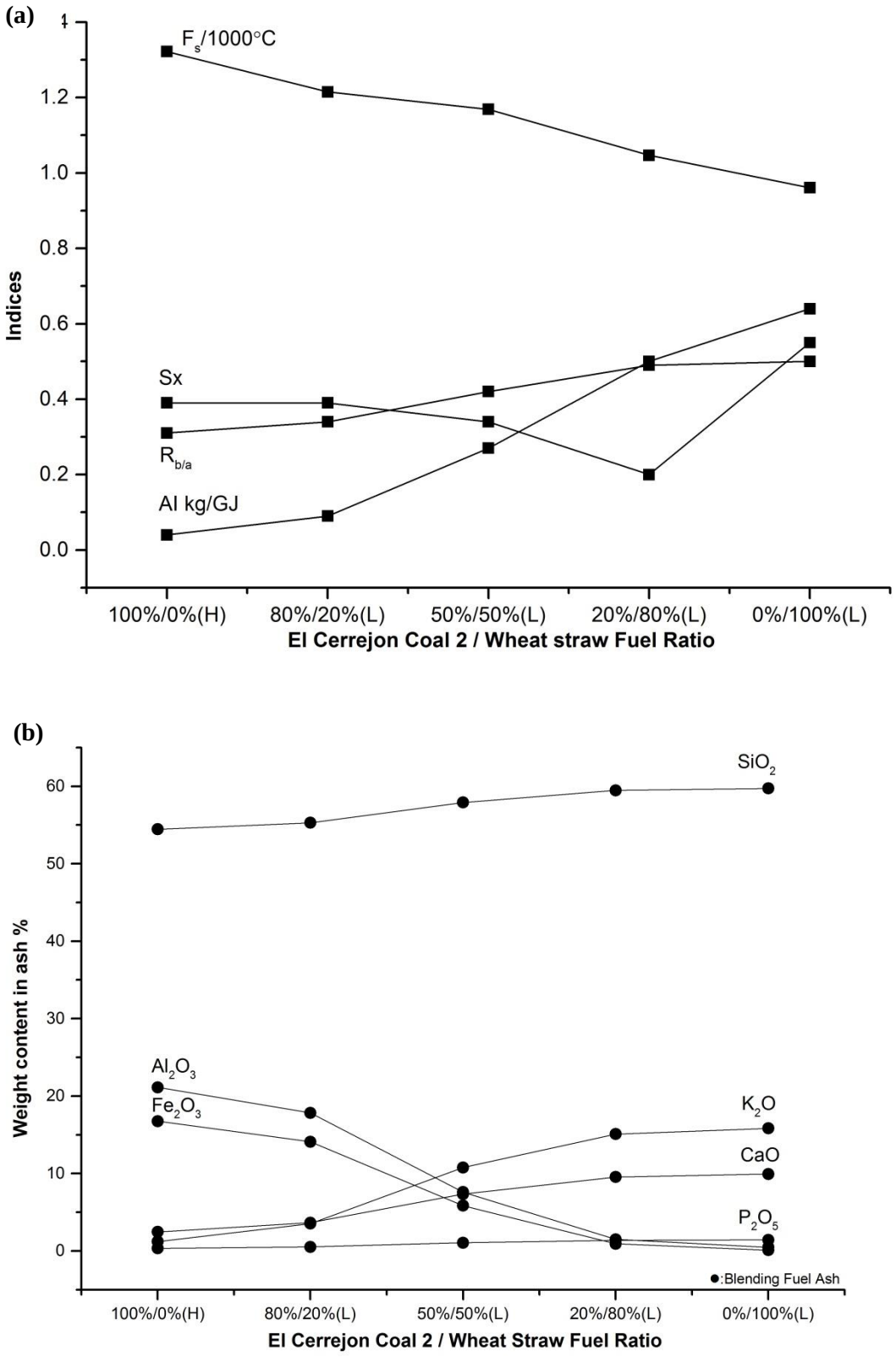

Figure 7.2 (a) Variation of values for different numerical indices for different El Cerrejon coal 2 /wheat straw ratios, and **(b)** composition (wt%) of main inorganics in the ash (expressed as oxides) with ashing conditions: (H)-800 ℃; (L)-550 ℃.

Using models described in **Chapter 6**, the ash viscosity as a function of temperature was calculated for different fuels and their blends. **Table 7.1** lists the relevant temperature needed for a particular viscosity and compares these predictions with the ash fusion temperatures.

Table 7.1 Comparison between relevant temperature of particular viscosity and ash fusion temperatures.

Samples	Temperature for viscosity [1000Pa·s] (℃)	Temperature for viscosity [100Pa·s] (℃)	Temperature for viscosity [10Pa·s] (℃)	SST (℃)	DT (℃)	HT (℃)	FT (℃)
[a]PCC1	1350	1600	>2000	980	1195	1315	1330
[a]PCC2	1450	1650	>2000	1005	1205	1360	1375
[a]PCC3	1605	1890	>2000	1050	1210	1370	1380
[b]PPA1	<500	<500	<500	1020	1225	1480	1510
[b]PPA2	<500	<500	500	1085	1285	1495	1515
[a]WS1	1745	>2000	>2000	855	925	1105	1165
[b]WS1	1320	1475	1550	855	925	1105	1165
[a]WS2	1355	1705	>2000	N/A	N/A	N/A	N/A
[b]WS2	1250	1355	1485	N/A	N/A	N/A	N/A
[a]WWP1	795	960	1305	1225	1245	1290	1295
[b]WWP1	1090	1195	1290	1225	1245	1290	1295
[a]WWP2	<500	<500	650	N/A	N/A	N/A	N/A
[b]WWP2	1190	1285	1390	N/A	N/A	N/A	N/A
[a]CA28	1355	1570	2000	1170	1210	1320	1335
[a]CA55	1145	1300	1650	1085	1180	1235	1250
[a]CA82	585	670	800	1120	1245	1290	1300
[a]BFPC28	1275	1480	1885	1095	1195	1265	1295
[a]BFPC55	1180	1195	1500	955	1025	1230	1245
[a]BFPC82	<500	550	620	1075	1210	1300	1325
[a]BWCA28	1605	1910	>2000	815	1010	1195	1225

[a]BWCA55	1685	>2000	>2000	860	1150	1245	1280
[a]BWCA82	1745	>2000	>2000	1080	1195	1295	1320
[a]CFA1	975	1170	1785	N/A	N/A	N/A	N/A
[a]CFA2	945	1185	1595	1160	1205	1475	1500
[a]CBA11	660	850	955	N/A	N/A	N/A	N/A
[a]CBA12	985	1120	1395	1060	1220	1335	1345
[b]CBA21	1370	1460	1550	N/A	N/A	N/A	N/A
[a]CBA22	1270	1420	1790	1065	1190	1395	1420

[a]: calculated by modified Watt-Fereday model [205-206]; [b]: calculated by Streeter model [209]. [1]: Viscosity of glass at its working temperature; [2]: Viscosity of glass at its melting temperature.

Comparing the temperature of glass working point viscosity (ca 1000 Pas) and the glass melting point viscosity (ca10 Pas) with the ash fusion temperatures, most temperatures of glass working point viscosity and melting point viscosity are higher than deformation temperatures and flow temperatures respectively. The viscosity models failed severely for PPA, WWP, and were poor for high biomass ash blends CA82 and BFPC82. The viscosity model over predicted ash viscosity in most cases and best results were for PCC1, CA28, CA55, BFPC28 and BFPC55.

As discussed in **Chapter 5** and **Chapter 6**, the fusion temperatures and behaviour observed for the different ash samples were evaluated by the FactSage model, which resulted in similar phase changes with temperature to the ones observed experimentally. FactSage also predicts ash composition with temperature, and these predictions are compared here with experimental XRD results. These are listed in **Table 7.2~Table7.6** as below. The compounds marked by the symbol "✓" are matched both by FactSage and XRD. According to the tables, most XRD tested results could be predicted by FactSage and exist in the calculated temperature range. Less well predicted were the 20% El Cerrejon coal 2 / 80% wheat straw co-firing ash (BWCA82) and the 550°C white

wood pellet ash (WWP1). Some of the more complex minerals predicted by FactSage were not detected by XRD, but this may be due to low concentrations.

The FactSage model preforms more reliability than numerical indices for the prediction of coal, biomass combustion and co-firing slagging potential, especially the phase change prediction, the transferring of chemical matters were deduced well. **Figure 7.3** indicates the comparison between Fs (an experimental index) and temperature when slag mass fraction ≥0.75 during phase change of different ash samples which were predicted by FactSage models in **Chapter 6**. For blends: CA28, CA82, BWCA28, BWCA55, similar Fs and ≥75% mass fraction slag predicted temperature are presented. The pine and wheat straw ash show higher predicted temperatures for ≥75% mass fraction slag than Fs calculated by AFT results. The similar performance is also observed in CBA12, CA55, CBA22, BWCA82, PCC2 and PCC3. In contrast, the white wood pellet ash (WWP) and re-burned fly ash (CFA2) show higher Fs than the temperature of ≥75% mass fraction slag.

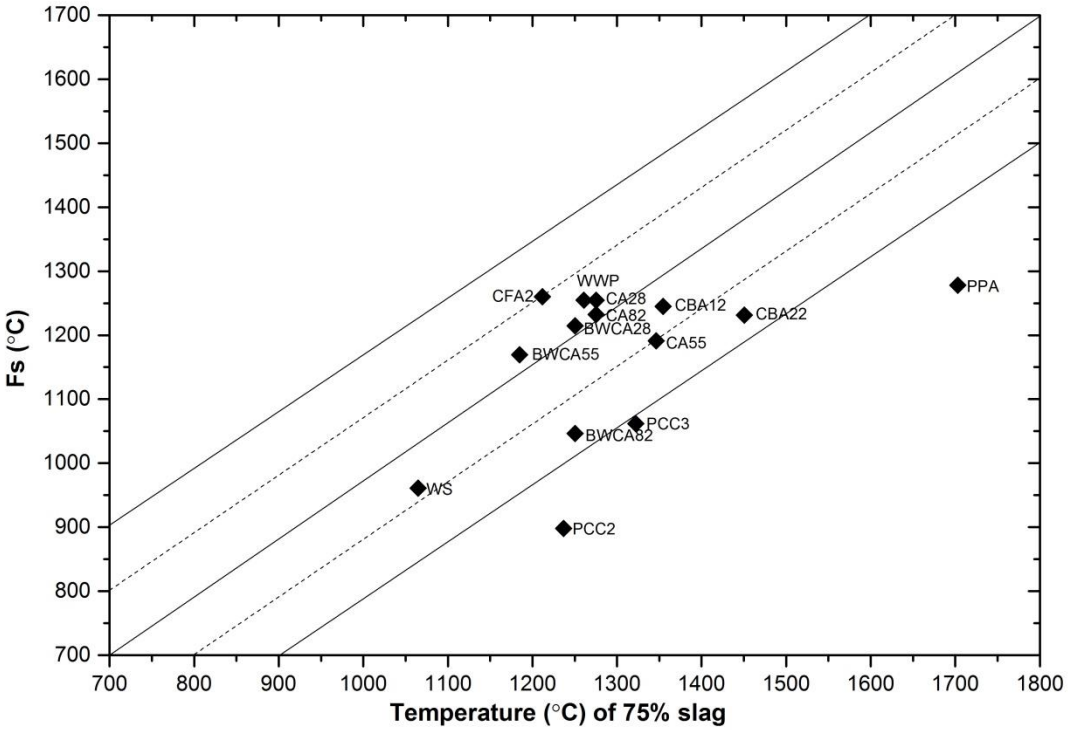

Figure 7.3 Comparison between Fs and temperature when slag mass fraction ≥0.75 during phase change (FactSage model of **Figure 6.9**, Figure **6.15**, **Figure 6.21**, and **Figure 6.23**) of different ash samples.

In summary, the ash viscosity models give reasonable predictions for coal and high-coal blends, but were often found to fail for biomass of high-biomass blends. FactSage showed good agreements with XRD data for the presence of mineral phases with temperature. It also performed the best over a wide range of fuel blends for the prediction of the slagging temperature, but tended to over predict, typically by 100~200 ℃.

Table 7.2 The comparison of mineral phase of El Cerrejon coal 1 and 2 by FactSage prediction and X-ray diffraction.

El Cerrejon Coal 1				El Cerrejon Coal 2		
FactSage		XRD		FactSage		XRD
Mineral Phase	Temperature range (℃)	PCC1(550 ℃)	PCC2(800 ℃)	Mineral Phase	Temperature range (℃)	PCC3(800 ℃)
$CaSO_4$	500~900	✓	✓	SiO_2	500~1200	✓
$NaAlSi_3O_8$	500~900		✓	Al_2SiO_5	500~1100	✓
Na_2SO_4	500~1000	✓	✓	Fe_2O_3	500~1200	
$MgSiO_3$	500~700	✓		$KAl(SO_4)_2$	500	
$Ca_5HO_{13}P_3$	500~1200	✓	✓	$CaSO_4$	500~700	
$Na_2Ca_3Si_6O_{16}$	500~600, 800~900	✓		Na_2SO_4	500	
Fe_2O_3	500~800, 1200	✓	✓	$MgSO_4$	500	
Mn_2O_3	500~900	✓	✓	TiO_2	500~1200	✓
$K_3Na(SO_4)_2$	500~600	✓		$AlPO_4$	500, 1100~1400	
$CaMgSi_2O_6$	700~1000		✓	$Mg_3P_2O_8$	500~700	
$Ca_3Fe_2Si_3O_{12}$	900~1100			$MnSO_4$	500~600	
$KAlSi_2O_6$	900			$NaAlSi_3O_8$	600~900	✓

$Na_2Ca_2Si_3O_9$	1000			$Mg_2Al_4Si_5O_{18}$	600~1200	✓
$CaSiO_3$	1000			$KAlSi_2O_6$	600~1200	✓
$Ca_3(PO_4)_2$	1300~1700			$Mn_2Al_4Si_5O_{18}$	700~1100	✓
SiO_2	500~800	✓	✓	$CaAl_2Si_2O_8$	800~1200	✓
				$Ca_3(PO_4)_2$	800~1000	✓
				$Al_2Fe_2O_6$	1200	

Table 7.3 The comparison of mineral phase of biomass by FactSage prediction and X-ray diffraction.

Pine				Straw				White wood pellet			
FactSage		XRD		FactSage		XRD		FactSage		XRD	
Mineral Phase	Temperature range (℃)	PPA1 (550 ℃)	PPA2 (800 ℃)	Mineral Phase	Temperature range (℃)	WS1 (550 ℃)	WS2 (800 ℃)	Mineral Phase	Temperature range (℃)	WWP1 (550 ℃)	WWP2 (800 ℃)
$KAl(SO_4)_2$	500	✓		$K_2Si_4O_9$	500~600	✓		$Ca_3MgSi_2O_8$	800~1200	✓	✓
$MnSO_4$	500~600	✓		$Na_2Ca_3Si_6O_{16}$	500~1000	✓	✓	Mg_2SiO_4	800~1200	✓	✓
Al_2O_3	500~1000, 1300~1800	✓	✓	$CaMgSi_2O_6$	500~1200	✓	✓	$Ca_5HO_{13}P_3$	800~1300	✓	✓
Al_2SiO_5	500~600	✓		$Ca_5HO_{13}P_3$	500~1100	✓	✓	Mn_2O_3	800~1100	✓	✓
Fe_2O_3	500~1100	✓	✓	$MgSiO_3$	500~700	✓		$CaTiO_3$	800~1000	✓	
$MgSO_4$	500	✓		SiO_2	500~600, 900	✓	✓	$Ca_3(PO_4)_2$	1400~1800		
$CaSO_4$	500~800	✓	✓	$CaSiTiO_5$	500~900	✓					
$K_3Na(SO_4)_2$	500~800	✓	✓	Mn_2O_3	500~800	✓	✓				
Na_2SO_4	500	✓		Fe_2O_3	500~700	✓	✓				
TiO_2	500~900	✓	✓	$MgSiO_3$	900~1100						
K_2SO_4	600~1000		✓	$Ca_3Fe_2Si_3O_{12}$	1000~1200						

$Mg_4Al_{10}Si_2O_{23}$	600~700			$CaSiO_3$	1000~1200						
Mn_2O_3	700~800		✓	$MnSiO_3$	1000~1800						
$KAlSi_2O_6$	700~900,1300			$Ca_3(PO_4)_2$	1200~1600						
$CaMg_2Al_{16}O_{27}$	800~1400										
$MnAl_2O_4$	900~1500										
$Ca_2Mg_2Al_{28}O_{46}$	900~1200										
$NaAlSiO_4$	900~1100										
$KAlSiO_4$	1000~1200										
$CaTiO_3$	1000~1100										
KAl_9O_{14}	1100~1200										
$Al_2Fe_2O_6$	1200~1300										

Table 7.4 The comparison of mineral phase of El Cerrejon coal 1 and pine co-firing by FactSage prediction and X-ray diffraction.

BFPC28			BFPC55			BFPC82		
FactSage		XRD	FactSage		XRD	FactSage		XRD
Mineral Phase	Temperature range (℃)	550 ℃	Mineral Phase	Temperature range (℃)	550 ℃	Mineral Phase	Temperature range (℃)	550 ℃
SiO_2	500~800	✓	$CaSO_4$	500~900	✓	$CaSO_4$	500~900	✓
Al_2SiO_5	500~700	✓	SiO_2	500~800	✓	$K_3Na(SO_4)_2$	500, 700~800	✓
$CaSO_4$	500~800	✓	$KAl(SO_4)_2$	500	✓	SiO_2	500~600	✓
$KAl(SO_4)_2$	500	✓	Al_2SiO_5	500~700	✓	Al_2SiO_5	500	✓
Fe_2O_3	500~1200	✓	Fe_2O_3	500~900	✓	$Mg_3P_2O_8$	500~800	✓
$MgSO_4$	500	✓	$K_3Na(SO_4)_2$	500	✓	K_2SO_4	500~600, 1000~1100	✓
Na_2SO_4	500		$Mg_3P_2O_8$	500~700	✓	$AlPO_4$	500~700	✓
$AlPO_4$	500	✓	Na_2SO_4	500	✓	Fe_2O_3	500~800, 1100	✓
TiO_2	500~1100	✓	$AlPO_4$	500~700	✓	TiO_2	500~700	✓
$NaAlSi_3O_8$	600~900		$MnSO_4$	400~600	✓	$MnSO_4$	500	✓
K_2SO_4	600		$KAlSi_2O_6$	600~1400		$KAlSi_2O_6$	600~900	
$Mg_2Al_4Si_5O_{18}$	600~1200		$NaAlSi_3O_8$	600~800		$NaAlSi_3O_8$	600	

$Mg_3P_2O_8$	600~700		$Mn_2Al_4Si_5O_{18}$	700		Mn_2O_3	600~900	
$KAlSi_2O_6$	600~1400		$Mg_2Al_4Si_5O_{18}$	800		$Ca_3(PO_4)_2$	700, 1500~1800	
$CaAl_2Si_2O_8$	800~1300		$Ca_5HO_{13}P_3$	800~1200		Na_2SO_4	700	
$Ca_3(PO_4)_2$	800,1000~1500		$Mg_4Al_{10}Si_2O_{23}$	800		$Ca_5HO_{13}P_3$	800~1400	
$Ca_5HO_{13}P_3$	900		$CaAl_2Si_2O_8$	800~1100		$NaAlSiO_4$	800~900	
$MgSiO_3$	900		Mn_2O_3	800~900		$MgTi_2O_5$	800	
Mg_2SiO_4	1000		$CaMgSi_2O6$	900		$K_2Ca_2(SO_4)_3$	900~1000	
			$NaAlSiO_4$	900~1000		Mg2SiO4	900	
			$CaSiTiO_5$	900		$CaTiO_3$	900~1200	
			$Ca_3Fe_2Si_3O_{12}$	1000~1200		$Ca_3MgSi_2O_8$	1000~1200	
			$CaTiO_3$	1000~1200		$Ca_3Fe_2Si_3O_{12}$	1000	
			TiO_2	500~800	✓	$Ca_2Al_2SiO_7$	1000~1200	
			$Ca_2MgSi_2O_7$	1000		$Ca_3(PO_4)_2$	600, 1500~1800	
			$Ca_3(PO4)_2$	1300~1700				

Table 7.5 The comparison of mineral phase of El Cerrejon coal 2 and wheat straw co-firing by FactSage prediction and X-ray diffraction.

BWCA28			BWCA55			BWCA82		
FactSage		XRD	FactSage		XRD	FactSage		XRD
Mineral Phase	Temperature range (℃)	550 ℃	Mineral Phase	Temperature range (℃)	550 ℃	Mineral Phase	Temperature range (℃)	550 ℃
SiO_2	500~900	✓	$KAlSi_3O_8$	500	✓	$Na_2Ca_3Si_6O_{16}$	800~900	
Al_2SiO_5	500~700	✓	SiO_2	500~700	✓	$CaMgSi_2O_6$	800~1300	✓
Fe_2O_3	500~1200	✓	$NaAlSi_3O_8$	500~800	✓	K_2SO_4	800~900	✓
$CaSO_4$	500~700	✓	K_2SO_4	500~700	✓	$Ca_5HO_{13}P_3$	900~1100	✓
$K_3Na(SO_4)_2$	500	✓	$Na_2Ca_3Si_6O_{16}$	500~700	✓	Fe_2O_3	800	✓
Na_2SO_4	500		$CaSO_4$	500~800	✓	Mn_2O_3	800~900	✓
$MgSO_4$	500	✓	Fe_2O_3	500~1200	✓	$Ca_3Fe_2Si_3O_{12}$	900~1200	
TiO_2	500~1200	✓	$MgSiO_3$	500~600	✓	$CaSiO_3$	1000~1300	
$Mg_3P_2O_8$	500~700	✓	$Ca_5HO_{13}P_3$	500~1100	✓	$MnSiO_3$	1000~1100	
$MnSO_4$	500~600	✓	TiO_2	500	✓	$Ca_3(PO_4)_2$	1200~1600	
$NaAlSi_3O_8$	600~900		Mn_2O_3	500~1000	✓			
$KAlSi_2O_6$	600~1000, 1300~1600		$KAlSi_2O_6$	600~700， 900				
$Mg_2Al_4Si_5O_{18}$	600~1200		$CaSiTiO_5$	600~1100				
$Mn_2Al_4Si_5O_{18}$	700~1000		$CaMgSi_2O_6$	700~1300				
$CaAl_2Si_2O_8$	800~1200		Mg_2SiO_4	800				
$Ca_3(PO_4)_2$	800~1200		$Ca_3Fe_2Si_3O_{12}$	900~1200				
$AlPO_4$	1300~1400		$Ca_3(PO_4)_2$	1200~1600				

Table 7.6 The comparison of mineral phase of original PACT ash and re-burned ash by FactSage prediction and X-ray diffraction.

CFA1			CFA2			CBA11			CBA12			CBA21			CBA22		
FactSage		XRD	FactSage		XRD	FactSage		XRD	FactSage		XRD	FactSage		XRD	FactSage		XRD
Mineral Phase	Temperature range (℃)	800°C	Mineral Phase	Temperature range (℃)	800°C	Mineral Phase	Temperature range (℃)	800°C	Mineral Phase	Temperature range (℃)	800°C	Mineral Phase	Temperature range (℃)	800°C	Mineral Phase	Temperature range (℃)	800°C
SiO_2	500~1500	✓	SiO_2	500~1500	✓	SiO_2	500~1500	✓	Al_2SiO_5	500~1400	✓	SiO_2	500~1300	✓	Al_2SiO5	500~1400	✓
$CaAl_2Si_2O_8$	500~1300	✓	$CaAl_2Si_2O_8$	500~1300	✓	$CaAl_2Si_2O_8$	500~1300	✓	$CaAl_2Si_2O_8$	500~1400	✓	$CaAl_2Si_2O_8$	500~1300	✓	SiO_2	500~1300	✓
Al_2SiO_5	500~1300	✓	Al_2SiO_5	500~1400	✓	Al_2SiO_5	500~1400	✓	SiO_2	500~1300	✓	Al_2SiO_5	500~1300	✓	$CaAl_2Si_2O_8$	500~1300	✓
$KAlSi_3O_8$	500		$KAlSi_3O_8$	500	✓	$KAlSi_3O_8$	500	✓	$KAlSi_3O_8$	500	✓				$KAlSi_3O_8$	500	✓
$KAlSi_2O_6$	600~1100		$KAlSi_2O_6$	600~1100		$KAlSi_2O_6$	600~1100		$KAlSi_2O_6$	500~1400					$KAlSi_2O_6$	600~1200	
						Al_2O_3	1500		Al_2O_3	1500~1600					Al_2O_3	1500~1600	

Chapter 8 Conclusions

Knowledge of the composition of the inorganic content of solid fuel is important in relation to the combustion behaviour in furnaces since it influences corrosion and ash deposition in cooler regions such as heat exchange surfaces. Results presented in this study concern firstly, the analysis of the inorganics present in solid fuels and their blends, and secondly the mineral phases present when they are burned, either under laboratory or pilot scale testing conditions.

In terms of analysis of inorganics, both wet chemical methods and XRF are used for the ashes under study. Sometimes there is a deviation between the two methods for some elements, and this is most significant when there is high carbon in ash or where vaporisation of volatile inorganics takes place. A revised method of XRF analysis was developed which gave much better correlation with the wet chemical analysis methods. 815°C was used as the ashing temperature and 1100°C (for 9 mins) as the glass fusion temperature. This appears to give a good compromise of minimising C in ash without significant loss of volatile metals. The correlation equation is recommended as $Y_{[WCA]}=0.9927X_{[XRF]}+0.1314$ with $R^2=0.9971$.

The ash fusion characteristics of a range coal and biomass ashes and their blends have been determined. High carbon in ash can make determination of characteristic temperatures difficult due to excessive release of gas causing swelling and even breaking of the ash test pieces. STA-MS can easily identify those samples high in carbon from detection of both rapid weight loss at 600°C and evolution of CO, CO_2 and H_2O. Of the fuels studied (El Cerrejon coal (2 batches), pine, wheat straw, white wood pellets), wheat straw has the lowest fusion temperature and acts to lower the melting temperature of ash when blended with El Cerrejon coal. Pine has the highest

fusion temperature and acts to increase the melting temperature of ash when blended with the coal. Ash produced in pilot scale combustion of the coal had very high C in ash and required an additional ashing step in the laboratory prior to study. These ashes had different fusion characteristics (generally) than the laboratory prepared ashes, possibly due to ash fractionation in the high temperature combustion tests.

The inorganic compounds analysed in the ash were used to calculate indices to determine the slagging and fouling potential of pure fuel ash, ash blends and their fuel blends ash. Base-to-acid ratio ($R_{b/a}$) results indicate that pine ash has a higher slagging potential than coal ash, which is not substantiated by the ash fusion measurements. Pine ash has a higher shrinkage starting temperature, deformation temperature, hemisphere temperature and flow temperature with a much higher mass loss process than El Cerrejon coal 1 ash. High percentages of pine in the fuel blend resulted in decreased slagging propensity. In contrast, the ash fusion tests were less conclusive, since the ash fusion temperature was lowest for the 50/50 fuel blend than for any other blend tested here. This may be attributed to the significant change of SiO_2 and CaO content. During this simulated co-combustion of El Cerrejon coal 2 and wheat straw, higher percentages of wheat straw in the fuel blends, as indicated by $R_{b/a}$ and AI results in increased slagging and fouling propensities. An exception is the 80% wheat straw fuel blends which show a decreased slagging potential, and is in contrast with the ash fusion test results.

The coal numerical slagging index (Sx) performs better and closer to the laboratory test results than the other indices to predict the slagging tendency of co-firing with different fuel ratio. The viscosity model results of co-firing tend to predict higher temperatures than seen in ash fusion test results for ash softening and melting. The pine ash is poorly predicted by both the Streeter model [209] and the modified Wat-

Fereday model [205-206]. For white wood pellet and wheat straw, the Streeter model shows more reasonable results than the modified Watt-Fereday model, but is still under predicting the ash softening temperatures considerably. Ash viscosity models perform reasonable predictions for coal and high-coal blends, but poorly for biomass and high-biomass blend.

The fusion temperatures and behaviour observed for the different ash samples were used to validate the FactSage model, which resulted in similar phase changes with temperature to the ones observed experimentally. XRD showed complex interactions between inorganics which changed with biomass type, blend ratio and temperature. Most minerals present in the XRD tested results could be predicted by FactSage in the correct temperature range except the 20% El Cerrejon coal 2 / 80% wheat straw co-firing ash (BWCA82) and 550°C white wood pellet ash (WWP1). The FactSage model showed good agreements with XRD data for the presence of mineral phases with temperature.

The FactSage model also preforms more reliability than numerical indices and viscosity models for the prediction of coal, biomass combustion and co-firing slagging potential, especially the phase change prediction. It also performed the best over a wide range of fuel blends for the prediction of the slagging temperature, but tended to over predict, typically by 100 ℃ for most of the blends studied.

Future Works

The above lists of limitations give rise to a number of new research opportunities and blank areas:

- Compile and systematize a reliable database related to the composition of biomass ashes. More biomass and fuel blends ash could be tested by X-ray fluorescence and wet chemical method. The results could be used to enhance the accuracy of calibration system.
- Indicate the potential applications and environmental risks connected with biomass ashes. The viscosities of ash samples could be tested with increasing temperatures by temperature rotary viscosimeter, and compared with numerical viscosity model results.
- The fuel blends could be burned in pilot scale boiler at the UKCCSPACT site in Sheffield. Describe the basic findings and clarify some of the problems associated with the composition of these combustion residues. Supply additional results related to composition and properties of biomass ashes. The ash weight from different collection point should be weighted according to quantitative fuel combustion.
- The pilot scale burned ash should be analysed follow the experimental procedure as introduced in this study. Understand how the fundamental knowledge on the composition and properties may be exploited for the most innovative and sustainable utilization of these combustion residues. And the tested results could be compared with laboratory scale test results to improve modelling results from FactSage model.

References

[1] The Intergovernmental Panel on Climate Change (IPCC). 2014. Climate Change 2014. [Online]. [Accessed 10 October 2015]. Available from: https://www.ipcc.ch/report/ar5/wg3/.

[2] Carbon Dioxide Information Analysis Center. 2014. A Compendium of Data on Global Change 2008. [Online]. [Accessed 10 October 2015]. Available from: http://cdiac.ornl.gov/CO2_Emission/.

[3] European Commission. 2014. Report from the commission to the European parliament and the council. COM 689, pp.final.

[4] European Commission. 2015. Causes of climate change. [Online]. [Accessed October 2015]. Available from: http://ec.europa.eu/clima/change/causes/index_en.htm.

[5] U.S. Energy Information Administration (EIA). 2002. Biomass for Electricity Generation. [Online]. [Accessed 12 October 2015]. Available from: http://www.eia.gov/oiaf/analysispaper/biomass/.

[6] World energy council. 2013. World Energy Resources 2013. [Online]. [Accessed October 2015]. Available from: http://www.worldenergy.org/work-programme/strategic-insight/survey-of-energy-resources-and-technologies/

[7] Chen, Y., Duan, J., Lin, P. and Luo Y.H. 2008. Effect of Oxygen Concentration on Combustion Characteristics of Typical Biomass Materials. Proceedings of the CSEE. 28(2), pp.0258-8013.

[8] Gavrilescu, M. 2008. Biomass power for energy and sustainable development. Environmental Engineering and Management Journal. 7(5), pp.617-640.

[9] National Statistics. 2015. Energy: chapter 1, Digest of United Kingdom energy statistics (DUKES). [Online]. [Accessed October 2015]. Available from : https://www.gov.uk/government/statistics/energy-chapter-1-digest-of-united-kingdom-energy-statistics-dukes.

[10] Global Forest Resources Assessment. Progress Towards Sustainable Forest Management. 2005. Food and Agriculture Organization. [Accessed 12 October 2015]. Available from: http://www.fao.org/forestry/fra/en/.

[11] International Energy Agency. 2015. Biomass Task Force 2015. [Online]. [Accessed 13 October 2015]. Available from: http://www.worldenergyoutlook.org/.

[12] Anderson, K., Bows, A. and Mander, S. 2008. From long-term targets to cumulative emission pathways: reframing UK climate policy. Energy Policy. 36(10), pp.3714-3722.

[13] UK Legislation. 2008. Climate Change Act. 2008. [Online]. [Accessed 13 October 2015]. Available from: http://www.legislation.gov.uk/ukpga/2008/27/contents.

[14] HM Government. 2009. The UK Renewable Energy Strategy. [Online]. [Accessed 13 October 2015]. Available from: http://www.officialdocuments.gov.uk/document/cm76/7686/7686.pdf.

[15] Biomass Supply Curves for the UK. 2009. Summary for DECC. E4Tech. [Online]. [Accessed 13 October 2015]. Available from: http://www.decc.gov.uk/en/content/cms/what_we_do/uk_supply/energy_mix/renewable/res/res.aspx.

[16] Gilbert, P., Thornley, P. and Riche, A.B. 2011. The influence of organic and inorganic fertiliser application rates on UK biomass crop sustainability, Biomass and bio energy. 35(3), pp.1170-1181.

[17] Renewable Energy Policy Network For The 21st Century (REN21). 2014. 10 Years Of Renewable Energy Progress (THE FIRST DECADE: 2004–2014). [Online]. [Accessed 13 October 2015]. Available from: http://www.ren21.net/Portals/0/documents/activities/Topical%20Reports/REN21_10yr.pdf.

[18] Ecoprog. 2015. Biomass to Power 2015/2016. [Online]. [Accessed 25 November 2015]. Available from: http://www.ecoprog.com/en/publications/energy-industry/biomass-to-power.htm.

[19]Skrifvars, B., Backman, R. and Hupa, M. 1998. Characterization of the sintering tendency often biomass ashes in FBC conditions by a laboratory test and by phase equilibrium calculations. Fuel Process Technology. 56(1-2), pp.55-67.

[20] Michelsen, H.P. Frandsen, F.F., Dam-Johansen, K. and Larsen, O.H. 1998. Deposition and hightemperature corrosion in a 10 MW straw fired boiler. Fuel Process Technology. 54(1-3), pp.95–108.

[21] Tonn, B., Thumm, U., Lewandowski, I. and Claupein, W. 2012. Leaching of biomass from semi-natural grasslands-Effects on chemical composition and ash high-temperature behaviour. Biomass & Bioenergy. 36(2012), pp.390-403.

[22] Lindstrom, E., Larsson, SH., Bostrom, D. and Ohman, M. 2010. Slagging Characteristics during Combustion of Woody Biomass Pellets Made from a Range of Different Forestry Assortments. Energy & Fuels. 24(6), pp.3456–3461.

[23] Werkelin, J, Skrifvars, B.J. and Hupa, M. 2005. Ash-forming elements in four Scandinavian wood species. Part 1: Summer harvest. Biomass & Bioenergy. 29(2005), pp.451-66.

[24] Visser, H.J.M., Kiel, J.H.A. and Veringa, H.J. 2004. The influence of fuel composition on agglomeration behaviour in fluidised-bed combustion. Delft: Energy research Centre of the Netherlands ECN.

[25] IEA Task 32 and Thermalnet. 2006. Ash related issues in biomass combustion. [Online]. [Accessed 10 November 2015]. Available from: https://ec.europa.eu/energy/intelligent/projects/sites/iee-projects/files/projects/documents/thermalnet_ash_related_issues_in_biomas_combustion.pdf.

[26] Nutalapati, D., Gupta, R., Moghtaderi, B. and Wall, T.F. 2007. Assessing slagging and fouling during biomass combustion: A thermodynamic approach allowing for alkali/ash reactions. Fuel Processing Technology. 88(11-12), pp.1044-1052.

[27] Van-Loo, T.L.S., and Koppejan, J. 2013. Biomass Ash Characteristics and Behaviour in Combustion Systems. [Online]. [Accessed 12 November 2015].

Available from: http://www.ieabioenergy.com/wp-content/uploads/2013/10/IEA-Bioenergy-Update-44-Task-32-Technology-Report.pdf.

[28] Arvelakis, S., Koukios, E.G. 2002. Physicochemical upgrading of agro residues as feedstock for energy production via thermochemical conversion methods. Biomass & Bioenergy. 22(5), pp.331–348.

[29] Lin, W.G, Dam-Johansen, K. and Frandsen, F. 2003. Agglomeration in bio-fuel fired fluidized bed combustors. Chemical Engineering Journal. 96(1-3), pp.171-185.

[30] Williams, A., Pourkashanian, M. and Jones, J.M. 2000. The combustion of coal and someother solid fuels. Symp (Int) Combust. 28(2), pp.2141–2162.

[31] Weber, R., Mancini, M., Schaffel-Mancini, N. and Kupka, T. 2013. On predicting the ash behaviour using Computational Fluid Dynamics. Fuel Processing Technology. 105(2013), pp.113–128.

[32] Nussbaumer, T. 2013. Combustion and Co-combustion of Biomass: Fundamentals, Technologies, and Primary Measures for Emission Reduction, Energy & Fuels. 17(6), pp.1510-1521.

[33] US DOE. 2012. The Early Days of Coal Research. [Online]. [Accessed 17 October 2015]. Available from:http://fossil.energy.gov/aboutus/history/syntheticfuels_history.html.

[34]Bevan, R.R. 1981. “Coal Cleaning.” In Coal Handbook. Meyers, R.A. ed.,New York: Marcel Dekker Inc.

[35] Speight, J.G. 2013. The Chemistry and Technology of Coal. Third Edition. Florida: CRC Press, Taylor & Francis Group.

[36] Aslan, N., Unal, I. 2009. Optimization of some parameters on agglomeration performance of Zonguldak bituminous coal by oil agglomeration. Fuel. 88(2009), pp.490–496.

[37] Aslan, N., Unal, I. 2011. Multi-response optimization of oil agglomeration with multiple performance characteristics. Fuel Process Technology. 92(2011), pp.1157–1163.

[38] Chary, G.H.V.C., Dastidar, M.G. 2012. Investigation of conditions in coal-oil agglomeration using Taguchi experimental design. Fuel. 98(2012), pp.259–264.

[39] Sahinoglu, E. Uslu, T. 2015. Cleaning of high sulphur coal by agglomeration with waste vegetable oil, Energy Sources Part A: Recovery, Utilization, and Environmental Effects. 37(24), pp:2724-2731. [Accessed 19 October 2015]. Available from: http://www.tandfonline.com/doi/full/10.1080/15567036.2011.652760.

[40] Chevanan, N., Womac, A.R., Bitra, V.S.P. 2009. Flowability parameters for chopped switchgrass, wheat straw and corn stover. Powder Technology. 193(1), pp.79-86.

[41] Liu, Y., Guo, X., Lu, H., and Gong, X. 2015. An investigation of the effect of particle size on the flow behaviour of pulverized coal. Procedia Engineering. 102(2015) pp.698 – 713.

[42] Couch, G.R. 1991. Advanced Coal Cleaning Technology. London: International Energy Agency, IEA Coal Research.

[43] Couch, G.R. 1995. Power from Coal - Where to Remove Impurities. London: International Energy Agency, IEA Coal Research.

[44] Sahinoglu, E., Uslu, T. 2008. Amenability of Muzret bituminous coal to oil agglomeration. Energy Convers. 49(2008), pp.3684–3690.

[45] Uslu, T., Sahinoglu, E., and Yavuz, M. 2012. Desulphurization and deashing of oxidized fine coal by knelson concentrator. Fuel Process Technology. 101(2012), pp.94–100.

[46] Chary, G.H.V.C., Dastidar, M.G. 2013. Comprehensive study of process parameters affecting oil agglomeration using vegetable oils. Fuel. 106(2013), pp.285–292.

[47] Isaac Plains Coal Management. 2012. The Coal Handling and Preparation Plant (CHPP). [Online]. [Accessed 20 October 2015]. Available from: http://www.isaacplains.com.au/Information.

[48] Karthikeyan, M., Zhonghua, W. Mujumdar, A.S. 2009. Low-Rank Coal Drying Technologies- Current Status and New Developments. Drying Technology. 27(3), pp.403–415.

[49] Chen, Y., Mori, S., and Pan, W. 1996. "Studying the Mechanisms of Ignition of Coal Particles by TGDTA." Thermochimica Acta, 275(1996), pp.149–158.

[50] Wiley, J. Wiley, S. 2013. Coal-Fired Power Generation Handbook. Canada: Scrivener Publishing LLC.

[51] Glaser, B., Lehmann, J., Zech, W. 2002. Ameliorating physical and chemical properties of highly weathered soils in the tropics with charcoal–a review. Biology and fertility of soils. 35(4), pp.219-230.

[52] Berkowitz, N. 1979. An Introduction to Coal Technology. Academic Press Inc., New York.

[53] Wu, Z. 2005. Fundamentals of pulverised coal combustion. [Online]. [Accessed 20 October 2015]. Available from: http://www.metts.com.au/lignite-new-dedicated-approach.html.

[54] Bozkurt, Y., Misirlioglu, Z., Sinag, A., Tekes, A.T., and Canel, M. 2008. Behavior of Chars from Bursa Mustafa Kemal Pasa Alpagut and Balkesir Dursunbey Cakrca Lignite (Turkey) During Non-Catalytic and Catalytic Gasification. Energy Sources Part A. Recovery Utilization and Environmental Effects. 30(2008), pp.1797–1810.

[55] Chen, J., Niksa, S. 1992. Suppressed nitrogen evolution from coal-derived soot and low volatility coal chars. Twenty-Fourth Symposium (International) on Combustion. 24(1), pp.1269-1276.

[56] Chen, J., Niksa, S. 1992. Coal Devolatilization during Rapid Transient Heating-Part 1: Primary Devolatilization. Energy and Fuels. 6(1992), pp.254.

[57] Chen, J., Castagnoli, C., Niksa, S. 1992. Coal Devolatilization during Rapid Transient Heating- Part 2. Secondary Pyrolysis. Energy and Fuels. 6(1992), pp.264.

[58] Reid, W.T. 1971. External Corrosion and Deposits in Boilers and Gas Turbines. New York: Elsevier.

[59] Ceely, F.J., and Daman, E.L. 1981. Combustion Process Technology. In: Elliott, M.A. ed. Chemistry of Coal Utilization. New York: John Wiley & Sons Inc., pp.1313.

[60] Dainton, A.D. 1979. The Combustion of Coal. In: Pitt, J.G., Millward, G.R. eds. Coal and Modern Coal Processing: An Introduction. London: Academic Press Inc.

[61] Flagan, R.C., Friedlander, S.K. 1978. Particle Formation in Pulverized Coal Combustion – A Review. In: Shaw, D.T. ed. Recent Developments in Aerosol Science. New York : John Wiley & Sons Inc.

[62] Sahinoglu, E., Uslu, T. 2014. Effect of particle size on cleaning of high-sulphur fine coal by oil agglomeration. Fuel Processing Technology. 128(2014), pp.211–219.

[63] Merrick, D. 1984. Coal Combustion and Conversion Technology. London: Macmillan Publishers Ltd.

[64] Skinner, D.G. 1971. Fluidized Bed Combustion of Coal. London: Mills and Boon.

[65] Sahinoglu. E., Uslu, T. 2015. Role of recovery sieve size in upgrading of fine coal via oil agglomeration technique. Fuel Processing Technology. 138(2015), pp.21-29.

[66] McIlveen-Wright, D.R., Huang, Y., Rezvani, S. 2007. A technical and environmental analysis of co-combustion of coal and biomass in fluidised bed technologies. Fuel. 86(14), pp.2032-2042.

[67] Fluidized Bed Combustion (FBC) Boiler. [Online]. [Accessed 20 October 2015]. Available from: http://www.photomemorabilia.co.uk/FBC.html.

[68] Metaxas, A. C., Meredith, R. J. 1983. Industrial microwave heating. London: Peregrinus.

[69] Decareau, R. V. 1985. Microwaves in the food processing industry. Orlando: Academic Press.

[70] Decareau, R. V., Peterson, R. A. 1986. Microwave processing and engineering.

Chichester: Ellis Horwood.

[71] Ishida, M., Zheng, D., Akehata, T. 1987. Evaluation of a chemical-looping-combustion power-generation system by graphic exergy analysis. Energy. 12(1987), pp.147–154.

[72] Lyngfelt, A., Thunman, H. 2005. Construction and 100 h of operational experience of a 10-kW chemical looping combustor. In: Thomas, D. ed. Carbon dioxide capture for storage in deep geologic formations-results from the CO_2 capture project. Oxford: Elsevier.

[73] Noorman, S., Gallucci, F., Van-Sint-Annaland, M., Kuipers, J. 2011. A theoretical investigation of CLC in packed beds. Part 1: particle model. Chemical Engineer Journal. 167(1), pp.297–307.

[74] Noorman, S., Gallucci, F., van-Sint-Annaland, M., Kuipers, J. 2011. A theoretical investigation of CLC in packed beds. Part 2: reactor model. Chemical Engineer Journal. 167(1), pp.369–376.

[75] Lyngfelt, A., Leckner, B., Mattisson, T. 2001. A fluidized-bed combustion process with inherent CO_2 separation; application of chemical-looping combustion. Chemical Engineer Science. 56(10), pp.3101–3113.

[76] How does a Circulating Fluidized Bed Boiler Work. .[Online]. [Accessed 20 October 2015]. Available from: http://www.brighthubengineering.com/power-plants/26547-how-does-a-circulating-fluidized-bed-boiler-work/.

[77] Kanniche, M., Gros-Bonnivard, R., Jaud, P., Valle-Marcos, J., Amann, J.M., Bouallou, C. 2010. Pre-combustion, post-combustion and oxy-combustion in thermal power plant for CO_2 capture. Applied Thermal Engineering. 30(1), pp.53–62.

[78] Skorek-Osikowska, A., Bartela, L., Kotowicz, J., Job, M. Thermodynamic and economic analysis of the different variants of a coal-fired, 460 MW power plant using oxy-combustion technology. Energy Conversion and Management. 76(2013), pp.109–120.

[79] Wall, T.F. 2007. Combustion processes for carbon capture. Proceedings of the combustion institute. 31(1), pp.31-47.

[80] Maurstad, O. 2005. An overview of coal based integrated gasification combined cycle (IGCC) technology. Cambridge: Laboratory for energy and the environment.

[81] Toftegaard, M.B., Brix, J., Jensen, P.A., Glarborg, P., Jensen, A.D. 2010. Oxy-fuel combustion of solid fuels. Progress in energy combusttion science. 36(5), pp.581–625.

[82] Buhre, B.J.P., Elliott, L.K., Sheng, C.D., Gupta, R.P., Wall, T.F. 2005. Oxy-fuel combustion technology for coal-fired power generation. Progress in energy combusttion science. 31(4), pp.283–307.

[83] Liszka, M., Ziebik, A. 2010. Coal-fired oxy-fuel power unit – process and system analysis. Energy. 35(2), pp.943–951.

[84] Kakaras, E., Koumanakos, A., Doukelis, A., Giannakopoulos, D., Vorrias, I. 2007. Simulation of a Greenfield oxyfuel lignite-fired power plant. Energy Convers Manage. 48(11), pp.2879–2887.

[85] Chen, L., Yong, S.Z., Ghoniem, A.F. 2012. Oxy-fuel combustion of pulverized coal: Characterization, fundamentals, stabilization and CFD modelling. Progress in Energy and Combustion Science. 38(2), pp.156-214.

[86] Groves, S., Betterton, W.J., Benzel, W. 2011. Geochemical database of feed coal and coal combustion products (CCPs) from five power plants in the United States. Washington: US Department of the Interior, US Geological Survey.

[87] Rajan, S., and Raghavan, J.K. 1989.. Sixth Annual International Pittsburgh Coal Conference. Pittsburgh: University of Pittsburgh, Proceedings Pennsylvania, pp.979.

[88] Bend, S.L., Edwards, I.A.S., Marsh, H. 1992. The Influence of Rank upon Char Morphology and Combustion. Fuel. 71(5), pp.493-501.

[89] Chen, J.C., Niksa, S. 1992. Suppressed nitrogen evolution from coal-derived soot and low-volatility coal chars. Symposium (International) on Combustion. Elsevier. 24(1), pp.1269-1276.

[90] Mitchell, R.E. 1989. The Influence of the mineral matter content of coal on the temperatures and burning rates of char particles during pulverized coal combustion. Sixth Annual International Pittsburgh Coal Conference. University of Pittsburgh, Pittsburgh. pp. 32.

[91] Skrifvars, B.J., Backman, R., Hupa, M. 1998. Characterization of the sintering tendency of ten biomass ashes in FBC conditions by a laboratory test and by phase equilibrium calculations. Fuel Processing Technology. 56(1), pp.55-67.

[92] Bartels, M., Lin, W., Nijenhuis, J. 2008. Agglomeration in fluidized beds at high temperatures: Mechanisms, detection and prevention. Progress in Energy and Combustion Science. 34(5), pp.633-666.

[93] Nussbaumer, T. 2003. Combustion and co-combustion of biomass: fundamentals, technologies, and primary measures for emission reduction. Energy & fuels. 17(6), pp.1510-1521.

[94] van Loo, S.; Koppejan, J. 2002. Handbook of Biomass Combustion and Co-Firing. Twente: Twente University Press.

[95] Palmowski, L.M., Müller, J.A. 2000. Influence of the size reduction of organic waste on their anaerobic digestion. Water Science and Technology. 41(3), pp.155-162.

[96] Cadoche, L., López, G.D. 1989. Assessment of size reduction as a preliminary step in the production of ethanol from lignocellulosic wastes. Biological Wastes. 30(2), pp.153-157.

[97] Bougrier, C., Albasi, C., Delgenès, J.P. 2006. Effect of ultrasonic, thermal and ozone pre-treatments on waste activated sludge solubilisation and anaerobic biodegradability. Chemical Engineering and Processing: Process Intensification. 45(8), pp.711-718.

[98] Fengel, D., Wegener, G. 1983. Wood: chemistry, ultrastructure, reactions. New York: Walter de Gruyter.

[99] Chandra, R.P., Bura, R., Mabee, W.E. 2007. Substrate pretreatment: The key to effective enzymatic hydrolysis of lignocellulosics?. Biofuels. Springer Berlin Heidelberg(2007), pp.67-93.

[100] Hatakka, A. 1994. Lignin-modifying enzymes from selected white-rot fungi: production and role from in lignin degradation. FEMS microbiology reviews. 13(2-3), pp.125-135.

[101] Bergman, P.C.A., Kiel, J.H.A. 2005. Torrefaction for biomass upgrading. Proc. 14th European Biomass Conference, Paris, France. 2005: 17-21.

[102] Baxter, L.L., Miles, T.R., Jenkins, B.M. 1988. The behaviour of inorganic material in biomass-fired power boilers: field and laboratory experiences. Fuel processing technology. 54(1), pp.47-78.

[103] Nussbaumer, T. 2003. Combustion and co-combustion of biomass: fundamentals, technologies, and primary measures for emission reduction. Energy & fuels. 17(6), pp.1510-1521.

[104] Nussbaumer, T. 1999. Stromerzeugung aus biogenen Brennstoffen. Brennstoff-Wärme-Kraft. 51(7-8), pp.51-55.

[105] Obernberger, I., Brunner, T., Jöller, M. 2001. Characterisation and formation of aerosols and fly-ashes from fixed-bed biomass combustion. Aerosol from Biomass Combustion. 27(2001), pp.69-74.

[106] Werther, J., Saenger, M., Hartge, E.U. 2000. Combustion of agricultural residues. Progress in energy and combustion science. 26(1), pp.1-27.

[107] Li, J., Li, B., Zhang, X. 2002. Comparative studies of thermal degradation between larch lignin and manchurian ash lignin. Polymer degradation and stability. 78(2), pp.279-285.

[108] Fang, M.X., Shen, D.K., Li, Y.X. 2006. Kinetic study on pyrolysis and combustion of wood under different oxygen concentrations by using TG-FTIR analysis. Journal of analytical and applied pyrolysis. 77(1), pp.22-27.

[109] Nussbaumer, T., Hasler, P. 1999. Bildung und Eigenschaften von Aerosolen aus Holzfeuerungen. European Journal of Wood and Wood Products. 57(1), pp.13-22.

[110] Brunner, T., Obernberger, I., Jöller, M. 2001. Behaviour of Ash Forming Compounds in Biomass Furnaces-Measurement and Analyses of Aerosols Formed during Fixed-Bed Biomass Combustion. Aerosols from Biomass Combustion. Verenum, Zürich(2001), pp.75-80.

[111] Oser, M., Nussbaumer, T., Schweizer, B. 2001. Influences on aerosol formation in an automatic wood furnace. Aerosols from Biomass Combustion. 2001, pp.59-64.

[112] Niu, Y., Zhu, Y., Tan, H., Hui, S., Jing, Z., Xu, W. 2014. Investigations on biomass slagging in utility boiler: Criterion numbers and slagging growth mechanisms. Fuel Processing Technology. 128(2014), pp.499-508.

[113] Walsh, P.M., Sarofim, A.F., Beer, J.M. 1992. Fouling of convection heat exchangers bylignitic coal ash. Energy Fuels. 6(6), pp.709–15.

[114] Brus, E., Ohman, M., Nordin, A. 2005. Mechanisms of bed agglomeration during fluidized-bed combustion of biomass fuels. Energy & Fuels. 19(3), pp.825-832.

[115] Grimm, A., Skoglund, N., Bostrom, D., Ohman, M. 2011. Bed agglomeration characteristics in fluidized quartz bed combustion of phosphorus-rich biomass fuels. Energy & Fuels. 25(3), pp.937-47.

[116] Melissari, B. 2014. Ash related problems with high alkalii biomass and its mitigation-Experimental evaluation. Memoria Investigaciones en Ingenier á. 12(2014), pp.31-44.

[117] Ohman, M., Boman, C., Hedman, H., Nordin, A., Bostrom, D. 2004. Slagging tendencies of wood pellet ash during combustion in residential pellet burners. Biomass & Bioenergy. 27(6), pp.585-96.

[118] Ohman, M., Nordin, A., Skrifvars, B.J., Backman, R., Hupa, M. 2000. Bed agglomeration characteristics during fluidized bed combustion of biomass fuels. Energy & Fuels. 14(1), pp.169-78.

[119] Grimm, A., Ohman, M., Lindberg, T., Fredriksson, A., Bostrom, D. 2012. Bed agglomeration characteristics in fluidized-bed combustion of biomass fuels using olivine as bed material. Energy & Fuels. 26(7), pp.4550-4559.

[120] Visser, H.J.M. 2004. The influence of fuel composition on agglomeration behaviour in fluidised-bed combustion. Netherlands: Energy research centre of the Netherlands ECN.

[121] Visser, H.J.M., Hofmans, H., Huijnen, H. 2008. Biomass ash-bed material interactions leading to agglomeration in fluidised bed combustion and gasification. Progress in thermochemical biomass conversion. 2008, pp.272.

[122] Arvelakis, S., Frandsen, F.J. 2010. Rheology of fly ashes from coal and biomass co-combustion. Fuel. 89(10), pp.3132-3140.

[123] Asadullah, M., Miyazawa, T., Ito, S. 2004. Gasification of different biomasses in a dual-bed gasifier system combined with novel catalysts with high energy efficiency. Applied Catalysis A: General. 267(1), pp.95-102.

[124] L.F. Calvo, et, al, (2012), Gasification of rice straw in a fluidized-bed gasifier for syngas application in close-coupled boiler-gasifier systems, Bioresource Technology 109, 206–214.

[125] Kruse, A. 2008. Supercritical water gasification. Biofuels, Bioproducts and Biorefining. 2(5), pp.415-437.

[126] Chen, H., Li, B., Yang, H., Yang, G., Zhang, S. 2008. Experimental investigation of biomass gasification in a fluidized bed reactor, Energy & Fuels. 22(5), pp.3493–3498.

[127] Directive, C. 1986. Council directive on the protection of the environment, and in particular of the soil, when sewage sludge is used in agriculture. Offic. J. Eur. Comm. 181(1986), pp. 06-12.

[128] Vassilev, S.V., Baxter, D., Andersen. L.K. 2013. An overview of the composition and application of biomass ash. Part 1. Phase–mineral and chemical composition and classification. Fuel.105(2013), pp.40-76..

[129] López, I.C., Ward, C.R. 2008. Composition and mode of occurrence of mineral matter in some Colombian coals. International Journal of Coal Geology. 73(1), pp.3-18.

[130] Wieland, C., Kreutzkam, B., Balan, G. 2012. Evaluation, comparison and validation of deposition criteria for numerical simulation of slagging. Applied Energy. 93(2012), pp.184-192..

[131] Barbosa, R., Lapa, N., Lopes, H. 2012. Chemical and ecotoxicological properties of ashes produced in the co-combustion of coal and meat and bone meal in a fluidized bed reactor. Fuel Processing Technology. 96(2012), pp.48-55.

[132] Nathan, Y., Dvorachek, M., Pelly, I. 1999. Characterization of coal fly ash from Israel. Fuel. 78(2), pp.205-213.

[133] Piñeres, J., Barraza, J. 2012. Effect of pH, air velocity and frother concentration on combustible recovery, ash and sulphur rejection using column flotation. Fuel Processing Technology. 97(2012), pp.30-37.

[134] Rincon, J.M., Angulo, R. 1986. Petroleum heavy oil mixtures as a source of hydrogen in the liquefaction of Cerrejon coal. Fuel. 65(7), pp.899-902.

[135] Quintero, J.A., Candela, S.A., Ríos, C.A. 2009. Spontaneous combustion of the upper paleocene cerrejón formation coal and generation of clinker in la guajira peninsula (Caribbean region of Colombia). International Journal of Coal Geology. 80(3), pp.196-210.

[136] Williams, A., Pourkashanian, M., Jones, J.M. 2000. The combustion of coal and some other solid fuels. Proceedings of the Combustion Institute. 28(2), pp.2141-2162.

[137] G. Couch. 1994. Understanding Slagging and Fouling during PF Combustion. London: IEA Coal Research.

[138] Bryers, R.W. 1996. Fireside slagging, fouling, and high-temperature corrosion of heat-transfer surface due to impurities in steam-raising fuels. Progress in energy and combustion science. 22(1), pp.29-120.

[139] Sarofim, A.F., Helble, J.J. 1994. Mechanisms of ash and deposit formation. In: Williamson, J., Wigley, F. eds. The Impact of Ash Deposition on Coal-Fired Power Plants. Birmingham: United Engineering Foundation International. pp.25-28.

[140] Demirbas, A. 2005. Potential applications of renewable energy sources, biomass combustion problems in boiler power systems and combustion related environmental issues. Progress in energy and combustion science. 31(2), pp.171-192.

[141] Dai, J., Sokhansanj, S., Grace, J.R. 2008. Overview and some issues related to co‐firing biomass and coal. The Canadian Journal of Chemical Engineering. 86(3), pp.367-386.

[142] Niu, Y., Liu, Y., Tan, H. 2013. Origination and formation of NH_4Cl in biomass-fired furnace. Fuel Processing Technology. 106(2013), pp.262-266.

[143] Lindström, E., Larsson, S.H., Boström, D. 2010. Slagging characteristics during combustion of woody biomass pellets made from a range of different forestry assortments. Energy & Fuel. 24(6), pp.3456-3461.

[144] Wang, X., Liu, Y., Tan, H. 2012. Mechanism research on the development of ash deposits on the heating surface of biomass furnaces. Industrial & Engineering Chemistry Research. 51(39), pp.12984-12992.

[145] Niu, Y.Q., Tan, H.Z., Ma, L., Pourkashanian, M., Liu, Z.N., Liu, Y. 2010. Slagging characteristics on the superheaters of a 12 MW biomass-fired boiler. Energy & Fuel. 24(9), pp.5222-5227.

[146] Liu, H., Tan, H., Liu, Y. 2011. Study of the layered structure of deposit in a biomass-fired boiler (case study). Energy & Fuels. 25(6), pp.2593-2600.

[147] Alstrup, I. 1995. On the kinetics of CO methanation on nickel surfaces. Journal of Catalysis. 151(1), pp.216-225..

[148] Boxiong, S., Chunfei, W., Lei, Q. 2006. MSW catalytic combustion by alkali and alkali–earth salts. Energy. 31(14), pp.2900-2914.

[149] Rustamov, V.R., Abdullayev, K.M., Samedov, E.A. 1998. Biomass conversion to liquid fuel by two-stage thermochemical cycle. Energy Conversion and Management. 39(9), pp.869-875.

[150] Yu, Z., Ma, X., Ao, L. 2008. Kinetic studies on catalytic combustion of rice and wheat straw under air-and oxygen-enriched atmospheres, by using thermogravimetric analysis. Biomass and Bioenergy. 32(11), pp.1046-1055.

[151] Vassilev, S.V., Baxter, D., Andersen, L.K. 2013. An overview of the composition and application of biomass ash.: Part 2. Potential utilisation, technological and ecological advantages and challenges. Fuel. 105(2013), pp.19-39.

[152] Vamvuka, D., Kakaras, E. 2011. Ash properties and environmental impact of various biomass and coal fuels and their blends. Fuel Processing Technology. 92(3), pp.570-581.

[153] Steenari, B.M., Lindqvist, O. 1998. High-temperature reactions of straw ash and the anti-sintering additives kaolin and dolomite. Biomass and Bioenergy. 14(1), pp.67-76.

[154] Kyi, S., Chadwick, B.L. 1999. Screening of potential mineral additives for use as fouling preventatives in Victorian brown coal combustion. Fuel. 78(7), pp.845-855.

[155] Koukouzas, N., Ward, C.R., Papanikolaou, D. 2009. Quantitative evaluation of minerals in fly ashes of biomass, coal and biomass–coal mixture derived from circulating fluidised bed combustion technology. Journal of Hazardous Materials. 169(1), pp.100-107.

[156] Pera, J., Amrouz, A. 1998. Development of highly reactive metakaolin from paper sludge. Advanced Cement Based Materials. 7(2), pp.49-56.

[157] Dare, P., Gifford, J., Hooper, R.J. 2001. Combustion performance of biomass residue and purpose grown species. Biomass and Bioenergy. 21(4), pp.277-287.

[158] Williams, A., Jones, J.M., Ma, L. 2012. Pollutants from the combustion of solid biomass fuel. Progress in Energy and Combustion Science. 38(2), pp.113-137.

[159] Roman, M., Bobasu, E., Selisteanu, D. 2011. Modelling of biomass combustion process. Energy procedia. 6(2011), pp.432-440.

[160] Venturini, P., Borello, D., Iossa, C. 2010. Modeling of multiphase combustion and deposit formation in a biomass-fed furnace. Energy. 35(7), pp.3008-3021.

[161] Favre, A. 1965. Equations de gaz turbulents compressibles. Journal de Mécanique. 4(1965), pp.361-421.

[162] Ross, A.B., Jones, J.M., Chaiklangmuang, S. 2002. Measurement and prediction of the emission of pollutants from the combustion of coal and biomass in a fixed bed furnace. Fuel. 81(5), pp.571-582..

[163] Brus, E., Öhman, M., Nordin, A. 2004. Bed agglomeration characteristics of biomass fuels using blast-furnace slag as bed material. Energy & fuels. 18(4), pp.1187-1193.

[164] Chen, A., Yang, X., Lin, W. 2007. Thermodynamic equilibrium analysis on release characteristics of chlorine and alkali metals during combustion of biomass residues. CHINESE JOURNAL OF PROCESS ENGINEERING. 7(5), pp.989.

[165] Xiong, S., Ohman, M., Zhang, Y. 2010. Corn stalk ash composition and its melting (slagging) behavior during combustion. Energy & Fuels. 24(9), pp.4866-4871.

[166] Boström, D., Skoglund, N., Grimm, A. 2011. Ash transformation chemistry during combustion of biomass. Energy & Fuels. 26(1), pp.85-93.

[167] Garba, M.U., Ingham, D.B., Ma, L. 2012. Prediction of potassium chloride sulfation and its effect on deposition in biomass-fired boilers. Energy & Fuels. 26(11), pp.6501-6508.

[168] Aho, M. 2001. Reduction of chlorine deposition in FB boilers with aluminium-containing additives. Fuel. 80(13), pp.1943-195.

[169] Jimenez, S., Ballester, J. 2005. Influence of operating conditions and the role of sulfur in the formation of aerosols from biomass combustion. Combustion and Flame. 140(4), pp.346-358.

[170] Reichelt, J., Pfrang-Stotz, G., Bergfeldt, B. 2013. Formation of deposits on the surfaces of superheaters and economisers of MSW incinerator plants. Waste Management. 33(1), pp.43-51.

[171] Nutalapati, D., Gupta, R., Moghtaderi, B. 2007. Assessing slagging and fouling during biomass combustion: A thermodynamic approach allowing for alkali/ash reactions. Fuel Processing Technology. 88(11), pp.1044-1052.

[172] Li, L., Yu, C., Huang, F. 2012. Study on the deposits derived from a biomass circulating fluidized-bed boiler. Energy & Fuels. 26(9), pp.6008-6014.

[173] Davidsson, K.O., Amand, L.E., Steenari, B.M. 2008. Countermeasures against alkali-related problems during combustion of biomass in a circulating fluidized bed boiler. Chemical Engineering Science. 63(21), pp.5314-5329.

[174] Oleschko, H., Müller, M. 2007. Influence of coal composition and operating conditions on the release of alkali species during combustion of hard coal. Energy & Fuels. 21(6), pp.3240-3248.

[175] Díaz-Ramírez, M., Boman, C., Sebastián, F. 2012. Ash characterization and transformation behavior of the fixed-bed combustion of novel crops: poplar, brassica, and cassava fuels. Energy & Fuels. 26(6), pp.3218-3229.

[176] Vamvuka, D., Zografos, D., Alevizos, G. 2008. Control methods for mitigating biomass ash-related problems in fluidized beds. Bioresource Technology. 99(9), pp.3534-3544.

[177] Tran, Q.K., Steenari, B.M., Iisa, K. 2004. Capture of potassium and cadmium by kaolin in oxidizing and reducing atmospheres. Energy & fuels. 18(6), pp.1870-1876.

[178] Steenari, B.M., Lindqvist, O. 1998. High-temperature reactions of straw ash and the anti-sintering additives kaolin and dolomite. Biomass and Bioenergy. 14(1), pp.67-76.

[179] Dare, P., Gifford, J., Hooper, R.J. 2001. Combustion performance of biomass residue and purpose grown species. Biomass and Bioenergy. 21(4), pp.277-287.

[180] Friedl, A., Padouvas, E., Rotter, H. 2005. Prediction of heating values of biomass fuel from elemental composition. Analytica Chimica Acta. 544(1), pp.191-198.

[181] Majumder, A.K., Jain, R., Banerjee, P. 2008. Development of a new proximate analysis based correlation to predict calorific value of coal. Fuel. 87(13), pp.3077-3081.

[182] Collura S, Chaoui N, Azambre B, et al. Influence of the soluble organic fraction on the thermal behaviour, texture and surface chemistry of diesel exhaust soot. Carbon, 2005, 43(3): 605-613..

[183] Niu, Y., Tan, H., Wang, X. 2010. Study on fusion characteristics of biomass ash. Bioresource technology. 101(23), pp.9373-9381.

[184] Werkelin, J., Skrifvars, B.J., Zevenhoven, M. 2010. Chemical forms of ash-forming elements in woody biomass fuels. Fuel. 89(2), p.481-493.

[185] Tonn, B., Thumm, U., Lewandowski, I. 2012. Leaching of biomass from semi-natural grasslands–Effects on chemical composition and ash high-temperature behaviour. Biomass and Bioenergy. 36(2012), pp.390-403.

[186] Nowakowski, D.J., Jones, J.M., Brydson, R.M.D. 2007. Potassium catalysis in the pyrolysis behaviour of short rotation willow coppic. Fuel. 86(15), pp.2389-2402.

[187] Thyrel, M., Samuelsson, R., Finell, M. 2013. Critical ash elements in biorefinery feedstock determined by X-ray spectroscopy. Applied Energy. 102(2013), pp.1288-1294.

[188] C.E.N. Standard, BS EN 15290:2011 Solid biofuels - Determination of major elements, in, BSI, 2011.

[189] BS EN 14775:2009 Solid biofuels - Determination of ash content in, CEN 2009.

[190] CEN/TS 15370-1:2006 Solid biofuels - Method for the determination of ash melting behaviour - Part 1: Characteristic temperatures method in, CEN 2006.

[191] Du, S., Yang, H., Qian, K., Wang, X., Chen, H. 2014. Fusion and transformation properties of the inorganic components in biomass ash. Fuel. 117(2014), pp.1281–1287.

[192] Baxter, X.C., Darvell, L.I., Jones, J.M., Barraclough, T., Yates, N.E., Shield, I. 2012. Study of Miscanthus x giganteus ash composition – Variation with agronomy and assessment method. Fuel. 95(2012), pp.50–62.

[193] Pang, C.H., Hewakandamby, B., Wu, T., Lester, E. 2013. An automated ash fusion test for characterisation of the behaviour of ashes from biomass and coal at elevated temperatures. Fuel. 103(2013), pp.454–466.

[194] McLennen, A.R., Bryant, G.W., Bailey, C.W., Stanmore, B.R., Wall, T.F.. 2000. Index for iron-based slagging for pulverized coal firing in oxidizing and reducing conditions. Energy & Fuel. 14(2000), pp.349–54.

[195] Erickson, T.A., Allan, S.E., McCollor, D.P. 1995. Modelling of fouling and slagging in coal-fired utility boilers. Fuel Processing Technology. 44(1), pp.155-171.

[196] Raask, E. 1979. Sintering characteristics of coal ashes by simultaneous dilatometry-electrical conductance measurements. Journal of Thermal Analysis and Calorimetry.16(1), pp.91-102.

[197] Wigley, F., Williamson, J., Jones, A.R. 1990. Slagging indices for UK coals and their relationship with mineral matter. Fuel Processing Technology. 24(1990), pp.383-389.

[198] Lawrence, A., Kumar, R., Nandakumar, K. 2008. A Novel tool for assessing slagging propensity of coals in PF boilers. Fuel. 87(6), pp.946-950.

[199] Yin, C., Luo, Z., Ni, M. 1998. Predicting coal ash fusion temperature with a back-propagation neural network model. Fuel. 77(15), pp.1777-1782.

[200] Gupta, S.K., Wall, T.F., Creelman, R.A. 1998. Ash fusion temperatures and the transformations of coal ash particles to slag. Fuel processing technology. 56(1), pp.33-43.

[201] Wang, G., Pinto, T., Costa, M. 2014. Investigation on ash deposit formation during the co-firing of coal with agricultural residues in a large-scale laboratory furnace. Fuel. 117(2014), pp.269-277.

[202] Jenkins, B.M., Baxter, L.L., Miles, T.R. 1998. Combustion properties of biomass. Fuel processing technology. 54(1), pp.17-46.

[203] Li, Q.H., Zhang, Y.G., Meng, A.H., Li, L., Li, G.X. 2013. Study on ash fusion temperature using original and simulated biomass ashes. Fuel Processing Technology. 107(2013), pp.107–112.

[204] Wang, G., Silva, R.B., Azevedo, J.L.T., Martins-Dias, S., Costa, M. 2014. Evaluation of the combustion behaviour and ash characteristics of biomass waste derived fuels, pine and coal in a drop tube furnace. Fuel. 117(2014), pp.809–824.

[205] Degereji, M.U., Ingham, D.B., Ma, L., Pourkashanian, M., Williams, A. 2012. Numerical assessment of coals/blends slagging potential in pulverized coal boilers. Fuel. 102(2012), pp.345–353.

[206] Degereji, M.U., Gubba, S.R., Ingham, D.B., Ma, L., Pourkashanian, M., Williams, A., Williamson, J. 2013. Predicting the slagging potential of co-fired coal with sewage sludge and wood biomass. Fuel. 108(2013), pp.550–556.

[207] Watt, J.D., Fereday, F. 1969. The flow properties of slag formed from the ashes of British coals: Part 1: viscosity of homogeneous liquid slag in relation to slag composition. J Inst Fuel. 42(1969), pp.99–103.

[208] Vargas, S., Frandsen, F.J., Dam-Johansen. K. 2001. Rheological properties of high-temperature melts of coal ashes and other silicates. Progress in Energy and Combustion Science. 27(3), pp.237-429.

[209] Streeter, R.C., Diehl, E.K., Schobert, H.H. 1984. ACS Symposium Series. 1984, pp. 195-209

[210] Urbain, G., Cambier, F., Deletter, M., Anseau, M.R. 1981. Trans J Br Ceram Soc. 80(1981), pp.139-141.

[211] Nordgren, D., Hedman, H., Padban, N., Boström, D., Öhman, M. 2013. Ash transformations in pulverised fuel co-combustion of straw and woody biomass. Fuel Processing Technology. 105(2013), pp.52–58.

[212] Rizvi, T., Xing, P., Pourkashanian, M., Darvell, L.I., Jones, J., Nimmo, W. 2015. Prediction of biomass ash fusion behaviour by the use of detailed characterisation methods coupled with thermodynamic analysis. Fuel. 141(2015), pp.275–284.